

**GASEOUS SECONDARY ELECTRON
DETECTION AND CASCADE
AMPLIFICATION IN THE ENVIRONMENTAL
SCANNING ELECTRON MICROSCOPE**

By
Scott Warwick Morgan

A THESIS SUBMITTED IN FULFILMENT OF THE
REQUIREMENTS FOR THE DEGREE OF
DOCTOR OF PHILOSOPHY

FACULTY OF SCIENCE
UNIVERSITY OF TECHNOLOGY, SYDNEY
AUSTRALIA
2005

Certificate

I certify that the work in this thesis has not previously been submitted for a degree nor has it been submitted as part of requirements for a degree except as fully acknowledged within the text.

I also certify that the thesis has been written by me. Any help that I have received in my research work and the preparation of the thesis itself has been acknowledged. In addition, I certify that all information sources and literature used are indicated in the thesis.

Signature of Author

To My Family.

Acknowledgments

This work in this thesis was conducted under the supervision of Assoc. Prof. Matthew Phillips, director of the Microstructural Analysis Unit (MAU), University of Technology, Sydney (UTS). I would like to sincerely thank Assoc. Prof. Phillips for his undivided help and support during the entirety of my research. His cool, calm and collected, but rigorous, approach to science made my time spent with him very learned and enjoyable.

I would like to thank Dr Miloš Tóth, currently at the FEI company, Boston, for his ongoing help, fruitful discussions and experimental collaboration both at UTS and the Polymer and Colloids Group, Cavendish Laboratory, University of Cambridge. I would also like to thank the staff of the physics department at UTS for valuable discussions and for the loan of some of the equipment used in experiments. I wish to thank the staff at the MAU, consisting of Richard Wuhrer, Mark Berkahn and Katie McBean, for outstanding technical support and friendly advice.

I would especially like to thank my fiancé Larissa Lembke for her devoted love and support over the entire course of my PhD. I am grateful to Larissa for putting up with my ‘occasional’ bad moods, late nights, missing dinners and proof-reading this thesis. “Thanks darling”.

I sincerely thank my parents (Warwick and Lynette), nanna (Pearl) for their utmost moral and financial support, and for continuously being there for me. I also gratefully thank the other close members of my family and friends for their help,

support, physics discussions and for sharing a beer with me when I needed it most. I apologize to anyone for whom felt at times my PhD was of more importance than them.

Lastly, I wish to thank Chris Cornell, James Hetfield and my Ibanez RG 450 for the jam sessions when my brain could not take anymore.

Table of Contents

List of Figures	viii
List of Tables	xix
Nomenclature	xxi
Abstract	xxxv
1 Introduction	1
2 Background to Environmental Scanning Electron Microscopy	5
2.1 Introduction	6
2.2 Vacuum System	8
2.3 Primary Electron Beam-Gas Scattering	11
2.3.1 Scattering Cross Sections	12
2.3.2 Primary Electron Beam Transmission	23
2.3.3 Electron Distribution and Skirt Profiles	26
2.4 Signal Detection	36
2.4.1 Induced Signals	41
2.4.2 Gaseous Secondary Electron Detector Electronics	50
3 Gaseous Cascade Amplification in Partially Ionized Gases - Townsend Gas Capacitor Model	54
3.1 Introduction	55
3.2 General Overview of Cascade Amplification	56
3.3 Cascade Amplification of Electrons	59
3.4 Cascade Amplification of Primary Electrons	61
3.5 Cascade Amplification of Backscattered Electrons	63
3.6 Cascade Amplification of Secondary Electrons	64

3.7	Cascade Amplification of Secondary Electrons Generated by Ion, Photon, Metastable and Neutral Molecule Surface Collisions	65
3.8	Electron Impact Ionization Cross sections	75
3.9	Ionization Efficiency of Primary and Backscattered Electrons	80
3.10	Ionization Efficiency of Secondary and Environmental Electrons - First Townsend Ionization Coefficient	81
3.11	Gaseous Cascade Amplification Profiles	85
4	Transient Analysis of Gaseous Electron-Ion Recombination in the Environmental Scanning Electron Microscope	98
4.1	Introduction	99
4.2	Theory	101
4.2.1	Gaseous Electron-Ion Recombination	101
4.3	Transient SE-Ion Recombination Model	109
4.4	Experimental Techniques	117
4.4.1	Measurement of Electronic Gas Amplification	118
4.4.2	Determination of Recombination Coefficients, Recombination Rates, Ionization Rates, Electron Drift Velocities and Time Constants	120
4.5	Preamble	122
4.6	Results and Discussion	132
4.6.1	Generation Rates	132
4.6.2	Electron Drift Velocities	136
4.6.3	Recombination Coefficients	138
4.6.4	Recombination Rates	142
4.6.5	Time Constants	144
4.7	Future Work	146
4.8	Conclusions	148
5	A Preliminary Investigation of Gaseous Scintillation Detection and Amplification in Environmental SEM	150
5.1	Introduction	151
5.2	Theory	153
5.2.1	Gaseous Proportional Scintillation and Electroluminescence	153
5.3	Gaseous Scintillation and Electroluminescence Amplification Model	159
5.4	Experimental Techniques	164
5.4.1	Determination of Photon Amplification	166
5.4.2	Determination of Electronic Amplification	171
5.5	Results and Discussion	173

5.5.1	Images Obtained Using GSD and GSED	173
5.5.2	Photon and Electronic Amplification Using the GSED to Generate Gaseous Scintillation	179
5.5.3	Photon and Electronic Amplification Using the GSD to Generate Gaseous Scintillation - Enhancement of Photon Collection Utilizing Electrostatic Focusing	190
5.6	Future Work	197
5.7	Conclusions	198
6	Photon Emission Spectra of Electroluminescent Imaging Gases Commonly Utilized in the Environmental SEM	200
6.1	Introduction	201
6.2	Experimental Techniques	203
6.3	Results and Analysis	205
6.3.1	Emission Spectra of Argon	205
6.3.2	Emission Spectra of Nitrogen	208
6.4	Conclusions	211
A	Atomic and Molecular Collisions in Partially Ionized Gases	213
	Bibliography	225

List of Figures

2.1	Schematic diagram showing the ESEM vacuum system. The vacuum system consists of five stages of increasing vacuum level. The stages are the specimen chamber, first environmental chamber (EC1), second environmental chamber (EC2), electron column and electron gun. The column and chamber regions are separated by two pressure limiting apertures (PLAs). The PLAs are placed close together to minimize PE scattering (adapted from Philips Electron Optics (1996)). [IP=ion pump, DP=diffusion pump, RT=rotary pump]	10
2.2	Differential scattering cross section $d\sigma/d\Omega$ (elastic, inelastic and total) versus scattering angle θ in argon (Ar) (adapted from Danilatos (1988) and Jost & Kessler (1963)). [$\varepsilon_{PE} = 30$ keV]	17
2.3	Total scattering cross section (σ_T^s) of monotonic (argon (Ar)), diatomic (nitrogen (N ₂)) and polyatomic (water vapour (H ₂ O)) gases versus primary electron beam energy (ε_{PE}) (Danilatos 1988, Jost & Kessler 1963).	20
2.4	Experimentally obtained total scattering cross sections (σ_T^s) versus primary electron beam energy (ε_{PE}) for water vapour (H ₂ O) and nitrogen (N ₂) (Phillips <i>et al.</i> 1999). [$d = 6.5$ mm, $T = 298$ K]	23

2.5	Schematic diagram illustrating the scattering regimes for an electron beam traversing a gaseous medium. A conventional high vacuum SEM operates in the ‘minimal scattering regime’ whilst an ESEM operates in the ‘partial scattering regime’. Complete scattering of the PE beam conveys no useful image information (taken from Philips Electron Optics 1996).	24
2.6	Experimental primary electron beam transmission (unscattered probe current (I_{PE}^0) to beam current (I_{PE}) ratio) versus (a) nitrogen pressure (p_{N_2}) and (b) water vapour pressure (p_{H_2O}) at various primary electron beam energies (ε_{PE}) (Phillips <i>et al.</i> 1999). [$d = 6.45$ mm, $T = 298$ K]	27
2.7	Schematic diagram illustrating PE-gas scattering in the ESEM. A PE of energy ε_{PE} undergoing a collision with a gas atom or molecule between z and $z + dz$ is scattered through an angle θ and $\theta + d\theta$ into the solid angle $d\Omega$. The scattered PE then strikes the sample surface between r and $r + dr$ (Danilatos 1988, Kadoun <i>et al.</i> 2003).	28
2.8	Theoretical plural scattering normalized beam intensity versus radial distance (r) from beam center for an infinitely thin electron beam (delta function) in argon (Ar) acquired as a function of argon pressure (p_{Ar}) (adapted from Danilatos 1988 and Jost & Kessler 1963). [$\varepsilon_{PE} = 50$ keV, $d = 6.45$ mm, $T = 298$ K]	32
2.9	Experimental normalized beam intensity versus radial distance (r) from beam center acquired as a function of (a) nitrogen pressure (p_{N_2}) and (b) water vapour pressure (p_{H_2O}) (Phillips <i>et al.</i> 1999). [$\varepsilon_{PE} = 30$ keV, $d = 10.0$ mm]	33

2.10	Theoretical plural scattering skirt half radius ($r_{1/2}$) versus argon pressure (p_{Ar}) and sample-electrode separation (d) for an infinitely thin electron beam in argon (Ar) (adapted from Danilatos 1988 and Jost & Kessler 1963). [$\varepsilon_{PE} = 50$ keV, $T = 298$ K]	35
2.11	Image showing the gaseous secondary electron detector (GSED). The suppressor electrode is placed at +9 volts relative to the ring voltage to discriminate against backscattered and type III secondary electrons.	37
2.12	Schematic diagram showing the various signals used to generate gaseous secondary electron detector (GSED) and induced stage current (ISC) images in an ESEM. Primary beam electrons (PEs) generate secondary electrons (SEs) and backscattered electrons (BSEs) which ionize gas molecules producing positive ions (PIs) and environmental secondary electrons (ESEs). These signals induce current flows I_{GSED} and I_{ISC} in the ring and stage, respectively, which are then amplified to produce images.	39
2.13	Schematic diagram showing the generation of the induced signals I_{GSED} and I_{ISC} by a particle of charge $-e$ traversing the gap in a typical ESEM containing distributed capacitances and resistances. The gaseous secondary electron detector (GSED) and induced stage current (ISC) amplifiers have time constants R_1C_1 and R_2C_2 , respectively. The time constant of an insulating sample is R_3C_3 . The GSED or ISC electronics can be represented by an equivalent circuit of total time constant RC . [d = sample-electrode separation, ds = particle displacement, E = electric field, v_d = drift velocity, R = resistance, C = capacitance]	40

2.14	Voltage signal (V_S) versus time (t) at various time constants (RC) when an electron and a positive ion (PI) of transit times Γ_e and Γ_i , respectively, are accelerated across a potential difference (V) after being released in the center of the gap. For clarity, the drift velocity of the electron was set to twice that of the ion ($v_e = 2v_i$ or $\Gamma_e = \Gamma_i/2$). . . .	47
2.15	Schematic diagram of the gaseous secondary electron detector (GSED) preamplifier circuit (adapted from Philips Electron Optics 1997). . . .	51
3.1	Second Townsend coefficient (γ) versus reduced electric field (E/p) for various gases (nitrogen (N_2), argon (Ar)) and cathode materials (Pt, Na, Cu, Fe) (adapted from von Engel 1965)	71
3.2	Total electron impact ionization cross sections (σ_T^i) for argon (Ar) as a function of electron energy (ε). Experimentally and theoretically obtained cross sections are represented by points and line plots, respectively (Asundi & Kurepa 1963, Fletcher & Cowling 1972, Märk 1982, Rapp & Englander-Golden 1965, Schram <i>et al.</i> 1966, Smith 1930, Srinivasan & Rees 1967, Straub <i>et al.</i> 1995, Wallace <i>et al.</i> 1973).	76
3.3	Total electron impact ionization cross sections (σ_T^i) for nitrogen (N_2) as a function of electron energy (ε). Experimentally and theoretically obtained cross sections are represented by points and line plots, respectively (Deutsch <i>et al.</i> 2000, Hwang <i>et al.</i> 1996, Khare & Meath 1987, Krishnakumar & Srivastava 1992, Rapp & Englander-Golden 1965, Saksena <i>et al.</i> 1997a, Saksena <i>et al.</i> 1997b, Schram <i>et al.</i> 1965, Schram <i>et al.</i> 1966, Straub <i>et al.</i> 1996). [BEB=binary-encounter-Bethe method, BED=binary-encounter-dipole method]	77

3.4	Total electron impact ionization cross sections (σ_T^i) for water vapour (H_2O) as a function of electron energy (ε). Experimentally and theoretically obtained cross sections are represented by points and line plots, respectively (Bolorizadeh & Rudd 1986, Deutsch <i>et al.</i> 2000, Djurić <i>et al.</i> 1988, Hwang <i>et al.</i> 1996, Jain & Khare 1976, Kim & Rudd 1994, Saksena <i>et al.</i> 1997a, Saksena <i>et al.</i> 1997b, Schutten <i>et al.</i> 1966, Straub <i>et al.</i> 1998, Terrissol <i>et al.</i> 1989).	78
3.5	First Townsend ionization coefficient ($\alpha_{ion}(z)$) versus gap distance (z) traversed, acquired as a function of (a) water vapour pressure (p_{H_2O}) [$V_{GSED} = 290$ V] and (b) gaseous secondary electron detector bias (V_{GSED}) [$p = 1$ torr]. Region I: minimal ionization; Region II: increasing ionization efficiency; Region III: the attainment of swarm conditions (adapted from Thiel <i>et al.</i> 1997).	83
3.6	Total electronic amplification (A_e) versus water vapour pressure (p_{H_2O}) acquired as a function of (a) gaseous secondary electron detector bias (V_{GSED}) [$d = 5$ mm] and (b) sample-electrode separation (d) [$V_{GSED} = 400$ V]. [see table 2.4 for gas and sample data used to generate profiles]	89
3.7	Total electronic amplification (A_e) versus (a) gaseous secondary electron detector bias (V_{GSED}) [$d = 5$ mm] and (b) sample-electrode separation (d) [$V_{GSED} = 400$ V] acquired as a function of water vapour pressure (p_{H_2O}). [see table 2.4 for gas and sample data used to generate profiles]	91
3.8	Total electronic amplification (A_e) versus water vapour pressure (p_{H_2O}) acquired as a function of signal type: (a) [$V_{GSED} = 200$ V], (b) [$V_{GSED} = 400$ V]. [see table 2.4 for gas and sample data used to generate profiles]	92

3.9	Normalized electronic amplification ($A_e^{PE/BSE/SE}/A_e$) versus water vapour pressure (p_{H_2O}) acquired as a function of signal type: (a) [$V_{GSED} = 200$ V], (b) [$V_{GSED} = 400$ V]. [see table 2.4 for gas and sample data used to generate profiles]	94
4.1	Radiative recombination (RR) coefficient (ρ_{RR}) versus incident electron energy (ε) for Si^{6+} (from Hahn 1997). [nl: excited electronic state] .	103
4.2	Dissociative recombination (DSR) coefficient (ρ_{DSR}) versus incident electron energy (ε) at various electron number densities (n_e) (adapted from Nasser 1971).	106
4.3	Equivalent circuit diagram of the gaseous secondary electron detector (GSED) system of total distributed time constant (RC). RC being equal to the summation of the time constant of the GSED low-pass noise filters, RC_{nf} , the time constant due to the input resistance and capacitance of the GSED electronics, and the time constant associated with coaxial cables used to transmit signals, R_4C_4 . [$I_{GSED}(t)$ =induced GSED current, $I_{ion}(t)$ =ionization current, $V_S(t)$ = output voltage signal]	113
4.4	Streaking in gaseous secondary electron detector (GSED) images acquired as a function of GSED bias (V_{GSED}). [$p_{H_2O} = 0.7$ torr, $d = 9.2$ mm, $HFW = 73$ μ m, $\tau_L = 120$ ms]	124
4.5	Streaking in gaseous secondary electron detector (GSED) images acquired as a function of water vapour pressure (p_{H_2O}). [$V_{GSED} = 342$ V, $d = 9.2$ mm, $HFW = 73$ μ m, $\tau_L = 120$ ms]	125
4.6	Streaking in gaseous secondary electron detector (GSED) images acquired as a function of sample-electrode separation (d). [$V_{GSED} = 342$ V, $p_{H_2O} = 0.7$ torr, $HFW = 73$ μ m, $\tau_L = 120$ ms]	126

4.7	Streaking in gaseous secondary electron detector (GSED) images acquired as a function of line scan time (τ_L). [$V_{GSED} = 342$ V, $p_{H_2O} = 0.7$ torr, $d = 9.2$ mm, $HFW = 73$ μ m]	127
4.8	Streaking in induced stage current images (ISC) acquired as a function of series resistance (R_S). [$V_{GSED} = 342$ V, $p_{H_2O} = 0.7$ torr, $d = 9.2$ mm, $HFW = 73$ μ m, $\tau_L = 120$ ms]	129
4.9	Profiles of greyscale intensity (GSI) versus time (t) acquired as a function of series resistance (R_S) in induced stage current (ISC) images. The dark lines show fits to experimental data using equation 4.3.18. [$V_{GSED} = 342$ V, $p_{H_2O} = 0.7$ torr, $d = 9.2$ mm, $\tau_L = 120$ ms]	130
4.10	Minimum greyscale intensity (GSI) time (τ_{min}) of streaks in induced stage current (ISC) images versus series resistance (R_S). [$V_{GSED} = 342$ V, $p_{H_2O} = 0.7$ torr, $d = 9.2$ mm, $\tau_L = 120$ ms]	131
4.11	Ionization rate (ψ) versus (a) gaseous secondary electron detector (GSED) bias (V_{GSED}) [$p_{H_2O} = 0.7$ torr, $d = 9.2$ mm, $\tau_L = 120$ ms]; (b) water vapour pressure (p_{H_2O}) [$V_{GSED} = 342$ V, $d = 9.2$ mm, $\tau_L = 120$ ms]; (c) sample-electrode separation (d) [$V_{GSED} = 342$ V, $p_{H_2O} = 0.7$ torr, $\tau_L = 120$ ms] and (d) line scan time (τ_L) [$V_{GSED} = 342$ V, $p_{H_2O} = 0.7$ torr, $d = 9.2$ mm].	133
4.12	Steady state gaseous electronic amplification (A_e) versus gaseous secondary electron detector (GSED) bias (V_{GSED}) [$p_{H_2O} = 0.7$ torr, $d = 9.2$ mm, $\tau_L = 120$ ms]; (b) water vapour pressure (p_{H_2O}) [$V_{GSED} = 342$ V, $d = 9.2$ mm, $\tau_L = 120$ ms]; (c) sample-electrode separation (d) [$V_{GSED} = 342$ V, $p_{H_2O} = 0.7$ torr, $\tau_L = 120$ ms] and (d) line scan time (τ_L) [$V_{GSED} = 342$ V, $p_{H_2O} = 0.7$ torr, $d = 9.2$ mm].	135
4.13	Electron drift velocity (v_e) versus reduced electric field (E/p_{H_2O}).	137

4.14	Recombination coefficient (ρ) versus (a) gaseous secondary electron detector (GSED) bias (V_{GSED}) [$p_{H_2O} = 0.7$ torr, $d = 9.2$ mm, $\tau_L = 120$ ms]; (b) water vapour pressure (p_{H_2O}) [$V_{GSED} = 342$ V, $d = 9.2$ mm, $\tau_L = 120$ ms]; (c) sample-electrode separation (d) [$V_{GSED} = 342$ V, $p_{H_2O} = 0.7$ torr, $\tau_L = 120$ ms] and (d) line scan time (τ_L) [$V_{GSED} = 342$ V, $p_{H_2O} = 0.7$ torr, $d = 9.2$ mm].	139
4.15	Recombination coefficient (ρ) versus reduced pressure (E/p_{H_2O}). [$\tau_L = 120$ ms]	142
4.16	Normalized recombination rate (ζ) versus time (t) acquired as a function of (a) gaseous secondary electron detector (GSED) bias (V_{GSED}) [$p_{H_2O} = 0.7$ torr, $d = 9.2$ mm, $\tau_L = 120$ ms]; (b) water vapour pressure (p_{H_2O}) [$V_{GSED} = 342$ V, $d = 9.2$ mm, $\tau_L = 120$ ms]; (c) sample-electrode separation (d) [$V_{GSED} = 342$ V, $p_{H_2O} = 0.7$ torr, $\tau_L = 120$ ms] and (d) line scan time (τ_L) [$V_{GSED} = 342$ V, $p_{H_2O} = 0.7$ torr, $d = 9.2$ mm].	143
4.17	Total detection system time constant (RC) and gaseous secondary electron detector (GSED) noise filter time constant (RC_{nf}) versus line scan time (τ_L). [$V_{GSED} = 342$ V, $p_{H_2O} = 0.7$ torr, $d = 9.2$ mm]	145
5.1	Schematic diagram showing the various photon and electronic signals produced in the low vacuum specimen chamber of an ESEM. Excitation and ionizing collisions [*] between gas molecules and (i) primary electrons (PEs), (ii) backscattered electrons (BSEs) and (iii) secondary electrons (SEs) produce photons ($h\nu$) or positive ions (PIs) and environmental SEs (ESEs), respectively. The photons generated in the gas are detected and amplified by a gaseous scintillation detector (GSD).	161

5.2	PMT photocathode spectral sensitivity ($sk_e(\lambda)_p$) and total (quartz window + perspex light pipe + perspex vacuum seal) transmission response ($T(\lambda)$) versus photon wavelength (λ).	165
5.3	PMT gain (G_{PMT}) versus PMT high tension voltage (V_{HT}).	169
5.4	PMT high tension voltage (V_{HT}) versus gaseous scintillation detector contrast (C_{GSD}).	170
5.5	Gaseous scintillation detector (GSD) and gaseous secondary electron detector (GSED) images of the microscope stage acquired at various Ar pressures (p_{Ar}) and electric field strengths (E): (a) $V_{GSD} = 390$ V, $p_{Ar} = 0.5$ torr; (b) $V_{GSED} = 334$ V, $p_{Ar} = 0.5$; (c) $V_{GSD} = 330$ V, $p_{Ar} = 0.7$ torr; (d) $V_{GSED} = 248$ V, $p_{Ar} = 0.7$ torr; (e) $V_{GSD} = 290$ V, $p_{Ar} = 0.9$ torr; (f) $V_{GSED} = 221$ V, $p_{Ar} = 0.9$ torr. [$\varepsilon_{PE} = 30$ keV, $WD = 15$ mm, $\tau_L = 60$ ms, $HFW = 190$ μm]	174
5.6	Gaseous scintillation detector (GSD) and gaseous secondary electron detector (GSED) images of the microscope stage acquired at various N_2 pressures (p_{N_2}) and electric field strengths (E): (a) $V_{GSD} = 460$ V, $p_{N_2} = 0.5$ torr; (b) $V_{GSED} = 460$ V, $p_{N_2} = 0.5$; (c) $V_{GSD} = 420$ V, $p_{N_2} = 0.7$ torr; (d) $V_{GSED} = 350$ V, $p_{N_2} = 0.7$ torr; (e) $V_{GSD} = 390$ V, $p_{N_2} = 0.9$ torr; (f) $V_{GSED} = 317$ V, $p_{N_2} = 0.9$ torr. [$\varepsilon_{PE} = 30$ keV, $WD = 15$ mm, $\tau_L = 60$ ms, $HFW = 190$ μm]	175
5.7	Gaseous scintillation detector (GSD) and gaseous secondary electron detector (GSED) images of the microscope stage acquired at various H_2O pressures (p_{H_2O}) and electric field strengths (E): (a) $V_{GSD} = 550$ V, $p_{H_2O} = 0.5$ torr; (b) $V_{GSED} = 550$ V, $p_{H_2O} = 0.5$; (c) $V_{GSD} = 550$ V, $p_{H_2O} = 0.7$ torr; (d) $V_{GSED} = 434$ V, $p_{H_2O} = 0.7$ torr; (e) $V_{GSD} = 560$ V, $p_{H_2O} = 0.9$ torr; (f) $V_{GSED} = 353$ V, $p_{H_2O} = 0.9$ torr. [$\varepsilon_{PE} = 30$ keV, $WD = 15$ mm, $\tau_L = 60$ ms, $HFW = 190$ μm]	176

5.8	Backscattered electron (BSE) (a) and secondary electron (SE) (b) images of the microscope stage acquired under high vacuum conditions, respectively. [$\varepsilon_{PE} = 30$ keV, $WD = 15$ mm, $\tau_L = 60$ ms, $FWHM = 190$ μm]	178
5.9	Steady state photon amplification (A_{hv}) and electronic amplification (A_e) versus gaseous secondary electron detector (GSED) bias (V_{GSED}) in (a) Ar, (b) N_2 and (c) H_2O . [$\varepsilon_{PE} = 30$ keV, $p_{Ar} = p_{N_2} = p_{H_2O} = 1$ torr, $WD = 15$ mm]	181
5.10	Steady state photon amplification (A_{hv}) and electronic amplification (A_e) versus specimen chamber pressure (p) in (a) Ar [$V_{GSED} = 186$ V], (b) N_2 [$V_{GSED} = 186$ V] and (c) N_2 [$V_{GSED} = 290$ V]. [$\varepsilon_{PE} = 30$ keV, $WD = 15$ mm]	183
5.11	Steady state photon amplification (A_{hv}) and electronic amplification (A_e) versus specimen chamber pressure (p) in (a) H_2O [$V_{GSED} = 186$ V], (b) H_2O [$V_{GSED} = 238$ V], (c) H_2O [$V_{GSED} = 446$ V] and (d) H_2O [$V_{GSED} = 498$ V]. [$\varepsilon_{PE} = 30$ keV, $WD = 15$ mm]	184
5.12	Steady state photon amplification (A_{hv}) and electronic amplification (A_e) versus working distance (WD) in (a) Ar, (b) N_2 and (c) H_2O . [$\varepsilon_{PE} = 30$ keV, $V_{GSED} = 186$ V, $p_{Ar} = p_{N_2} = p_{H_2O} = 1$ torr]	189
5.13	Visible gas luminescence produced in argon (Ar) under discharge conditions. [$\varepsilon_{PE} = 30$ keV, $V_{GSED} = 290$ V, $p_{Ar} = 1$ torr, $WD = 15\text{mm}$] .	191
5.14	Steady state photon amplification (A_{hv}) and electronic amplification (A_e) versus gaseous scintillation detector (GSD) grid bias (V_{GSD}) in (a) Ar, (b) N_2 and (c) H_2O . [$\varepsilon_{PE} = 30$ keV, $p_{Ar} = p_{N_2} = p_{H_2O} = 1$ torr, $WD = 15\text{mm}$]	193

5.15	Steady state photon amplification (A_{hv}) and electronic amplification (A_e) versus working distance (WD) in (a) Ar, (b) N ₂ and (c) H ₂ O. [$\varepsilon_{PE} = 30$ keV, $V_{GSD} = 186$ V, $p_{Ar} = p_{N_2} = p_{H_2O} = 1$ torr]	194
5.16	Steady state photon amplification (A_{hv}) and electronic amplification (A_e) versus specimen chamber pressure (p) in (a) Ar [$V_{GSD} = 186$ V], (b) N ₂ [$V_{GSD} = 186$ V], (c) N ₂ [$V_{GSD} = 290$ V], (d) H ₂ O [$V_{GSD} = 186$ V] and (e) H ₂ O [$V_{GSD} = 446$ V]. [$\varepsilon_{PE} = 30$ keV, $p_{Ar} = p_{N_2} = p_{H_2O} = 1$ torr, $WD = 15$ mm]	196
6.1	Schematic diagram showing the Gaseous Scintillation Detector (GSD) and spectroscopy system used to detect photon wavelengths.	204
6.2	Emission spectra of Ar at $p_{Ar} = 0.3, 0.4$ and 1.0 torr. [$V_{GSD} = 238$ V]	205
6.3	Emission intensities versus p_{Ar} for the major 375.79 nm, 384.45 nm, 561.59 nm, 567.11 nm, and 588.42 nm wavelengths found in Ar.	207
6.4	Emission spectra of N ₂ at $p_{N_2} = 0.7, 1.0$ and 2.0 torr. [$V_{GSD} = 342$ V]	208
6.5	Emission intensities versus p_{N_2} for the major 313.83 nm, 336.23 nm, 356.26 nm, 390.04 nm, 425.96 nm, 470.04 nm, 630.38 nm and 673.22 nm wavelengths found in N ₂	209

List of Tables

1	List of symbols and abbreviations.	xxi
2.1	First ionization potentials (V_i^1) and scattering amplitudes ($f_e(0)$) of several atoms (Danilatos 1988, von Engel 1965)	18
2.2	Time constant (RC_{nf}) and bandwidth (BWD) of the Philips XL 30 ESEM [®] gaseous secondary electron detector (GSED) preamplifier low-pass passive noise filters at various line scan times (τ_L) and digital filter codes (Philips Electron Optics 1997).	53
3.1	First ionization potentials (V_i^1) and gas dependent constants A and B for argon (Ar), nitrogen (N_2) and water vapour (H_2O) (von Engel 1965, Thiel <i>et al.</i> 1997)	82
3.2	Data used to generate the electronic amplification profiles shown in figures 2.21-2.23.	88
6.1	Atomic transitions and accompanying wavelengths in neural Ar (Ar I) (Shirai <i>et al.</i> 1999).	206

A.1 Atomic and molecular collisions in partially ionized gases (adopted from von Engel 1965, Hahn 1997, Hasted 1964, Nasser 1971). [A, B, C, D = ground state atom or molecule, $[AB]$ = ground state molecule, $h\nu$ = photon of frequency ν , e^- = incident electron, e_{ESE}^- = ejected or environmental secondary electron, $+$ = positive ion, $-$ = negative ion, $*$ = singly excited, $**$ = doubly excited, e = electronic state, m = metastable state, v = vibrational state, s = slow, f = fast] 214

Nomenclature

Table 1: List of symbols and abbreviations.

a_H	Bohr radius
A	atom
A_e	total electronic gas amplification
A_e^{BSE}	gaseous BSE electronic amplification
A_e^{PE}	gaseous PE electronic amplification
A_e^{SE}	gaseous SE electronic amplification
A_{hv}	photon amplification
Al_2O_3	alumina
Ar	argon gas
BSE	backscattered electron
BWD	bandwidth
c	vacuum speed of light

Table 1: Continued...

C	capacitance
C_{GSD}	GSD contrast
CL	cathodoluminescence
CO ₂	carbon dioxide gas
d	sample-electrode separation
d_{eff}	effective gap distance
\bar{d}_{BSE}	average BSE path length
D	transition region distance (below PLA1)
DC	direct current
DP	diffusion pump
DR	dielectronic recombination
DSR	dissociative recombination
e	electron charge
e^-	electron
E	electric field strength
E_{ion}	ion electric field strength/space charge field strength
E_{net}	net electric field strength

Table 1: Continued...

E_{GSED}	GSED electric field strength
E/p	reduced electric field
EBIC	electron beam induced current
EC	environmental chamber
ESE	environmental secondary electron
ESEM	environmental scanning electron microscope
E-T	Everhart-Thornley
$f_e(\theta)$	scattering amplitude
FET	field effect transistor
g_m	metastable geometrical loss factor
g_p	photon geometrical loss factor
G_{PMT}	PMT gain
GSD	gaseous scintillation detector
GSED	gaseous secondary electron detector
GSI	greyscale intensity
h	Planks constant
h	transition region distance (above PLA1)

Table 1: Continued...

$h\nu$	photon
H	distance between PLA1 and PLA2
H_n	Struve's function of order n
H_2	hydrogen gas
H_2O	water vapour
He	helium gas
$HF\!W$	horizontal field width
I_e^{hv}	electron avalanche generated photon current
I_{ind}	induced current
I_{ion}	total ionization current
I_{BSE}^g	gaseous BSE ionization current (<i>ad infinitum</i> avalanches)
I_{BSE}^{hv}	total scintillation BSE photon current
$I_{BSE_0}^g$	gaseous BSE ionization current (single avalanche)
$I_{BSE_0}^{hv}$	primary scintillation BSE photon current
$I_{BSE_1}^{hv}$	secondary scintillation BSE photon current
I_{GSED}	GSED current
I_{PE}	PE beam current

Table 1: Continued...

I_{PE}^g	gaseous PE ionization current (<i>ad infinitum</i> avalanches)
I_{PE}^{hv}	total scintillation PE photon current
$I_{PE_0}^g$	gaseous PE ionization current (single avalanche)
$I_{PE_0}^{hv}$	primary scintillation PE photon current
$I_{PE_1}^{hv}$	secondary scintillation PE photon current
I_{PMT}^{in}	PMT input current
I_{PMT}^{out}	PMT output current
I_R	resistor current
I_{SE}^g	gaseous SE ionization current (<i>ad infinitum</i> avalanches)
I_{SE}^{hv}	total scintillation SE photon current
$I_{SE_0}^g$	gaseous SE ionization current (single avalanche)
IP	ion pump
IR	infrared spectrum
ISC	induced stage current
J	ionization energy
J_n	Bessel function of order n
k	Boltzmann constant

Table 1: Continued...

k	cascade amplification feedback factor
K	kinetic energy
K_i	ion kinetic energy
K_n	neutral atom/molecule kinetic energy
K_{SE}	SE kinetic energy
K_0	modified Bessel function of the second kind of zero order
L	dimensional unit of length
LED	light emitting diode
m	average number of scattering events
m_e	electron rest mass
M	metastable-cathodic electron emission probability
M	molecule
MGSI	mean greyscale intensity
n	number density/concentration
n_e	electron number density/concentration
n_i	ion number density/concentration
N_e^c	number of cathodic electrons

Table 1: Continued...

N_e^g	number of gaseous electrons
N_{hv}^g	number of gaseous photons
N_n	Neumann's Bessel function of the second kind of order n
N_p^c	number of cathodic photoelectrons
N_{BSE}^{hv}	number of photons generated by BSEs
N_{CL}^{hv}	number of photons generated by CL
N_{PE}^{hv}	number of photons generated by PEs
N_{SE}^{hv}	number of photons generated by SEs
N_T^{hv}	total number of photons
N_2	nitrogen gas
NO	nitrous oxide gas
O_2	oxygen gas
p	pressure
p_{max}	maximum efficiency pressure
p_{max}^e	maximum ionization efficiency pressure
p_{max}^{hv}	maximum excitation efficiency pressure
p_{Ar}	argon pressure

Table 1: Continued...

p_{H_2O}	water vapour pressure
p_{N_2}	nitrogen pressure
p_1	stagnation pressure
P	photoelectric yield
$P(x)$	collision probability
PCB	printed circuit board
PE	potential energy
PE	primary electron
PI	positive ion
PLA	pressure-limiting aperture
PMT	photomultiplier tube
Q	charge
r	radial distance
r_{ij}	molecular inter-atomic distance
r_0	minimum atomic distance
$r_{1/2}$	skirt half-width radius
R	correlation coefficient

Table 1: Continued...

R	effective atomic radius
R	resistance
R_m	maximum electron interaction range
R_L	load resistance
R_S	series resistance
RC	time constant
RC_{nf}	noise filter time constant
RDR	radiative dielectronic recombination
RE	resonant excitation
RP	rotary pump
RR	radiative recombination
s	particle displacement
$sk_e(\lambda)_p$	photocathode spectral sensitivity
S_{BSE}	BSE ionization efficiency
S_{PE}	PE ionization efficiency
SbKCs	Baikaline
$(S/B)_{SE}$	SE signal-to-background ratio

Table 1: Continued...

$(S/B)_{SE}^e$	electronic SE signal-to-background ratio
$(S/B)_{SE}^{hv}$	electroluminescent SE signal-to-background ratio
SE	secondary electron
SEM	scanning electron microscope
SNR	signal-to-noise ratio
t	time
T	absolute temperature
T	dimensional unit of time
TBR	three-body recombination
TV	television
$T(\lambda)$	transmission response
UV	ultra violet spectrum
ν	photon frequency
ν_c	critical photon frequency
ν_e	electron drift velocity
$\bar{\nu}_e$	average electron velocity
ν_i	ion drift velocity

Table 1: Continued...

V	voltage
V_e^1	first excitation potential
V_i^1	first ionization potential
$V_p(\rho)$	plural scattering probability distribution
$V_s(r)$	single scattering probability distribution
V_{GSD}	GSD voltage
V_{GSED}	GSED voltage
V_{HT}	PMT high tension voltage
V_{PMT}^{out}	PMT output voltage
V_S	voltage signal
VIS	visible spectrum
VPSEM	variable pressure scanning electron microscope
VUV	vacuum ultra violet spectrum
WD	working distance
z	gap distance
z_Ω	maximum SE-ion recombination distance
Z	atomic number

Table 1: Continued...

α_{exc}	excitation coefficient
α_{ion}	first Townsend ionization coefficient SE/ESE ionization efficiency
α_{ion}^{sw}	first Townsend ionization coefficient SE/ESE ionization efficiency (swarm conditions)
γ	total second Townsend coefficient
γ_i	ion second Townsend coefficient
γ_m	metastable second Townsend coefficient
γ_n	neutral atom/molecule second Townsend coefficient
γ_p	photoelectron second Townsend coefficient
Γ_e	electron transit time
Γ_i	ion transit time
δ	SE emission coefficient
δ_{eff}	effective SE emission coefficient
Δ	reaction by-products
ε	electron energy
ε_{BSE}	BSE energy
ε_{PE}	PE energy
$\bar{\varepsilon}_{SE}$	average SE energy
ε_0	electron rest energy

Table 1: Continued...

ζ_T	mass thickness of transition region
$\zeta(t)$	SE-ion recombination rate
η	BSE emission coefficient
θ	scattering angle
λ	photon wavelength
λ_c	critical photon wavelength
λ_e	relativistic electron wavelength
λ_{SE}	SE inelastic mean free path
λ_{SE}^e	SE mean free path (ionization)
λ_{SE}^{hv}	SE mean free path (excitation)
λ_1	minimum photon wavelength
λ_2	maximum photon wavelength
μ_m	metastable absorption coefficient
μ_p	photon absorption coefficient
ρ	reduced radial distance
ρ	total SE-ion recombination coefficient
ρ_{DSR}	SE-ion recombination coefficient (DSR)
ρ_{RR}	SE-ion recombination coefficient (RR)

Table 1: Continued...

σ_e^s	elastic scattering cross section
σ_i^s	inelastic scattering cross section
σ_T^i	total electron impact ionization cross section
σ_T^{ei}	total electron-ion recombination cross section
σ_T^s	total scattering cross section
$\bar{\tau}_i$	average ion lifetime
τ_{min}	minimum greyscale intensity time
τ_p	pixel dwell time
τ_L	line scan time
ν	fraction of SEs escaping back diffusion
Φ	work function
$\Phi_{hv}(\lambda)$	radiant photon flux
χ	metastable coefficient
ψ	ionization rate
ω_{BSE}	BSE excitation efficiency
ω_{PE}	PE excitation efficiency
Ω	scattering solid angle
$\bar{\Omega}$	average SE-ion capture probability

Abstract

This thesis quantitatively investigates gaseous electron-ion recombination in an environmental scanning electron microscope (ESEM) at a transient level by utilizing the dark shadows/streaks seen in gaseous secondary electron detector (GSED) images immediately after a region of enhanced secondary electron (SE) emission is encountered by a scanning electron beam. The investigation firstly derives a theoretical model of gaseous electron-ion recombination that takes into consideration transients caused by the time constant of the GSED electronics and external circuitry used to generate images. Experimental data of pixel intensity versus time of the streaks is then simulated using the model enabling the relative magnitudes of (i) ionization and recombination rates, (ii) recombination coefficients, and (iii) electron drift velocities, as well as absolute values of the total time constant of the detection system, to be determined as a function of microscope operating parameters. Results reveal the exact dependence that the effects of SE-ion recombination on signal formation have on reduced electric field intensity and time in ESEM. Furthermore, the model implicitly demonstrates that signal loss as a consequence of field retardation due to ion space charges, although obviously present, is not the foremost phenomenon causing streaking in images, as previously thought.

Following that the generation and detection of gaseous scintillation and electroluminescence produced via electron-gas molecule excitation reactions in ESEM is investigated. Here a novel gaseous scintillation detection (GSD) system is developed

to efficiently detect photons produced. Images acquired using GSD are compared to those obtained using conventional GSED detection, and demonstrate that images rich in SE contrast can be achieved using such systems. A theoretical model is developed that describes the generation of photon signals by cascading SEs, high energy backscattered electrons (BSEs) and primary beam electrons (PEs). Photon amplification, or the total number of photons produced per sample emissive electron, is then investigated, and compared to conventional electronic amplification, over a wide range of microscope operating parameters, imaging gases and photon collection geometries. The main findings of the investigation revealed that detected electroluminescent signals exhibit larger SE signal-to-background levels than that of conventional electronic signals detected via GSED. Also, dragging the electron cascade towards the light pipe assemblage of GSD systems, or electrostatic focusing, dramatically increases photon collection efficiencies. The attainment of such an improvement being a direct consequence of increasing the ‘effective’ solid angle for photon collection.

Finally, in attempt to characterize the scintillating wavelengths arising from sample emissive SEs, PEs, BSEs, and their respective cascaded electrons, such that future photon filtering techniques can be employed to extract nominated GSD imaging signals, the emission spectra of commonly utilized electroluminescent gases in ESEM, such as argon (Ar) and nitrogen (N_2), were collected and investigated. Spectra of Ar and N_2 reveal several major emission lines that occur in the ultraviolet (UV) to near-infrared (NIR) regions of the electromagnetic spectrum. The major photon emissions discovered in Ar are attributed to occur via atomic de-excitation transitions of neutral Ar (Ar I), whilst for N_2 , major emissions are attributed to be a consequence of second positive band vibrational de-excitation reactions. Major wavelength intensity versus gas pressure data, for both Ar and N_2 , illustrate that wavelength intensities increase with decreasing pressure. This phenomenon strongly suggesting that quenching effects and reductions in excitation mean free paths increase with imaging gas pressure.

Chapter 1

Introduction

The conventional (high vacuum) scanning electron microscope (SEM) requires specimen chamber pressures of the order of 10^{-6} torr in order to prevent flashover and electrical arcing of the high voltage scintillator of its Everhart-Thornley (E-T) secondary electron (SE) detector (Danilatos 1988, Goldstein *et al.* 1992, Mohan *et al.* 1998, Reimer 1985). The scintillator of the ET detector requires a bias of +12 kV for efficient SE collection and amplification (Danilatos 1988, Danilatos 1990c, Goldstein *et al.* 1992). Pressures better than 10^{-6} torr are also required in the conventional SEM to minimize loss of beam current due to primary electron (PE)-gas molecule elastic scattering, which reduces the signal-to-noise ratio and brightness of images (Danilatos 1988, Goldstein *et al.* 1992, Reimer 1985). The high vacuum requirements of a conventional SEM means that insulating samples must be electrically grounded via conductive coatings in order to prevent sample charging at PE beam energies (ε_{PE}) in excess of a few keV (Goldstein *et al.* 1992). Sample charging causes detrimental effects such as image distortion, image drift, streaking in images, image mirror effects, dielectric breakdown and deflection of the primary electron beam (Goldstein *et al.* 1992, Reimer 1985).

The introduction of the environmental scanning electron microscope (ESEM) in the 1980s revolutionized the field of scanning electron microscopy. Imaging and microanalysis of uncoated insulating (Bower *et al.* 1994, Craven *et al.* 2002, Danilatos 1980a, Danilatos 1985, Danilatos 1988, Danilatos 1990b, Farley & Shah 1991, Griffin 2000, Mohan *et al.* 1998, Newbury 1996, Robinson 1975a, Thiel & Donald 1999, Toth & Phillips 2000a, Toth & Phillips 2000b, Toth *et al.* 2002b, Toth *et al.* 2002c), biological (Danilatos 1980b, Danilatos 1981, Danilatos 1985, Danilatos 1988, Danilatos & Postle 1982, Farley & Shah 1991, Mohan *et al.* 1998, Ray *et al.* 1997, Robinson 1975b, Robinson 1975a, Robinson 1978, Schnarr & Fütting 1997, Shah & Beckett 1979), hydrated (Danilatos 1981, Danilatos 1985, Danilatos 1988, Danilatos & Postle 1982, Meredith & Donald 1996, Robinson 1975b, Robinson 1978, Thiel &

Donald 1999), liquid (Royall *et al.* 2001, Stelmashenko *et al.* 2001, Stokes *et al.* 1998, Stokes *et al.* 2000, Thiel & Donald 1999) and semiconducting materials (Farley & Shah 1991, Mohan *et al.* 1998, Stevens-Kalceff 2001, Toth *et al.* 2000) close to their natural state was now attainable without the necessary sample preparation generally needed to eliminate detrimental charging effects encountered in conventional SEM (Danilatos 1988, Moncreiff *et al.* 1978, Robinson 1975b). The ESEM eliminates the need for conductive coatings via the presence of a partially ionized gas into the specimen chamber of a SEM. To do this the ESEM is equipped with a differential pumping system, which consists of a series of pressure limiting apertures (PLAs), as well as a gaseous secondary electron detector (GSED). The series of PLAs separate the high vacuum electron gun and column regions (usually held at 10^{-5} torr) from the sample chamber, which is typically held at pressures up to 20 torr (Danilatos 1988, Philips Electron Optics 1996). The vacuum system employed in an ESEM is described in chapter 2.2. The GSED consists of a positively biased conducting metallic ring placed above the sample on the optical axis of the microscope. The GSED utilizes the gas as an amplification medium generating a cascaded electron signal and positive ions (Danilatos 1990c). The cascaded electron signal is collected by the GSED, interpreted by an appropriate electronics system and converted to an image, while the positive ions neutralize excess charge build up on the surface of insulating materials (Danilatos 1988, Farley & Shah 1991, Moncreiff *et al.* 1978). A full description of signal detection via the GSED and associated electronics is described in chapter 2.4.

The following two chapters contain a literature review on the fundamentals governing ESEM, such as (i) electron scattering in a low vacuum environment, (ii) signal detection in ESEM and (iii) gaseous cascade amplification in partially ionized gases based on Townsend theories. These chapters also outline the existing knowledge and areas of research and development that need to be improved in the ESEM. Chapter 4 investigates gaseous electron-ion recombination in the ESEM at a transient

level. The chapter develops a transient model of electron-ion recombination based on shadowing seen in ESEM images. The model is then used to calculate relative magnitudes of electron drift velocities, recombination and ionization rates, recombination coefficients and time constants associated with detection electronics. Chapter 5 investigates gaseous scintillation detection and amplification in ESEM. Here, a novel photon detection system is developed, denoted a gaseous scintillation detector (GSD), to efficiently detect photons generated in gaseous electron cascades. A model on gaseous scintillation and electroluminescence generation, or photon amplification, is then developed based on existing Townsend theory. Images and amplification data are then generated using the GSD and compared to those produced by existing modes of signal detection, that utilize electronic signals, over a range of microscope operating parameters and imaging gases. Finally chapter 6 investigates photon emission spectra of luminescent imaging gases used in ESEM, such as argon and nitrogen. The spectra is collected using the novel GSD and investigated as a function of imaging gas pressure.

Chapter 2

Background to Environmental Scanning Electron Microscopy

2.1 Introduction

Conventional (high vacuum) scanning electron microscopy (SEM) is a mature, indispensable technology in materials research. The physics relating to electron optics, vacuum systems, electron detection, electron-specimen interactions and image formation in a high vacuum environment can be found in typical SEM textbooks such as Goldstein *et al.* (1992) and Reimer (1985).

However, unlike conventional high vacuum SEM, environmental scanning electron microscopy (ESEM) is a relatively new technique and therefore the principles governing its operation are still currently being developed. Over the last several decades, many studies have attempted to gain insight into various aspects of signal generation and contrast formation in an ESEM. The main areas of research have included primary electron (PE)-gas phase scattering and skirt formation, secondary electron (SE) and backscattered electron (BSE) detection, sample charging in a low vacuum environment and gaseous amplification of imaging signals.

This chapter contains a detailed overview of the current literature relating to the physical principles governing ESEM. A background to the vacuum system employed in an ESEM is covered in section 2.2. Following that, section 2.3 describes PE-gas scattering and related phenomena such as: (i) theoretically and experimentally derived scattering cross sections; (ii) primary beam transmission; and (iii) primary electron beam distributions and skirt profiles, which are essential in the determination of signal-to-noise ratio (SNR) and resolution in images obtained using ESEM. Subsequently, section 2.4 gives a comprehensive background to signal detection in the ESEM, which comprises: (i) gaseous secondary electron (GSE) detection; (ii) signal induction mechanisms and charge collection; (iii) a description of the gaseous secondary electron detector (GSED) electronics used to generate images from sample emergent signals after being simultaneously amplified in the gas and induced on the

GSED anode ring. When necessary, extensions to the theories covered in this chapter will be presented in the respective chapters comprising this thesis.

2.2 Vacuum System

In order to obtain a focused PE beam, the electron gun and column regions of a SEM require pressures of less than 10^{-7} torr and 10^{-5} torr, respectively (Philips Electron Optics 1996). If high vacuum conditions are not employed in the gun region, electrical arcing between the high voltage cathode (held at 0.1 to 30 kV) and the anode (maintained at ground potential) will cause an unstable PE beam (Goldstein *et al.* 1992). Elevated pressures in the column region cause gas phase scattering of the PE beam, which reduces its intensity and consequently a loss in image signal (Danilatos 1988, Farley & Shah 1990a, Moncreiff *et al.* 1979).

In a conventional high vacuum SEM, the sample chamber remains at the same pressure as the gun/column regions of the microscope. However, in a typical ESEM, such as the FEI Philips XL 30 ESEM[®], the sample chamber can be maintained at pressures ranging between 0.1 and 20 torr whilst the gun and column regions are sustained at pressures of 10^{-7} torr and 10^{-5} torr, respectively (Mohan *et al.* 1998, Philips Electron Optics 1996). This is achieved by separating the column and chamber regions with a series of pressure limiting apertures (PLAs) and a multistage differential pumping system (Philips Electron Optics 1996). The regions above, below and between the PLAs are separately pumped to obtain a graduated vacuum between the sample chamber and the gun (Philips Electron Optics 1996)¹. The PLAs are located in the final lens assembly of the microscope and are placed close together to reduce the distance that the PEs must travel through the larger pressures. Hence, the loss of PEs due to gas phase elastic scattering in the region between the two PLAs is kept to a minimum. The vacuum chamber of an ESEM caters for different

¹A new breed of LEO[®] brand SEMs only contain a single PLA due to strict patenting laws set by Philips on their multi aperture systems (Philips Electron Optics 1996). Due to there only being one PLA present the pressure in the chamber is limited to a maximum of ≈ 0.9 torr. These types of microscopes, due to their limited pressure ranges and different detection systems, are referred to as variable pressure scanning electron microscopes (VPSEMs).

types of imaging gases via an auxiliary inlet. Typical gases used are hydrogen (H_2), helium (He), argon (Ar), oxygen (O_2), nitrogen (N_2), nitrous oxide (NO) and carbon dioxide (CO_2) (Danilatos 1990c, Fletcher *et al.* 1997). However, all gases used in an ESEM possess different gaseous amplification characteristics and hence image quality is governed by the choice of gas used. Gas amplification properties of the gases used in this thesis are described in chapter 3. Water vapour (H_2O) is the most commonly used gas due to its high gain, signal-to-background properties (Fletcher *et al.* 1997) and ability to keep biological samples hydrated. More detailed descriptions of the vacuum system employed in an ESEM can be found in Danilatos (1980a), Danilatos (1981), Danilatos (1985), Danilatos (1988), Danilatos (1991), Danilatos (1992a), Danilatos (1994); and Philips Electron Optics (1996). A schematic diagram of the vacuum system is shown in figure 2.1.

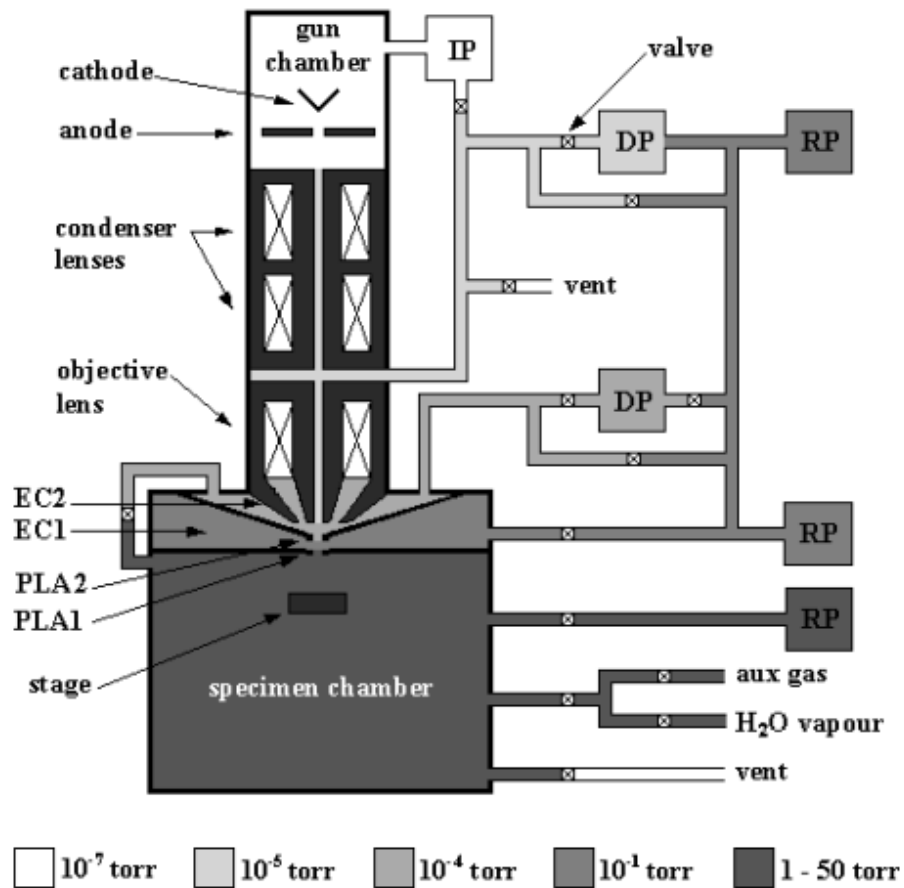


Figure 2.1: Schematic diagram showing the ESEM vacuum system. The vacuum system consists of five stages of increasing vacuum level. The stages are the specimen chamber, first environmental chamber (EC1), second environmental chamber (EC2), electron column and electron gun. The column and chamber regions are separated by two pressure limiting apertures (PLAs). The PLAs are placed close together to minimize PE scattering (adapted from Philips Electron Optics (1996)). [IP=ion pump, DP=diffusion pump, RT=rotary pump]

2.3 Primary Electron Beam-Gas Scattering

The interaction of the electron beam with the imaging gas in an ESEM produces several phenomena such as scattering of PEs and the generation of (i) gaseous SEs, (ii) positive and/or negative gas ions, (iii) gaseous x-rays, (iv) excited atoms and/or molecules, (v) gaseous scintillation and (vi) molecular dissociation (Danilatos 1988). The phenomena ascribed above generally degrade image quality by introducing unwanted background noise components that are additional to desired sample emissive signals. The PEs that are scattered introduce background noise ‘directly’ by generating SEs and x-rays from the sample at large distances away from the focused probe, thus reducing the SNR in images and x-ray microanalysis, respectively. The PEs that are scattered contribute to what is known as an electron ‘skirt’ that surrounds the focused, unscattered probe component of the beam (Danilatos 1988). The additional phenomena ascribed above (i to vi), which are produced in conjunction with the scattering, introduce background noise ‘indirectly’ as these signals are created in the gas. However, these signals can be amplified in the gas, and detected along with electrons generated from the sample by the probe. This background noise component added to the signal is, however, dependent on the detection mode being used. For example, when detecting electrons in an ESEM any x-rays or light generated in the gas will not be detected and vice versa. The theory relating to the detection and amplification of the ‘indirect’ gaseous phenomena described above will be covered in following sections of this chapter.

The scattering of the electron beam is of primary importance, as the amount of PE scattering determines the fundamental limits of spatial resolution, SNR and contrast in images and x-ray microanalysis obtained in an ESEM (Danilatos 1988, Gauvin 1999). Several authors, such as Adamiak & Mathieu (2000), Danilatos (1988), Danilatos (1990a), Danilatos (1994), Farley & Shah (1990a), Gillen *et al.* (1998),

Kadoun *et al.* (2003), Moncreiff *et al.* (1979), Phillips *et al.* (1999), Stowe & Robinson (1998), Thiel *et al.* (2000), Wight *et al.* (1997), Wight & Zeissler (1999) and Wight (2001) have investigated PE-gas scattering in an ESEM and a summation of their work is presented below. Before any direct theoretical analysis of electron beam scattering and skirt formation in the ESEM can be attempted, it is essential to know the cross sections associated with PE-gas scattering.

2.3.1 Scattering Cross Sections

As PEs exit the final PLA (PLA1 in figure 2.1) of an ESEM and enter the specimen chamber, a certain percentage of them undergo scattering events with gas atoms or molecules. The fraction of PEs scattered depends on the gas type, sample chamber pressure (p), PE beam energy (ε_{PE}) and the working distance (WD). Collisions occur when the PEs interact with gas particles within an effective area known as the total scattering cross section (σ_T^s), which represents the probability that a scattering event will occur. The total scattering cross section is a combination of elastic scattering, where the electron energy before a collision is approximately equal to the electron energy after a collision, and inelastic scattering, where energy from the incident electron is transferred to the gaseous atom or molecule in producing ionization, excitation, molecular dissociation, molecular rotation and molecular vibration. Before total scattering cross sections can be derived, one must first consider the total elastic and total inelastic scattering cross sections independently. At this stage, there is no unique set of equations to describe elastic or inelastic scattering cross sections for all gases and therefore a careful choice of experimental or theoretical scattering cross sections must be made for the particular gas in question. In addition, the theory present is based on many assumptions and simplifications and needs to be altered to accommodate the additional processes that are occurring in an ESEM.

One of the first studies of electron scattering in a low vacuum microscope environment was performed by Moncreiff *et al.* (1979). In that paper, a theoretical analysis of electron scattering in a low vacuum microscope containing N_2 gas was compared to experimental results obtained. However, the studies were performed using a single scattering regime, where 95% of the electrons in the beam suffer zero or one scattering event only (Danilatos 1988). Moncreiff *et al.* (1979) used differential scattering cross sections that were theoretically derived by Lenz (1954), which describe single electron scattering in atomic solids. These authors suggested that the atomic scattering cross sections of Lenz (1954) were also applicable to single scattering in gases, but needed to be modified to account for scattering in molecular gases. This assumption was based on the fact that scattering in a low vacuum environment could be considered as singular *i.e.* the probability of electrons undergoing more than one collision is small. The atomic differential elastic scattering cross sections obtained by Lenz (1954) were generated using Rutherford scattering cross sections that were quantum mechanically modified using theoretical models of Wentzel (1926). Atomic differential inelastic scattering cross sections used were derived from Compton scattering of x-rays. However, incoherent scattering factors needed were only obtainable for large scattering angles and so Moncreiff *et al.* (1979) used an analytical atomic inelastic scattering cross section expression from Burge & Smith (1962) for small scattering angles. As N_2 was used in experiments, the atomic differential scattering cross sections were altered to account for diatomic molecules. The molecular elastic scattering cross sections were obtained using the independent scattering centre approximation of Massey *et al.* (1969), which gives the molecular differential elastic scattering cross section as simply twice that of the atomic differential elastic scattering cross section multiplied by an expression based on diffraction effects between atoms of the molecule. However, numerous assumptions are made in this approach such as: (i) the electron wavelength is small compared with the separation of the atoms in the molecule so that each atom

in the molecule can be considered as separate scattering centres; (ii) molecular electron bonding configurations do not effect the incident electron trajectory compared to that of an atom; (iii) multiple scattering within a molecule was negligible; (iv) no ionization is occurring in the gas (Moncreiff *et al.* 1979). The molecular inelastic scattering cross sections were obtained assuming that molecular scattering is incoherent, giving the molecular differential inelastic scattering cross section as exactly twice that of the atomic differential inelastic scattering cross section.

Farley & Shah (1990a) also examined electron beam scattering in a low vacuum environment for the case of N_2 and H_2O . Theoretical scattering cross sections for N_2 were obtained using the same general procedures and assumptions as that of Moncreiff *et al.* (1979). However, the theoretical total scattering cross sections obtained by Farley & Shah (1990a) were found to be approximately 50% higher in magnitude for the same beam energy. This difference was attributed to the use of different effective atomic radii. Differences would also arise as a result of not opting to incorporate a diffraction expression into the molecular elastic differential scattering cross sections utilized.

Gauvin (1999) theoretically studied electron scattering to obtain new correction procedures for reducing the effects of skirt formation on quantitative x-ray microanalysis in the ESEM or variable pressure scanning electron microscope (VPSEM). Gauvin (1999) based his theory on single electron scattering under the assumption that inelastic collisions are negligible, and therefore most of the beam scattering is caused by elastic collisions. Gauvin (1999) based models on 'screened' Rutherford elastic scattering cross sections, which have been shown to be appropriate for use with light elements and therefore for most of the gases employed in ESEM work (Gauvin & Drouin 1993). It was shown, using Monte Carlo simulations, that elastic scattering can be formulated using simple single scattering theory rather than more complicated plural scattering theory under suitable imaging conditions in an ESEM.

Suitable imaging conditions have been defined as when the average number of scattering events per PE is less than three (Danilatos 1994). These findings are applicable when one only needs to compute the fraction of electrons left totally unscattered in an electron beam. However if electron beam profiles, skirt distributions and spot sizes are to be derived in ESEM we need to consider both elastic and inelastic scattering at a plural level.

Danilatos (1988) and Danilatos (1990a) have also investigated electron scattering in a low vacuum environment. However, unlike Moncreiff *et al.* (1979), Farley & Shah (1990a) and Gauvin (1999), whose investigations were based on single scattering, Danilatos (1988) performed a rigorous theoretical and experimental analysis based on plural scattering. Danilatos (1988) also used the equations of Lenz (1954) to calculate cross sections for monotonic gases, however instead of using the theoretical models of Wentzel (1926), Danilatos (1988) chose to use formulae developed by Jost & Kessler (1963) who studied plural scattering of electrons. The scattering cross sections adapted by Danilatos (1988) were therefore chosen to exemplify PE scattering applicable to ESEM and are shown below.

Monatomic Gases

Expressions for atomic differential elastic and inelastic scattering cross sections for monatomic gases, originally derived by Lenz (1954), are

$$\left(\frac{d\sigma_e^s}{d\Omega}\right)_A = \frac{AZ}{16 \left[\sin^2\left(\frac{\theta}{2}\right) + \sin^2\left(\frac{\theta_0}{2}\right)\right]^2}, \quad (2.3.1)$$

$$\left(\frac{d\sigma_i^s}{d\Omega}\right)_A = \frac{A(\theta^2 + \theta_E^2 + 2\theta_0^2)}{(\theta^2 + \theta_E^2)(\theta^2 + \theta_E^2 + \theta_0^2)}, \quad (2.3.2)$$

where

$$A = \frac{\lambda_e^4 Z \left(1 + \frac{\varepsilon_{PE}}{\varepsilon_0}\right)^2}{4\pi^4 a_H^2}, \quad (2.3.3)$$

$$\theta_0 = \frac{\lambda_e}{2\pi R}, \quad (2.3.4)$$

$$\theta_E = \frac{J}{4\varepsilon_{PE}}. \quad (2.3.5)$$

Z is the atom atomic number, σ_e^s is the atomic elastic scattering cross section, σ_i^s is the atomic inelastic scattering cross section, Ω is the scattering solid angle, θ is the scattering angle in radians, ε_{PE} is the PE beam energy in eV, $\varepsilon_0 = 5.11 \times 10^5$ eV (electron rest energy), $a_H = 5.29 \times 10^{-11}$ m (Bohr radius of the hydrogen atom), R is the effective radius of the atom, J is the ionization energy in eV and

$$\lambda_e = \frac{h}{2\pi [2\varepsilon_{PE}em_e (1 + 2\varepsilon_{PE}em_e c^2)]^{1/2}} \quad (2.3.6)$$

is the relativistic electron wavelength, where h is Planks constant, e is the electron charge, m_e is the electron rest mass and c is the speed of light in vacuum (Danilatos 1988). The effective radius of the atom can be determined from the atomic potential model by Wentzel (1926) which has been adapted by Burge & Smith (1962) as

$$R = \left[f_e(0) \frac{a_H}{2Z} \right], \quad (2.3.7)$$

where $f_e(0)$ is the atomic scattering amplitude for zero angle scattering, which are shown below for several gaseous atoms in table 2.1. The mean ionization energy J , needed in equation (2.3.5), can be taken as the first ionization potential (V_i^1) (energy needed to remove a single outer shell electron), however it is recommended that J be derived experimentally (Danilatos 1988). First ionization potentials of several gases are shown in table 2.1. Figure 2.2 shows the elastic, inelastic and total differential scattering cross section versus scattering angle for Ar at PE energies of 30 keV. It can be seen from the figure that inelastic scattering is greatly dominant over elastic scattering up to ~ 0.01 radians until at ~ 0.1 radians the elastic component prevails. The figure therefore demonstrates that elastically scattered electrons are deflected

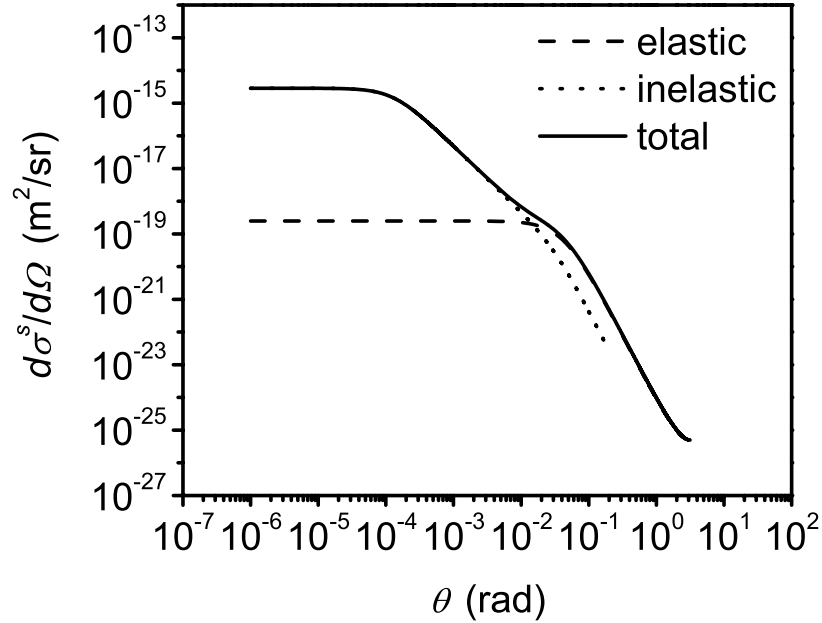


Figure 2.2: Differential scattering cross section $d\sigma/d\Omega$ (elastic, inelastic and total) versus scattering angle θ in argon (Ar) (adapted from Danilatos (1988) and Jost & Kessler (1963)). [$\varepsilon_{PE} = 30$ keV]

at larger angles and therefore cause a greater reduction in beam current, and hence image SNR, than that of inelastically scattered electrons.

Molecular Gases

In order to account for the assumptions made by Moncreiff *et al.* (1979) and Farley & Shah (1990a), who assumed that the total scattering cross section for a molecule is simply the sum of the elastic and inelastic scattering cross sections, Danilatos (1988) performed a thorough investigation into molecular cross sections based on the theory of Mott & Massey (1965). Mott & Massey (1965) took into consideration additional effects of binding between atoms in a molecule.

Table 2.1: First ionization potentials (V_i^1) and scattering amplitudes ($f_e(0)$) of several atoms (Danilatos 1988, von Engel 1965)

Atom	V_i^1 (eV)	$f_e(0)$ (10^{-10} m)
Ar	15.75	4.71
H	13.6	0.529
N	14.5	2.20
O	13.5	2.01

The elastic differential scattering cross section of a molecule is (Danilatos 1988, Danilatos 1990a)

$$\left(\frac{d\sigma_e^s}{d\Omega}\right)_M = \sum_i \sum_j f_i(\theta) f_j(\theta) \frac{\sin(sr_{ij})}{sr_{ij}}, \quad (2.3.8)$$

where r_{ij} is the interatomic distance between atoms i and j in the molecule, and

$$s = \frac{4\pi \sin\left(\frac{\theta}{2}\right)}{\lambda_e}. \quad (2.3.9)$$

The function $f(\theta)$ in equation (2.3.8) is the scattering amplitude of each atom in the molecule which is defined as

$$|f(\theta)|^2 = \left(\frac{d\sigma_e^s}{d\Omega}\right)_A, \quad (2.3.10)$$

which can be obtained from equation (2.3.1). Equation (2.3.8) is only valid if the scattering can be considered coherent and the conditions

$$\frac{2\pi r_0}{\lambda} \gg 1 \quad (2.3.11)$$

and

$$r_0 \gg R_m \quad (2.3.12)$$

are satisfied, where r_0 is the minimum distance between atomic centres and R_m is the maximum interaction range of the incident electrons. The condition in equation (2.3.11) is adequately satisfied with the beam energies utilized in an ESEM, however, the condition in equation (2.3.12) is generally not satisfied, but is within the limits of accuracy after the integration of equations (2.3.8) and (2.3.10) (Danilatos 1988).

As a first approximation, inelastic scattering of a molecule can be considered incoherent and therefore the differential inelastic scattering cross section can be taken as the sum of the individual i atomic differential inelastic scattering cross sections:

$$\left(\frac{d\sigma_i^s}{d\Omega}\right)_M = \sum_{i=1}^n \left(\frac{d\sigma_i^s}{d\Omega}\right)_{Ai}, \quad (2.3.13)$$

where n is the total number of atoms in the molecule (Danilatos 1988, Farley & Shah 1990a, Moncreiff *et al.* 1979).

Figure 2.3 shows several total scattering cross sections versus primary beam energy for monatomic Ar, diatomic (nitrogen (N₂)) and polyatomic (water vapour (H₂O)) gases obtained using the theory stated above. The curves were generated by numerical integration of equations (2.3.1) and (2.3.2), for the case of Ar, and the sum of equations (2.3.10) and (2.3.13), for N₂ and H₂O, from 10⁻⁶ to π radians. The scattering cross sections of Ar, N₂ and H₂O are shown in figure 2.3 as they represent gases with completely different bonding properties, electron configurations and degrees of freedom. They were also chosen because they are gases commonly employed in ESEM and were used extensively throughout experimental studies presented in this thesis. It can be seen from figure 2.3 that the scattering cross sections for Ar are largest, followed by N₂ and H₂O, despite classical theory showing that H₂O has the largest diameter followed by N₂ and then Ar. The diameters of Ar, N₂ and H₂O are 3.64 Å, 3.75 Å and 4.60 Å, respectively (McDaniel 1964). This demonstrates that gaseous

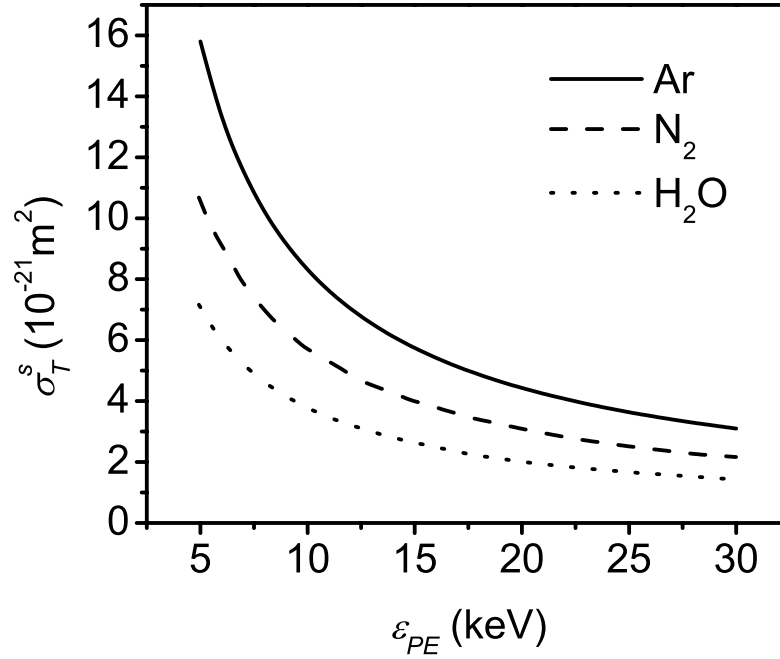
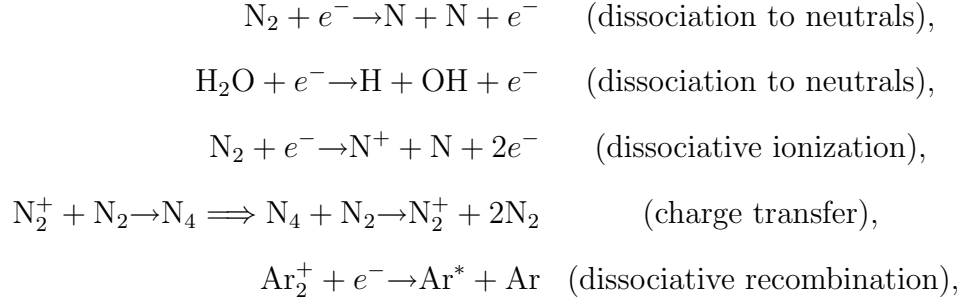


Figure 2.3: Total scattering cross section (σ_T^s) of monotonic (argon (Ar)), diatomic (nitrogen (N_2)) and polyatomic (water vapour (H_2O)) gases versus primary electron beam energy (ϵ_{PE}) (Danilatos 1988, Jost & Kessler 1963).

electron scattering probabilities are inversely proportional to atomic and molecular diameters and also reveals the complexities associated with deriving mathematical expressions for scattering cross sections based on the fact that ionization energies and scattering amplitudes are not directly related to atomic or molecular size.

Along with the several assumptions stated above, theory neglects the effects of ionization, dissociation, charge transfer and recombination occurring in the gas, as well as electric fields resulting from detection electrodes and sample charging. Reactions

such as



for example, where * and + denotes a singly electronically excited molecule and a positive ion (PI), respectively (von Engel 1965, Nasser 1971, Varney 1953, Yousfi & Benabdessadok 1996), can cause significant concentrations of additional atomic species to be present in a parent molecular gas. Atomic and molecular collisions that readily occur in partially ionized gas, such as that in an ESEM, can be found in Appendix A. It should also be noted that under typical ESEM chamber conditions where: (i) imaging gases are varied regularly, (ii) chamber bake-outs are not often performed and (iii) sample outgassing occurs, residual atomic or molecular species can be present in addition to the parent imaging gas being used. PIs generated by signal (SE and BSE)-gas interactions and PE-gas interactions have the ability to generate an ion space charge in the sample-electrode gap due to the mobility of ions being ≈ 1000 times smaller than that of electrons (von Engel 1965, Farley & Shah 1990a). When insulating materials are irradiated, the ion space charge has been shown to increase the landing energy of PEs (Toth *et al.* 2002b). The energy of the PEs are increased via the electric field generated by the ‘cloud’ of PIs above the sample surface. An increase in the PE landing energy is also observed as a consequence of the electric field generated by the GSED and the large field gaseous secondary electron detector (LFGSED) of an ESEM (Toth *et al.* 2002b). The electric field generated by trapped charge in insulating materials has also been shown to increase the PE landing energy when the net charge in the sample is positive and

decrease the landing energy for the case of negative charging. The extent to which the primary beam is affected is a summation of all of the processes described above, however, under imaging conditions commonly employed in an ESEM the PE landing energy is generally increased. Therefore, underestimating the PE beam energies used in equations to calculate elastic and inelastic scattering cross sections, as well as neglecting the various reaction processes and subsequent addition of impure atomic species, will produce underdeveloped theoretical scattering models.

Due to the complexities, and hence assumptions, arising in theoretical derivations of scattering cross sections, one would prefer to use cross sections that have been obtained directly in an ESEM. Phillips *et al.* (1999) have experimentally obtained total scattering cross sections for several gases by measuring the electron beam induced current (EBIC) generated in the depletion region of a cross-sectioned silicon $p-n$ junction diode by the unscattered probe as a function of pressure. The experimental total scattering cross sections for H_2O and N_2 at various primary beam energies are shown in figure 2.4. Comparing figures 2.3 and 2.4, it can be seen that the theoretical scattering cross sections of Danilatos (1988) and Jost & Kessler (1963) are approximately double the value of those obtained by Phillips *et al.* (1999). This can be explained by the fact that the cross-sectioned $p-n$ junction diode used by Phillips *et al.* (1999) measured both the unscattered probe component of the PE beam as well as a contribution from scattered/skirt PEs as a result of the diodes relatively large depletion region. The measured probe currents were therefore slightly overestimated which in turn underestimated the experimental scattering cross sections obtained. A more accurate way of measuring PE scattering cross sections in an ESEM, utilizing the advantages of EBIC methods, which allow direct current measurements, would be to use an array of quantum dots whereby the unscattered and skirt PEs could be collected independently as a function of position. Utilizing this method would also allow direct measurements of PE beam spatial distributions or beam intensity profiles and skirt widths.

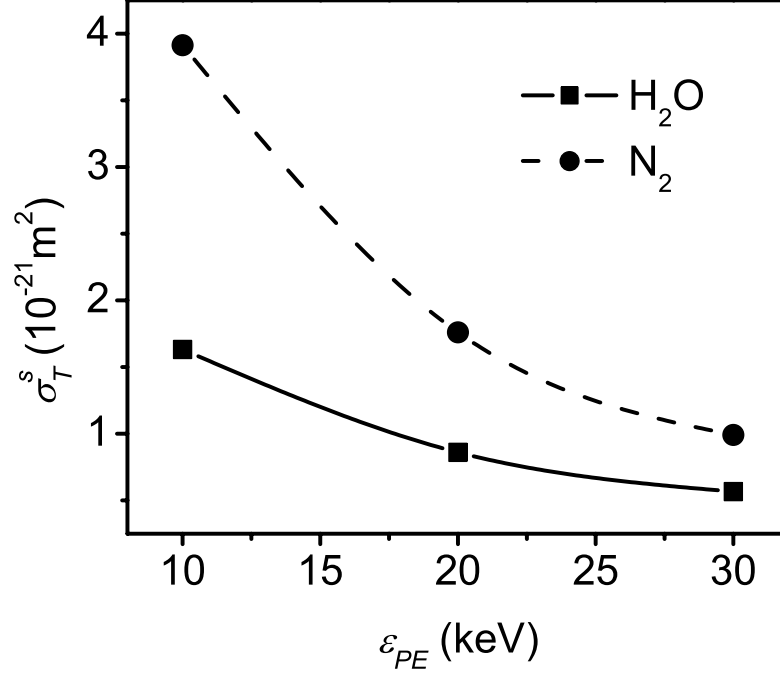


Figure 2.4: Experimentally obtained total scattering cross sections (σ_T^s) versus primary electron beam energy (ϵ_{PE}) for water vapour (H_2O) and nitrogen (N_2) (Phillips *et al.* 1999). [$d = 6.5$ mm, $T = 298$ K]

2.3.2 Primary Electron Beam Transmission

Poisson statistics shows that the probability $P(x)$ that a PE undergoes x collisions ($x = 0, 1, 2, \dots$) is

$$P(x) = \frac{m^x e^{-m}}{x!}, \quad (2.3.14)$$

where m is the average number of scattering events per PE, which is defined as

$$m = \sigma_T^s n d, \quad (2.3.15)$$

where n is the concentration of gas particles in the chamber and d is the distance between the final PLA and the sample surface or the sample-electrode separation

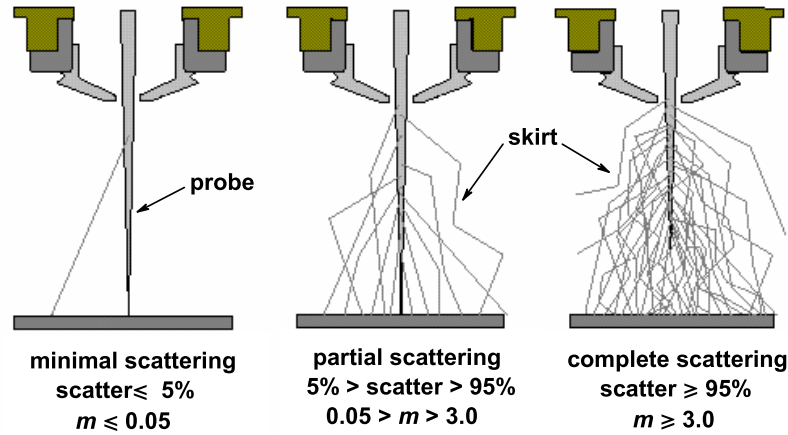


Figure 2.5: Schematic diagram illustrating the scattering regimes for an electron beam traversing a gaseous medium. A conventional high vacuum SEM operates in the ‘minimal scattering regime’ whilst an ESEM operates in the ‘partial scattering regime’. Complete scattering of the PE beam conveys no useful image information (taken from Philips Electron Optics 1996).

(Danilatos 1988). In order to obtain a substantial electron current in the focused probe and hence an acceptable SNR (probe to skirt intensity) in ESEM images, 5% of the beam needs to remain totally unscattered, which corresponds to $m \leq 3$ (Danilatos 1994). The condition $m > 3$ is termed complete scattering and is not suitable for imaging (Philips Electron Optics 1996). Ideally, in an ESEM, we require the condition $m \leq 1$ (partial scattering regime) whereby more than 37% of the beam remains in the focused probe and 63% of the beam is contributed to the skirt (Danilatos 1994). Figure 2.5 illustrates the various scattering regimes for an electron beam traversing a gas. If we treat the gas inside the specimen chamber of an ESEM as ideal then

$$n = \frac{p}{kT}, \quad (2.3.16)$$

where k is Boltzmann’s constant and T is the absolute temperature of the gas.

If the PE current exiting PLA1 is I_{PE}^0 , then the current in the completely unscattered probe ($x = 0$) component of the beam reaching the sample is given by (Danilatos 1994)

$$I_{PE} = I_{PE}^0 e^{-\frac{\sigma_T^s p d}{kT}}. \quad (2.3.17)$$

It can be seen from the equation above that the current in the probe will decrease as the pressure and working distance are increased. Equation (2.3.17) has been derived under the assumption that the pressure, and hence gas concentration, between PLA1 and the sample is homogeneous. It also assumes that there is no loss of PE current between PLA1 and PLA2, hence the term I_{PE}^0 can also be taken as the beam current under high vacuum conditions. Danilatos (1994) has derived expressions for PE-gas scattering under non-idealistic conditions whereby gas density and temperature gradients (known as a transition region) exist between the two PLAs and extend approximately one aperture diameter below PLA1 into the specimen chamber (Danilatos 1991, Danilatos 1992a, Danilatos 1994). The transition region is formed as a result of localized variations in gas flow velocity in the vicinity of PLA1 as gas escapes from the sample chamber to the lower pressure EC1 and EC2 regions of the microscope (the EC1 and EC2 regions of an ESEM are illustrated in figure 2.1). The size and density distribution of the transition region is affected by the geometry of PLA1, d and gas type (Danilatos 1991, Danilatos 1992a, Danilatos 1994). In general, the effects of the transition region can be neglected when sharp edged PLAs, condensable gases and gas path lengths less than the aperture diameter are avoided (Danilatos 1991, Danilatos 1994).

A more generalized equation for the average number of scattering events per PE, which takes into consideration the effects of the gas density and temperature gradients

within the transition region, is given by

$$m_T = \frac{\sigma_T^s}{kT} [p(d - D) + pD\zeta_T + p_1(H - h)]$$

$$p > p_1, \quad d > D, \quad H > h, \quad (2.3.18)$$

where p is the background sample chamber pressure, T is the background sample chamber temperature, D is the distance that the transition region extends below PLA1 into the chamber (generally 1 PLA diameter), ζ_T is the mass thickness of the transition region, p_1 is the background or ‘stagnation’ pressure between PLA1 and PLA2, H is the axial distance between PLA1 and PLA2, and h is the distance that the transition region extends above PLA1 (Danilatos 1994). It can easily be seen that when p_1 is made very low, which is the case in most ESEMs, and $d \gg D$, equation (2.3.18) reduces to equation (2.3.15).

Figure 2.6 shows experimentally obtained electron beam transmission (unscattered probe current (I_{PE}^0) to beam current (I_{PE}) ratio) versus (a) nitrogen pressure (p_{N_2}) and (b) water vapour pressure (p_{H_2O}) acquired as a function of ε_{PE} . It can be seen that the number of electrons scattered out of the focused probe is consistent with equation (2.3.17) and that H_2O should be used as an imaging gas in preference to N_2 if image SNR is of importance. Recent studies of electron beam-gas scattering have found that minimal PE skirting occurs when using He gas and is therefore an excellent choice of imaging gas for low vacuum x-ray microanalysis (Adamiak & Mathieu 2000, Kadoun *et al.* 2003, Stowe & Robinson 1998).

2.3.3 Electron Distribution and Skirt Profiles

In order to study the effects of electron beam scattering on resolution and SNR in images obtained using ESEM, one must know the distribution of electrons in the beam. The electron distribution and intensity must be considered for both the relatively

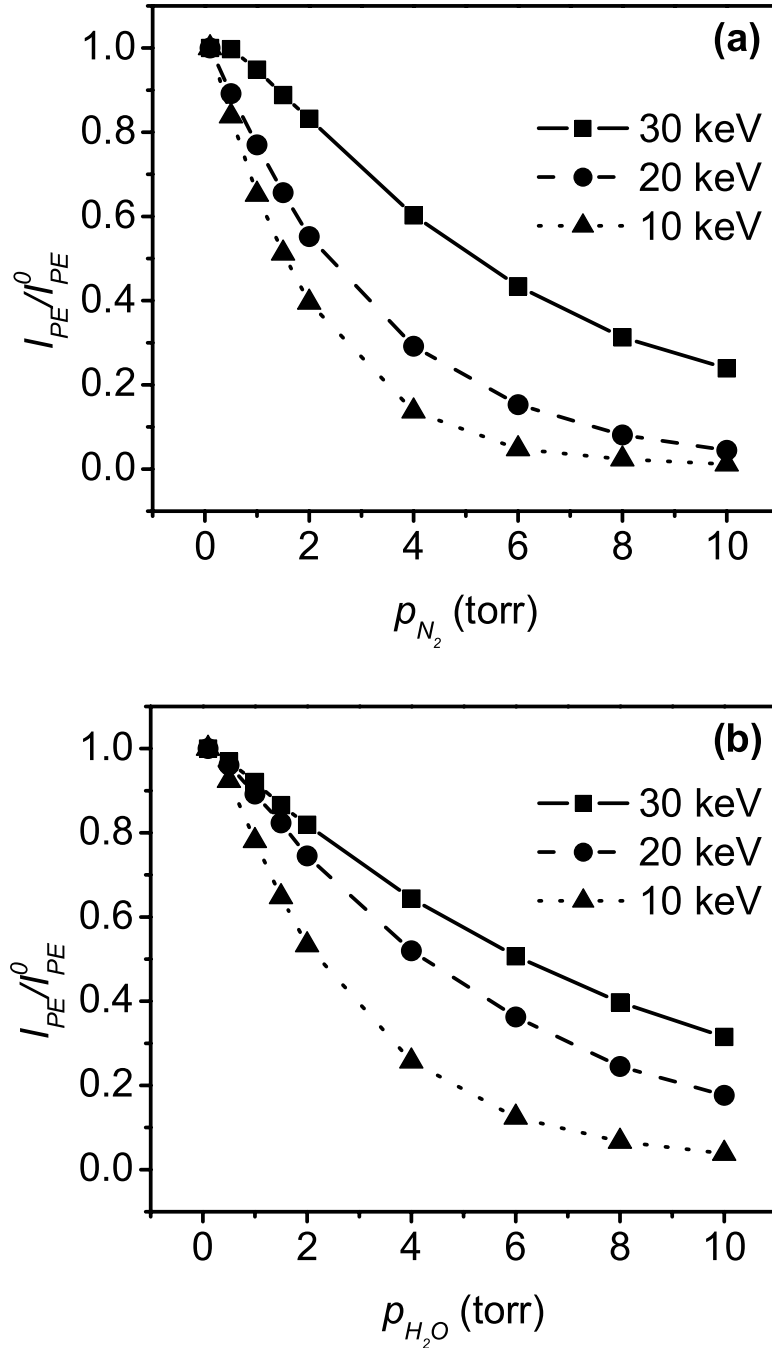


Figure 2.6: Experimental primary electron beam transmission (unscattered probe current (I_{PE}^0) to beam current (I_{PE}) ratio) versus (a) nitrogen pressure (p_{N_2}) and (b) water vapour pressure (p_{H_2O}) at various primary electron beam energies (ε_{PE}) (Phillips *et al.* 1999). [$d = 6.45$ mm, $T = 298$ K]

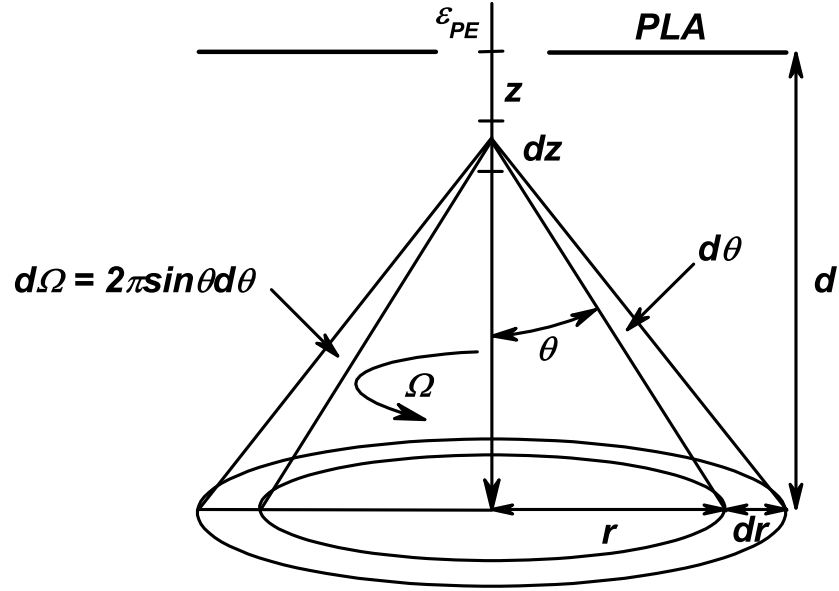


Figure 2.7: Schematic diagram illustrating PE-gas scattering in the ESEM. A PE of energy ε_{PE} undergoing a collision with a gas atom or molecule between z and $z + dz$ is scattered through an angle θ and $\theta + d\theta$ into the solid angle $d\Omega$. The scattered PE then strikes the sample surface between r and $r + dr$ (Danilatos 1988, Kadoun *et al.* 2003).

unscattered central portion of the beam, which forms a focused spot on the sample, and the skirt, which contains electrons that have been scattered through larger angles.

A means of quantifying the distribution of electrons in the primary beam is to calculate the probability distribution ($V_s(r)$), which when multiplied by $2\pi r dr$, gives the probability that an electron is scattered within the solid angle of the annulus $2\pi r dr$ located a distance d from the beam entrance point into the gas (PLA1). Figure 2.7 illustrates the scattering of a single electron. The electron is released into the chamber through PLA1 where after travelling a distance z undergoes a collision with a gas atom

or molecule between z and $z+dz$. After the collision, the electron is scattered through an angle between θ and $d\theta$ and strikes the sample in an annulus between r and dr at a distance d from PLA1. If we first consider the case of single scattering the total probability that the electron strikes the annulus from anywhere along z is

$$V_s(r) 2\pi r dr = \int_0^d n e^{-\sigma_T^s n z} \frac{d\sigma_T^s}{d\Omega} d\Omega dz, \quad (2.3.19)$$

where

$$\frac{d\sigma_T^s}{d\Omega} = \frac{d\sigma_e^s}{d\Omega} + \frac{d\sigma_i^s}{d\Omega} \quad (2.3.20)$$

is the total differential scattering cross section, which is applicable for both atomic (equations (2.3.1) and (2.3.2)) and molecular (equations (2.3.10) and (2.3.13)) gases; and $d\Omega$ is the scattering solid angle, defined as (Danilatos 1988)

$$d\Omega = 2\pi \sin \theta d\theta. \quad (2.3.21)$$

Substituting equation (2.3.20) into equation (2.3.19), and knowing that

$$dr = \frac{r d\theta}{\sin \theta \cos \theta} \quad (2.3.22)$$

from figure 2.7, we find the single scattering probability distribution to be

$$V_s(r) = n e^{-\sigma_T^s n d} \int_{\arctan(\frac{d}{r})}^{\pi/2} \frac{\cos \theta}{r} \frac{d\sigma_T^s}{d\Omega}(\theta) e^{\frac{r}{\tan \theta}} d\theta, \quad (2.3.23)$$

where the total differential scattering cross section needs to be known as a function of the scattering angle, which was derived for atomic and molecular gases in section 2.3.1. The condition of single scattering gives, from equation (2.3.14), $m \leq 0.36$ (95% of electrons suffer zero or one collision). However, in an ESEM, imaging is generally performed at values of m up to three as mentioned previously. In the most common case, of $m = 1$, and from equation (2.3.14), we can see that 37% of electrons suffer no collisions, 37% suffer one collision, 18% two collisions, 6% three collisions etc., and therefore we cannot be certain that equation (2.3.23) will adequately predict

correct scattering probability distributions. Probability distributions based on plural scattering are therefore needed to provide a more accurate description of electron distributions in an ESEM.

Jost & Kessler (1963) have shown, for an infinitely narrow electron beam, that the probability distribution for plural scattering ($V_p(\rho)$) of electrons is

$$V_p(\rho) = \frac{1}{\pi^2} \int_0^\infty \tau K_0(\rho\tau) \sin[m\varphi_1(\tau)] e^{-m[1-\varphi_2(\tau)]} d\tau, \quad (2.3.24)$$

where the radial distance (r) has been replaced with a reduced radial distance (ρ) to assist with calculations:

$$\rho = \frac{2\pi Rr}{\lambda_e d}. \quad (2.3.25)$$

In equation 2.3.24, $\varphi_1(\tau)$ and $\varphi_2(\tau)$ are given by

$$\begin{aligned} \varphi_1(\tau) = & -\frac{\pi^2}{4(Z-1-4\ln\beta)} \left\{ (Z-5) [J_0(\tau) H_1(\tau) - J_1(\tau) H_0(\tau)] \right. \\ & \left. + 4 [J_0(\beta\tau) H_1(\beta\tau) - J_1(\beta\tau) H_0(\beta\tau)] + \frac{8}{\pi} [J_0(\tau) - J_0(\beta\tau)] \right\} \end{aligned} \quad (2.3.26)$$

and

$$\begin{aligned} \varphi_2(\tau) = & -\frac{\pi^2}{4(Z-1-4\ln\beta)} \left\{ (Z-5) [N_0(\tau) H_1(\tau) - N_1(\tau) H_0(\tau)] \right. \\ & \left. + 4 [N_0(\beta\tau) H_1(\beta\tau) - N_1(\beta\tau) H_0(\beta\tau)] + \frac{8}{\pi} [N_0(\tau) - N_0(\beta\tau)] \right\} \end{aligned} \quad (2.3.27)$$

respectively, where J_n is the Bessel function of order n , H_n is the Struve's function of order n , N_n is the Neumann's Bessel function of the second kind of order n , K_0 is the modified Bessel function of the second kind of zero order, and (Danilatos 1988)

$$\beta = \frac{\theta_E}{\theta_0} = \frac{\pi R J}{2\lambda_e \varepsilon_{PE}}. \quad (2.3.28)$$

It must be stressed that $V_p(\rho)2\pi\rho d\rho$ is the probability that a PE, initially travelling along an infinitely thin beam axis, is scattered within the annulus $2\pi\rho d\rho$ of a plane

at a distance d from PLA1. This means that $V_p(\rho)$ can be used to represent a 2-dimensional intensity profile of the fraction of PEs that are scattered out of the infinitely thin beam. The probability that a PE remains wholly unscattered, and hence remains in the infinitely thin beam, was previously described by equations (2.3.14) and (2.3.17). Therefore, PE beam intensity profiles can be constructed using equation (2.3.24) as the scattered or skirt component of the beam, and a delta function on the beam axis of total magnitude given by equation (2.3.17). As the beam intensity profiles represent a true probability distribution, the condition:

$$\int_0^{\infty} e^{-\frac{\sigma_T^s p d}{kT}} + V_p(\rho) 2\pi\rho d\rho = 1, \quad (2.3.29)$$

must be satisfied (Danilatos 1988).

Figure 2.8 shows theoretical normalized beam intensity verses r acquired as a function of argon pressure (p_{Ar}) ($p_{Ar} = 0.5 - 16.2$ torr) for an infinitely thin beam (delta function). The beam profiles were obtained using plural scattering models of Jost & Kessler (1963) (equations (2.3.24)-(2.3.29)). It can be clearly seen from figure 2.8 that as p_{Ar} increases the number of PEs scattered out of the infinitely thin delta function, forming the skirt, increases whilst the unscattered fraction of electrons remaining in the infinitely thin delta function decreases. However, it is also seen that even at relatively high pressures of 16.2 torr, where a significant proportion of electrons are scattered, the central portion of the beam is still clearly distinguishable from the scattered component which implies that the probe does not significantly broaden, but instead acquires a skirt of scattered electrons around it. Increased pressures, and sample-electrode separations for that matter, merely decrease the number of PEs in the probe and therefore reduce the signal or contrast in images rather than degrading resolution. The effects of the skirt are to enhance the background noise in images and hence the SNR is reduced as p , and or d , is increased. The implications to this are that high resolution imaging is attainable in an ESEM provided there is a sufficient

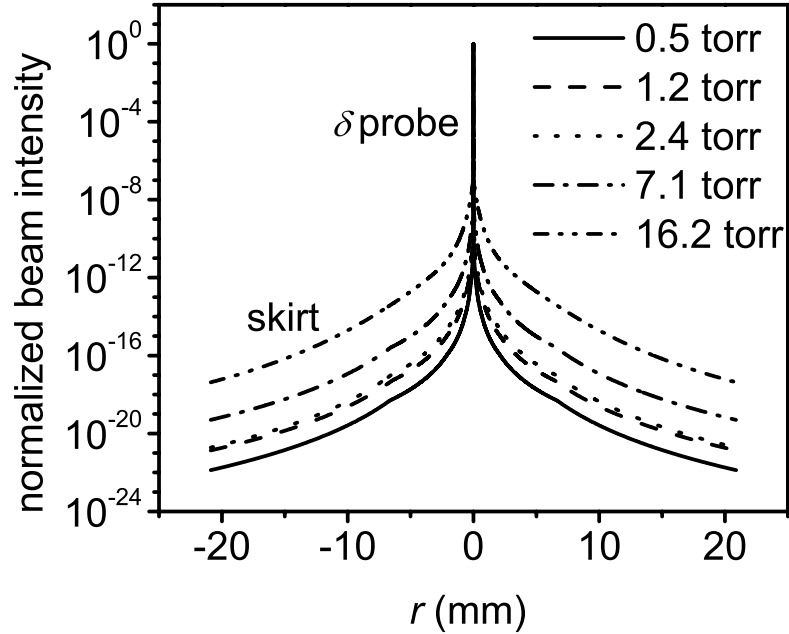


Figure 2.8: Theoretical plural scattering normalized beam intensity versus radial distance (r) from beam center for an infinitely thin electron beam (delta function) in argon (Ar) acquired as a function of argon pressure (p_{Ar}) (adapted from Danilatos 1988 and Jost & Kessler 1963). [$\varepsilon_{PE} = 50$ keV, $d = 6.45$ mm, $T = 298$ K]

current of PEs in the probe and that the probe is significantly smaller in diameter than that of the skirt.

To justify the theoretical statements implied above, experimental normalized beam intensity versus r , acquired as a function of p_{N_2} and p_{H_2O} (2-16 torr), adopted from Phillips *et al.* (1999), are shown in figures 2.9(a) and (b), respectively. Again, it can clearly be seen that the unscattered probe is surrounded by a scattered electron skirt that extends over several micrometres.

In order to depict exactly how image SNR and resolution are affected by PE-gas scattering one must know how the skirt behaves as a function of microscope operating

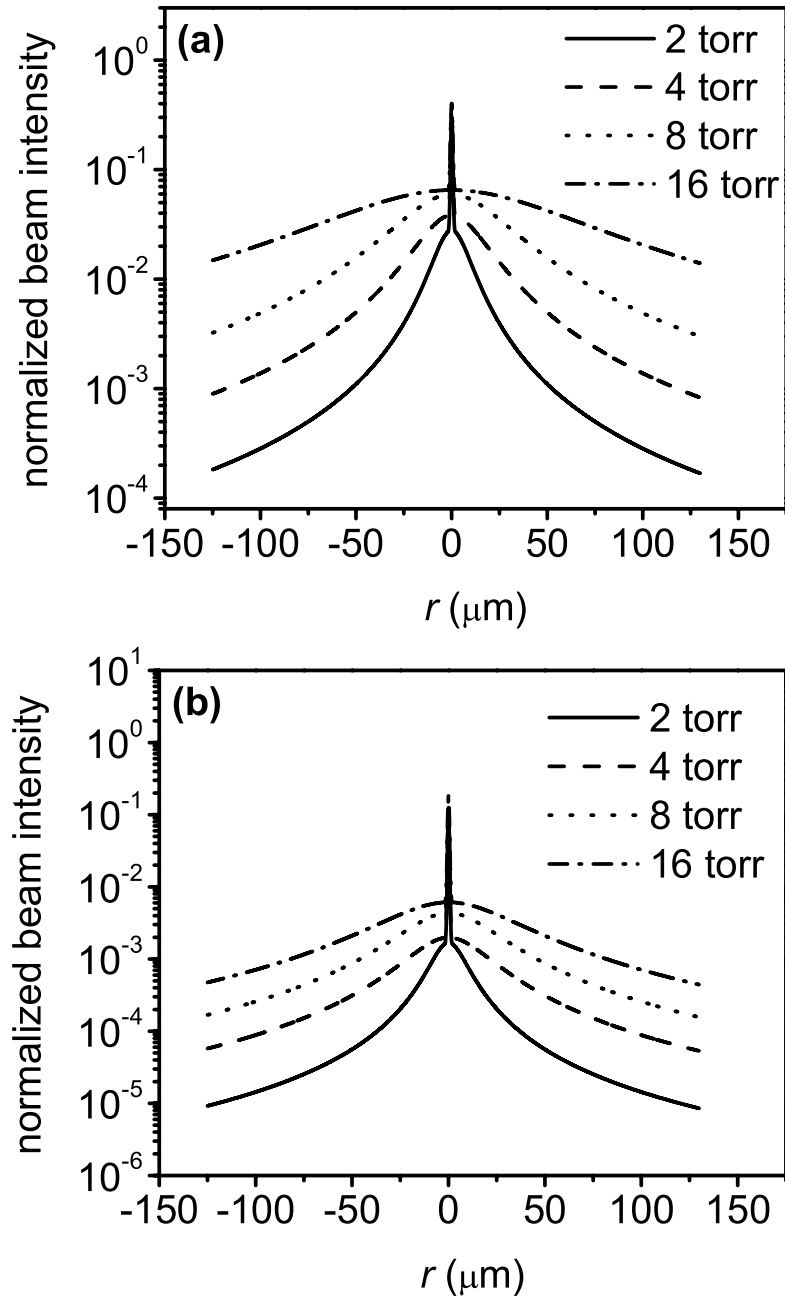


Figure 2.9: Experimental normalized beam intensity versus radial distance (r) from beam center acquired as a function of (a) nitrogen pressure (p_{N_2}) and (b) water vapour pressure (p_{H_2O}) (Phillips *et al.* 1999). [$\varepsilon_{PE} = 30$ keV, $d = 10.0$ mm]

parameters. A means of quantifying the width of the skirt is to measure the skirt half-width-radius ($r_{1/2}$), which is defined as the radial distance from the beam axis ($r = 0$) to a point on the sample plane in which half of the skirt electrons are contained ($r = r_{1/2}$). In order to obtain $r_{1/2}$, the current of electrons in the infinitely thin beam must first be subtracted from the total current in the beam leaving the current of electrons in the skirt. The skirt intensity profile is then integrated from $r = 0$ to $r = r_{1/2}$ over its entire solid angle, such that

$$\int_0^{r_{1/2}} V_p(r) 2\pi r dr = 0.5. \quad (2.3.30)$$

Shown in figure 2.10 is a three-dimensional plot of $r_{1/2}$ versus p_{Ar} and d for an infinitely thin electron beam obtained from the plural scattering equations of Jost & Kessler (1963) described above. It can be seen from the plot that $r_{1/2}$ varies exponentially with d at large p_{Ar} , but at low p_{Ar} varies linearly with d . It can also be seen that at small total gas path lengths skirt broadening is independent of p_{Ar} . Curve fitting reveals that $r_{1/2}$ has power law dependencies on both p and d given by

$$r_{1/2}(p) = A + Bp^C \quad (2.3.31)$$

and

$$r_{1/2}(d) = Dd + Ed^F \quad (2.3.32)$$

respectively, where A to F are constants dependent on scattering cross sections, electron wavelengths, atomic radii, temperature and beam energy. Experimental observations by Doehne & Bower (1993) revealed that the width of the skirt varies linearly with p (Carlton 1997). This effect is in agreement with the theory of Jost & Kessler (1963) provided p is greater than approximately 2 torr as seen from figure 2.10. Doehne & Bower (1993) also speculate that variations in the skirt width with p , and or d , are minimal compared to changes in the intensity of the skirt (Doehne 1997). Kadoun *et al.* (2003) has revealed, using Monte Carlo simulations of PE scattering in He, that the skirt radius is independent of p up to approximately 0.75 torr.

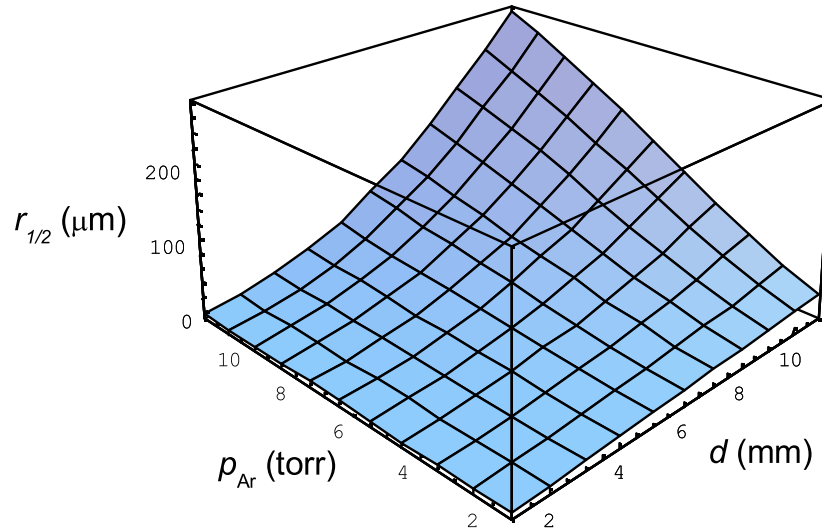


Figure 2.10: Theoretical plural scattering skirt half radius ($r_{1/2}$) versus argon pressure (p_{Ar}) and sample-electrode separation (d) for an infinitely thin electron beam in argon (Ar) (adapted from Danilatos 1988 and Jost & Kessler 1963). [$\varepsilon_{PE} = 50$ keV, $T = 298$ K]

This section therefore described how the PE beam is affected by the imaging gas between its chamber entry point, at the final PLA, and the sample surface. It showed that in order to theoretically investigate the loss of current in the high resolution probe, through scattering, and the spatial distribution of the beam one must know the cross sections associated with PE-gas scattering. However, as scattering cross sections have been mostly derived theoretically, one must be careful in choosing correct scattering models. To overcome this problem experimentally obtained cross sections should be used whenever possible provided that correct procedures have been used in obtaining them.

The next section of this chapter describes how the signals generated by the PE beam at the sample surface, and in the gas, are detected by an ESEM's gaseous secondary electron detector (GSED) ring and associated electronics to generate images.

2.4 Signal Detection

A gaseous secondary electron detector (GSED), consisting of a 3 mm diameter positively biased metallic ring (with a voltage, $V_{GSED} = +30$ to $+550$ volts) placed above the sample stage and concentrically around the optical axis of the microscope, accelerates low energy SEs generated at the sample surface by the PE beam through the gas. The SEs emitted from the sample enter the gas with a Maxwellian energy distribution of maximum energy of approximately 3 eV and range between 0 and 50 eV (Goldstein *et al.* 1992, Reimer 1985). Once the SEs have exceeded the first ionization potential of the gas they undergo ionizing collisions with gas molecules producing additional electrons known as environmental secondary electrons (ESEs) and positive ions (PIs) (Danilatos 1990c). Electron-gas molecule collisions are also capable of generating photons and long lived excited species (metastables), which will be considered in chapter 3.7. Negative ion concentrations are assumed negligible when Ar, N₂ or H₂O is used as the imaging gas (von Engel 1965, Nasser 1971, Thiel *et al.* 1997). The ESEs further ionize the gas on their way to the ring producing an amplified electron signal (Danilatos 1990c, Meredith *et al.* 1996) that is up to three orders of magnitude greater than the original SE signal leaving the sample (Fletcher *et al.* 1997, Thiel *et al.* 1997). The magnitude of the amplified electron signal, and hence the contrast in images, can be controlled by varying the imaging gas type, working distance (WD) or sample-electrode separation (d), pressure (p), electron beam energy (ε_{PE}) (Fletcher *et al.* 1997, Fletcher *et al.* 1999, Meredith *et al.* 1996, Thiel *et al.* 1997) as well as the sample-electrode geometry (Newbury 1996). Theory relating to gaseous cascade amplification is covered in chapter 3.

High energy PEs and BSEs are also capable of ionizing collisions and subsequent amplification of their ionizing products, however, this signal component contributes to a constant background noise in images (Fletcher *et al.* 1999). The spatial distribution

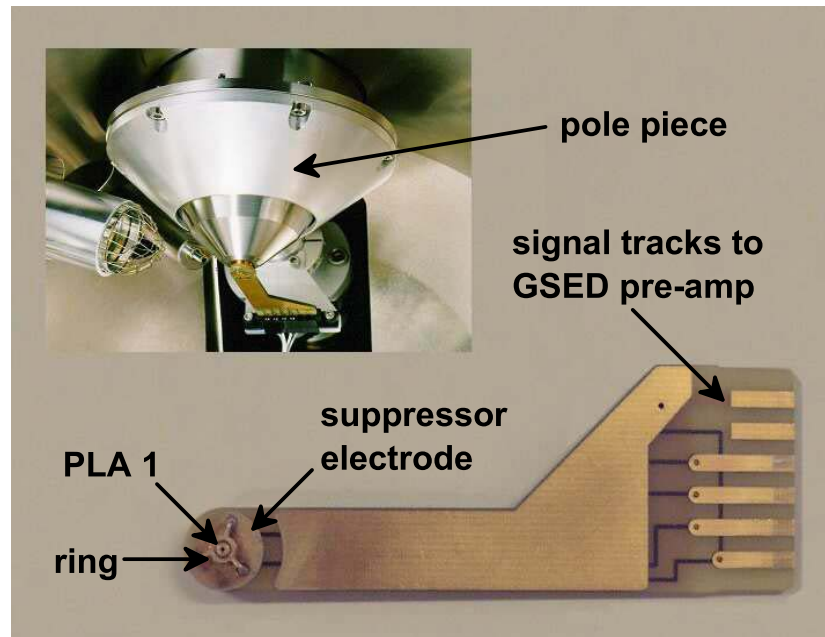


Figure 2.11: Image showing the gaseous secondary electron detector (GSED). The suppressor electrode is placed at +9 volts relative to the ring voltage to discriminate against backscattered and type III secondary electrons.

of BSEs emerging from the sample follows a cosine function (Goldstein *et al.* 1992), which means that BSEs have a higher probability of being collected by the GSED and generating type III SEs (spurious electrons generated at chamber walls or other non detecting media (Goldstein *et al.* 1992, Reimer 1985)) on the ring and the surrounding areas. For this reason the GSED is equipped with a suppressor electrode, located below PLA1, and above the ring, which is held at +9 volts with respect to V_{GSED} so that any type III SEs generated in the vicinity of the GSED will not contribute to imaging signals. An image of the GSED is shown in figure 2.11.

The PIs generated in the cascade by the SEs, PEs and BSEs drift towards the sample, under the influence of the electric field generated by the ring, neutralizing

any excess charge build up on the surface of insulating materials (Danilatos 1988, Moncreiff *et al.* 1978). Neutralization of excess charge by PIs allows imaging and microanalysis of wet, hydrated, biological and insulating specimens without the need for conductive coatings (Danilatos 1988, Farley & Shah 1991, Moncreiff *et al.* 1978, Philips Electron Optics 1996). The PIs, photons and metastables, generated in each electron avalanche (single traverse of field accelerated electrons from the cathode to the anode) are capable of impacting the sample surface or stage, liberating SEs, which subsequently initialize additional electron avalanches and produce a cascaded electron signal (von Engel 1965, Nasser 1971). The signal caused by this phenomenon adds to background noise, however, when H₂O is used as the imaging gas this noise component is negligible (Fletcher *et al.* 1997, Thiel *et al.* 1997). The processes described above are illustrated in figure 2.12.

The flow of electrons and ions in the gap, by virtue of V_{GSED} and its associated electric field (E), induces a current signal on the biased ring, I_{GSED} , and the stage, I_{ISC} (see section 2.4.1), respectively. These signals can be detected by the GSED electronic amplification system or a specimen current amplifier to generate GSED and induced stage current (ISC) images, respectively, as illustrated in figure 2.13. Indeed, the current can be detected from an insulated or non-insulated conductor located anywhere in the specimen chamber provided it is measured by an appropriate electronics system (Danilatos 1990c). Theory relating to signal induction in an ESEM will be discussed in the proceeding section of this chapter.

The amplifiers used to generate the images have large input resistances, R_1 (GSED electronics) and R_2 (ISC electronics), in the mega ohm range, that are necessary to convert small induced currents, of the order 10^{-9} - 10^{-6} amperes, to several volts (Knowles *et al.* 1994). The amplifiers also contain finite input capacitances, C_1 (GSED electronics) and C_2 (ISC electronics), that act in parallel to the resistances described above. The coaxial cables used to transmit the induced signals will also have finite

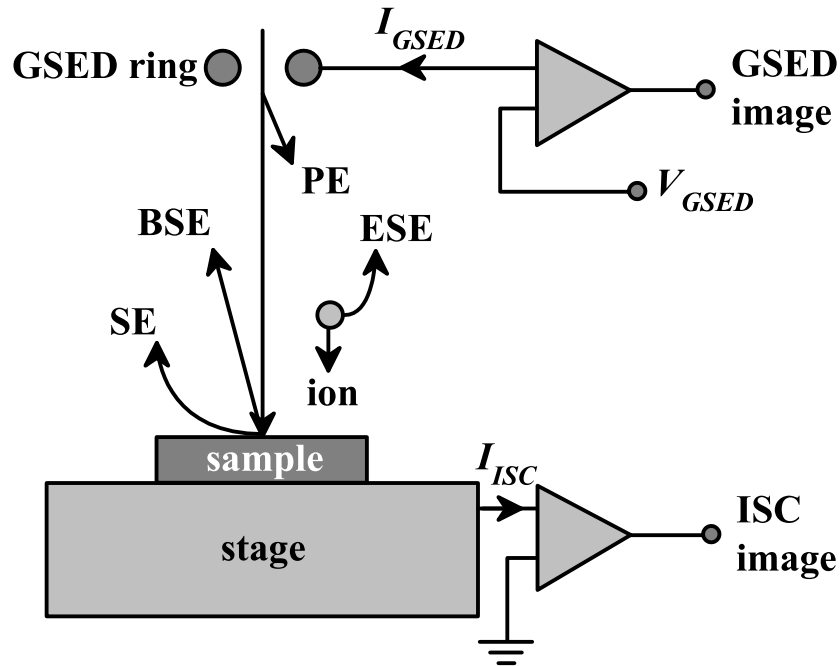


Figure 2.12: Schematic diagram showing the various signals used to generate gaseous secondary electron detector (GSED) and induced stage current (ISC) images in an ESEM. Primary beam electrons (PEs) generate secondary electrons (SEs) and backscattered electrons (BSEs) which ionize gas molecules producing positive ions (PIs) and environmental secondary electrons (ESEs). These signals induce current flows I_{GSED} and I_{ISC} in the ring and stage, respectively, which are then amplified to produce images.

resistances, R_4 and capacitances C_4 (Danilatos 1990c, Farley & Shah 1991, Raether 1964). The GSED preamplifier also contains two low pass filters which extract high frequency shot and thermal noise from signals (Philips Electron Optics 1997). The GSED preamplifier controls the clipping time or time constant of the noise filters, RC_{nf} , and hence the bandwidth (BWD) of the GSED system, as a function of scan speed by selecting alternative combinations of resistors and capacitors. The signals collected to form images in an ESEM therefore contain an associated total time

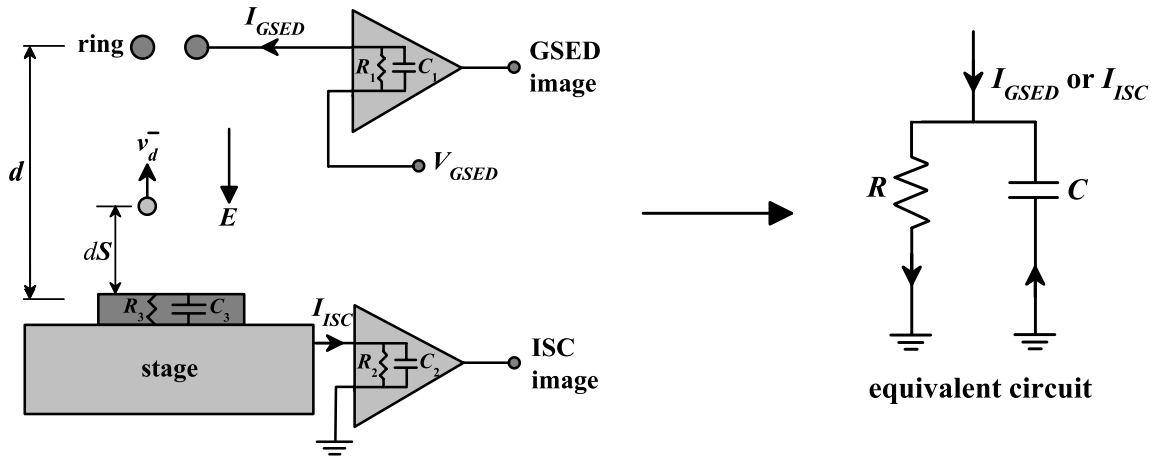


Figure 2.13: Schematic diagram showing the generation of the induced signals I_{GSED} and I_{ISC} by a particle of charge $-e$ traversing the gap in a typical ESEM containing distributed capacitances and resistances. The gaseous secondary electron detector (GSED) and induced stage current (ISC) amplifiers have time constants R_1C_1 and R_2C_2 , respectively. The time constant of an insulating sample is R_3C_3 . The GSED or ISC electronics can be represented by an equivalent circuit of total time constant RC . [d = sample-electrode separation, ds = particle displacement, E = electric field, v_d = drift velocity, R = resistance, C = capacitance]

constant (RC). RC being the summation of R_1C_1 , RC_{nf} and R_4C_4 in the case of GSED imaging; or R_2C_2 , R_3C_3 and R_4C_4 in the case of ISC imaging, as illustrated in figure 2.13. RC controls the rate at which charge carriers in the gap can be collected to generate an image.

The following section contains a theoretical background to signal induction in a gaseous environment and hence describes how the various signals introduced above are collected at their respective electrodes prior to being amplified by the GSED amplifier or a specimen current amplifier to produce images in the ESEM. Subsequently, a brief description of the GSED electronics is given, which describes what happens to the electron signal after it has been induced on the GSED ring. Following that, in chapter 3, the Townsend gas capacitor model is used to theoretically describe how

signals emanating from the sample surface and primary beam are amplified in the gas to produce the cascaded electron signal that is detected via the induction mechanisms described.

2.4.1 Induced Signals

As mentioned previously, the total contributed signal induced by SEs, BSEs, PEs and PIs can be detected by the biased metallic ring detector (Danilatos 1990c, Danilatos 1990b) or from the conducting stage (Durkin & Shah 1993, Farley & Shah 1990a, Farley & Shah 1990b, Farley & Shah 1991, Mohan *et al.* 1998). The total current detected at the virtual earth of a current amplifier in electrical contact with the stage is comprised of (i) an induced current via the motion of charge carriers within the gap (Farley & Shah 1991) and (ii) an absorbed current or current flowing through the sample as a consequence of charge carriers recombining on the sample surface. As the current signal detected is normally dominated by the induced component (Mohan *et al.* 1998), which is due to the motion of both electrons and ions, it is more appropriate to label this mode of detection as induced stage current (ISC) imaging rather than ‘specimen current’ (Durkin & Shah 1993, Farley & Shah 1990b, Farley & Shah 1991, Mohan *et al.* 1998, Moncreiff *et al.* 1978) or ‘ion current’² (Fletcher *et al.* 1997, Thiel *et al.* 1997, Toth & Phillips 2000a, Toth & Phillips 2000b, Toth *et al.* 2002c, Toth *et al.* 2002d) imaging (see figures 2.12 and 2.13). In the case when the sample is strongly insulating the leakage current flowing from the surface of the sample to the conducting stage can be considered negligible (Farley & Shah 1991).

Theory relating to the signals induced on conducting electrodes by moving charge carriers in an ionized gas has been revised by several authors in the past. Danilatos

²By convention, it is assumed that the stage is at ground potential and any other detection electrode placed above the stage (e.g GSED ring electrode) or elsewhere in the sample chamber is at a positive potential. Hence, the electric field generated between the detection electrode and the stage will drive PIs towards the stage.

(1990c), Danilatos (1990b), Durkin & Shah (1993), Mohan *et al.* (1998), Raether (1964) and Toth & Phillips (2000b) have discussed signal induction in the ESEM. Since the ESEM operates in the proportional region of a gas discharge, theory relating to the induced signals in proportional counters is also applicable (Danilatos 1990c). A thorough description of induction in proportional counters can be found in Wilkinson (1958). A brief summary of signal induction in the ESEM is given below.

Consider a particle such as an electron or ion of charge e travelling under the influence of an applied electric field (E), generated by a voltage (V), between two plane parallel conducting electrodes, each of capacitance C' and separation d , which is analogous to figure 2.13. The motion of the charged particle, possessing its own electric field, produces a time varying electric field in the electrodes of the parallel plate system. The time varying electric field causes charge carriers in the conducting electrodes to displace, inducing charge and hence a potential on the surface of each of the electrodes. The surface potential caused by the induced charges exists along with any potential already present on each electrode, normally V and ground. However, it is assumed that the surface potentials placed on the electrodes are small and do not change the original electric field acting on the charged particle (Wilkinson 1958). The instant the charged particle stops moving via recombination with a gas molecule, the time varying electric field ceases and induced free charges redistribute on the surface of the conductor in order to cancel any external electric field inside the electrode and maintain the steady state voltage (V) between the electrodes.

Assuming at this stage that the electrodes are interconnected through a circuit that contains an infinite resistance, or are not connected at all, conservation of energy states that the work done in moving the charged particle is equal to the work supplied by the potential, that is

$$VdQ = eE \cdot ds, \quad (2.4.1)$$

where dQ is the total amount of charge induced on each of the electrodes and ds is

the distance traversed by the charged particle (Danilatos 1990c). However, it must be noted that even though the same amount of charge is induced on each electrode, the charge is opposite in polarity. For example, an electron and PI will both induce positive charge on the positive collecting electrode, an equal negative charge being placed on the negative electrode or grounded stage as the ion and electron traverse the gap in opposing directions (Wilkinson 1958). As the electric field in the gap, is equal to V/d , equation (2.4.1) reduces to

$$dQ = \frac{eds}{d}. \quad (2.4.2)$$

It can be seen from equation (2.4.2) that the amount of charge induced on each electrode is proportional to the amount of potential traversed by the charge. If the electron or ion traverses the total distance between the electrodes, the charge induced is equal to the charge of the particle, e . On the other hand, if a particle is suddenly introduced into the gap (for example due to an ionization event) the charge induced on each electrode is not equal to e but a fraction of e . The fraction of e being equal to the proportion of total gap potential traversed before the particle recombines on one of the electrodes or with a charge carrier of opposite polarity (Danilatos 1990c).

As current and velocity are defined as dQ/dt and ds/dt , respectively, the current flowing into an isolated electrode or external circuit of very large or infinite resistance, due to a single charge carrier (superscript s), is therefore

$$I_{ind}^s = I_{GSED}^s = I_{ISC}^s = \frac{ev_d}{d}, \quad (2.4.3)$$

where v_d is the drift velocity of the electron or ion parallel to the direction of E . It can be seen from equation (2.4.3) that the amount of current induced is directly proportional to the drift velocity of electrons and ions in the gap. The drift velocity of charge carriers being dependent on gas type and proportional to the pressure and electric field strength (von Engel 1965, Nasser 1971). When an electron or ion

recombines on its respective electrode and the electric field is no longer traversed, the velocity of the charge and hence the current induced becomes zero. It must be noted that the electric field in an ESEM is not constant due to the toroidal symmetry of the GSED ring and therefore electron and ion drift velocities, and hence the current induced, will be dependent on ds . In general, drift velocities will be greatest close to the GSED ring as this is where the field gradient in the gap maximizes. However, the statement above is generally only applicable to highly mobile electrons such as SEs and ESEs that are strongly influenced by E . High energy PEs and BSEs, whose trajectories are not influenced by E as a consequence of their high velocities, will induce a constant current in the ring and stage. The current induced per BSE or PE will in general be greater than that of an SE or ESE as a consequence of their faster drift velocities, however, as SEs and ESEs are efficiently amplified in the gas, their concentration is greater than that BSEs and PEs and will therefore produce a greater current in the external circuit. If there are more than one electron or ion traversing the gap, and diffusion effects are neglected, equation (2.4.3) can be rewritten as

$$I_{ind} = I_{GSED} = I_{ISC} = \frac{e}{d} (N_e v_e + N_i v_i), \quad (2.4.4)$$

where N_e and N_i are the number of electrons and ions traversing the gap, respectively, and v_e and v_i are the electron and ion drift velocities, respectively. As the velocity of a charged particle being accelerated across the gap is inversely proportional to the particles mass and collision cross section (von Engel 1965, Nasser 1971), it can be seen that most of the charge induced is due to the highly mobile electrons (Danilatos 1990c).

As mentioned previously, the detection system used to generate images in an ESEM, and any detection system for that matter, will contain an associated time constant due to finite input impedances and distributed capacitances of the electronics. For sake of example, now assume we have a simple detection system where one of

the collecting electrodes, described above, is connected to a resistor and the potential drop across the resistor produces a voltage signal ($V_S(t)$) that is then amplified by an appropriate electronic amplifier that is neither integrating nor differentiating. The resistor described above will be supplemented by the input impedance of the amplifier giving a total system resistance (R). R will be shunted by an unavoidable parallel capacitance (C) due to the input capacitance of the amplifier, the capacitance of the actual electrode C' and capacities of the wires used to connect the resistor to the amplifier. There will also be a capacitance associated with the gap itself if the electrodes are connected to each other through, for example, the voltage source being used to drive the charge carriers in the gap, as is the case in the current example (Raether 1964). However, in an ESEM, the GSED (Knowles *et al.* 1994) and most conventional specimen current amplifiers (Farley & Shah 1991) used for ISC detection operate in the so called virtual-earth mode where the amplifiers are isolated from common ground and float at their respective potentials. Therefore, the electrodes are electrically isolated from each other and the capacitance of the gap can be considered negligible.

Basic electronic circuit theory shows that the voltage signal produced across the resistor or input to the amplifier can be described by

$$V_S(t) = RI_{ind}(t) - RC \frac{dV_S(t)}{dt}, \quad (2.4.5)$$

where $I_{ind}(t)$ is the current induced in the collecting electrode due to the motion of charge carriers in the gap when the electrodes are isolated or connected through a circuit of infinite time constant, whereby all charge induced remains on the electrode(s) as given by equation (2.4.4) (Raether 1964). It must be noted, however, that the current induced via the movement of charge carriers is supplemented by a displacement current which occurs as a result of the charging and discharging of the capacities in the external circuit, hence the second term in equation (2.4.5). The displacement current

becomes significant when the total time constant (RC) of the circuit is much greater than the transit times (time from the introduction of a particle to when it recombines on an electrode or with a charge carrier of opposite polarity) of electrons (Γ_e) and ions (Γ_i) in the gas.

Assuming that the circuit has had sufficient time to charge the distributed capacities of the system since the onset of V and therefore the displacement current through R is zero the moment carriers begin traversing the gap at $t = 0$, then

$$V_S(t) = \frac{1}{C} e^{-t/RC} \int_0^t e^{v/RC} I_{ind}(v) dv. \quad (2.4.6)$$

Figure 2.14 shows a plot of the voltage signal produced across the resistor at various circuit time constants, using equation (2.4.6), when an electron and ion of equal charge are released in the centre of the gap. Values of R and C were chosen so that $V_S(t)$ produces a maximum of 1 Volt after all charge has been dissipated on the electrode for the case when the electrodes are not connected to each other or the external circuit contains an infinite time constant. For clarity, the drift velocity of the electron was set to twice that of the ion ($v_e = 2v_i$), however under real cascade conditions in an ESEM v_e is several orders of magnitude greater than that of an ion (von Engel 1965, Nasser 1971). It can be seen from figure 2.14 that when RC is much smaller than Γ_e or Γ_i the signal produced closely resembles that of the carrier current in the gap (the transit time of electrons and ions obviously being equal to the ratio of the sample-electrode separation and their respective drift velocities ($\Gamma_e = d/v_e$, $\Gamma_i = d/v_i$)). However, as RC increases, the displacement current acting in the circuit becomes more pronounced and the voltage pulse produced by the charge carriers have an associated decay time even after all of the actual charge has been induced on the electrode. RC will not only affect how $V_S(t)$ will decay after Γ_i , but also how $V_S(t)$ rises from the beginning of the pulse to Γ_e and between Γ_e and Γ_i . When RC is much greater than Γ_i , the voltage pulse continues to rise until $t = \Gamma_i$ is reached where all of

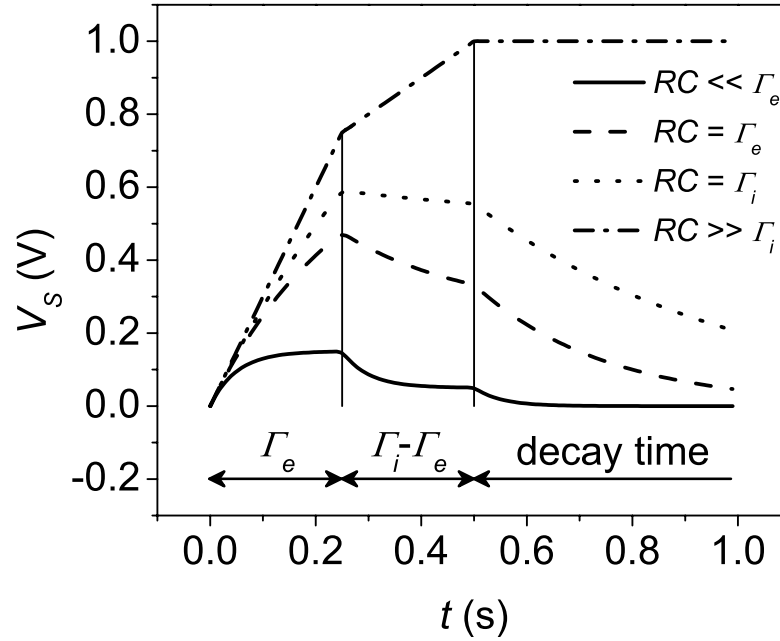


Figure 2.14: Voltage signal (V_S) versus time (t) at various time constants (RC) when an electron and a positive ion (PI) of transit times Γ_e and Γ_i , respectively, are accelerated across a potential difference (V) after being released in the center of the gap. For clarity, the drift velocity of the electron was set to twice that of the ion ($v_e = 2v_i$ or $\Gamma_e = \Gamma_i/2$).

the charge induced by the motion of the carriers in the gap has been dissipated on the electrode. After this time the voltage across the resistor appears to remain constant due to the very slow exponentially decaying response of the circuit as a direct result of its long time constant. If more charge carriers are introduced into the gap during the slowly decaying component of the signal, or the slowly rising component for that matter, $V_S(t)$ will once again keep continuing to rise until all of the charge has been induced on the surface of collecting electrode. In a realistic situation, where there is more than one electron and ion traversing the gap per unit time, the voltage pulse

produced will be a superposition of the pulse produced by a single charge carrier and therefore the obvious discontinuities in $V_S(t)$ at $t = \Gamma_i$ and $t = \Gamma_e$ will become less pronounced due to diffusion effects and variations in the carrier drift velocities. It can also be seen from figure 2.14 that the magnitude of $V_S(t)$ decreases as RC decreases. The reduction in pulse height therefore produces a subsequent deterioration in SNR as RC is reduced (Wilkinson 1958). The time constant of the detection system must therefore be large enough so that the height of the pulse is substantially greater than the amplifier noise, Johnson noise in the resistor in which the signal is extracted, and shot noise associated with charge carriers traversing the gap. Conversely, the time constant must not be too large that the transient response of the system becomes slow causing pulse pile up and subsequent smearing or shadowing in ESEM images. RC should therefore be approximately equal to Γ_i , ensuring that the pulse height is not dampened and the response is not significantly reduced (Wilkinson 1958).

In an ESEM, we want the maximum height of the signal to be proportional to the number of ionization events occurring in the gas so that the total charge produced at each pixel is wholly transferred to the detection electrode and electronics so that image quality is not impeded. This can be achieved when the pixel dwell time is equal to the total pulse length including the decay time after all charge carriers have ceased traversing the gap (Durkin & Shah 1993). When imaging in an ESEM the GSED preamplifier digitally varies its frequency response and hence effective time constant proportionally to the scan speed to ensure that the sampling rate is equal to the pixel dwell time and full pulses are observed (Philips Electron Optics 1997). Under ESEM imaging conditions in N_2 gas where, for example, $V_{GSED} = 100$ V, $d = 10$ mm, $p = 1$ torr and the stage is grounded, electron and ion drift velocities are 4.25×10^5 m/s (Gill & von Engel 1949) and 800 m/s (Varney 1953), respectively, which corresponds to transit times of 23.5 ns and 12.5 μ s. If the majority of the pulse(s) is to be collected then the amplifier detecting the signals must have a BWD

of approximately 80 kHz, which is easily achieved with current amplifier technology. However, if we wish to detect electrons alone, without the slower contribution from ions, the amplifier BWD must be of the order of 40 MHz, which is very difficult to accomplish. The only possible way to detect the ‘fast’ electron signal alone, under the conditions stated above, would be to operate under very large gas path lengths. However, increasing the gas path length increases the scattering of the PE beam and therefore images obtained would contain excessive noise.

The maximum BWD of the GSED preamplifier is 1 MHz (Philips Electron Optics 1997) so that if attempts are made to collect the electron signal alone then the maximum transit time of electrons in the gap must be of the order of 1 μ s and the pixel dwell must also be of this order, which corresponds to a line scan time of 0.7 ms when a standard image width of 712 pixels is employed. Slow electron transit times in the microsecond time scale are only attainable at significantly low reduced electric fields (E/p) which means that imaging quality will be appreciably reduced as a consequence of having to operate at low electric fields, which reduces gas cascade gain; or high pressures, which increase beam scattering and background noise from PE and BSE amplification.

The above considerations show that the relative contribution to the total signal induced by that of electrons can be controlled by an appropriate choice of circuit time constant and raster scan speed. Moreover, there is a trade off between the speed at which images can be generated and the quality or SNR in images obtained using ESEM. If one is wishing to image at fast scan rates and attempt to detect the fast electron signal then image contrast and quality will be severely reduced. Conversely, if high contrast and low noise images are to be obtained then detection must include the slower ionic component and hence scan speeds must be reduced. Above also demonstrates that the current amplifier technology currently attainable in ESEM (*i.e.* gain \times BWD) must be improved or special signal processing

techniques must be adopted in order to produce high quality images over the entire frequency domain.

The above theory demonstrates the correct way for measuring currents in an ESEM. Adopting the arbitrary method of counting charge carriers as they arrive at their respective electrodes will only lead to correct results when steady state conditions are attained (Danilatos 1990c, von Engel 1965).

2.4.2 Gaseous Secondary Electron Detector Electronics

This section describes how the cascaded electron signal induced in the GSED ring is amplified and filtered to produce a video signal that is then digitized to produce an image. Further theory relating to the GSED preamplifier and associated electronics can be found in Philips Electron Optics (1997).

A schematic diagram of the GSED preamplifier circuit is illustrated in figure 2.15. The cascaded electron signal induced in the GSED ring is passed through a vacuum sealed connector via a coaxial cable to a BWD-limiting low-pass active filter, denoted as A1 in figure 2.15. High frequency noise picked up in the microscope chamber via an open ended noise track on the GSED printed circuit board (PCB) (shown previously in figure 2.11) is also passed through the vacuum sealed connector and coaxial cable to a BWD-limiting low-pass active filter A2. The suppressor plate located above the ring, which picks up unwanted noise from PEs and BSEs as previously described, is connected to the shield of both the signal and noise cables and is held at 9 V lower than V_{GSED} . The amplified ring signal and noise signal emerging from A1 and A2, respectively, are then passed through a difference amplifier A3 which subtracts the noise signal from the ring signal. This needs to be performed as the high frequency noise picked up in the noise track is also picked up by the GSED ring. The signal from A3 is then passed to two operational amplifiers A4a and A4b each containing light

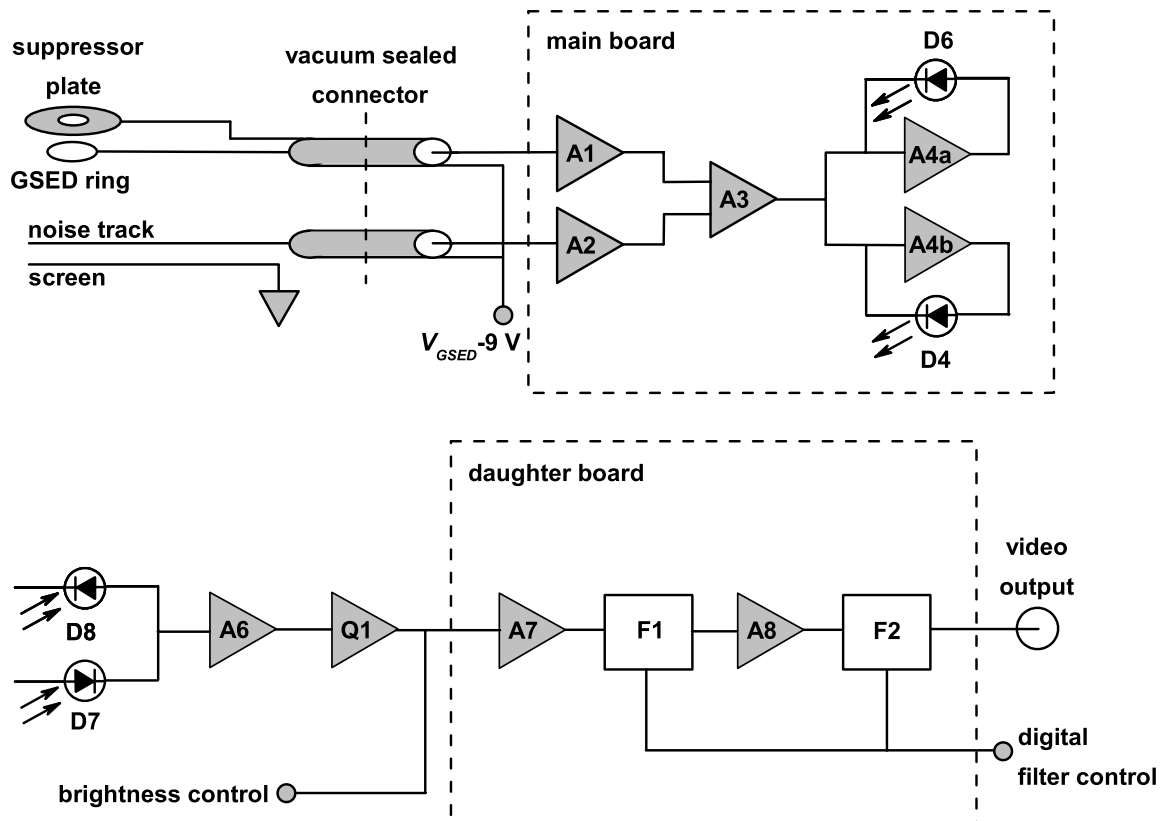


Figure 2.15: Schematic diagram of the gaseous secondary electron detector (GSED) preamplifier circuit (adapted from Philips Electron Optics 1997).

emitting diodes (LEDs) D6 and D7 in their feedback loops, respectively. Optical signals from D4 and D6 are then coupled to amplifier A6 on the GSED daughter board via two photodiodes D7 and D8, respectively. The signal from A6 is then passed through a field effect transistor (FET) fine gain control Q1 that enables the signal to be amplified further if low signal imaging is to be performed. Q1 is controlled via a variable resistor box located on the microscope control panel. When Q1 is set to maximum amplification (resistor knob fully clockwise) the SNR of the output video signal is reduced by a factor of ten compared to the SNR of images at television (TV)

scan rates (Philips Electron Optics 1997). The signal emerging from Q1 is then passed through a digital brightness control that allows the direct current (DC) offset of the resulting digital image to be altered. After a DC offset has been added or subtracted from the signal it is then passed through two low-pass passive filters F1 and F2 that remove high frequency shot and thermal noise. The cutoff frequency and hence BWD of the filters is varied as a function of scan speed or can be manually controlled by assigning a particular filter code (decimal number 0-31) in the user interface software. When the line scan time (τ_L), or lines/frame is altered, a digital signal is sent to a switching circuit on the GSED filter daughter board that selects a combination of resistors and capacitors within each filter. Table 2.2 lists BWD and clipping time or time constant (RC_{nf}) of filters F1 and F2 for various line scan times and filter codes at a lines/frame setting of 484. The cutoff frequency or BWD of any first order active filter combination, such as F1 and F2, being (Chen 1986):

$$BWD = \frac{1}{2\pi RC_{nf}}. \quad (2.4.7)$$

Both filters F1 and F2 operate at the same digitally set BWD. After low pass filtering has been performed the output video signal is then interpreted by an appropriate video card and software for subsequent GSED imaging. All operational amplifiers on the GSED preamplifier are operated in a so called ‘virtual earth mode’ whereby the preamplifier input stage floats at the ring voltage V_{GSED} .

The next chapter contains a theoretical background relating to the amplification of charge carriers in the gas under steady state conditions whereby the rate at which electrons and ions exit the gas (recombination rate) is equal to the rate at which electrons and ions are created in the gas (generation rate). Hence, the amplified PE, BSE and SE signals induced in the GSED ring/electronics described above, or in the stage/specimen current amplifier, can be related to the signals emergent from the sample.

Table 2.2: Time constant (RC_{nf}) and bandwidth (BWD) of the Philips XL 30 ESEM[®] gaseous secondary electron detector (GSED) preamplifier low-pass passive noise filters at various line scan times (τ_L) and digital filter codes (Philips Electron Optics 1997).

τ_L (ms)	Digital filter code	RC_{nf} (μ s)	BWD (kHz)
TV	14	0.1592	1000
1.68	12	0.3788	420.15
-	10	0.6594	241.36
-	8	1.038	153.30
6.72	13	1.269	125.42
13.4	11	2.209	72.05
-	9	3.478	45.76
60	6	11.51	13.83
-	4	11.89	13.39
-	2	12.17	13.08
-	0	12.54	12.69
120	7	38.54	4.13
-	5	39.79	4.00
-	3	40.70	3.91
-	1	41.99	3.79

Chapter 3

Gaseous Cascade Amplification in Partially Ionized Gases - Townsend Gas Capacitor Model

3.1 Introduction

Increasing the voltage on the gaseous secondary electron detector (GSED) electrode, and hence the voltage across the sample-electrode gap, produces an exponential increase in the current collected by the ring electrode or the stage. The exponential increase in current as V_{GSED} is raised is due to an increasing number of ionization events between field accelerated electrons and neutral, excited or ionic gas atoms/molecules occurring in the gas due to an increase in the number of electrons with energies greater than the ionization potential of the gas as a consequence of the increased field. An exponentially increasing current-voltage relationship in a gaseous discharge between two parallel electrodes can be identified as a Townsend discharge (von Engel 1965, Nasser 1971) and it is for this reason the amplification of charge carriers in an environmental scanning electron microscope (ESEM) can be closely approximated by Townsend's gaseous capacitor model. Theory relating to the Townsend gaseous capacitor model can be found in standard texts on gas discharge physics and ionized gases such as von Engel (1965), Llewellyn-Jones (1957) and Nasser (1971). The ESEM is also capable of operation in the glow and corona regions of a gas discharge, however, under these breakdown conditions imaging is not possible due to signal saturation of the GSED and induced stage current (ISC) electronics as a result of excessively high current densities.

Several authors, such as Danilatos (1990c), Durkin & Shah (1993), Farley & Shah (1990a), Farley & Shah (1990b), Farley & Shah (1991), Meredith *et al.* (1996), Moncreiff *et al.* (1978), Thiel *et al.* (1997) and Thiel (2003) have extended the theories of Townsend and other such authors to describe the amplification and detection of secondary electrons (SEs), backscattered electrons (BSEs) and primary electrons (PEs) under typical pressures, detector biases, beam currents and gap distances typically employed in ESEM. The following contains a review of such work.

3.2 General Overview of Cascade Amplification

In models of gaseous cascade amplification in an ESEM it is generally assumed that each ionizing collision between an electron (SE, PE, BSE or environmental secondary electron (ESE)) and a neutral atom or molecule (A) produces a single low energy gaseous or environmental secondary electron, denoted e_{ESE}^- , and a single positive atomic or molecular ion (A^+) in accordance with the equation



However, in reality, there are numerous additional collision processes and reactions that may occur in a partially ionized gas that are also capable of generating additional gas excitation phenomena or avalanche electrons in the ESEM. Some of these being for example: (i) multiple ionization events where two or more electrons are ejected from an ionized atom/molecule (*e.g.* Appendix A-collisions 32, 99); (ii) the generation of excited species, which may in time de-excite and emit photon(s) (*e.g.* Appendix A-collisions 5, 7, 8, 18, 19, 39, 41, 51, 71, 82, 108) or free electron(s) (*e.g.* Appendix A-collisions 11, 12, 16, 17, 39, 49, 50, 52, 66, 83, 85, 86, 91, 94). In the case where photons are emitted, the photons may excite further gas molecules and emit subsequent electrons or quanta, or decouple bound electrons in the stage or sample, which can then contribute to the amplification process; (iii) PI impact reactions, where excited or unexcited PIs impact the stage or sample causing the emission of SEs (*e.g.* Appendix A-collision 66); (iv) dissociation reactions, where the incident electron or photon energy, which is normally used to ionize a gas molecule, is transferred to the molecule in separating it into its constituents (*e.g.* Appendix A-collisions 5, 13-15, 23, 25, 26, 34-38, 53-56, 62, 63, 73); (v) electron-ion recombination reactions, where, in general, the incident electron is captured by a PI and the extra excitation energy given to the ion by the electron is released in the form of an Auger electron (resonant excitation or autoionization) or photon (radiative or dielectronic

recombination) (von Engel 1965, Hahn 1997, Nasser 1971). Appendix A summarizes most of the atomic/molecular collision reactions that may occur in a partially ionized gas such as that in an ESEM. It must be noted that in order to completely describe cascade amplification in an ESEM one must know all of the cross sections and efficiencies related to all of the collision processes summarized in Appendix A, which would be a formidable task. For most gases used in an ESEM, the most probable collision event is that of a single ionization and it is for this reason that equation (3.2.1) is generally accepted as the main equation to theoretically describe cascade amplification in an ESEM (Moncreiff *et al.* 1978).

The total ionization current (I_{ion}) or current of ESEs produced in the cascade via PE, BSE, SE-gas ionizing collisions that is collected by the GSED ring under steady state conditions, where charges can be counted as they arrive at their respective electrodes, can be described by

$$I_{ion} = I_{PE}^g + I_{BSE}^g + I_{SE}^g, \quad (3.2.2)$$

where I_{PE}^g , I_{BSE}^g and I_{SE}^g are the steady state gaseous amplified currents produced by PEs, BSEs and SEs, respectively (Farley & Shah 1990b, Meredith *et al.* 1996, Moncreiff *et al.* 1978). As was briefly mentioned in chapter 2.4, and will be described in more detail in section 3.7, PIs, long lived excited atoms/molecules (metastables), photons and neutral atoms/molecules generated by electron-gas molecule ionizations and excitations in each electron avalanche (single traverse of field accelerated electrons from the cathode to the anode) are capable of impacting the sample surface and liberating SEs. The SEs produced will then be accelerated and amplified through the gap, by V_{GSED} , producing more of the primary phenomena ascribed above which will subsequently impact the sample resulting in further SE emission and so on, contributing to a feedback process (multiple avalanches or an electron cascade). Due to the complexities associated with the amplification of charge carriers in a gaseous

environment it is easier to consider the feedback process, or steady state current(s) produced after *ad infinitum* avalanches, by firstly considering the steady state amplification current(s) produced after only a single electron avalanche, and therefore simpler to express equation (3.2.2) as

$$I_{ion} = k (I_{PE_0}^g + I_{BSE_0}^g + I_{SE_0}^g), \quad (3.2.3)$$

where k is the cascade amplification ‘feedback factor’, which represents the amplification of SEs generated by ion, photon, metastable and neutral molecule-cathode surface collisions; and $I_{PE_0}^g$, $I_{BSE_0}^g$, and $I_{SE_0}^g$ are the cascade amplification currents produced by PE-gas, BSE-gas, and SE-gas ionizing collisions for the case of a single electron avalanche. Sections 3.4-3.6 show theory relating to the development of expressions for $I_{PE_0}^g$, $I_{BSE_0}^g$, $I_{SE_0}^g$ and k respectively, which are then used in section 3.11 to schematically model gaseous cascade amplification in an ESEM as a function of microscope operating parameters.

3.3 Cascade Amplification of Electrons

Field accelerated electrons, exceeding the ionization potential of the gas, are capable of ionizing collisions with gas molecules. Each electron undergoes on average α_{ion} ionizing collisions per unit length of distance (z) traversed through the gas. Thus at any given point in the gap, the number of new electrons generated in the electron avalanche is given by

$$dN_e^g(z) = N_e^g(z)\alpha_{ion}dz, \quad (3.3.1)$$

where $N_e^g(z)$ is the original number of electrons in the increment dz and α_{ion} is the first Townsend ionization coefficient, which is defined as the number of ionization events or ion-pairs generated per unit path traversed by each electron (von Engel 1965, Nasser 1971, Thiel *et al.* 1997). The first Townsend ionization coefficient is also sometimes referred to as the primary ionization coefficient or SE/ESE ionization efficiency. Rearrangement and integration of equation (3.3.1) shows that the number of electrons reaching a plane at a distance z is

$$N_e^g(z) = N_e^g(0) e^{\alpha_{ion}z}, \quad (3.3.2)$$

where $N_e^g(0)$ is the original number of electrons at $z = 0$ (Danilatos 1990c, Moncreiff *et al.* 1978). Under single ionization conditions whereby each ionization event produces a single electron and a single PI the number of ionization collisions occurring and hence the number of ions created in a single avalanche will be equal to the number of electrons in the avalanche less the original electrons in the gas before the onset of amplification (Thiel *et al.* 1997):

$$N_i^g(z) = N_e^g(0) (e^{\alpha_{ion}z} - 1). \quad (3.3.3)$$

Assuming that the avalanche has attained steady state, whereby the rate of ionization is equal to the ion recombination rate, equation (3.3.2) gives the electron current

$I_e^g(z)$ reaching a plane at a distance z as

$$I_e^g(z) = I_e^g(0) e^{\alpha_{ion} z}, \quad (3.3.4)$$

where $I_e^g(0)$ is the original current of electrons at $z = 0$ (Danilatos 1990c, Moncreiff *et al.* 1978). It must be reiterated that the equations shown above are only valid if each ionization collision produces a single ESE and a PI and saturation or ‘swarm’ conditions are present in the gas whereby the energy lost by cascading electrons during excitation and ionization collisions is equal to the energy gained by the electric field between successive collisions (Thiel *et al.* 1997, Thiel 2003). Therefore, the kinetic energy distribution and hence the ionization efficiency of SEs and ESEs can be assumed to be constant. Under typical ESEM conditions, and in most ionized gases for that matter, the first Townsend ionization coefficient cannot generally be considered constant over the gap distance as electrons accelerated in the field need a finite time to (i) reach the ionization potential of the gas after leaving the sample and (ii) gain sufficient energy after an inelastic scattering event to cause subsequent ionization. Thiel *et al.* (1997) has improved gaseous amplification models for an ESEM by developing a z dependent expression for the ionization coefficient. The theory developed by Thiel *et al.* (1997) and data on Townsend coefficients for various gases is discussed in preceding sections of this chapter.

3.4 Cascade Amplification of Primary Electrons

Along with being scattered as described previously in chapter 2.3, PEs entering the gas from the final pressure limiting aperture (PLA1) are also capable of ionization events with gas molecules. The ESEs generated at each ionization event are then capable of subsequent amplification. The PE beam will therefore generate a series of electron avalanches along its path from PLA1 to the sample surface. If each PE generates S_{PE} ion pairs per unit path length traversed per unit pressure, then the increment of current produced by the primary beam current (I_{PE}) at each point z' is

$$dI_{PE_0}^g(z') = -I_{PE}S_{PE}pdz', \quad (3.4.1)$$

where z' is the distance travelled by each PE in the negative z direction, p is gas pressure and S_{PE} is the ionization efficiency of PEs (Moncreiff *et al.* 1978). Theory relating to the evaluation of ionization efficiencies of various gases will be considered later. In an ESEM, the GSED ring and the stage are normally held at a positive bias and ground potential, respectively. This means that conventional current (flow of positive charge carriers) will flow from the ring to the stage; or electrons and ions generated in the gas will travel in positive z and negative z directions, respectively. The expression above is therefore negative in magnitude because the PEs that constitute I_{PE} flow in an opposite direction to that traversed by field accelerated cascading electrons and hence I_{PE} is negative in magnitude.

The ESEs generated at z' , via the PE ionizing collisions, are accelerated by the electric field in the positive z direction a total distance $d - z'$ producing a cascaded electron signal. The expression for the current of ESEs produced by direct PE-gas collisions, equation (3.4.1), therefore needs to be inserted into the general expression for electron amplification (equation (3.3.4)) yielding

$$dI_{PE_0}^g(z') = -I_{PE}S_{PE}pe^{\alpha_{ion}(d-z')}dz', \quad (3.4.2)$$

where d is the total gas path length or sample-electrode separation. As the ionization path of the primary beam extends over the entire path length of the gas, equation (3.4.2) needs to be integrated from $z' = d$ to $z' = 0$:

$$I_{PE_0}^g(d) = - \int_d^0 I_{PE} S_{PEP} e^{\alpha_{ion}(d-z')} dz'. \quad (3.4.3)$$

Once again assuming steady state and saturation/swarm conditions, the total electron current produced by PE-gas ionizing collisions reaching the GSED ring located a distance d from the sample is (Farley & Shah 1990b, Meredith *et al.* 1996, Moncreiff *et al.* 1978, Thiel *et al.* 1997):

$$I_{PE_0}^g(d) = \frac{I_{PE} S_{PEP}}{\alpha_{ion}} (e^{\alpha_{ion}d} - 1). \quad (3.4.4)$$

In the derivation(s) above, it is assumed that the final PLA is located at the same z plane as the GSED ring and hence PE-gas ionization events are not occurring above or below the ring. All experiments conducted as part of this thesis were performed using an FEI-Philips XL 30 ESEM[®] where the final PLA and the ring are located on the same plane, as can be seen by close inspection of figure 2.11. It must also be noted that the expressions obtained above assume that the increased path lengths of skirt electrons caused by PE-gas scattering are negligible. Future work therefore needs to incorporate the theory described in chapter 2.3 into the equations shown above.

3.5 Cascade Amplification of Backscattered Electrons

As previously described in chapter 2.4, BSEs are capable of ionizing the gas as they traverse the gap, producing additional ESEs that are amplified between their point of production and the GSED ring. BSEs traverse the gap with an average energy of approximately 50 to 80% to that of PEs (Moncreiff *et al.* 1978) and therefore the efficiency at which they ionize the gas is very similar to that of PEs. However, unlike PEs, BSEs traverse the gas in a positive z direction and therefore equation (3.4.3) needs to be modified accordingly to give

$$I_{BSE_0}^g(d) = \int_0^d \eta I_{PE} S_{BSEP} \left(\frac{\bar{d}_{BSE}}{d} \right) e^{\alpha_{ion} z} dz, \quad (3.5.1)$$

where η is the BSE coefficient or the number of BSEs emitted from the sample per incident PE, S_{BSE} is the ionization efficiency of BSEs and \bar{d}_{BSE} is the average gas path length that BSEs travel in traversing the gap distance d (Farley & Shah 1990b, Meredith *et al.* 1996, Moncreiff *et al.* 1978, Thiel *et al.* 1997). The term \bar{d}_{BSE}/d is introduced to correct for the angular trajectories that BSEs travel between the sample and the GSED ring. In general, the angular distribution of BSEs obeys the Lambert cosine law and therefore the average gas path length of BSEs is usually taken to be twice that of the total gas path length (Farley & Shah 1990b).

Integration of equation (3.5.1) gives the total electron current arriving at the GSED ring arising from BSE-gas ionizations as

$$I_{BSE_0}^g(d) = \frac{\eta I_{PE} S_{BSEP}}{\alpha_{ion}} \left(\frac{\bar{d}_{BSE}}{d} \right) (e^{\alpha_{ion} d} - 1), \quad (3.5.2)$$

where steady state and saturation/swarm conditions are assumed to be occurring in the gas (Farley & Shah 1990b, Meredith *et al.* 1996, Moncreiff *et al.* 1978, Thiel *et al.* 1997).

3.6 Cascade Amplification of Secondary Electrons

Unlike PEs and BSEs, SEs leave the sample surface with a Maxwellian energy distribution of maximum energy of approximately 3 eV (Goldstein *et al.* 1992, Reimer 1985) and therefore can easily be accelerated through the gap, under the influence of the electric field generated by V_{GSED} , efficiently producing ESEs.

It can easily be seen from equation (3.3.4) that the total electron current reaching the GSED ring can be described by

$$I_{SE_0}^g(d) = \delta I_{PE} e^{\alpha_{ion} d}, \quad (3.6.1)$$

where δ is the SE coefficient, defined as the number of SEs emitted per incident PE (Moncreiff *et al.* 1978). Close inspection of the equation above reveals that it also includes the original electrons leaving the sample, δI_{PE} . Subtracting this term from equation (3.6.1) gives the electron current produced by SE-gas ionizing collisions reaching the GSED ring located a distance d from the sample as (Farley & Shah 1990b, Meredith *et al.* 1996, Moncreiff *et al.* 1978, Thiel *et al.* 1997):

$$I_{SE_0}^g(d) = \delta I_{PE} (e^{\alpha_{ion} d} - 1). \quad (3.6.2)$$

Once again, the equation above is only applicable under steady state and saturation/swarm conditions. It will be shown later that the amplification of SEs can be better approximated when d is replaced by a pressure and field dependent effective path length. The effective path length corrects for variations in the kinetic energy distribution of cascading SEs and ESEs over the gap distance.

3.7 Cascade Amplification of Secondary Electrons Generated by Ion, Photon, Metastable and Neutral Molecule Surface Collisions

As mentioned previously, PIs generated in the cascade are capable of generating SEs and subsequent electron avalanches upon impact with the sample surface (von Engel 1965, Farley & Shah 1990b, Farley & Shah 1991, Moncreiff *et al.* 1978, Nasser 1971). In fact, early experiments have also shown that SEs can also be released from the cathode by avalanche liberated photons, metastable and neutral atoms (Druyvesteyn & Penning 1940, von Engel 1965, Loeb 1952, Loeb 1961, Molnar 1951, Newton 1948). Unionized excited atoms have a low probability of emitting SEs from the cathode due to their rapid resonant transitions back to ground state (Llewellyn-Jones 1957). In general, the photoelectric phenomenon has been found to dominate at low values of reduced electric field (E/p), whilst SE emission via PI bombardment dominates at higher E/p values (Loeb 1952).

The emission of SEs from the sample or cathodic material of the stage by monatomic or diatomic PIs can occur through various processes: (i) A PI approaching the cathode extracts an electron from the sample once the ion is several atomic radii from surface. The ion then captures the released electron into one of its higher energy levels forming a metastable excited neutral atom. The atom then remains in a metastable state for a short period until, upon interaction with the sample/cathode, transfers its excitation energy, resulting in SE emission (Druyvesteyn & Penning 1940, von Engel 1965). The SEs generated are then accelerated towards the GSED producing a cascaded electron signal; (ii) Upon capture of the released sample/cathodic electron the ion is forced into an electronically excited state. Some of the excess energy occupied by the atom,

which would occasionally be directly emitted as a photon, as in radiative recombination (*e.g.* Appendix A-collision 64), is then transferred to another atomic electron producing an unstable doubly excited atom. The atom then de-excites by either emitting an Auger electron(s) (*e.g.* Appendix A-collision 66), which is subsequently amplified; or via photon emission (*e.g.* Appendix A-collision 65) (Nasser 1971). In the case of radiative or dielectronic recombination the photons generated are then in turn capable of extracting bound sample/cathodic electrons via the photoelectric effect (von Engel 1965).

SEs will only be ejected from a surface by a PI if the sum of its kinetic (K_i) and potential energy (eV_i) is greater than $2e$ times the work function (Φ) of the sample/cathode or

$$K_i + eV_i \geq 2e\Phi, \quad (3.7.1)$$

where V_i and Φ are in volts (von Engel 1965, Loeb 1961). This follows from the fact that for each SE escaping the surface and entering the cascade, a second SE must be emitted to neutralize the ion in order to satisfy energy requirements. It has been found that the condition stated above still holds true even when the kinetic energy of the ion is approximately zero (von Engel 1965). Under the conditions utilized in an ESEM, whereby the drift velocity of ions is diffusion limited, ions impact the sample with no more kinetic energy than that of a neutral gas atom/molecule (Thiel *et al.* 1997). It is for this reason that the number of SEs liberated from the cathode per single ionization event (Llewellyn-Jones 1957) or ion formed (Molnar 1951) in the cascade under steady state conditions, γ_i , is mostly governed by the potential energy of the ion rather than its kinetic energy (von Engel 1965). It must be noted, however, that γ_i is also strongly dependent on the electronic surface state of the sample (Druyvesteyn & Penning 1940, Llewellyn-Jones 1957) and is generally large when the incident ions are excited (von Engel 1965).

SEs will only be emitted from a surface by photons provided the energy of the incident monochromatic radiation exceeds e times the work function in volts or exceeds a critical frequency, which is directly related to Φ as shown below:

$$hv \geq e\Phi = hv_c = \frac{hc}{\lambda_c}. \quad (3.7.2)$$

Above h is Planks constant, v is the frequency of the incoming radiation, c is the speed of light in a vacuum, v_c is the critical frequency or lowest incident photon frequency in which SE emission will occur and λ_c is the critical wavelength or maximum incident photon wavelength for SE emission. If the above requirement is satisfied, then the kinetic energy of each SE emitted will be

$$K_{SE} = hv - e\Phi. \quad (3.7.3)$$

Along with ESEs, photons are also produced in each avalanche via PE, BSE and SE-gas atom/molecule collisions. Hence, like α_{ion} , which as previously mentioned is the number of new electrons and ions (ion-pairs) produced by a single SE or ESE per unit path of distance traversed in the field direction, α_{exc} , is the excitation coefficient or total number of excitations producing photons of varying wavelength per unit electron path traversed in the field direction (Dias *et al.* 1997, Dias *et al.* 1999, von Engel 1965, Feio & Policarpo 1983, Massey *et al.* 1969). By definition, γ_p is the total number of photoelectrons liberated from the cathode per gaseous ionization event or avalanche liberated ion under steady state conditions. γ_p is a function of the wavelength of the incoming cathodic radiation and is strongly dependent on the electronic state (Druyvesteyn & Penning 1940) and the geometry (Loeb 1952) of the sample or cathode surface. γ_p increases with decreasing photon wavelength and generally reaches a maximum in the ultraviolet (UV) region of the electromagnetic spectrum but decreases in the x-ray region for most commonly used metallic materials (von Engel 1965). If $N_e^g(z)$ avalanche electrons traverse an element of gap distance

dz at z , exciting neutral gas molecules, then the number of new photons produced is (Llewellyn-Jones 1957):

$$dN_{hv}^g(z) = N_e^g(z) \alpha_{exc} dz. \quad (3.7.4)$$

Substitution of equation (3.3.2) into the equation above and integrating over the entire gap distance gives the total number of electron avalanche liberated photons created in the gas between the sample/cathode ($z = 0$) and the anode ($z = d$) to be:

$$N_{hv}^g(d) = \frac{N_e^g(0) \alpha_{exc}}{\alpha_{ion}} (e^{\alpha_{ion} d} - 1). \quad (3.7.5)$$

The number of photons incident on the sample/cathode will then be equal to

$$g_p N_p^g(d) e^{-\mu_p z'}, \quad (3.7.6)$$

where g_p is a geometrical factor, which describes the number of photons actually headed towards the cathode as photons are emitted in all directions from their point of production (Loeb 1952, Molnar 1951). g_p will therefore be larger for cathodes or samples of greater surface area. μ_p is the photon absorption coefficient of the gas, which defines the number of quanta absorbed per unit path length traversed, and z' is the distance that quanta travel from their point of production to the cathode. It must be noted that μ_p is normally specified for a certain wavelength of light, however, in the expression above it defines the net absorption for all wavelengths produced in the gas. Under static low pressure/high electric field strength conditions ($pd \ll 150$ torr·cm) absorption of photons in the gas may be considered negligible (Llewellyn-Jones 1957). In an ESEM, the maximum pd obtainable is approximately 80-100 torr·cm which suggests that μ_p can generally be taken as zero. The number of photoelectrons emitted from the sample/cathode $N_e^c(d)$ will be equal to the total number of photons reaching the cathode multiplied by the photoelectric yield P or the number of SEs emitted per incident photon. A certain fraction of the $N_e^c(d)$ SEs emitted will return to the sample/cathode via back diffusion. If we let v be the

fraction of SEs that escape back diffusion, then (Loeb 1952):

$$N_e^c(d) = vPg_p N_p^g(d) e^{-\mu_p z'} . \quad (3.7.7)$$

As γ_p is, as previously mentioned, equal to the number of photoelectrons liberated from the cathode per ion created in the avalanche, $N_p^c(d)/N_i^g(d)$, then it is seen from equations (3.3.3) and (3.7.7) that (Loeb 1952):

$$\gamma_p = \frac{vPg_p \alpha_{exc} e^{-\mu_p z'}}{\alpha_{ion}} . \quad (3.7.8)$$

In analogy to equation (3.7.8), the number of SEs emitted from the cathode due to incident avalanche generated metastables per avalanche liberated ion will be

$$\gamma_m = \frac{vMg_m \chi e^{-\mu_m z'}}{\alpha_{ion}} , \quad (3.7.9)$$

where M is the probability of SEs being emitted from the sample/cathode by metastable atoms/molecules, g_m is a geometrical loss factor relating to the loss of surface incident metastables in the gas through diffusion, χ is the number of metastable atoms/molecules produced per cascading electron per unit path traversed in the direction of E , and μ_m is the metastable absorption coefficient, which has the same definition as that described previously for photon absorption (Loeb 1952). An absorption coefficient is required as metastables may transfer their excitation energy to other atoms/molecules in the gas via momentum transfer or excitation transfer collisions such as, for example, in Penning ionization (Appendix A-collision 83). In gases where metastable atoms/molecules exist in appreciable concentrations γ_m is generally less than γ_i but greater than γ_p (Loeb 1952).

Along with ions, photons and metastables, neutral molecules are also, in some rare circumstances, capable of generating SEs when they collide with the sample or stage. The number of SEs emitted per surface incident neutral gas atom/molecule is given by γ_n . A neutral atom/molecule will only eject a SE if its energy is greater

than e times Φ in volts. A neutral atom/molecule, which consists entirely of kinetic energy, will therefore only eject a SE from a surface if

$$K_n = kT \geq e\Phi. \quad (3.7.10)$$

As most elements have work functions generally of a few to several volts, it can be seen from above that in order to eject electrons from a surface the absolute temperature of the gas must be extremely high: $T \approx 50000$ K for a Silicon sample ($\Phi_{Si} = 4.3$ V (Young 1992)). As the ESEM operates well outside this temperature range γ_n can generally be neglected in ESEM cascade amplification models.

From the aforementioned it can be seen that, in an ESEM, the total number of SEs emitted from the cathode by avalanche created ions, photons and metastables per ionization collision in the gas under steady state conditions, referred to as the secondary emission coefficient or Townsend's second ionization coefficient is (von Engel 1965, Llewellyn-Jones 1957, Molnar 1951):

$$\gamma = \gamma_i + \gamma_p + \gamma_m + \gamma_n. \quad (3.7.11)$$

Figure 3.1 shows some typical values of γ versus E/p for various gases and cathode materials obtained from breakdown measurements. It can be seen that for molecular gases such as N_2 , γ increases as E/p . At low E/p the number of excitations occurring in the gas is much greater than that of ionizations (von Engel 1965). As the absolute number of excitations taking place in the gas, per cascading electron per unit of gap distance traversed in the field direction, is small but increasing, γ rises at low E/p and is mostly due to photoelectron production (von Engel 1965, Llewellyn-Jones 1957). As E/p becomes larger, the fraction of ions to photons produced in the gas becomes greater as a higher percentage of cascading electrons are capable of exceeding the ionization potential of gas molecules between successive collisions instead of the lower energy atomic electron transitions associated with photon production. As γ_i

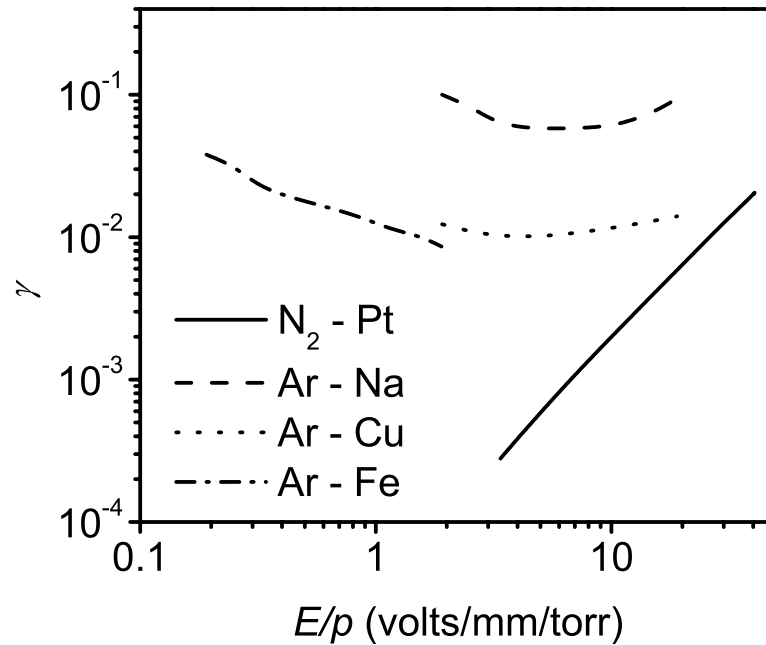


Figure 3.1: Second Townsend coefficient (γ) versus reduced electric field (E/p) for various gases (nitrogen (N_2), argon (Ar)) and cathode materials (Pt, Na, Cu, Fe) (adapted from von Engel 1965)

is generally greater than γ_p , as previously mentioned, γ further rises. At large E/p the drift velocity and hence kinetic energy of ions becomes appreciable such that, in addition to the ion-cathode inelastic processes described previously, SEs are also capable of being elastically extracted from the cathode via ionic collisions and hence γ increases furthermore. In the case of noble atomic gases, such as Ar, γ initially decreases and then subsequently increases as E/p is raised. The relatively large values of γ at low E/p are attributed to extremely high concentrations of photons and metastables being produced in the gas (von Engel 1965). However, as E/p increases these concentrations rapidly fall off relative to the continually increasing ion concentration with E/p , and after the minima in γ , ion production and subsequent

ionic SE emission becomes dominant. The differences in the absolute values of γ over the entire E/p range for a particular cathode material is generally attributed to differing work functions. In general, higher work function materials produce lower γ values, as greater ion, photon and metastable energies are required to extract electrons from the surface. γ is generally smaller for molecular gases than that of atomic gases because molecules have additional mechanisms (vibration and dissociation) for absorbing excitation energies (von Engel 1965, Thiel *et al.* 1997). It is for this reason that complex gases such as H₂O, which have numerous vibrational modes, have very low γ values. von Engel (1965) quotes γ for H₂O and ethanol to be of the order $\approx 10^{-10}$, which means that the amplification due to secondary effects occurring at the cathode can be neglected and cascade models can be modelled using only a single avalanche of electrons.

Consider a typical electron cascade process whereby successive avalanches are initiated by $N_e^g(0)$ electrons leaving the cathode. If electron-molecule collisions in the gas produce all of the primary phenomena described above (*i.e.* ions, photons and metastables) then from equations (3.3.3) and (3.7.11) the number of electrons ejected from the cathode after the first avalanche will be:

$$\begin{aligned} {}^1N_e^c &= N_e^g(0) \gamma_i (e^{\alpha_{ion}d} - 1) + N_e^g(0) \gamma_p (e^{\alpha_{ion}d} - 1) \\ &+ N_e^g(0) \gamma_m (e^{\alpha_{ion}d} - 1) + N_e^g(0) \gamma_n (e^{\alpha_{ion}d} - 1) \\ &= N_e^g(0) \gamma (e^{\alpha_{ion}d} - 1) \end{aligned} \quad (3.7.12)$$

The electrons ejected from the cathode will then be amplified in the gas producing subsequent ions, photons and metastables, such that the number of electrons liberated from the cathode after the second and third avalanches will be

$${}^2N_e^c = {}^1N_e^c \gamma (e^{\alpha_{ion}d} - 1) = N_e^g(0) \gamma^2 (e^{\alpha_{ion}d} - 1)^2 \quad (3.7.13)$$

and

$${}^3N_e^c = {}^2N_e^c \gamma (e^{\alpha_{ion}d} - 1) = N_e^g(0) \gamma^3 (e^{\alpha_{ion}d} - 1)^3, \quad (3.7.14)$$

respectively. It can therefore be clearly seen from the equations presented above that if this avalanche feedback process was to repeat *ad infinitum* that the total number of electrons ejected from the cathode would be

$${}^{\infty}N_e^c = N_e^g(0) \left\{ 1 + \gamma (e^{\alpha_{ion}d} - 1) + \gamma^2 (e^{\alpha_{ion}d} - 1)^2 + \gamma^3 (e^{\alpha_{ion}d} - 1)^3 + \dots \right\}, \quad (3.7.15)$$

which is more conveniently expressed as the infinite series (Thiel *et al.* 1997):

$${}^{\infty}N_e^c = N_e^g(0) \sum_{n=0}^{\infty} \gamma^n (e^{\alpha_{ion}d} - 1)^n. \quad (3.7.16)$$

An approximation to the infinite series above, which is readily encountered in theory on ionized gases, is (Druyvesteyn & Penning 1940, von Engel 1965, Llewellyn-Jones 1957, Loeb 1952, Molnar 1951, Pejović *et al.* 2002):

$${}^{\infty}N_e^c = \frac{N_e^g(0)}{1 - \gamma (e^{\alpha_{ion}d} - 1)}. \quad (3.7.17)$$

In order for the equation above to be an acceptable approximation, the convergence criterion,

$$\gamma^2 (e^{\alpha_{ion}d} - 1)^2 < 1 \quad (3.7.18)$$

must be satisfied (Thiel *et al.* 1997). It can be seen that if γ is small the series converges, producing a finite cascade amplification current. On the other hand, if γ is large the series diverges and the cascade will, after a small increment of time and several avalanches, result in breakdown (flashover, spark discharge, arc discharge) (von Engel 1965, Danilatos 1990c, Nasser 1971, Pejović *et al.* 2002).

As equation (3.7.17) relates the number of electrons produced in a single avalanche to the total number of electrons produced in an entire cascade, or *ad infinitum* avalanches, it can be seen that under steady state conditions $N_e^g(0)$ and ${}^{\infty}N_e^c$ can be replaced by the single avalanche ($I_{PE_0}^g$, $I_{BSE_0}^g$, $I_{SE_0}^g$) and *ad infinitum* avalanche (I_{PE}^g , I_{BSE}^g , I_{SE}^g) expressions of equations (3.2.2) and (3.2.3). From this it can easily be seen that the ‘feedback factor’ k , needed to model cascade amplification in

an ESEM, can be expressed as (Danilatos 1990c, Farley & Shah 1990b, Farley & Shah 1991, Meredith *et al.* 1996, Moncreiff *et al.* 1978, Thiel *et al.* 1997):

$$k = \frac{1}{1 - \gamma (e^{\alpha_{ion}d} - 1)}. \quad (3.7.19)$$

Existing theoretical models of cascade amplification in an ESEM generally neglect the generation of photons and metastables produced in the cascade as well as the secondary emission produced by these phenomena. Most models make the assumption that only ions are created in the gas and hence γ_i is the only contributor to secondary processes. It is for these reasons that models of cascade amplification in an ESEM need to be modified to account for these additional modes of amplification. In doing so existing discrepancies between experimental and theoretical gas cascade amplification curves should be much smaller. Theoretical cascade amplification curves/profiles for several gases, calculated using existing knowledge, are shown in section 3.11.

3.8 Electron Impact Ionization Cross sections

In order to theoretically investigate gaseous cascade amplification in a partially ionized gas, and hence apply the equations derived in sections 3.2-3.7, one must know the inelastic scattering cross sections associated with electron impact ionization. There is an abundance of electron impact ionization cross section data for most gases, both experimental and theoretical, but one must be careful in choosing the appropriate cross sections for the models at hand. In general, experimental cross sections should be chosen when possible over theoretical models and users should be very wary of the experimental procedures used to obtain the data.

Figures 3.2-3.4 show experimental and theoretical total electron impact ionization cross sections versus electron energy for Ar (Asundi & Kurepa 1963, Fletcher & Cowling 1973, Märk 1982, Rapp & Englander-Golden 1965, Schram *et al.* 1966, Smith 1930, Srinivasan & Rees 1967, Straub *et al.* 1995, Wallace *et al.* 1973); N₂ (Deutsch *et al.* 2000, Hwang *et al.* 1996, Khare & Meath 1987, Krishnakumar & Srivastava 1992, Rapp & Englander-Golden 1965, Saksena *et al.* 1997a, Saksena *et al.* 1997b, Schram *et al.* 1965, Schram *et al.* 1966, Straub *et al.* 1996); and H₂O (Bolorizadeh & Rudd 1986, Deutsch *et al.* 2000, Djurić *et al.* 1988, Hwang *et al.* 1996, Jain & Khare 1976, Kim & Rudd 1994, Saksena *et al.* 1997b, Saksena *et al.* 1997a, Schutten *et al.* 1966, Straub *et al.* 1998, Terrissol *et al.* 1989). Total electron impact ionization cross sections are a summation of all of the cross sections for the production of a specific parent or fragment ion (partial ionization cross section) for a particular gas (Deutsch *et al.* 2000). For example, electrons impacting H₂O molecules are capable of not only producing H₂O⁺ but also, in order of largest to smallest probability, OH⁺, H⁺, O⁺, H₂O⁺⁺, *etc.* ions (Dolan 1993, Rao *et al.* 1995, Straub *et al.* 1998, Yousfi & Benabdessadok 1996). Electrons impacting H₂O are also capable of producing additional ion species to those stated above, however the partial ionization cross sections

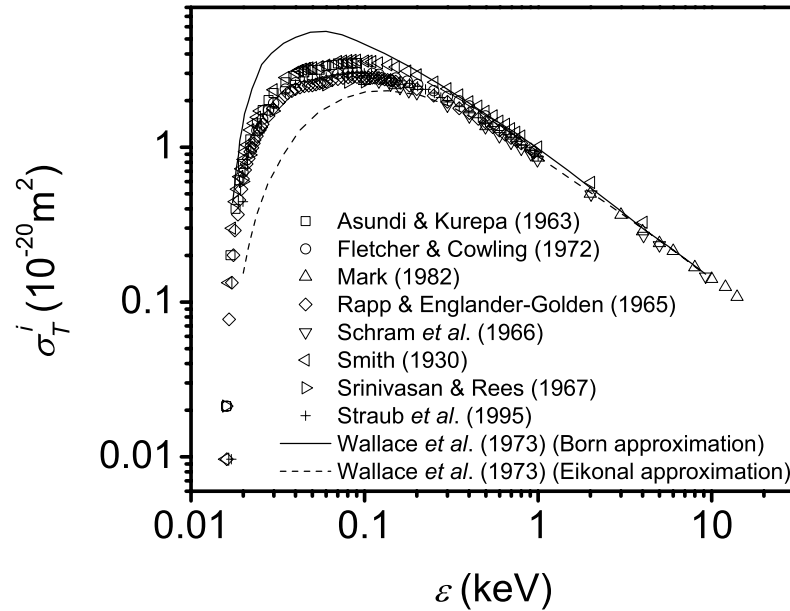


Figure 3.2: Total electron impact ionization cross sections (σ_T^i) for argon (Ar) as a function of electron energy (ϵ). Experimentally and theoretically obtained cross sections are represented by points and line plots, respectively (Asundi & Kurepa 1963, Fletcher & Cowling 1972, Märk 1982, Rapp & Englander-Golden 1965, Schram *et al.* 1966, Smith 1930, Srinivasan & Rees 1967, Straub *et al.* 1995, Wallace *et al.* 1973).

associated with their production is small and therefore generally neglected in models. Dolan (1993) tabulates a large number of the partial ionization reactions that occur in H_2O . Akin to H_2O , electrons impacting Ar and N_2 are mostly capable of producing the partial ion products Ar^{n+} ($n = 1 - 8$) (Almeida *et al.* 1994, Almeida *et al.* 1997, Märk 1982, Straub *et al.* 1995, Wallace *et al.* 1973, Wetzel *et al.* 1987) and N_2^{n+} ($n = 1 - 4$) (Märk 1982, Spekowius & Brehm 1991), respectively. Parent ion species occurring in addition to those stated above are present in negligible concentrations. It can be seen from the cross sections in figures 3.2-3.4 that below the

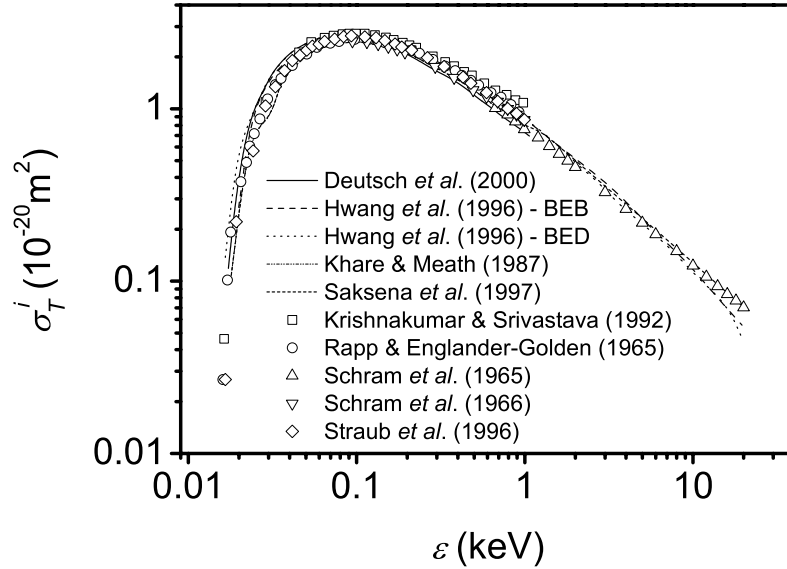


Figure 3.3: Total electron impact ionization cross sections (σ_T^i) for nitrogen (N_2) as a function of electron energy (ϵ). Experimentally and theoretically obtained cross sections are represented by points and line plots, respectively (Deutsch *et al.* 2000, Hwang *et al.* 1996, Khare & Meath 1987, Krishnakumar & Srivastava 1992, Rapp & Englander-Golden 1965, Saksena *et al.* 1997a, Saksena *et al.* 1997b, Schram *et al.* 1965, Schram *et al.* 1966, Straub *et al.* 1996). [BEB=binary-encounter-Bethe method, BED=binary-encounter-dipole method]

threshold energy (ionization potential) electron impact does not produce any ions as the total ionization cross section is zero (first ionization potentials of the gases used in this thesis are given in table 3.1). Instead, this region ($\epsilon < V_i$) is mostly governed by excitation scattering whereby low energy electrons transfer their kinetic energy to gas molecules in the form of vibrational and electronic excitations during collisions (von Engel 1965, Nasser 1971). As the electron energy increases above the ionization potential the total ionization cross section increases sharply up to approximately 100 eV, after which it falls off exponentially. As mentioned previously, SEs enter the

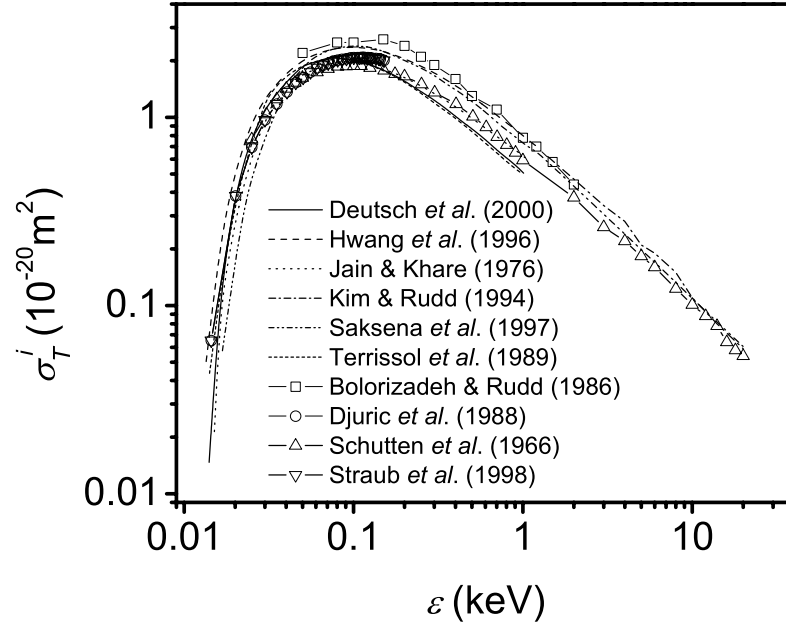


Figure 3.4: Total electron impact ionization cross sections (σ_T^i) for water vapour (H_2O) as a function of electron energy (ε). Experimentally and theoretically obtained cross sections are represented by points and line plots, respectively (Bolorizadeh & Rudd 1986, Deutsch *et al.* 2000, Djurić *et al.* 1988, Hwang *et al.* 1996, Jain & Khare 1976, Kim & Rudd 1994, Saksena *et al.* 1997a, Saksena *et al.* 1997b, Schutten *et al.* 1966, Straub *et al.* 1998, Terrissol *et al.* 1989).

gas with a Maxwellian energy distribution maximizing at approximately 3 eV and ranging between 0 and 50 eV (Goldstein *et al.* 1992, Reimer 1985). This means that increasing SE kinetic energies cause an increase in the probability of ion formation. Conversely BSEs enter the gas with average energies in excess of $\sim 0.5\varepsilon_{PE}$ (Goldstein *et al.* 1992, Reimer 1985), which means that their total ionization cross sections are in the keV range and therefore decrease exponentially with increasing energy. This

phenomenon is due to the fact that greater free electron energies, hence greater velocities, cause a reduction in the time available for bound atomic electrons in gas molecules to be displaced relative to their nuclei (referred to as polarization) by the free electrons' electric field (von Engel 1965). Ionization therefore cannot take place as efficiently, as the dipole moments induced in gas molecules during polarization diminish. In addition, head-on type collisions between fast free electrons and gas molecules need to occur in order for ionization to occur. This is because the trajectories of free electrons are not as easily altered by the electric force experienced between gas molecules and the higher momentum free electrons. Slow electrons, on the other hand, are more easily displaced towards gas molecules during interactions and can therefore penetrate larger distances into bound orbitals, increasing the probability of ionization. The degree of polarization required to cause ionization is proportional to the number of bound atomic electrons in gas atoms/molecules and hence increases with atomic number (von Engel 1965). This statement is reflected in figures 3.2-3.4 by the fact that electron impact ionization cross sections are seen to be greatest for Ar followed by N_2 and then H_2O .

3.9 Ionization Efficiency of Primary and Backscattered Electrons

The number of ion-pairs produced per unit of path length of gas traversed by PEs and BSEs per unit pressure, the ionization efficiency S_{PE} and S_{BSE} are given by

$$S_{PE} = \frac{\sigma_T^i(\varepsilon_{PE})}{kT} \quad (3.9.1)$$

and

$$S_{BSE} = \frac{\sigma_T^i(\varepsilon_{BSE})}{kT}, \quad (3.9.2)$$

where $\sigma_T^i(\varepsilon)$ is the total electron impact ionization cross section, which is a function of the average energy of the PEs (ε_{PE}) or BSEs (ε_{BSE}), respectively, k is the Boltzmann constant and T the absolute temperature of the gas (von Engel 1965, Danilatos 1990c, Farley & Shah 1990a, Meredith *et al.* 1996). Total electron impact ionization cross sections for Ar, N₂ and H₂O were shown previously in section 3.8. In cascade amplification models the average energy of BSEs is usually taken to be 0.75 times that of PEs, $\varepsilon_{BSE} = 0.75\varepsilon_{PE}$ (Meredith *et al.* 1996).

3.10 Ionization Efficiency of Secondary and Environmental Electrons - First Townsend Ionization Coefficient

The Townsend model of gaseous cascade amplification between parallel plates gives the number of ionization events or ion-pairs generated per unit path length traversed by SEs and ESEs, where swarm conditions are assumed to be prevalent throughout the gap, as

$$\alpha_{ion}^{sw} = Ape^{-Bp/E}, \quad (3.10.1)$$

where p is the chamber pressure and E is the electric field strength in the gap generated by V_{GSED} between the GSED and the stage (Danilatos 1990c, von Engel 1965, Meredith *et al.* 1996, Nasser 1971, Thiel *et al.* 1997). A and B are gas dependent constants defined as

$$A = \frac{1}{\lambda_{SE}} \quad (3.10.2)$$

and

$$B = \frac{V_i^1}{\lambda_{SE}}, \quad (3.10.3)$$

where λ_{SE} is the inelastic mean free path of SEs and ESEs in the gas at 1 torr pressure, and as mentioned previously, V_i^1 is the first ionization potential of the gas in electron volts (von Engel 1965). Table 3.1 lists first ionization potentials and the constants A and B for gases used throughout this thesis.

As mentioned previously, the Townsend gas capacitor model assumes that amplified SEs and ESEs reach a steady state kinetic energy distribution within a negligible distance from the sample and therefore α_{ion} can be taken to be constant throughout the gap. However, it has been shown by Thiel *et al.* (1997), via Monte Carlo simulations, that the kinetic energy distribution and hence ionization efficiency of SEs and

Table 3.1: First ionization potentials (V_i^1) and gas dependent constants A and B for argon (Ar), nitrogen (N_2) and water vapour (H_2O) (von Engel 1965, Thiel *et al.* 1997)

Gas type	V_i^1 (eV)	A ($\text{mm}^{-1}\text{torr}^{-1}$)	B ($\text{Vmm}^{-1}\text{torr}^{-1}$)	Valid E/p range ($\text{Vmm}^{-1}\text{torr}^{-1}$)
Ar	15.75	1.2	18	10-60
N_2	15.5	1.2	34.2	10-60
H_2O	12.6	1.3	29	15-100

ESEs is not constant throughout the gap, but better described by

$$\alpha_{ion}(z) = \alpha_{ion}^{sw} [1 - e^{-Cp(z-z_0)}], \quad (3.10.4)$$

where C is a gas specific constant, α_{ion}^{sw} is the first Townsend ionization coefficient under swarm conditions which is identical to that given in equation (3.10.1), and z_0 is the average distance through which SEs must be accelerated in the electric field from their point of production at $z = 0$ in order to exceed the ionization potential of the gas (Thiel *et al.* 1997):

$$z_0 = \frac{(V_i^1 - \bar{\epsilon}_{SE})d}{eV_{GSED}}. \quad (3.10.5)$$

Above, $\bar{\epsilon}_{SE}$ is the most probable average energy at which SEs are emitted from the sample surface assuming a Maxwellian distribution of kinetic energies ($\bar{\epsilon}_{SE} \sim 3$ eV) (Reimer 1985) and e is the charge of an electron.

Figure 3.5 shows the ionization efficiency $\alpha_{ion}(z)$ of SEs and ESEs versus gap distance (z) traversed as a function of p_{H_2O} (figure 3.5(a)) and GSED detector bias

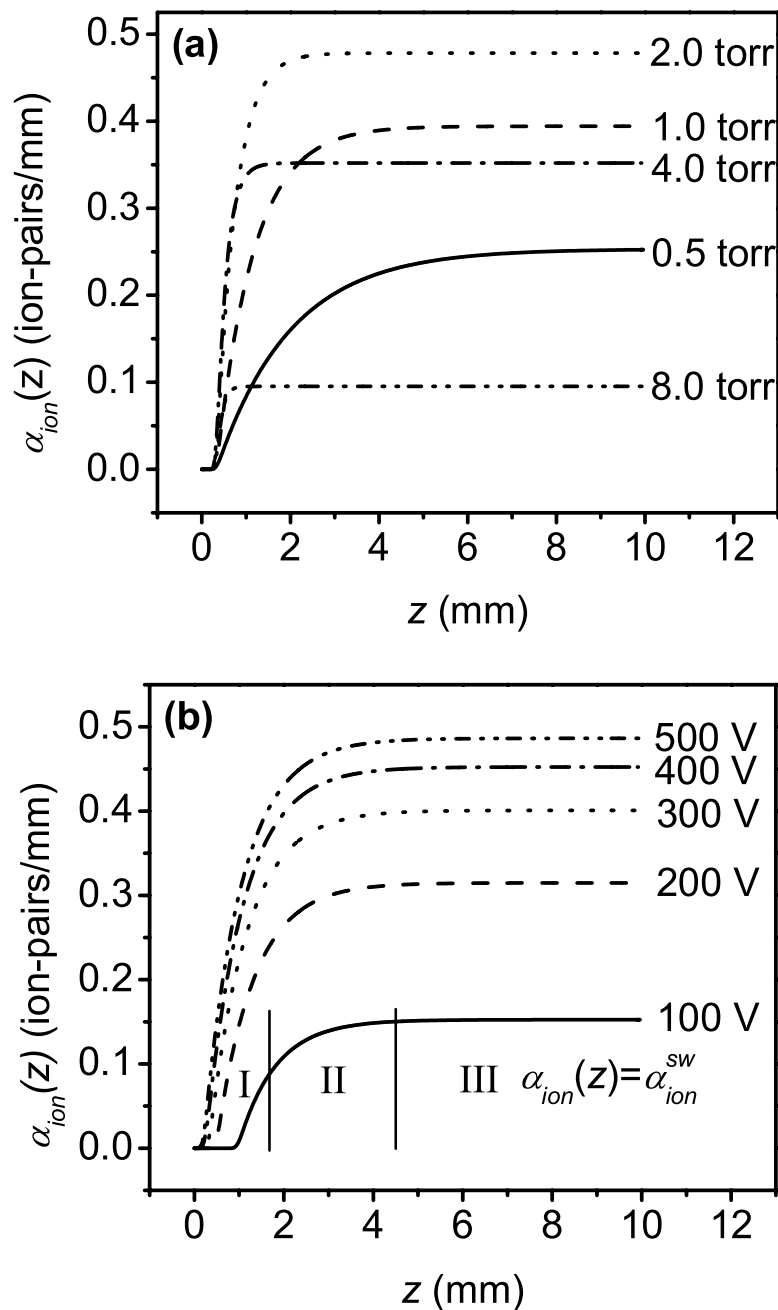


Figure 3.5: First Townsend ionization coefficient ($\alpha_{ion}(z)$) versus gap distance (z) traversed, acquired as a function of (a) water vapour pressure (p_{H_2O}) [$V_{GSED} = 290$ V] and (b) gaseous secondary electron detector bias (V_{GSED}) [$p = 1$ torr]. Region I: minimal ionization; Region II: increasing ionization efficiency; Region III: the attainment of swarm conditions (adapted from Thiel *et al.* 1997).

(figure 3.5(b)). It can be seen from both the figures that $\alpha_{ion}(z)$ is initially zero until $z = z_0$ at which electrons have exceeded V_i^1 and begin ionizing collisions (region I). At $z_0 < z \leq d$, $\alpha_{ion}(z)$ increases as an exponential function of decreasing gradient with z (region II) until swarm conditions are attained at which $\alpha_{ion}(z) = \alpha_{ion}^{sw}$ (region III). The exponential rise in $\alpha_{ion}(z)$ between the onset of ionization and swarm conditions is due to an increasing number of electrons being able to ionize the gas (Thiel *et al.* 1997). This is a direct reflection of the increasing total ionization cross section with electron energy as described previously in section 3.8. The flattening out of $\alpha_{ion}(z)$ at a characteristic swarm distance is, as previously mentioned, a result of the cascading SEs and ESEs attaining a steady state kinetic energy distribution as a result of inelastic collisional energy losses (ionization and excitation) being directly offset by energy gained from the electric field (Thiel *et al.* 1997). It can be seen that the gap distance traversed by electrons at which swarm conditions start, at constant V_{GSED} and d , decreases exponentially as p_{H_2O} is increased (figure 3.5(a)). It can also be seen that the ionization efficiency of SEs/ESEs at swarm initially increases with p_{H_2O} , reaches a maximum and then finally decreases with p_{H_2O} . At low pressures, the concentration of gas molecules in the gap is small and hence the collision frequency is reduced resulting in a low number of ionization collisions in the gap. As p increases, the collision frequency increases and the number of ion pairs produced per electron maximizes. However, as p is increased further the collision frequency becomes so high that large concentrations of electrons cannot gain enough energy by E between collisions and consequently the steady state ionization coefficient decreases. The pressure at which maximum steady state ionization efficiency of SEs and ESEs occurs is dependant on V_{GSED} , d and the gas species present.

It can be seen from figure 3.5(b) that the gap distance traversed by SEs before the onset of swarm conditions, at constant p_{H_2O} and d , stays approximately constant as V_{GSED} is increased.

3.11 Gaseous Cascade Amplification Profiles

Now that a description of the theory governing gaseous cascade amplification of PEs, BSEs and SEs in a partially ionized gas has been introduced the total cascaded electron current produced by PE and BSE and SE-gas ionizing collisions reaching the GSED ring located a distance d from the sample surface under steady state and saturation/swarm conditions can be determined. However, as seen previously in section 3.10, the efficiency at which cascading SEs and ESEs generate ion-pairs, α_{ion} , is not constant throughout the gap but a function of z . It has been demonstrated by Thiel *et al.* (1997) that in order to accommodate for the phenomenon ascribed above, and hence differences between calculated and experimental amplification, it is more convenient to use a pressure- and field-dependent ‘effective’ gap distance (d_{eff}) in conjunction with the z independent ionization efficiency (α_{ion}^{sw}) shown previously in equation (3.10.1). d_{eff} physically represents the portion of the gap whereby α_{ion} is essentially constant (*i.e.* region III in figure 3.5(b)) and is given as (Thiel *et al.* 1997):

$$d_{eff} = d - z_0 + \frac{1}{Cp} [e^{-Cp(d-z_0)} - 1]. \quad (3.11.1)$$

Multiplying equations (3.4.4), (3.5.2) and (3.6.2) by k , after replacing d with d_{eff} and α_{ion} with α_{ion}^{sw} , gives the ionization currents produced by PEs, BSEs and SEs after *ad infinitum* avalanches, respectively, as (Farley & Shah 1990b, Meredith *et al.* 1996, Moncreiff *et al.* 1978, Thiel *et al.* 1997):

$$I_{PE}^g = \frac{I_{PE} S_{PEP}}{\alpha_{ion}^{sw}} (e^{\alpha_{ion}^{sw} d_{eff}} - 1) k, \quad (3.11.2)$$

$$I_{BSE}^g = \frac{\eta I_{PE} S_{BSEP}}{\alpha_{ion}^{sw}} \left(\frac{\bar{d}_{BSE}}{d} \right) (e^{\alpha_{ion}^{sw} d_{eff}} - 1) k, \quad (3.11.3)$$

$$I_{SE}^g = \delta I_{PE} (e^{\alpha_{ion}^{sw} d_{eff}} - 1) k. \quad (3.11.4)$$

Replacing d and α_{ion} in equation (3.7.19) with d_{eff} and α_{ion}^{sw} , respectively, gives the ‘feedback factor’ in equation (3.11.4) as

$$k = \frac{1}{1 - \gamma(e^{\alpha_{ion}^{sw} d_{eff}} - 1)} \quad \gamma^2 (e^{\alpha_{ion}^{sw} d_{eff}} - 1)^2 < 1. \quad (3.11.5)$$

Substituting equations (3.11.2)-(3.11.4) into equation (3.2.2) gives the total ionization current produced in the cascade after *ad infinitum* avalanches by PEs, BSEs and SEs as (Farley & Shah 1990b, Meredith *et al.* 1996, Moncreiff *et al.* 1978, Thiel *et al.* 1997):

$$I_{ion} = I_{PE} (e^{\alpha_{ion}^{sw} d_{eff}} - 1) \left\{ \frac{S_{PEP}}{\alpha_{ion}^{sw}} + \frac{\eta S_{BSEP}}{\alpha_{ion}^{sw}} \left(\frac{\bar{d}_{BSE}}{d} \right) + \delta \right\} k. \quad (3.11.6)$$

It must be further emphasized that equation (3.11.6) is the ionization current produced under steady state saturation conditions whereby (i) drifting electrons produced by PEs, BSEs and SEs have attained constant rates of ionization and recombination, (ii) several avalanches have been generated such that electrons can be considered to be collected by the GSED ring uniformly and continuously; and (iii) under the assumption that all electrons generated in the cascade and leaving the sample surface are collected by the GSED ring.

Gas amplification is usually defined as the ratio of the total number of ion-pairs or ESEs produced in the cascade per sample emissive electron (Fletcher *et al.* 1997), which is equivalent to the ratio of the ionization current and the current of electrons leaving the sample surface:

$$A_e = \frac{I_{ion}}{I_{PE}(\eta + \delta)}. \quad (3.11.7)$$

The subscript e denoting electronic amplification. Substituting equation (3.11.6) into equation (3.11.7) gives the total electronic amplification as

$$A_e = \frac{(e^{\alpha_{ion}^{sw} d_{eff}} - 1)}{(\eta + \delta)} \left\{ \frac{S_{PEP}}{\alpha_{ion}^{sw}} + \frac{\eta S_{BSEP}}{\alpha_{ion}^{sw}} \left(\frac{\bar{d}_{BSE}}{d} \right) + \delta \right\} k. \quad (3.11.8)$$

The total electronic amplification will obviously be comprised of individual PE, BSE and SE amplification components. Therefore, dividing equations (3.11.2)-(3.11.4) by

$I_{PE}(\eta + \delta)$ gives PE, BSE and SE electronic gas amplification, respectively, as:

$$A_e^{PE} = \frac{S_{PEP}}{\alpha_{ion}^{sw}(\eta + \delta)} (e^{\alpha_{ion}^{sw}d_{eff}} - 1) k, \quad (3.11.9)$$

$$A_e^{BSE} = \frac{\eta S_{BSEP}}{\alpha_{ion}^{sw}(\eta + \delta)} \left(\frac{\bar{d}_{BSE}}{d} \right) (e^{\alpha_{ion}^{sw}d_{eff}} - 1) k, \quad (3.11.10)$$

$$A_e^{SE} = \frac{\delta}{(\eta + \delta)} (e^{\alpha_{ion}^{sw}d_{eff}} - 1) k. \quad (3.11.11)$$

Figure 3.6 shows profiles of A_e versus p_{H_2O} , acquired as a function of (a) V_{GSED} and (b) d , calculated using equation (3.11.8). The profiles were generated using the data shown in table 3.2. It can be seen from figure 3.6 that, at constant d and V_{GSED} , A_e initially increases with p_{H_2O} , reaches a maximum, and then decreases with increasing p_{H_2O} except for the case when $V_{GSED} = 200$ V (figure 3.6(a)) where A_e increases slowly with p_{H_2O} after the maximum (Fletcher *et al.* 1997, Meredith *et al.* 1996, Newbury 1996, Thiel *et al.* 1997). The increases in A_e at low V_{GSED} is attributed to the enhancement of PE and BSE-gas molecule ionization at elevated pressures and reduced electric fields (Fletcher *et al.* 1997). The increase in electronic amplification with pressure, before maximum amplification is attained, is a result of an increase in the concentration of gas molecules within the chamber and hence an increase in the probability of ionization. The decrease in A_e with increasing p , after maximum amplification is attained, is a consequence of the increasing gas concentration effectively reducing the distance traversed, and hence the energy acquired, by ESEs and ESEs via the electric field, between successive collisions with gas molecules. This subsequent ‘slowing down’ of electrons causing a reduction in the number of electrons above the ionization potential of the gas (von Engel 1965, Nasser 1971, Thiel *et al.* 1997). It is also noticed from figure 3.6 that (i) the pressure at which maximum electronic amplification occurs increases with increasing V_{GSED} , at constant d , and decreases with increasing d , at constant V_{GSED} ; (ii) maximum A_e decreases with increasing d , at constant V_{GSED} ; (iii) the breadth of the profiles becomes larger with

Table 3.2: Data used to generate the electronic amplification profiles shown in figures 2.21-2.23.

Parameter	Value	Reference
Gas	H ₂ O	
Sample	Si	
δ	0.216	Reimer & Tolkamp (1980)
η	0.194	Reimer & Tolkamp (1980)
ε_{PE}	20 keV	
ε_{BSE}	$0.75\varepsilon_{PE}$	Meredith <i>et al.</i> (1996)
$\sigma_T^i(\varepsilon_{PE})$	$5.9 \times 10^{-16} \text{ mm}^2$	Kim & Rudd (1994)
$\sigma_T^i(\varepsilon_{BSE})$	$7.5 \times 10^{-16} \text{ mm}^2$	Kim & Rudd (1994)
T	298 K	
S_{PE}	0.019 ion-pairs/mm/torr	
S_{BSE}	0.024 ion-pairs/mm/torr	
$\frac{\bar{d}_{BSE}}{d}$	1	
A	0.65 ion-pairs/mm/torr	von Engel (1965)
B	14.5 V/mm/torr	von Engel (1965)
C	1.2 ion-pairs/mm/torr	Thiel <i>et al.</i> (1997)
γ	10^{-10}	von Engel (1965)

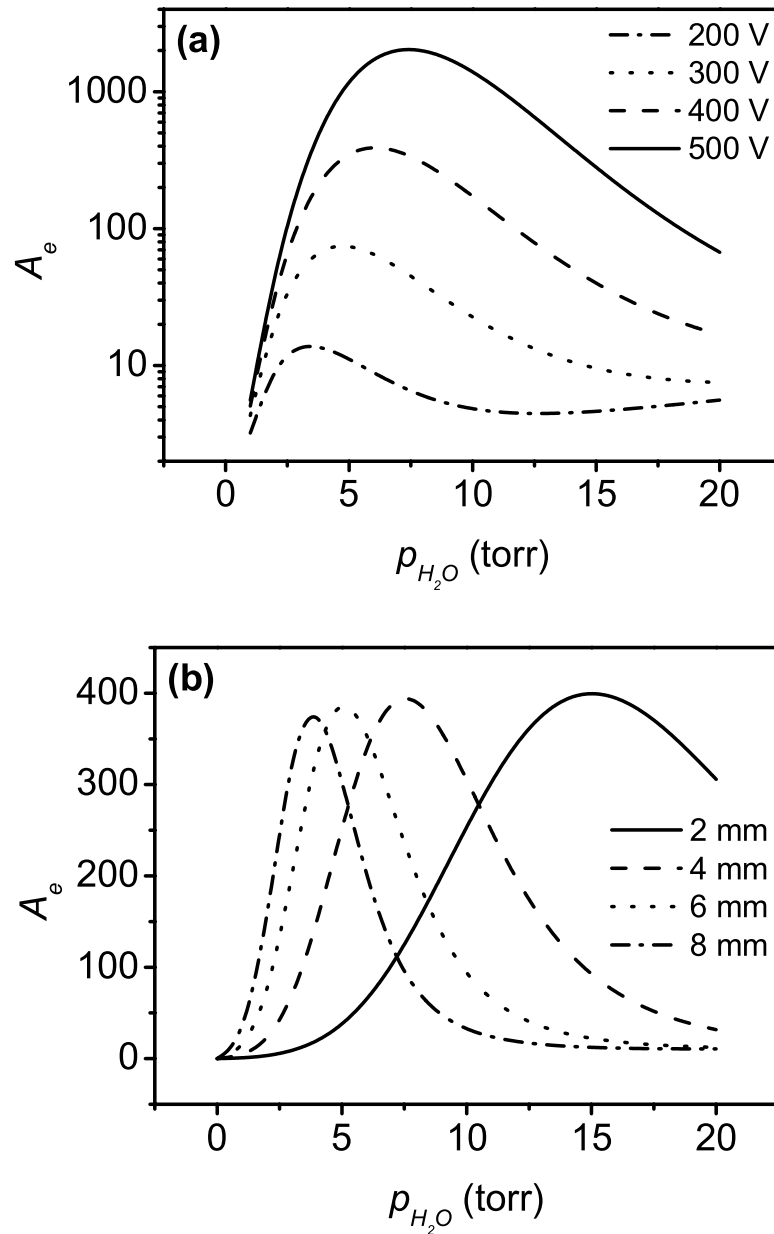


Figure 3.6: Total electronic amplification (A_e) versus water vapour pressure (p_{H_2O}) acquired as a function of (a) gaseous secondary electron detector bias (V_{GSED}) [$d = 5$ mm] and (b) sample-electrode separation (d) [$V_{GSED} = 400$ V]. [see table 2.4 for gas and sample data used to generate profiles]

increasing V_{GSED} and diminish with increasing d ; and (iv) the peak-to-plateau ratio, or SE contrast-to-BSE contrast/SE SNR¹ (Fletcher *et al.* 1997), increases with increasing V_{GSED} , at fixed d , and decreases with increasing d , at fixed V_{GSED} (Fletcher *et al.* 1997, Meredith *et al.* 1996, Newbury 1996, Thiel *et al.* 1997).

Shown in figure 3.7 are profiles of A_e versus (a) V_{GSED} and (b) d , acquired as a function of p_{H_2O} . Once again the profiles were generated using equation (3.11.8) in conjunction with the data presented in table 3.2. It can be seen from figure 3.7(a) that, at constant p_{H_2O} and d , A_e has an approximately exponential dependency on V_{GSED} (Fletcher *et al.* 1997, Meredith *et al.* 1996, Mohan *et al.* 1998, Thiel *et al.* 1997). Increasing V_{GSED} increases E and hence the average kinetic energy attained by SEs and ESEs between collisions with gas molecules (von Engel 1965, Nasser 1971). Associated with this increase in kinetic energy is an exponential increase in the population of SEs and ESEs above the ionization potential of the gas (von Engel 1965) and hence A_e increases exponentially with V_{GSED} . The electronic amplification profiles shown in figure 3.7(b) illustrates that, at fixed V_{GSED} and p_{H_2O} , A_e has a similar dependency with d as that of p , at fixed V_{GSED} and d . Figure 3.7(b) also illustrates that the maximum amplification attainable at a particular d , at constant V_{GSED} , remains rather independent of p .

As seen previously, the total ionization current and hence the total amplified signal is comprised of individual PE, BSE and SE signals. Figure 3.8 shows curves of A_e versus p_{H_2O} acquired as a function of signal type at (a) ‘low’ detector bias ($V_{GSED} = 200$ V) and (b) ‘high’ detector bias ($V_{GSED} = 400$ V). The total (PE+BSE+SE) amplification curves were generated using equation (3.11.8) and PE (A_e^{PE}), BSE (A_e^{BSE}) and SE (A_e^{SE}) amplification curves were simulated using equations (3.11.9)-(3.11.11),

¹The peak in A_e versus p profiles is dominated mostly by SE signals and the high p plateau region, or tail, is predominately made up of unwanted PE signals (Fletcher *et al.* 1997). Therefore the peak-to-plateau ratio can be used to estimate the average contribution of SE signal relative to background noise in images and therefore can also be labelled as SE SNR (see (Fletcher *et al.* 1997)).

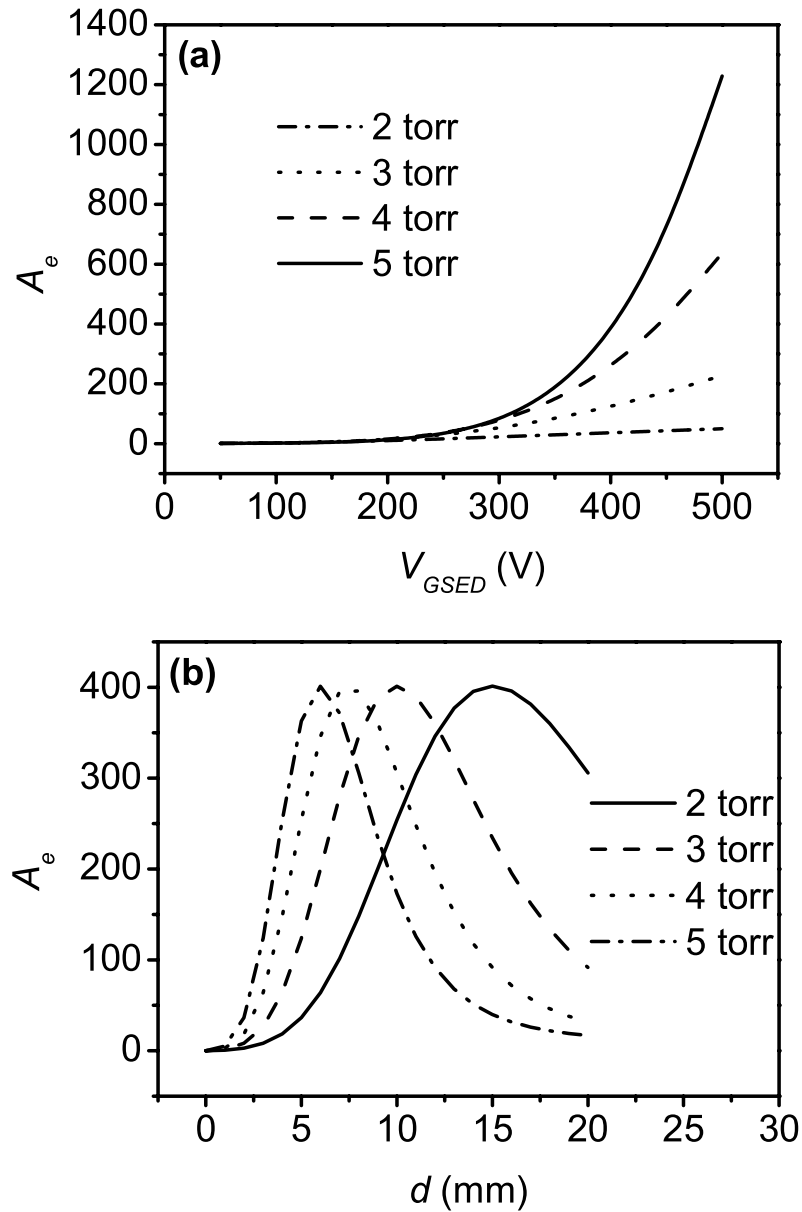


Figure 3.7: Total electronic amplification (A_e) versus (a) gaseous secondary electron detector bias (V_{GSED}) [$d = 5$ mm] and (b) sample-electrode separation (d) [$V_{GSED} = 400$ V] acquired as a function of water vapour pressure (p_{H_2O}). [see table 2.4 for gas and sample data used to generate profiles]

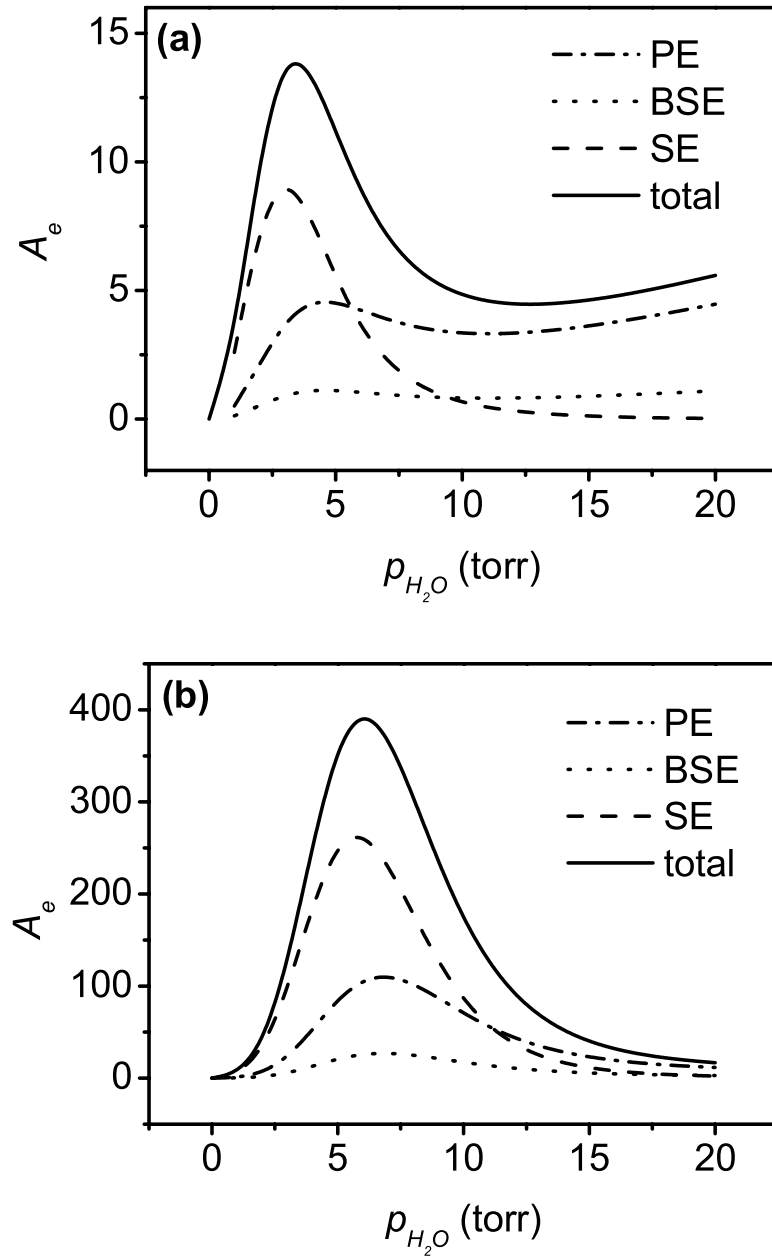


Figure 3.8: Total electronic amplification (A_e) versus water vapour pressure (p_{H_2O}) acquired as a function of signal type: (a) [$V_{GSED} = 200$ V], (b) [$V_{GSED} = 400$ V]. [see table 2.4 for gas and sample data used to generate profiles]

respectively. The curves show that A_e^{PE} , A_e^{BSE} and A_e^{SE} exhibit the same pressure dependency, at fixed V_{GSED} and d , as that discussed previously. The curves also illustrate that (i) SE amplification dominates the total amplification at low p , whereas (ii) PE and BSE amplification dominate at high p (Fletcher *et al.* 1999). The pressure range over which SE signals dominate being greater at ‘high’ detector bias (figure 3.8(b)) than that at ‘low’ detector bias (figure 3.8(a)). In order to demonstrate the actual contribution of PE, BSE and SE amplification to the total amplification, figure 3.9 shows normalized electronic amplification ($A_e^{PE/BSE/SE}/A_e$) versus p_{H_2O} , acquired as a function of the signal type. It can be seen that at ‘low’ V_{GSED} (figure 3.9(a)): (i) At $0 \leq p_{H_2O} \leq 5$ torr, SE amplification dominates followed by PE and BSE amplification; (ii) At $5 < p_{H_2O} < 10$ torr, PE amplification dominates followed by SE and BSE amplification; (iii) At $10 \leq p_{H_2O} \leq 20$, PE amplification dominates followed by BSE and SE amplification. At ‘high’ V_{GSED} (figure 3.9(b)): (i) At $0 \leq p_{H_2O} \leq 11.25$ torr, SE amplification dominates followed by PE and BSE amplification; (ii) At $11.25 < p_{H_2O} < 17.5$ torr, PE amplification dominates followed by SE and BSE amplification; (iii) At $17.5 \leq p_{H_2O} \leq 20$, PE amplification dominates followed by BSE and SE amplification. It is also noticed in figure 3.9 that normalized PE and BSE amplification continually increase with p_{H_2O} . Unlike SEs and ESEs which need to gain energy from the electric field between inelastic collisions in order to ionize the gas, PEs and BSEs, whose energies are much greater than the ionization potential of the gas, are not influenced by the electric field and hence do not exhibit the ‘slowing-down’ effect during inelastic collisions. Therefore as p increases, the concentration of gas molecules available for ionization increases, and the number of ESEs, hence amplification, produced by PEs and BSEs increases.

It can therefore be seen from all of the electronic amplification profiles shown in figures 3.8 and 3.9 that the plateau region, at the high pressure tail of the profiles, is predominantly made up of scattered PE signal and, to a lesser extent, BSE signal.

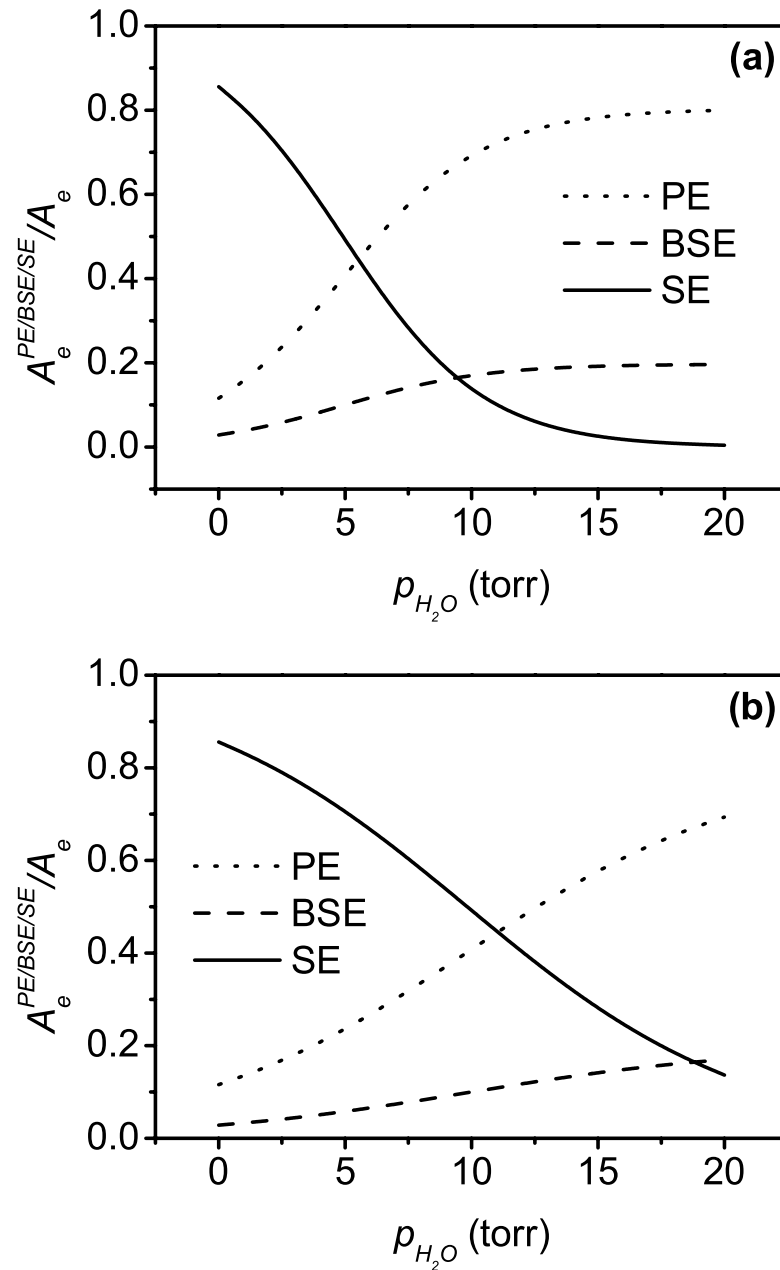


Figure 3.9: Normalized electronic amplification ($A_e^{PE/BSE/SE}/A_e$) versus water vapour pressure (p_{H_2O}) acquired as a function of signal type: (a) [$V_{GSED} = 200$ V], (b) [$V_{GSED} = 400$ V]. [see table 2.4 for gas and sample data used to generate profiles]

Conversely, at low pressures, where the amplification generally maximizes, the signal is mainly comprised of SE signal. Therefore, if ‘true’ high contrast SE imaging is to be performed, which obviously contains desirable topographical contrast (Goldstein *et al.* 1992, Reimer 1985), then PE and BSE signals will only contribute to an unwanted background signal component in images. Hence, the peak-to-plateau ratio (SE SNR or SE contrast) is a quantitative means of experimentally determining image quality (Fletcher *et al.* 1997, Thiel *et al.* 1997). The larger the ratio, the lower the contribution of unwanted PE (skirt) and BSE signals (Fletcher *et al.* 1997). It must be noted that when electronic gas amplification is obtained experimentally there is no accurate way of determining the relative PE, BSE and SE contributions. Hence the only way to make a qualitative judgment of image quality, at this stage of ESEM research, is to measure the peak-to-plateau ratio. However, the peak of any amplification profiles obtained experimentally will still contain some contributions from PE and BSE signals and therefore will not be a completely ‘true’ measure of SE SNR unlike the theoretical normalized electronic amplification profiles ($A_e^{PE/BSE/SE}/A_e$) shown here.

From the aforementioned it can be seen that in order to obtain ESEM images containing high SE contrast/SE SNR one must work at microscope operating parameters and imaging gas types that (i) give rise to an overall large enough total signal entering the GSED or ISC electronics to generate sufficient contrast and (ii) the largest possible peak-to-plateau ratio or normalized electronic amplification ($A_e^{PE/BSE/SE}/A_e$). Such operating parameters in general are (i) ‘high’ V_{GSED} , (ii) ‘low’ p , (iii) small d and (iv) mid to high ε_{PE} (Fletcher *et al.* 1997), in order to reduce PE scattering and subsequent skirt formation. Water vapour was used to simulate the electronic gas amplification profiles shown as it exhibits superior electronic amplification properties (Fletcher *et al.* 1997, Thiel *et al.* 1997) and an ability to keep samples hydrated.

In summary, figures 3.6-3.9 correctly predict the qualitative trends in electronic gas amplification and hence ionization currents in a low vacuum gas capacitor where

the cathode is irradiated by a constant current of high energy electrons (Fletcher *et al.* 1997, Meredith *et al.* 1996, Newbury 1996, Thiel *et al.* 1997). However, the Townsend gas capacitor model described, although modified by Thiel *et al.* (1997) to account for some of the differences between theoretical and experimental data using $\alpha_{ion}(z)$ and d_{eff} , has been modelled with several assumptions and hence still needs further improvements. Factors that may possibly affect gas amplification in an ESEM, which have not been considered in the modified Townsend model described are: (i) Electric field geometry, the model presented assumes that the field generated by V_{GSED} , E_{GSED} , is constant and homogeneous throughout the gap and hence the shape of the GSED ring or stage does not alter amplification; (ii) Electric field modification due to positive ion space charge formation (Toth & Phillips 2000a, Toth *et al.* 2002b); (iii) Suppression of electronic amplification as a consequence of electron-ion recombination within the gap and the vicinity of the sample surface ('signal scavenging') (Craven *et al.* 2002, Toth *et al.* 2002a, Toth *et al.* 2002c, Toth *et al.* 2002d); (iv) Perturbations in the net electric field in the gap as a result of charging in dielectrics (Toth *et al.* 2000, Toth *et al.* 2002b).

Although most of the phenomena mentioned above in (i)-(iv) have been shown to occur in an ESEM (see references above), their qualitative effects on gas cascade amplification is unknown. Recently, a model describing steady state electron-ion recombination in an ESEM has been developed by Toth *et al.* (2002a). The model enables an 'effective' SE emission coefficient to be calculated, and thence incorporated into existing gas amplification models, that accounts for losses in the number of low energy SEs entering the gas amplification process as a result of ion capture in the vicinity of the sample surface. The steady state model developed is briefly described ahead in chapter 4.2.1. A transient model of SE-ion recombination in the ESEM, which calculates relative magnitudes of ionization rates, recombination rates, recombination coefficients and electron drift velocities under non steady state conditions

is put forth in chapter 4. As well as determining the gaseous parameters, ascribed above, this model essentially enables the determination of a time dependent ‘effective’ SE emission coefficient. Furthermore, as opposed to electronic amplification, the efficiency at which photons are generated by cascading electrons, and detected, is shown for the first time for several commonly utilized gases in chapter 5.

Chapter 4

Transient Analysis of Gaseous Electron-Ion Recombination in the Environmental Scanning Electron Microscope

4.1 Introduction

When a scanning electron beam exits a region of enhanced secondary electron (SE) emission (bright feature in SE image mode), such as a localized area of high negative charge density at the surface of an insulator a streak in the form of a dark shadow trails the enhanced SE emission region parallel to the scan direction (Toth & Phillips 2000a). The contrast and length of the streak varies as a function of microscope operating parameters. The mechanisms behind enhanced SE emission at localized regions of excess negative charging in insulators in a low vacuum environment are not relevant to the present study and will therefore not be discussed further (see (Toth *et al.* 2002c) for more information). Streaking has also been observed in conducting materials, however, the mechanisms behind the streaking in this case are different and will be discussed in detail in a future publication.

It has recently been proposed that shadowing/streaking in images of insulators obtained using an environmental scanning electron microscope (ESEM) is attributed to a reduction in the magnitude of the net electric field in the region between the ring and the sample surface as a result of positive ion (PI) space charge formation (Toth & Phillips 2000a, Toth & Phillips 2000b). A space charge being an accumulation of excess PIs in the gap between the detector ring and the sample caused by differences in the mobility of electrons and ions (von Engel 1965, Farley & Shah 1990b). The mobility of an electron, under the conditions typically utilized in an ESEM, is up to three orders of magnitude greater than that of a water vapour ion (H_2O^+) (von Engel 1965, Nasser 1971). However, there is presently no direct quantitative evidence to suggest that streaking in images after enhanced SE emission regions is a consequence of field modification due to space charge effects and could not be attributed mostly to gaseous electron-ion recombination (also referred to as signal scavenging (Craven *et al.* 2002)).

It will be demonstrated in this chapter that the streaks seen in images after an enhanced SE emission region can be accurately described and modelled using a theoretically derived gaseous electron-ion recombination model (see section 4.3). The model takes into consideration transients in signal formation caused by the time constant of the detection electronics and external circuit. The model enables relative magnitudes of recombination coefficients (ρ), recombination rates ($\zeta(t)$), ionization rates (ψ), electron drift velocities (v_e) and absolute values of the total time constant (RC) of the detection system and external circuit to be determined as a function of microscope operating constraints such as gaseous secondary electron detector (GSED) bias (V_{GSED}), sample-electrode separation (d), water vapour pressure (p_{H_2O}) and scan speed. The aptness of such a model suggests that space charges, which are undoubtedly present, are not the dominant effect causing the dark streaks seen in images.

4.2 Theory

4.2.1 Gaseous Electron-Ion Recombination

Experimental and theoretical discussions into gaseous electron-ion recombination or SE-ion recombination can be found in standard texts on ionized gases such as von Engel (1965), and Nasser (1971) as well as review articles such as Hahn (1997) and Burke & Moiseiwitsch (1976). Experimental studies of steady state gaseous electron-ion recombination relevant to low vacuum SEM has been recently performed by Toth *et al.* (2002a), Toth *et al.* (2002c) and Toth *et al.* (2002d). The following contains a brief summary of such works.

Charge neutralization and hence signal loss within an ionized gas can occur as a result of several mechanisms such as PIs capturing free electrons (electron-ion recombination) or via charge transfer reactions in which negative ions transfer their outer valance electrons to PIs (ion-ion recombination) (von Engel 1965, Hahn 1997, Nasser 1971). The probability of negative ion formation (attachment) in water vapour (H_2O), and the other imaging gases used in this thesis, such as argon (Ar) and nitrogen (N_2), is considered to be insignificant (von Engel 1965, Yousfi & Benabdessadok 1996) and hence ion-ion recombination can be treated as negligible when Ar, N_2 or H_2O is used as the imaging gas and therefore will not be discussed further.

Gaseous electron-ion recombination, as a whole, can be grouped into several competing reaction processes, each of which having different reaction rates and cross sections, which are dependent on gas type and incident electron energy. The main reaction processes are (i) radiative recombination (Appendix A-collision 64), (ii) dielectronic recombination (Appendix A-collision 65), (iii) three-body recombination (Appendix A-collisions 68 & 69), and for the case of molecular gases (iv) dissociative recombination (Appendix A-collision 67). The processes are described below.

Radiative recombination (RR): Here, a free electron is captured by an ion placing the resulting neutral atom or molecule in a singly excited Auger stable state. The electronically excited atom then de-excites via photon emission. RR only occurs provided that the ion is either monotonic or a molecule that does not dissociate after capturing the electron. If the captured electron decays directly to ground state then the energy of the emitted photon will be equal to the sum of the ionization energy required to form the initial ion and the initial kinetic energy of the captured electron ((Nasser 1971):

$$hv = eV_i^1 + \frac{1}{2}m_e v_e^2. \quad (4.2.1)$$

Consequently, the emission spectrum for direct de-excitation is continuous. The maximum wavelength of the emission spectrum will be when $v_e = 0$, and is equal to:

$$\lambda = \frac{hc}{eV_i^1}. \quad (4.2.2)$$

Alternatively, if the captured electron does not decay directly to ground level, the Auger stable neutral atom/molecule will firstly de-excite via the emission of a photon of energy equal to the summation of (i) the initial kinetic energy of the captured electron and (ii) the difference between the ionization energy and a characteristic excitation energy of the atom/molecule. The atom/molecule then further de-excites by emitting a photon of energy equal to the aforementioned excitation energy. In this indirect radiative recombination process, the emission spectrum will obviously comprise of a continuous component from the first direct de-excitation process and characteristic line spectra from the latter. Recombination coefficients, which are directly proportional to recombination cross sections (see section 4.6.3), are found to be of the order of 10^{-14} cm³/s (von Engel 1965, Hahn 1997) for RR. Figure 4.1 shows RR coefficients (ρ_{RR}) versus incident electron energy (ε) in multi-ionized Si. The figure illustrates that the rate, and hence probability, of RR exponentially decreases with increasing ε .

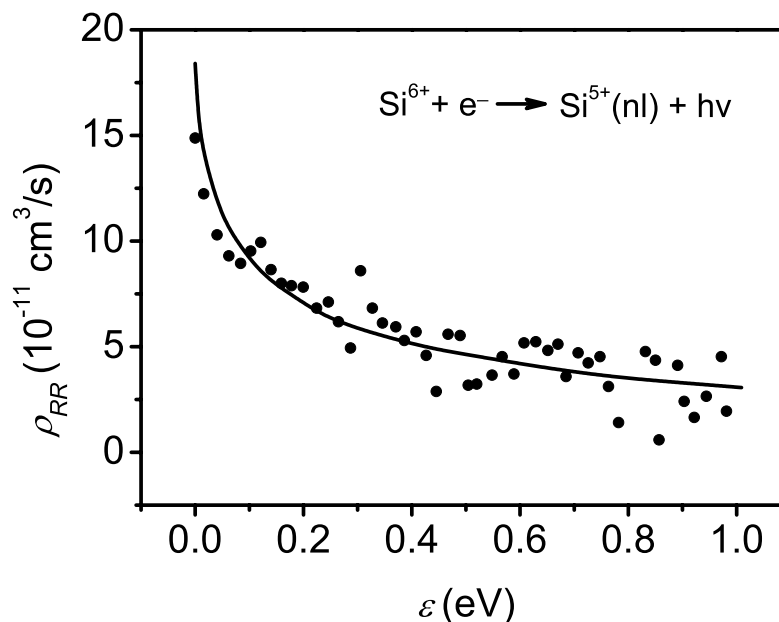


Figure 4.1: Radiative recombination (RR) coefficient (ρ_{RR}) versus incident electron energy (ε) for Si^{6+} (from Hahn 1997). [nl: excited electronic state]

Dielectronic recombination (DR): In this two-step resonance process a continuum electron is firstly captured into a particular excitation level of an ion. The excess energy, which would have normally been used to emit a photon, as in RR, promotes another atomic/molecular electron to a particular energy level. These processes cause the atom/molecule to be placed in a very unstable, hence short lived ($10^{-11} - 10^{-14}$ s), doubly excited Auger unstable state (Hahn 1997). The doubly excited atom/molecule can then de-excite through photon emission, leaving the atom/molecule in an singly excited Auger stable state that may further de-excite to ground level through multi-step photon emissions (radiative cascade). The doubly excited atom/molecule can

also relax by either: (i) Reverting back to a singly excited ionic state via autoionization/Auger emission (Appendix A-collision 66) followed by possible further de-excitation to ground state through subsequent autoionization/Auger emission and/or radiative cascades (known as resonant excitation (RE) (Hahn 1997)); (ii) Simultaneously emitting a photon of energy equal to the difference between the kinetic energy of the captured electron and the total energy of the doubly excited atom/molecule, followed by possible de-excitation from the doubly excited Auger unstable state to ground state via autoionization/Auger emission and/or radiative cascades (known as radiative dielectronic recombination (RDR) (Hahn 1997)). The DR and RE processes described above only occur at discrete resonance energies and hence produce discrete line spectra that is characteristic of the atom/molecule, provided that certain selection rules are satisfied. Conversely, RDR will produce a continuous emission spectrum that is proportional to the kinetic energy of the captured electron. If the doubly excited atom/molecule does further relax, through autoionization/Auger emission or radiative cascades, then discrete emission lines will be superimposed onto the continuous emission spectrum. Recombination coefficients for DR are of the order of 10^{-12} cm³/s (von Engel 1965, Hahn 1997). Hence, DR dominates RR by a factor of approximately 100. RE generally dominates greatly over DR, whereas the extent to which RDR operates is usually around 5% that of DR (Hahn 1997).

Three-body recombination (TBR): This process involves the simultaneous collision between either (i) a positive ion, neutral atom/molecule and a free electron, or (ii) a positive ion and two free electrons. In process (i) the positive ion neutralizes by capturing the free electron, placing it in a very short-lived excited state. The excess excitation energy carried by the neutralized ion (A), that would have normally been used to emit continuous radiation proportional to the initial kinetic energy of the captured electron, as in RR, is kinetically transferred to the neutral atom/molecule (B). The neutralized ion is then left in a singly excited Auger stable state that may

further relax through radiative cascades. Process (ii) is analogous to process (i) except the excess energy is kinetically carried away by the electron that remains uncaptured. At typical pressures employed in ESEM, TBR process (i) has been found to occur slowly and hence exhibits negligible cross sections (Nasser 1971). Conversely, TBR process (ii) occurs rather effectively relative to other mechanisms, exhibiting recombination rate coefficients, ρ_{TBR} , of the order of $10^{-12} - 10^{-10}$ cm³/s (von Engel 1965).

Dissociative recombination (DSR): In this process a molecular ion captures a free electron causing the neutralized ion to dissociate, in a time less than one period of molecular vibration (von Engel 1965), into two or more Auger stable neutral atoms. Any excess energy involved in the reaction is used to increase the translational kinetic energies of the resulting neutrals. The neutrals may de-excite via radiative cascades if permitted. Dissociative recombination coefficients (ρ_{DSR}) are of the order of 10^{-7} cm³/s (Nasser 1971) which implies that this mode of recombination largely dominates the other SE-ion recombination mechanisms. It has been found that atomic gases (*e.g.* the inert or rare gases), that energetically prefer to exist in a monatomic state in an ionized gas environment, due to bonding constraints, are capable of associating or forming molecules through charge transfer collisions. Consequently, DSR can occur at a significant level in such gases. DSR rate coefficients for atomic gases are of the order of 10^{-10} cm³/s (von Engel 1965). Figure 4.2 shows typical magnitudes of ρ_{DSR} versus ε , acquired at various electron number densities. The figure once again illustrates the exponentially decreasing rate of SE-ion recombination with increasing electron energy.

In an ESEM, PIs generated in the gas cascade drift and diffuse away from the GSED ring, under the action of the electric field (E), and can recombine with (i) ‘thermalized’ (low energy electrons in the sample at or below the Fermi level) and ‘hot’ (electrons excited by primary electrons (PEs) and backscattered electrons (BSEs))

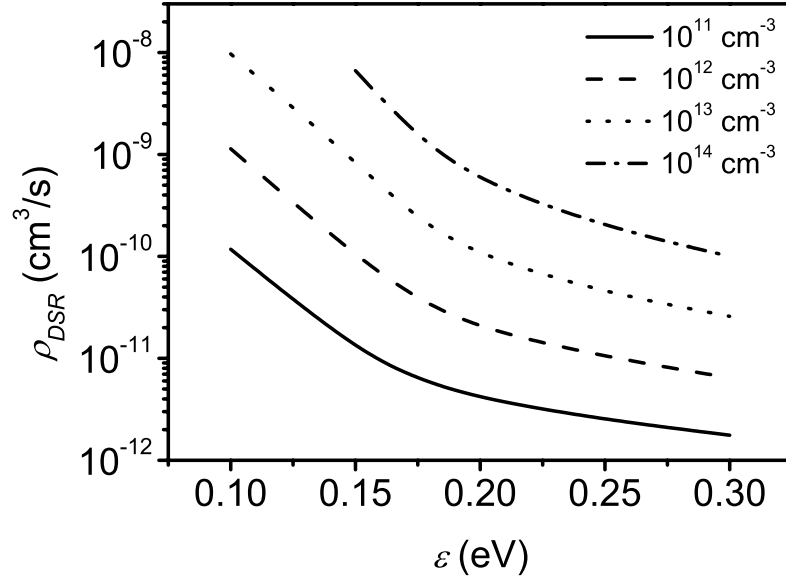


Figure 4.2: Dissociative recombination (DSR) coefficient (ρ_{DSR}) versus incident electron energy (ϵ) at various electron number densities (n_e) (adapted from Nasser 1971).

electrons at the sample surface (Hagstrum 1978), (ii) electrons in the chamber walls and surrounding parts of the microscope and (iii) sample emissive or free electrons in the gas, as described above (von Engel 1965, Hahn 1997, Nasser 1971). The probability of processes (i) and (ii) occurring depends on the electronic properties of the surface and the ion, and the surface-ion distance (Hagstrum 1978). The efficiency at which ions recombine with free electrons in the gas rapidly decreases with increasing electron kinetic energy, as seen previously in figures 4.1 and 4.2 (von Engel 1965, Hahn 1997, Nasser 1971). Consequently, recombination events between ions and electrons possessing high kinetic energies (ϵ), such as PEs ($1 \leq \epsilon_{PE} \leq 30$ keV) and BSEs ($\epsilon_{BSE} \gtrsim 0.5\epsilon_{PE}$) (Reimer 1985), can be considered negligible compared to that of with low energy SEs, which are emitted from the surface with energies of 2 – 5 eV

(Reimer 1985). SEs emitted from the sample surface are accelerated by the field up to energies in excess of 100 eV (Thiel *et al.* 1997). Therefore, SE-ion recombination will only be significant close to the sample surface, where the energy of SEs is minimized.

SE-ion recombination has previously been shown to inhibit sample emissive SE signals and hence gas amplification, causing ‘edge-darkening’ effects at topographical asperities on the surface of conductors (Toth *et al.* 2002d) as well as darkening or ‘inverse contrast’ at localized regions of elevated surface charge density in dielectric materials (Toth *et al.* 2002b). At topographical asperities or localized regions of elevated negative charge density the electric field generated by V_{GSED} locally maximizes producing strong lines of force for ions to follow. Provided that the detector field strength is high and the mean free path for ion-gas phase scattering is long (i.e. low p) then ions will follow these lines of force (also referred to as ‘ion focusing’) and will accumulate above the asperities or charged regions, causing a localized enhancement of the SE-ion recombination rate and a corresponding reduction in the number of SEs that are subsequently capable of being multiplied in the gas cascade. It has been demonstrated that the loss of signal as result of these lateral inhomogeneities in ion flux can be minimized by inserting a grounded wire mesh in the vicinity of the sample surface (Craven *et al.* 2002, Toth *et al.* 2002b). The mesh provides a more efficient path to ground for the ions, enhancing the ionic recombination efficiency within the gap.

In order to account for the effects of SE-ion recombination on gas amplification the secondary electron coefficient, encountered previously in equations (3.11.4) and (3.11.6)-(3.11.11), needs to be replaced by an ‘effective’ SE coefficient that includes the fraction of emitted SEs that are captured by ions prior to entering the gas cascade:

$$\delta_{eff} = (1 - \bar{\Omega})\delta \quad (0 < \bar{\Omega} < 1). \quad (4.2.3)$$

Here $\bar{\Omega}$ is the average probability that a sample emissive SE will be captured by an

ion and δ is the true SE yield of the sample (Toth *et al.* 2002a). $\bar{\Omega}$ being proportional to the overlap of the spatial distributions of SEs and ions in the SE-ion recombination volume,

$$\bar{\Omega} = \rho \int_0^{z_\Omega} \int_{-\infty}^{\infty} \int_{-\infty}^{\infty} n_e \times n_i dx dy dz, \quad (4.2.4)$$

where ρ is a recombination coefficient, $0 \leq z \leq z_\Omega$ defines the SE-ion recombination volume in the z plane, and n_e and n_i are the electron and ion number densities, respectively (Toth *et al.* 2002a).

4.3 Transient SE-Ion Recombination Model

This section derives an expression for the transient signal produced by the GSED electronics as a function of time immediately after a region of high electron emission is scanned upon by the PE beam. These derivations are based on the assumptions that: (i) The number density (particles per unit volume) of electrons, n_e , between the sample and the ring is always equal to the number density of positive ions (PIs), n_i . This assumption is based on the premises that all ions generated in the gas cascade are singly ionized and each recombination event neutralizes a single ion, and ionization cross sections for the production of negative ions in H_2O are sufficiently small and hence ion-ion recombination can be considered negligible; (ii) The average velocity of PEs and BSEs is sufficiently high that their probability of recombination with PIs can be considered negligible. Therefore, recombination is only taking place between PIs and low energy electrons emitted from the sample surface or generated in gaseous ionization events; (iii) There are no space charges present. The derivations take into consideration the transient effects of the total time constant (RC) associated with the GSED electronics and external circuitry.

The rate at which electrons exit the gas as a consequence of electron-ion recombination, the recombination rate, is proportional to the absolute values of $n_e(t)$ and $n_i(t)$ and therefore can be described by the second order rate equation

$$\left\{ \frac{dn_e(t)}{dt} \right\}_{rec} = -\rho n_e(t) n_i(t), \quad (4.3.1)$$

where ρ , the proportionality constant, is defined as the SE-ion recombination coefficient, which has dimensional units of L^6T^{-1} , where L is length and T is time (von Engel 1965, Nasser 1971). The negative sign in equation (4.3.1) indicates that electrons are lost through recombination processes. Letting $n_i(t) = n_e(t) = n(t)$, from

assumptions (i) and (ii) stated above, equation (4.3.1) becomes

$$\left\{ \frac{dn(t)}{dt} \right\}_{rec} = -\rho [n(t)]^2. \quad (4.3.2)$$

The rate at which electrons are generated in the gas cascade as a result of ionization of gas molecules by SEs, PEs and BSEs, the ionization rate, can be determined from the ionization current (equation (3.11.6)) divided by the charge of each electron (e), which arises from the fact that $dn/dt = (1/e)dq/dt$. As equation (3.11.6) is the ionization current at steady state, whereby cascading electrons have traversed the total gap distance ($z = d$), equation (3.11.6) needs to be modified by also replacing d_{eff} with $v_e t$, giving the ionization rate as

$$\left\{ \frac{dn(t)}{dt} \right\}_{ion} = \frac{kI_{PE} (e^{\alpha_{ion}^{sw} v_e t} - 1)}{e} \left\{ \frac{S_{PE} p}{\alpha_{ion}^{sw}} + \frac{\eta S_{BSEP}}{\alpha_{ion}^{sw}} \left(\frac{\bar{d}_{BSE}}{d} \right) + \delta \right\}. \quad (4.3.3)$$

Here, α is the first Townsend coefficient; S_{PE} and S_{BSE} are the ionization efficiencies of PEs and BSEs, respectively; I_{PE} is the primary electron beam current; η and δ are the BSE and SE yields, respectively; p is the sample chamber pressure; k is a feedback factor and v_e is the drift velocity of the cascading electrons. Under the assertions that: (i) The time taken for electrons to traverse the entire gap distance, the electron transit time (Γ_e), is much smaller than the pixel dwell time (τ_p) and hence a multitude of avalanches have been developed such that a large number of electrons are collected by the ring at each pixel point continuously and uniformly; (ii) Lateral variations in charge density and topography on the surface of the sample are negligible after the pre-irradiated enhanced contrast region is scanned by the PE beam, and hence δ remains unchanged; (iii) The average path length of BSEs is equal to the effective gap distance and hence \bar{d}_{BSE}/d is equal to unity; (iv) The cascading electrons acquire a steady state Maxwellian distribution of kinetic energies in a negligible distance from the sample surface and therefore $d_{eff} = d$; it can be seen that the ionization rate will

be equal to its limiting value of that at $t = \tau_p$:

$$\left\{ \frac{dn(t)}{dt} \right\}_{ion} = \frac{kI_{PE} (e^{\alpha_{ion}^{sw} d} - 1)}{e} \left\{ \frac{S_{PEP}}{\alpha_{ion}^{sw}} + \frac{\eta S_{BSEP}}{\alpha_{ion}^{sw}} + \delta \right\}. \quad (4.3.4)$$

The net rate at which SEs traverse the gap and are subsequently capable of reaching the GSED ring as a current signal will be equal to the summation of the ionization and recombination rates:

$$\left\{ \frac{dn(t)}{dt} \right\}_{net} = \left\{ \frac{dn(t)}{dt} \right\}_{ion} + \left\{ \frac{dn(t)}{dt} \right\}_{rec}. \quad (4.3.5)$$

Substituting equations (4.3.2) and (4.3.4) into above yields

$$\left\{ \frac{dn(t)}{dt} \right\}_{net} = \frac{kI_{PE} (e^{\alpha_{ion}^{sw} d} - 1)}{e} \left\{ \frac{S_{PEP}}{\alpha_{ion}^{sw}} + \frac{\eta S_{BSEP}}{\alpha_{ion}^{sw}} + \delta \right\} - \rho [n(t)]^2. \quad (4.3.6)$$

Equation (4.3.6) is more conveniently expressed by replacing the term for the ionization rate with the constant ψ :

$$\left\{ \frac{dn(t)}{dt} \right\}_{net} = \psi - \rho [n(t)]^2. \quad (4.3.7)$$

Solution of the differential equation above, with the boundary condition, $n(0) = n_0$, gives the net number density of electrons traversing the gap to be

$$n(t) = \sqrt{\frac{\psi}{\rho}} \tanh \left[\sqrt{\psi \rho} t + \operatorname{arctanh} \left(\sqrt{\frac{\rho}{\psi}} n_0 \right) \right]. \quad (4.3.8)$$

As the drift velocity of electrons traversing the gap is typically three orders of magnitude greater than that of ions (von Engel 1965, Nasser 1971), the current signal induced in the GSED ring by the drifting ions will be much smaller than that of electrons and therefore can be considered negligible. Substituting equation (4.3.8) into equation (2.4.4), assuming that the volume in which ionization takes place is constant and hence number densities can be replaced by absolute numbers, gives the current signal induced in the GSED ring, which is subsequently converted to a voltage signal by the GSED electronics to produce images, as

$$I_{GSED}(t) = \frac{ev_e}{d} \sqrt{\frac{\psi}{\rho}} \tanh \left[\sqrt{\psi \rho} t + \operatorname{arctanh} \left(\sqrt{\frac{\rho}{\psi}} n_0 \right) \right], \quad (4.3.9)$$

where v_e is the drift velocity of electrons in the cascade. It is worth noting that Γ_e can also be determined from the above equation. Γ_e being equal to the ratio of d and v_e .

The next step in developing the model is to derive an expression for the relative magnitude of the output voltage signal ($V_S(t)$) that the GSED electronics produces, taking into consideration the total time constant of the GSED electronics and external circuitry, RC , which includes (i) the time constant or clipping time of the GSED electronics, R_1C_1 , which comprises the time constant of low-pass noise filters, RC_{nf} , used to extract high frequency shot and thermal noises (Philips Electron Optics 1997), and the time constant due to the input resistance and capacitance of the GSED electronics; and (ii) the time constant associated with coaxial cables used to transmit signals, R_4C_4 , as illustrated in figure 2.13.

The GSED electronics or any current-to-voltage amplifier system connected to a current carrying electrode can be approximated as a distributed series resistance (R) shunted by an unavoidable distributed capacitance (C) acting in parallel, as illustrated by the equivalent circuit diagram of the GSED detection system in figure 4.3. The output voltage signal produced by the current induced in the electrode, $I_{GSED}(t)$, being proportional to the voltage generated across the resistor-capacitor element. By considering figure 4.3 it can easily be seen that the voltage drop across R will be equal to the voltage drop across C , hence

$$I_R(t) R = \frac{Q(t)}{C}, \quad (4.3.10)$$

where $I_R(t)$ is the current through R and $Q(t)$ is the total charge stored in C . Taking the time derivative of equation (4.3.10) gives

$$\frac{dI_R(t)}{dt} RC = I_C(t), \quad (4.3.11)$$

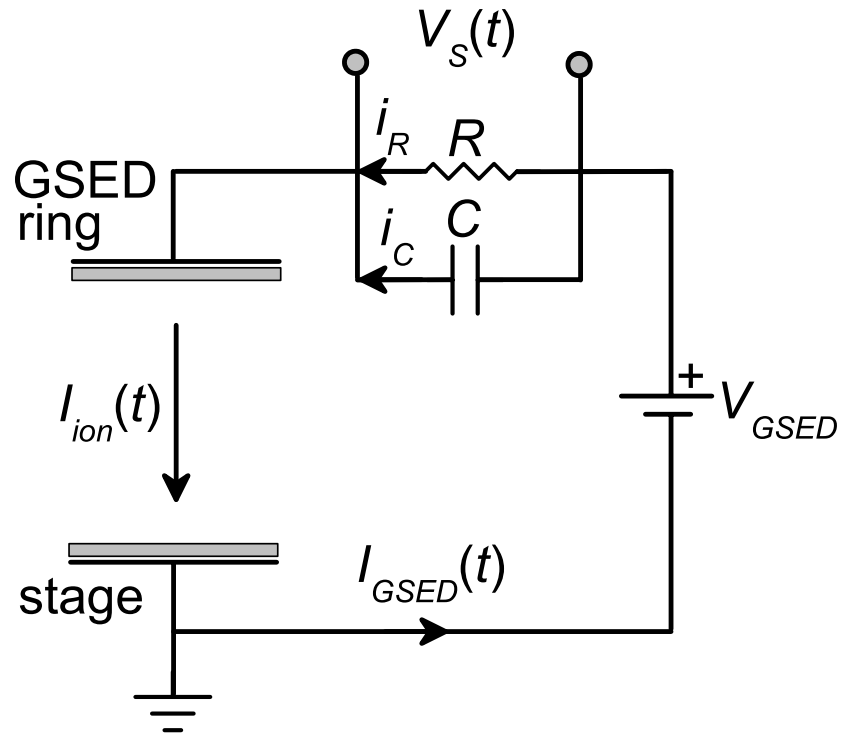


Figure 4.3: Equivalent circuit diagram of the gaseous secondary electron detector (GSED) system of total distributed time constant (RC). RC being equal to the summation of the time constant of the GSED low-pass noise filters, RC_{nf} , the time constant due to the input resistance and capacitance of the GSED electronics, and the time constant associated with coaxial cables used to transmit signals, R_4C_4 . [$I_{GSED}(t)$ =induced GSED current, $I_{ion}(t)$ =ionization current, $V_S(t)$ = output voltage signal]

where $I_C(t)$ is the displacement current due to the distributed capacitance. Kirchoff's current law shows that the displacement current will be equal to

$$I_C(t) = I_{GSED}(t) - I_R(t), \quad (4.3.12)$$

and therefore it can be seen from equations (4.3.11) and (4.3.12) that

$$RC \frac{dI_R(t)}{dt} + I_R(t) = I_{GSED}(t). \quad (4.3.13)$$

Substituting equation (4.3.9) into equation (4.3.13) yields

$$RC \frac{dI_R(t)}{dt} + I_R(t) = \frac{ev_e}{d} \sqrt{\frac{\psi}{\rho}} \tanh \left[\sqrt{\psi \rho} t + \operatorname{arctanh} \left(\sqrt{\frac{\rho}{\psi}} n_0 \right) \right]. \quad (4.3.14)$$

Solving the above differential equation with the assertion that the enhanced SE emission region is sufficiently long that at the leading edge of the streaks ($t = 0$) steady state conditions have been attained whereby the displacement current is zero, hence, $I_R(0) = I_{GSED}(0) = ev_e n_0 / d$, gives

$$I_R(t) = \frac{ev_e}{RCd} e^{-t/RC} \left\{ \sqrt{\frac{\psi}{\rho}} \int_0^t e^{v/RC} \tanh \left[\sqrt{\psi \rho} v + \operatorname{arctanh} \left(\sqrt{\frac{\rho}{\psi}} n_0 \right) \right] dv + RC n_0 \right\}. \quad (4.3.15)$$

As $V_S(t) = I_R(t)R$, the voltage signal produced at the output of the GSED will be

$$V_S(t) = \frac{ev_e}{Cd} e^{-t/RC} \left\{ \sqrt{\frac{\psi}{\rho}} \int_0^t e^{v/RC} \tanh \left[\sqrt{\psi \rho} v + \operatorname{arctanh} \left(\sqrt{\frac{\rho}{\psi}} n_0 \right) \right] dv + RC n_0 \right\}. \quad (4.3.16)$$

When $t \geq RC$ the integral in equation (4.3.16) is equal to

$$RC e^{t/RC} \tanh \left[\sqrt{\psi \rho} t + \operatorname{arctanh} \left(\sqrt{\frac{\rho}{\psi}} n_0 \right) \right],$$

and therefore $V_S(t)$ reduces to

$$V_S(t) = \frac{ev_e R}{d} \left\{ \sqrt{\frac{\psi}{\rho}} \tanh \left[\sqrt{\psi \rho t} + \operatorname{arctanh} \left(\sqrt{\frac{\rho}{\psi}} n_0 \right) \right] + n_0 e^{-t/RC} \right\}. \quad (4.3.17)$$

As $V_S(t)$ is directly proportional to the GSED output video signal and hence the greyscale intensity (GSI) of image pixels, multiplying equation (4.3.17) by a proportionality constant will enable it to be expressed as a function for the relative magnitude of the GSI signal, $GSI(t)$. However, it can be seen from the number of unknown variables in equation (4.3.17) that if absolute values of ψ , ρ and v_e are to be computed from experimental GSI profiles of the streaks formed in GSED images that (i) the proportionality constant ascribed above needs to be determined, (ii) an exact expression relating the input current of the GSED preamplifier circuit to the output voltage needs to be experimentally derived and (iii) an absolute value of n_0 or R needs to be initially estimated. As criteria (ii) and (iii) stated above are difficult to determine accurately, the present work is only concerned with the relative magnitudes of ψ , ρ and v_e rather than absolute values. Equation (4.3.17) can therefore be expressed as a concise function for the relative magnitude of the transient GSI signal by simply setting n_0 , R , e and d to arbitrary values of unity:

$$GSI(t) \propto v_e e^{-t/RC} + \sqrt{\frac{\psi}{\rho}} \tanh \left[\sqrt{\psi \rho t} + \operatorname{arctanh} \left(\sqrt{\frac{\rho}{\psi}} \right) \right]. \quad (4.3.18)$$

Equation (4.3.18) allows the relative magnitudes of ψ , ρ and v_e to be determined from experimentally obtained GSI profiles of the streaks seen in GSED images, and thence investigated as a function of microscope operating parameters. Although only relative values of ψ , ρ and v_e are achievable, equation (4.3.18) enables absolute values of RC to be determined.

The rate at which electron-ion recombination takes place will initially be maximized at the start of the streaks as a result of the large concentration of ions generated

during the scanning of the enhanced region. The recombination rate will then decrease, due to the dissipation of the ions as a result of electron-ion recombination in the gas and at chamber walls, ion-ion repulsion, and ion-molecule scattering; becoming equal to the ionization rate at the end of the streaks. It is obvious, from the aforementioned, that the magnitude of the recombination rate will always be greater than the magnitude of the ionization rate throughout the entirety of the streaks. The relative magnitude of the recombination rate ($\zeta(t)$) will therefore be equal to

$$\zeta(t) = \psi + \frac{dn(t)}{dt}. \quad (4.3.19)$$

Differentiating equation (4.3.8) with respect to time and inserting into equation (4.3.19) yields:

$$\zeta(t) = \psi \left\{ 1 + \operatorname{sech}^2 \left[\sqrt{\psi \rho} t + \operatorname{arctanh} \left(\sqrt{\frac{\rho}{\psi}} \right) \right] \right\}. \quad (4.3.20)$$

Therefore, once values of ψ and ρ have been determined, from fits of equation (4.3.18) to experimental $GSI(t)$ data, profiles of $\zeta(t)$ can easily be generated.

4.4 Experimental Techniques

Experiments were performed using a tungsten filament FEI-Philips XL 30 ESEM[®] equipped with a GSED. A 2 MHz bandwidth GW Electronics type-31 specimen current amplifier (GW Electronics Inc. 1988) was used to obtain ISC images. The induced stage current was collected from the microscope's conducting stage through a 75 Ω impedance coaxial cable and was electrically inverted by the specimen current amplifier. Electronic inversion of the ISC images ensured that contrast in ISC images could be directly compared to GSED images. Alumina, polished to an optical finish using diamond abrasives, was used as the sample and H₂O was used as the imaging gas throughout all experiments.

The PE beam used to generate GSED and ISC images was maintained at a constant energy of $\varepsilon_{PE} = 30$ keV and constant current of $I_{PE} = 5$ nA throughout all sets of measurements. I_{PE} was measured by grounding the GSED ring and reducing p_{H_2O} to 0.1 torr (minimum pressure obtainable in low vacuum mode). The PE beam (in spot mode) was then placed into the axial center of the depletion region of a cross-sectioned silicon $p - n$ junction diode. The n side of the diode was connected to microscope ground and the p side grounded through a Keithley 617 programmable electrometer that enabled the electron beam induced current (EBIC) to be read. The constant EBIC current used in experiments was converted to an I_{PE} value after the gain of the diode was calculated in high vacuum by measuring the ratio of the EBIC to the current read from a grounded Faraday cup.

Circular regions of enhanced SE emission were created using spot mode irradiation for 30 seconds at $p_{H_2O} = 1$ torr to fill deep charge traps. These parameters were selected to ensure that sufficient charge was implanted in the alumina sample without inducing dielectric breakdown. Each individual set of experiments (i.e. streaking versus (i) V_{GSED} , (ii) p_{H_2O} etc.) was performed swiftly to ensure that any charge

leakage from the enhanced SE region was kept to a minimum. A new enhanced SE spot was created prior to each individual set of experiments at a previously non-irradiated area of the sample to ensure that any charge accumulation on the alumina surface during image acquisition did not affect results.

4.4.1 Measurement of Electronic Gas Amplification

Assuming every electron that is (i) generated in the gas cascade and (ii) emitted from the sample surface is collected by the GSED ring then the rate of flow of electrons from the ring to the GSED preamplifier is (Farley & Shah 1991)(see figure 2.13):

$$I_{GSED} = I_{ion} + I_{PE} (\eta + \delta). \quad (4.4.1)$$

The second term in the above equation is the sum of the steady state SE and BSE emissive currents induced in the GSED ring under high vacuum conditions.

Gaseous electronic amplification (A_e) is defined here as the total number of environmental secondary electrons (ESEs) or PIs produced in the cascade between the sample and the GSED ring per electron entering the cascade. As the current of ESEs produced in the gap is I_{ion} and the current of electrons liberated from the sample is $I_{PE} (\eta + \delta)$, it can easily be seen that

$$A_e = \frac{I_{ion}}{I_{PE} (\eta + \delta)} = \frac{I_{GSED}}{I_{PE} (\eta + \delta)} - 1. \quad (4.4.2)$$

As the rate of electron flow into the GSED preamplifier is directly proportional to the GSED output video signal and hence the greyscale intensity (GSI) of image pixels, the current terms in the expression above can be replaced by GSI terms. Assuming that minimal gas ionization occurs at $p_{H_2O} \leq 0.1$ torr (the lowest chamber pressure obtainable in an ESEM operating in low vacuum mode) and $V_{GSED} = 0$ V (grounded), and hence I_{ion} can be considered negligible, then from equation (4.4.1), I_{GSED} will

be equal to $I_{PE}(\eta + \delta)$ and

$$A_e = \frac{\text{MGSI}(V_{GSED}, p_{H_2O}, d)}{\text{MGSI}(p_{H_2O} \leq 0.1 \text{ torr})} - 1, \quad (4.4.3)$$

where $\text{MGSI}(V_{GSED}, p_{H_2O}, d)$ is the mean greyscale intensity (MGSI) of pixels of a homogeneous contrast region within GSED images at a specific pressure, detector bias or sample-electrode distance *etc.*; and $\text{MGSI}(p_{H_2O} \leq 0.1 \text{ torr})$ is the MGSI of the same region at $p_{H_2O} = 0.1 \text{ torr}$ and $V_{GSED} = 0 \text{ V}$.

Steady state gaseous electronic amplification (A_e) curves, acquired as a function of the various microscope operating parameters were obtained using equation (4.4.3), shown above. The MGSI of homogeneous contrast regions within GSED images, needed to calculate gas amplification, were measured using Scion Image (Scion Corporation 2000) at a 256×256 pixel ($26 \times 26 \mu\text{m}$) region far away from the enhanced SE emission region. Prior to image acquisition, and subsequent amplification measurements, the PE beam was switched off with the GSED ring grounded and the GSED brightness set to a value that gave an image MGSI of zero in order to eliminate any DC background signal from images. It must be noted that the electronic amplification profiles used here were not intended to provide new accurate data on gas gain but to merely aid in the interpretation and relative trends in results. Hence, the crude assumption that minimal gas ionization occurs at $p \leq 0.1 \text{ torr}$. There is a good correlation between the electronic amplification data presented hereafter and existing models of gas amplification (Fletcher *et al.* 1997), hence, the assumption that minimal gas ionization occurs at $p_{H_2O} \leq 0.1 \text{ torr}$ seems valid.

The advantage of using equation (4.4.3) to measure electronic gas amplification is that unlike previous methods used, which measured electronic amplification from the stage using a purpose built Faraday cup (Fletcher *et al.* 1997, Meredith *et al.* 1996, Thiel *et al.* 1997), the coefficients η and δ do not need to be estimated. Furthermore, electronic gas amplification can be measured quickly and easily directly

from any conducting or insulating sample provided that the PE energy, PE current and brightness in GSED images remains constant.

4.4.2 Determination of Recombination Coefficients, Recombination Rates, Ionization Rates, Electron Drift Velocities and Time Constants

Transient profiles of the streaks produced in GSED images were generated by measuring the GSI of each pixel parallel to the PE beam scan direction in line with the radial center of the enhanced SE spots using Scion Image (Scion Corporation 2000). The time (t) scales shown on the lower axis of the streak profiles were generated by dividing the line scan time (τ_L) by the number of pixels in the horizontal plane of the image. The trailing edge of the enhanced contrast regions or leading edge of streaks was taken to be $t = 0$. All images were acquired at a horizontal field width, $HFW = 73 \mu\text{m}$, with a 712 pixel width and total number of lines per frame, $N_f = 484$. The contrast within each of the streak profiles were not altered or normalized.

The relative magnitude of the recombination coefficient (ρ), ionization rate (ψ) and electron drift velocity (v_e) at a certain microscope operating point (*e.g.* p_{H_2O} , V_{GSED} , d , *etc.*) were determined by fitting equation (4.3.18), theoretically derived in section 4.3, to the transient GSI streak profiles. Equation (4.3.18) also enabled the total time constant (RC) of the GSED electronics and external circuitry to be absolutely measured. Transient profiles of the relative magnitude of the recombination rate ($\zeta(t)$) were simulated by substituting the values of ρ and ψ obtained into equation (4.3.20).

Streak profiles, recombination coefficients, ionization and recombination rates, electron drift velocities and time constants were measured as a function of various microscope parameters such as V_{GSED} , d , p_{H_2O} , τ_L and reduced electric field (E/p_{H_2O}).

As the Philips XL 30 ESEM[®] measures WD from the electron gun pole piece, and the GSED ring sits 5.8 mm below the pole piece, d is equal to WD less 5.8 mm.

4.5 Preamble

PIs generated in the gas amplification process, due to their reduced mobility compared to that of electrons (von Engel 1965, Nasser 1971), are capable of building up to significant concentrations in the gap such that a positive space charge is generated in the vicinity of the sample surface (Farley & Shah 1990b, Toth & Phillips 2000a, Toth & Phillips 2000b, Toth *et al.* 2002c). The concentration of ions and hence the magnitude of the space charge being controlled by (i) the rate at which ions are generated in the cascade (the ion generation rate), (ii) the speed at which ions drift and diffuse through the gas, (iii) the rates at which ions can recombine with ‘thermalized’ and ‘hot’ electrons at the sample surface and chamber walls (the recombination efficiency) and (iv) the rate at which ions are lost in the gap as a result of SE-ion recombination, described previously in section 4.2.1 (Toth & Phillips 2000a, Toth & Phillips 2000b, Toth *et al.* 2002b, Toth *et al.* 2002c, Toth *et al.* 2002d). It has been reasonably predicted that the recombination efficiency when ions are incident on metal surfaces is greater than that of when ions are incident on insulating surfaces, and therefore the effects of ion buildup and space charge formation is expected to be more pronounced in insulating materials (Toth *et al.* 2002d). It has been shown that the buildup of PIs above the sample surface can not only reduce emissive SE signals, through ‘ion focusing’ described in section 4.2.1, but can also generate an electric field (E_{ion}) which (i) perturbs the intrinsic electric field in the gap generated by V_{GSED} between the GSED ring and sample surface, E_{GSED} (Toth *et al.* 2002b), and (ii) lowers the surface barrier of insulating materials through an extraction potential which increase the emission probability of low energy SEs (Toth *et al.* 2002b). The reduction of the net field in the gap, $E_{net} = E_{GSED} - E_{ion}$, has been proposed to reduce cascade amplification and hence the signal induced in the GSED ring and produce the streaking effects seen in GSED and ISC images (Toth & Phillips 2000a, Toth &

Phillips 2000b). Although an accumulation of excess PIs is undoubtedly present in the gap, there has been no direct quantitative evidence to suggest that the streaks seen after enhanced contrast regions are a result of field modification due to space charges alone, or at all, and that transient models of SE-ion recombination can be used to describe such a phenomenon.

Figures 4.4, 4.5, 4.6 and 4.7 show GSED images of alumina containing a spot of localized negative charge and its associated streak acquired as functions of p_{H_2O} and V_{GSED} , d , and τ_L , respectively. It can be seen that under conditions of high E/p_{H_2O} there is a pronounced suppression of signal from the bright pre-irradiated charged region, which is consistent with existing models of steady state SE-ion recombination and signal scavenging (Craven *et al.* 2002, Toth *et al.* 2002d). Furthermore, it can be noticed that when signal suppression is maximized in the charged region that there is a corresponding suppression of signal trailing the enhanced contrast region in the form of a dark streak. It can therefore be qualitatively predicated that the streaking effects seen can be attributed mostly to gaseous SE-ion recombination.

As the beam scans the enhanced contrast region the generation rate increases and as result a large concentration of PIs is produced in the chamber. Immediately after the enhanced region has been completely scanned there is a sudden drop in δ , as expected. However, as a result of the sample being insulating, and hence, the diminished recombination efficiency, as described above, the ions generated during the enhanced region have not had sufficient time to drift, diffuse and neutralize at the sample surface and chamber walls. Consequently, a large concentration of ions still exists in the chamber even after the enhanced region has been scanned upon which ‘scavenges’ sample emissive low energy SEs in the vicinity of the sample surface, effectively further reducing δ . The number of electrons capable of being amplified through ionization events and the cascade amplification process therefore drops and the net

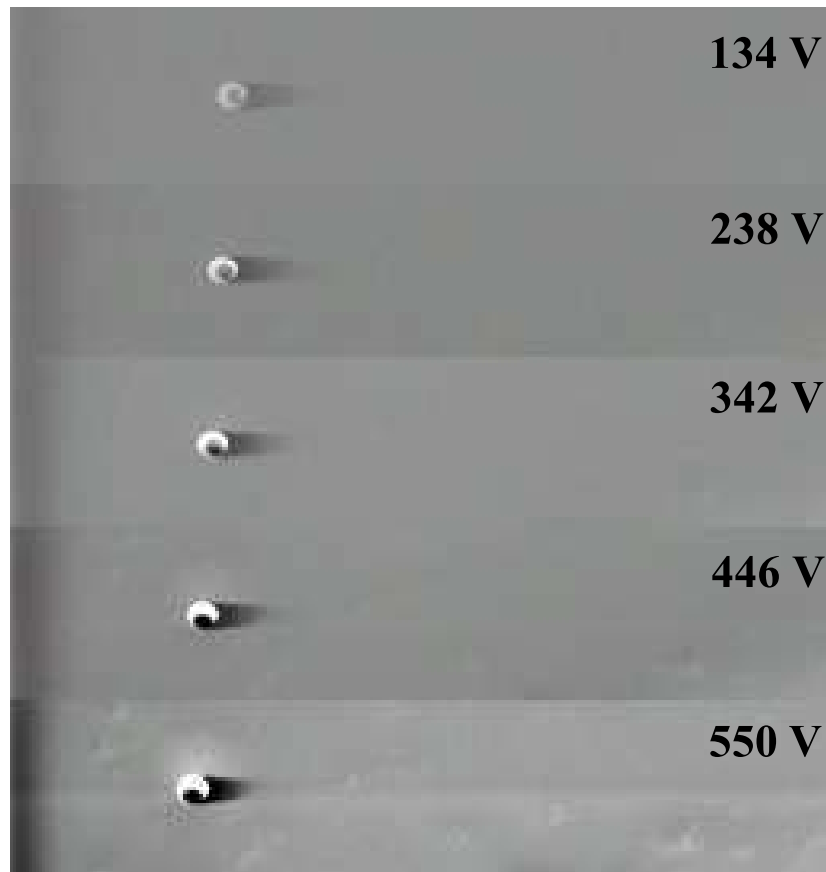


Figure 4.4: Streaking in gaseous secondary electron detector (GSED) images acquired as a function of GSED bias (V_{GSED}). [$p_{H_2O} = 0.7$ torr, $d = 9.2$ mm, $HFW = 73$ μm , $\tau_L = 120$ ms]

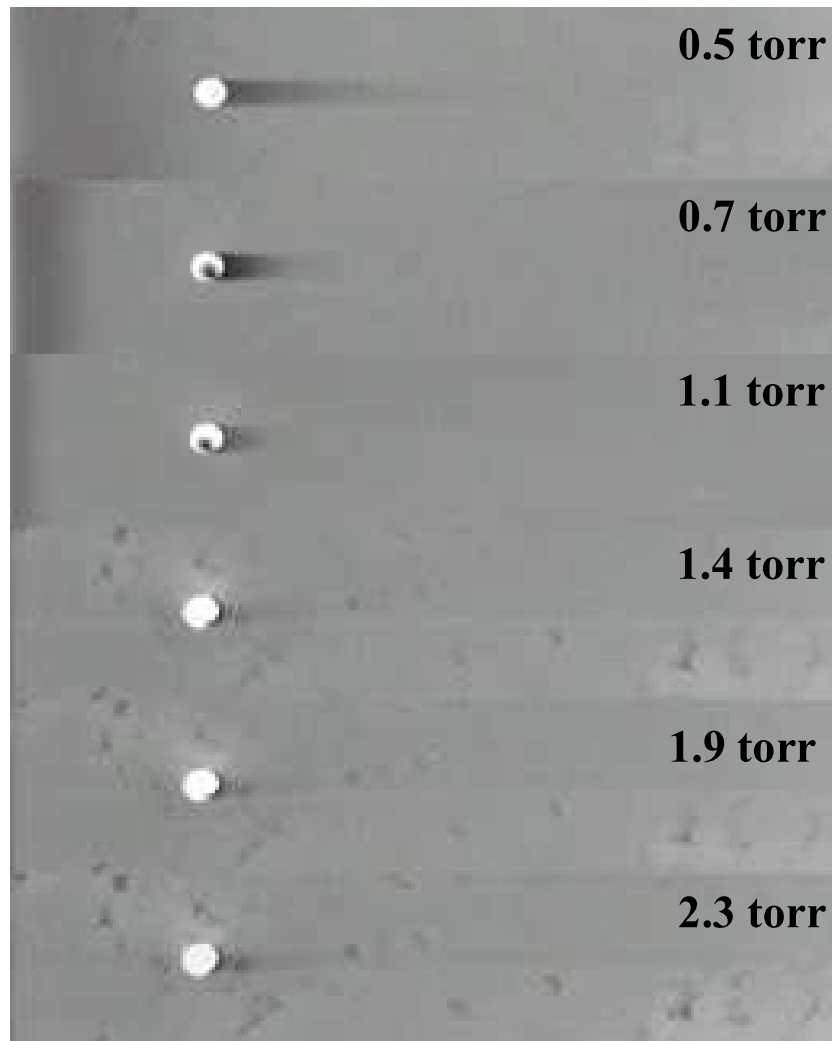


Figure 4.5: Streaking in gaseous secondary electron detector (GSED) images acquired as a function of water vapour pressure (p_{H_2O}). [$V_{GSED} = 342$ V, $d = 9.2$ mm, $FWM = 73$ μm , $\tau_L = 120$ ms]

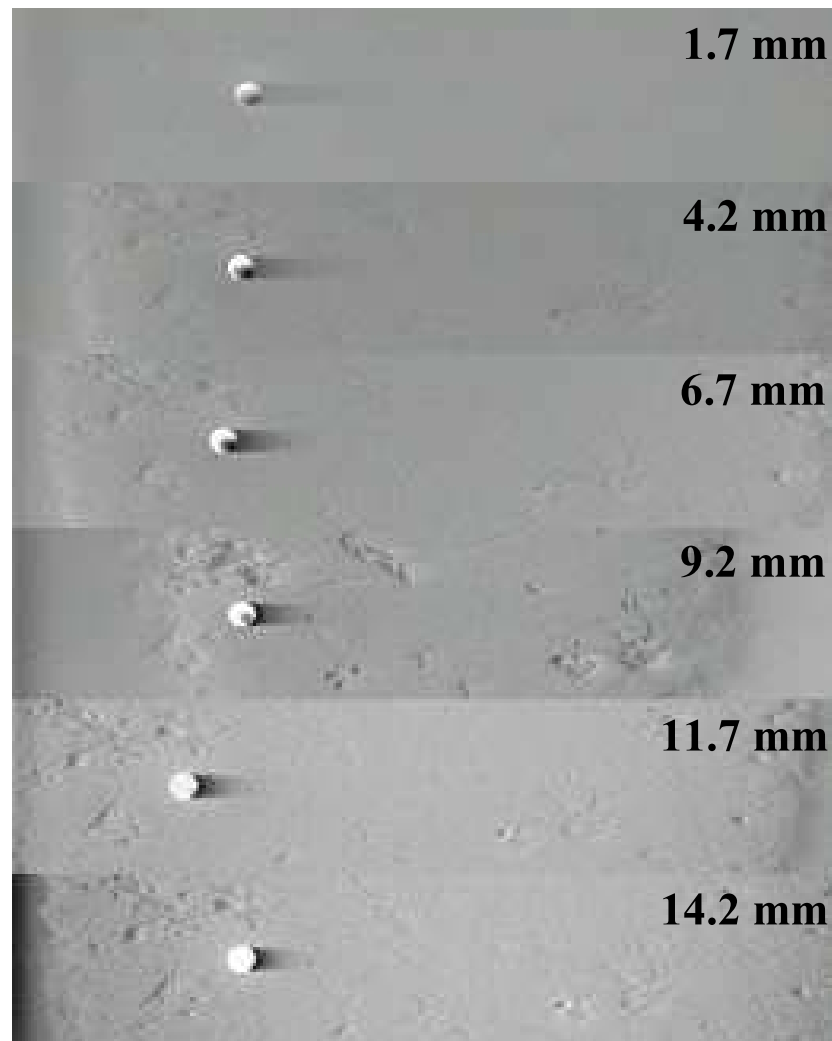


Figure 4.6: Streaking in gaseous secondary electron detector (GSED) images acquired as a function of sample-electrode separation (d). [$V_{GSED} = 342$ V, $p_{H_2O} = 0.7$ torr, $FWM = 73$ μm , $\tau_L = 120$ ms]

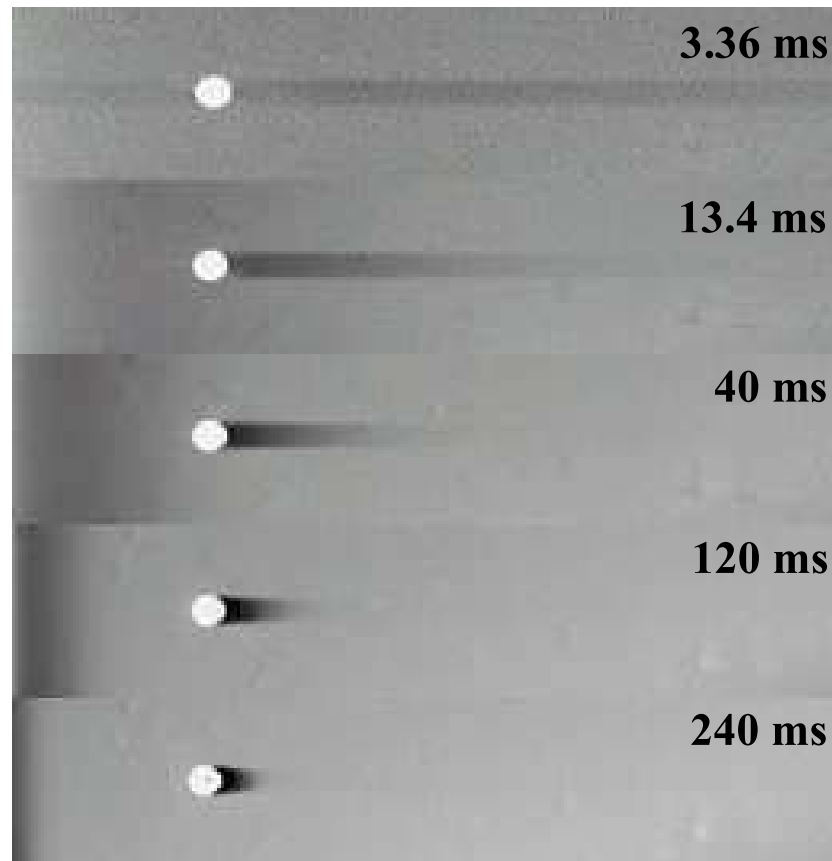


Figure 4.7: Streaking in gaseous secondary electron detector (GSED) images acquired as a function of line scan time (τ_L). [$V_{GSED} = 342$ V, $p_{H_2O} = 0.7$ torr, $d = 9.2$ mm, $FWM = 73$ μm]

electron signal traversing the gap, capable of inducing charge in the GSED ring, reduces. The reduction in signal generates a streak immediately after the enhanced region until steady state conditions are attained whereby the total rate of signal loss in the chamber (neutralization rate) is equal to the rate of signal generation (generation rate). The length of the streak obviously being controlled by (i) the speed at which ions can drift (ion drift velocity) and diffuse to the sample and chamber walls, (ii) the ion generation rate and (iii) the SE-ion recombination rate. All these parameters being affected by microscope operating parameters and reduced electric field.

To examine how the time constant of the electronics and external circuitry controls the degree of streaking in ESEM images, resistors of differing resistances, R_S , were placed in series between the stage and the specimen current amplifier used to generate ISC images. The dependency of R_S on the streaking produced in GSED images was not investigated as the signal cable between the ring and the GSED preamplifier could not be configured to accommodate a resistor without significantly altering the noise tracks used to reduce random and thermal noise in GSED images. Placing a resistor in series between the stage and the amplifier allowed the input resistance of the amplifier, hence the time constant of the particular detection system, to be varied in a controlled manner.

ISC images and their associated GSI profiles of an enhanced SE emission region, acquired as a function of R_S , are shown in figures 4.8 and 4.9, respectively. It can be seen that as R_S is raised from 0 Ω (no resistor in place) to 30 M Ω the time taken for the signal produced at the output of the ISC electronics to (i) reach steady state and (ii) to reach a minimum, τ_{min} , increases as R_S is raised. A plot of τ_{min} versus R_S in figure 4.10 shows the relationship to be linear. The increased time constant enhances the rate at which charge, induced by virtue of the motion of the carriers in the gap, accumulates on the electrode containing the added resistance. The processes

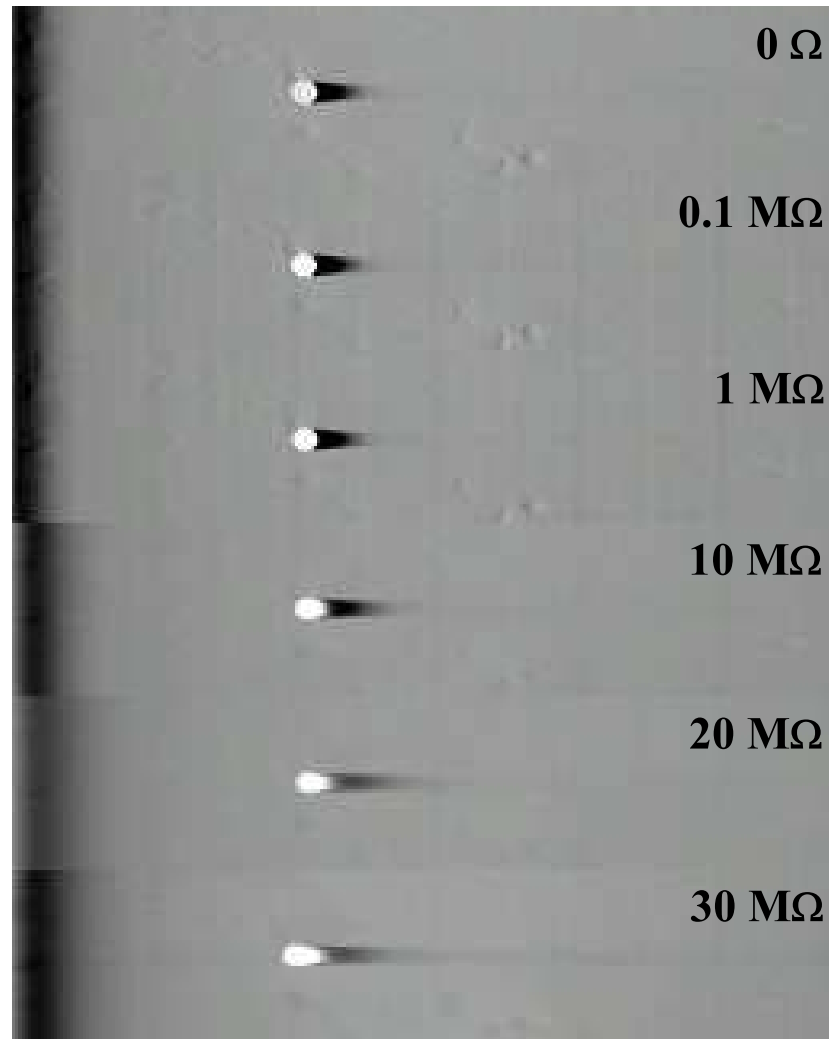


Figure 4.8: Streaking in induced stage current images (ISC) acquired as a function of series resistance (R_S). [$V_{GSED} = 342$ V, $p_{H_2O} = 0.7$ torr, $d = 9.2$ mm, $HFW = 73$ μm , $\tau_L = 120$ ms]

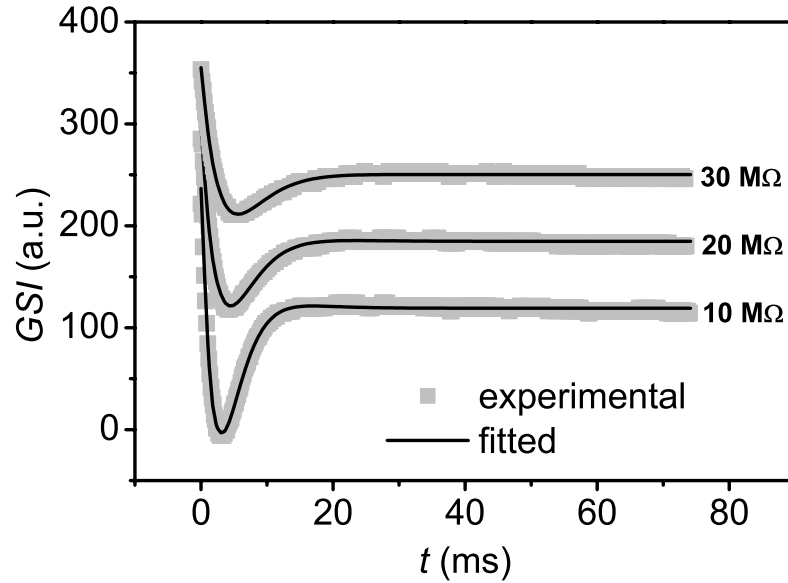


Figure 4.9: Profiles of greyscale intensity (GSI) versus time (t) acquired as a function of series resistance (R_S) in induced stage current (ISC) images. The dark lines show fits to experimental data using equation 4.3.18. [$V_{GSED} = 342$ V, $p_{H_2O} = 0.7$ torr, $d = 9.2$ mm, $\tau_L = 120$ ms]

occurring in the gas therefore cannot be measured as fast as they actually occur and therefore GSI profiles appeared elongated with respect to time. The contrast in the profiles also decreased as R_S was raised due to a reduction in the charge entering the ISC preamplifier per unit time as a consequence of the enhanced time constant.

The above clearly demonstrates that the time constant of the detection electronics effects the output signals produced in the form of images. Therefore, if information relating to processes that are occurring directly in the gas, such as recombination rates, ionization rates, recombination coefficients and drift velocities are to be determined then the time constant of the detection electronics needs to be incorporated into models on transient electron-ion recombination to account for such a phenomenon.

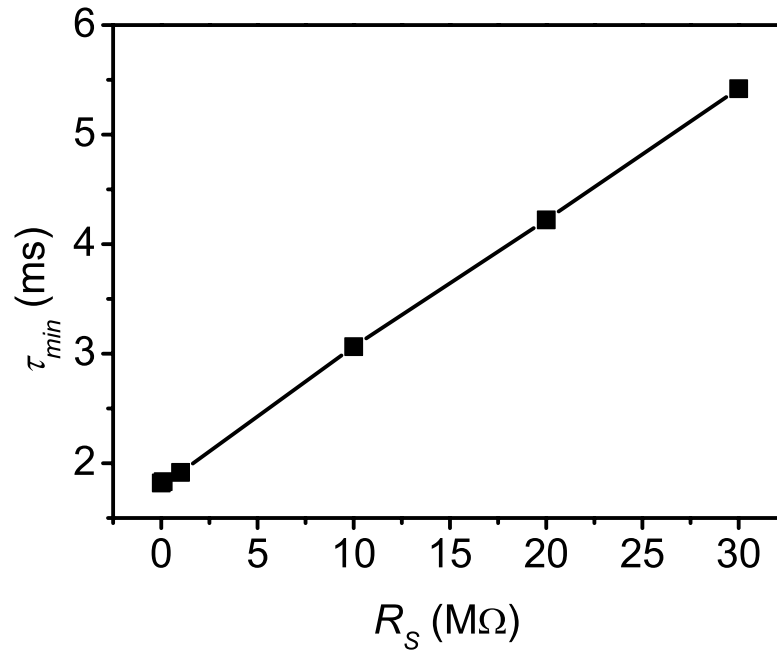


Figure 4.10: Minimum greyscale intensity (*GSI*) time (τ_{min}) of streaks in induced stage current (ISC) images versus series resistance (R_S). [$V_{GSED} = 342$ V, $p_{H_2O} = 0.7$ torr, $d = 9.2$ mm, $\tau_L = 120$ ms]

In order to demonstrate the aptness of the transient electron-ion recombination model, derived in section 4.3, the streak profiles in figure 4.9 were fitted using equation (4.3.18). It can be seen that there is a direct correlation between the experimental streak data obtained and the theoretical model over all series resistances. In fact, all of the experimental streak data simulated using equation (4.3.18) had a correlation coefficient, $R \geq 0.97$.

4.6 Results and Discussion

4.6.1 Generation Rates

Shown in figure 4.11 are plots of ψ versus (a) V_{GSED} , (b) p_{H_2O} , (c) d and (d) τ_L obtained from fits of equation (4.3.18) to the experimentally obtained GSI profiles of the GSED images shown in figures 4.4, 4.5, 4.6 and 4.7, respectively. It can be seen from the plots that ψ increases exponentially with V_{GSED} . An increase in V_{GSED} increases the average kinetic energy of electrons in the cascade, which enables them to reach the ionization potential (average energy required to ionize a gas molecule) of the imaging gas in shorter distances (Thiel *et al.* 1997, von Engel 1965). Consequently, there is an increase in the probability of ionization and the number of electrons and ions traversing the gap per unit time is enhanced.

Figure 4.11(b) shows that ψ increases with p_{H_2O} at $0.1 < p_{H_2O} < 3$ torr, reaches a maximum at $p_{H_2O} \sim 3$ torr, and then decreases with p_{H_2O} at $p_{H_2O} > 3$ torr. It can also be noticed from 4.11(b) that relative changes in the magnitude of ψ are largely dependent on p_{H_2O} . Increasing p_{H_2O} increases the number density of gas molecules in the chamber and hence initially enhances the probability of electron-gas molecule collisions and hence the probability of ionization. However, as p_{H_2O} is further increased, the concentration of gas molecules becomes significantly large that the distances traversed by SEs and ESEs, hence their energy acquired by the electric field between successive collisions with gas molecules, reduces, causing a subsequent decrease in the number of electrons above the ionization potential of the gas. As a consequence, the number of electrons traversing the gap per unit time is impeded and ψ decreases.

Figure 4.11(c) shows that ψ increases with a sigmoidal dependency on d . Increasing d increases the total path length that electrons traverse through the gas from

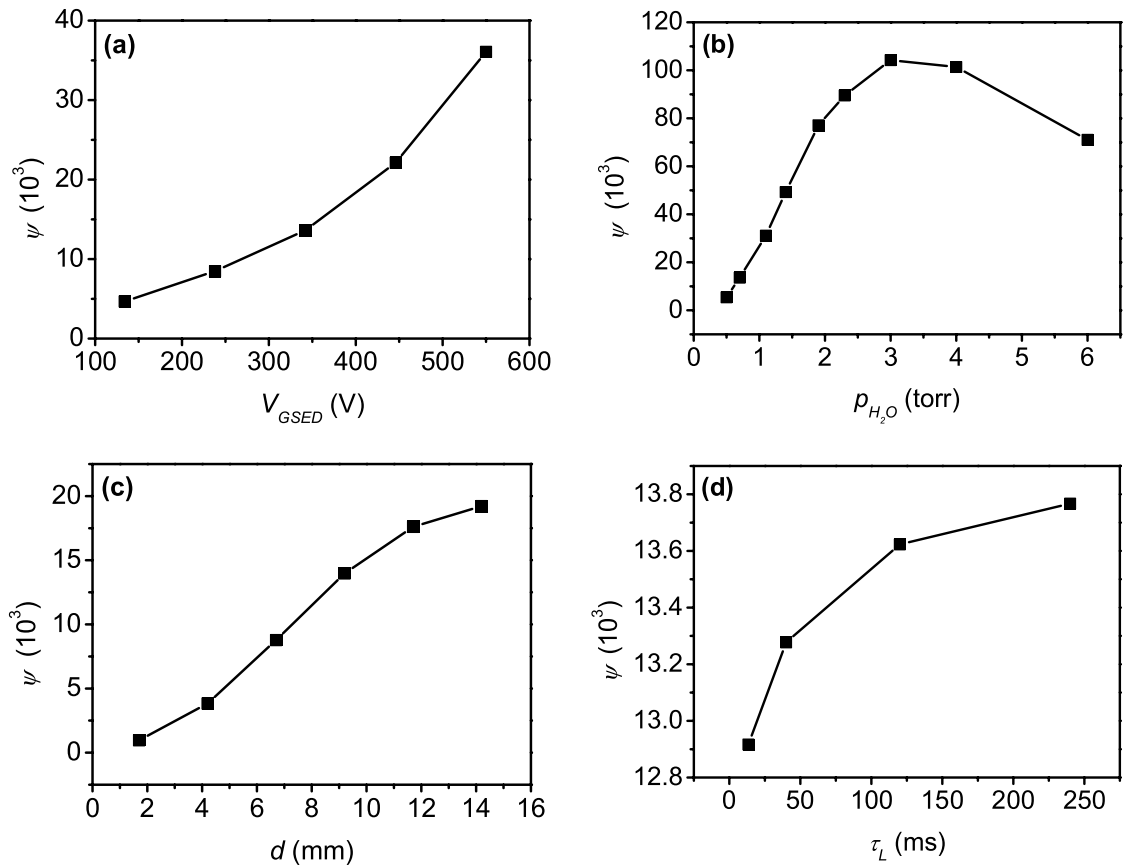


Figure 4.11: Ionization rate (ψ) versus (a) gaseous secondary electron detector (GSED) bias (V_{GSED}) [$p_{H_2O} = 0.7$ torr, $d = 9.2$ mm, $\tau_L = 120$ ms]; (b) water vapour pressure (p_{H_2O}) [$V_{GSED} = 342$ V, $d = 9.2$ mm, $\tau_L = 120$ ms]; (c) sample-electrode separation (d) [$V_{GSED} = 342$ V, $p_{H_2O} = 0.7$ torr, $\tau_L = 120$ ms] and (d) line scan time (τ_L) [$V_{GSED} = 342$ V, $p_{H_2O} = 0.7$ torr, $d = 9.2$ mm].

their point of production at the sample surface to their exit at the GSED ring. Assuming that electrons are not captured by an ion, a linear increase in d causes an exponential increase in the number of electrons generated in the gap per unit time (Meredith *et al.* 1996, Moncreiff *et al.* 1978, Thiel *et al.* 1997). Conversely, a linear increase in d causes E , and hence ψ , to vary inversely proportional to d (Meredith *et al.* 1996, Moncreiff *et al.* 1978, Thiel *et al.* 1997). Therefore, from the aforementioned, it can be postulated that ψ should have a sigmoidal dependency on d , which is in accordance with the results presented.

Shown in figure 4.11(d) is a plot of ψ versus τ_L . It can be seen that an increase in τ_L causes a relatively small but appreciable sub-linear increase in ψ . Increasing τ_L is analogous to enhancing the current injected into each pixel or I_{PE} provided that the emission coefficients of the sample remain unchanged. Consider an electron beam incident on a conducting or insulating sample. Increasing τ_L , at constant I_{PE} , will increase the number of electrons entering the gas cascade and hence the total amplified signal induced in the ring at each pixel point. The contrast within GSED images will therefore be enhanced as τ_L is increased. From the theory described in the section 4.3 and equation (4.3.4) it can be seen that an increase in τ_L should not vary ψ provided I_{PE} , p_{H_2O} , d and V_{GSED} *etc.* remain unchanged (Thiel *et al.* 1997, Meredith *et al.* 1996). An explanation for the trend observed is that whilst the GSED images were being collected (which were collected from low τ_L to high τ_L), a small but significant amount of excess negative charge was building up on the surface of the alumina sample, as a result of the high beam energy ($\varepsilon_{PE} = 30$ keV), which coincidentally caused an increase in δ ¹. An enhancement of δ causing more electrons to enter the gas cascade and hence increasing ψ .

¹The mechanisms behind the enhancement of SE emission from charged dielectrics as a result of negative charging is beyond the scope of this thesis. Relevant literature can be found in Cazaux (1999a), Cazaux (1999b) and Joy & Joy (1996).

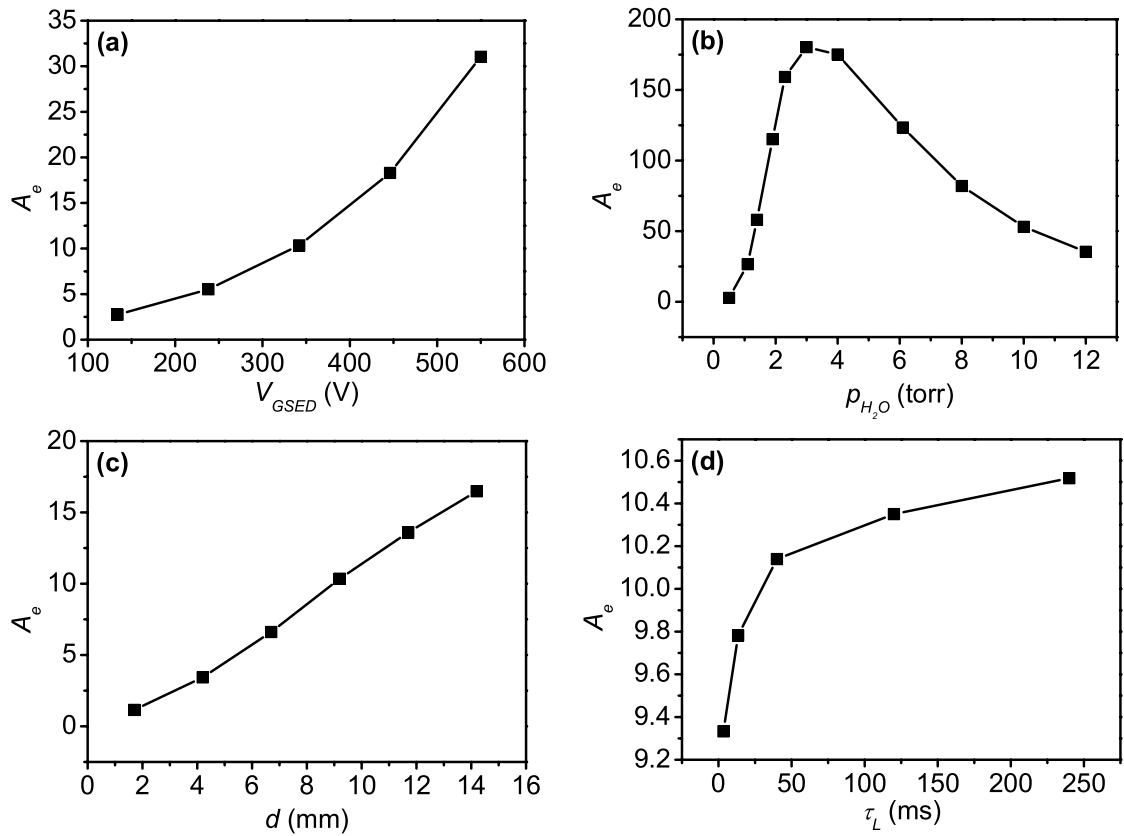


Figure 4.12: Steady state gaseous electronic amplification (A_e) versus gaseous secondary electron detector (GSED) bias (V_{GSED}) [$p_{H_2O} = 0.7$ torr, $d = 9.2$ mm, $\tau_L = 120$ ms]; (b) water vapour pressure (p_{H_2O}) [$V_{GSED} = 342$ V, $d = 9.2$ mm, $\tau_L = 120$ ms]; (c) sample-electrode separation (d) [$V_{GSED} = 342$ V, $p_{H_2O} = 0.7$ torr, $\tau_L = 120$ ms] and (d) line scan time (τ_L) [$V_{GSED} = 342$ V, $p_{H_2O} = 0.7$ torr, $d = 9.2$ mm].

Plots of A_e versus V_{GSED} , p_{H_2O} , d and τ_L are shown in figures 4.12(a), (b), (c) and (d), respectively. Comparing figures 4.11 and 4.12 it can be seen that ψ follows the same trend with all of the microscope operating parameters as that of A_e . The time taken for electrons to traverse the total gap distance, the electron transit time (τ_e), is of the order of 1 ns under conditions typically utilized in ESEM (Danilatos 1990c). However, the amount of time that the beam spends at each pixel element in images, the pixel dwell time (τ_p), is equal to 169 μ s for the results presented above. Therefore, during the generation of each image pixel (i) the electrons in each avalanche have had more than sufficient time to reach a steady state Maxwellian distribution of kinetic energies and (ii) a multitude of avalanches have been developed such that at $t = \tau_p$ a large number of electrons are being collected by the ring continuously and uniformly, and hence ψ will be equal to its limiting value of that given by equation (4.3.4). As A_e is defined as the total number of electrons produced in the cascade per electron leaving the sample surface, ($I_{PE}(\eta + \delta)$), it is easily seen from equations (3.11.8) and (4.3.4) that

$$\psi = \left\{ \frac{dn}{dt} \right\}_{ion} = \frac{(\eta + \delta)}{e} A_e. \quad (4.6.1)$$

Therefore, it is easily seen from equation (4.6.1) that the rate of ionization is directly proportional to gaseous cascade amplification over all microscope parameters and hence the theoretical predictions made are consistent with the experimental results obtained.

4.6.2 Electron Drift Velocities

Shown in figure 4.13 is a plot of v_e versus E/p_{H_2O} obtained from fits of equation (4.3.18) to the experimentally obtained GSI profiles of all of the microscope parameters used in this thesis. It can be seen that v_e has a square root dependence on E/p_{H_2O} as indicated by the dark line fitted to the data.

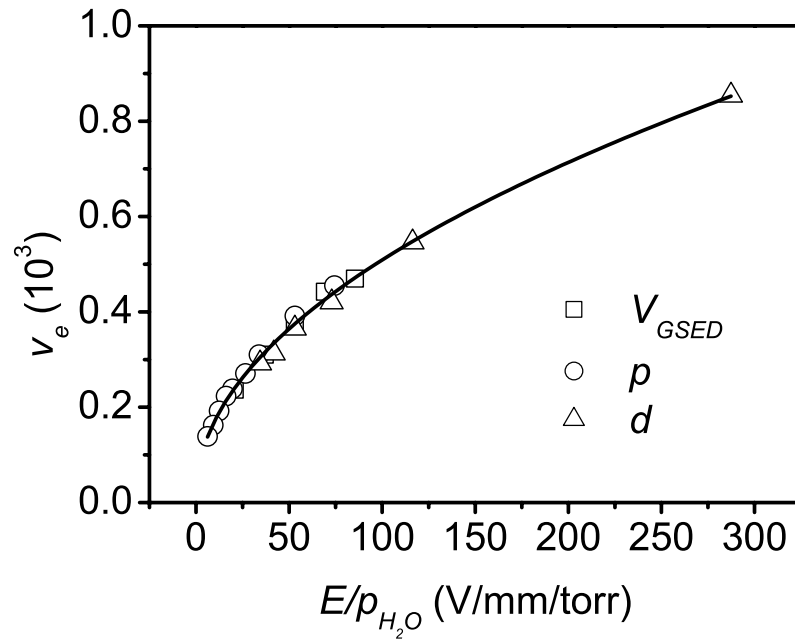


Figure 4.13: Electron drift velocity (v_e) versus reduced electric field (E/p_{H_2O}).

The drift velocity of electrons traversing a homogeneous electric field with no space charges present is proportional to $(E/p)^{1/2}$ (von Engel 1965, Nasser 1971). The fact that the relative magnitude of the electron drift velocity obtained follows the same trend with E/p_{H_2O} as that obtained from existing theoretical and experimental observations once again (i) demonstrates the veracity of the SE-ion recombination model derived and (ii) suggests that field modification due to space charges can be considered negligible in relation to streaking formation in GSED images.

4.6.3 Recombination Coefficients

Shown in figure 4.14 are plots of ρ versus (a) V_{GSED} , (b) p_{H_2O} , (c) d and (d) τ_L . It can be seen from the plots that ρ (i) increases in a sub linear fashion with V_{GSED} , (ii) decreases exponentially with p_{H_2O} , (iii) decreases slightly exponentially with d and (iv) increases as a function of decreasing gradient with τ_L .

The electron-ion recombination coefficient can be expressed as

$$\rho = \bar{v}_e \sigma_T^{ei}(\varepsilon) \propto \frac{1}{\bar{\tau}_i}, \quad (4.6.2)$$

where \bar{v}_e is the average electron velocity, σ_T^{ei} is the total (RR + DR + RE + RDR + TBR + DSR) electron-ion recombination cross section (being a function of electron energy, (ε)) and $\bar{\tau}_i$ is the average lifetime of an ion (von Engel 1965, Nasser 1971). As cross sections are a measure of the probability of a particular collision process occurring, it can be seen that σ_T^{ei} , and hence ρ , is proportional to the probability of an SE being captured by a PI. Therefore, from the aforementioned, ρ essentially describes the magnitude and average rate at which SE-ion recombination occurs in the gas due to all the possible recombination mechanisms (RR+DR+RE+RDR+TBR+DSR).

Increasing V_{GSED} increases the average kinetic energy of SEs and cascading electrons in the gap. As the probability of electron capture decreases with increasing electron energy (see figures 4.1 and 4.2) (Hahn 1997), ρ should in turn decrease with increasing V_{GSED} . However, increasing V_{GSED} also enhances the concentration of ions generated during the scanning of the pre-irradiated region. It can therefore be speculated that the magnitude of the ion density in the recombination volume dominates the amount of signal loss through SE-recombination than that caused by elevated electron drift velocities. Also, increasing V_{GSED} increases E which diminishes inhomogeneities in ion flux above the sample surface (Toth *et al.* 2002d). Hence, the probability of ions being ‘focused’ into regions of elevated charge density will increase, causing an elevation in the overall recombination efficiency (Toth *et al.* 2002c).

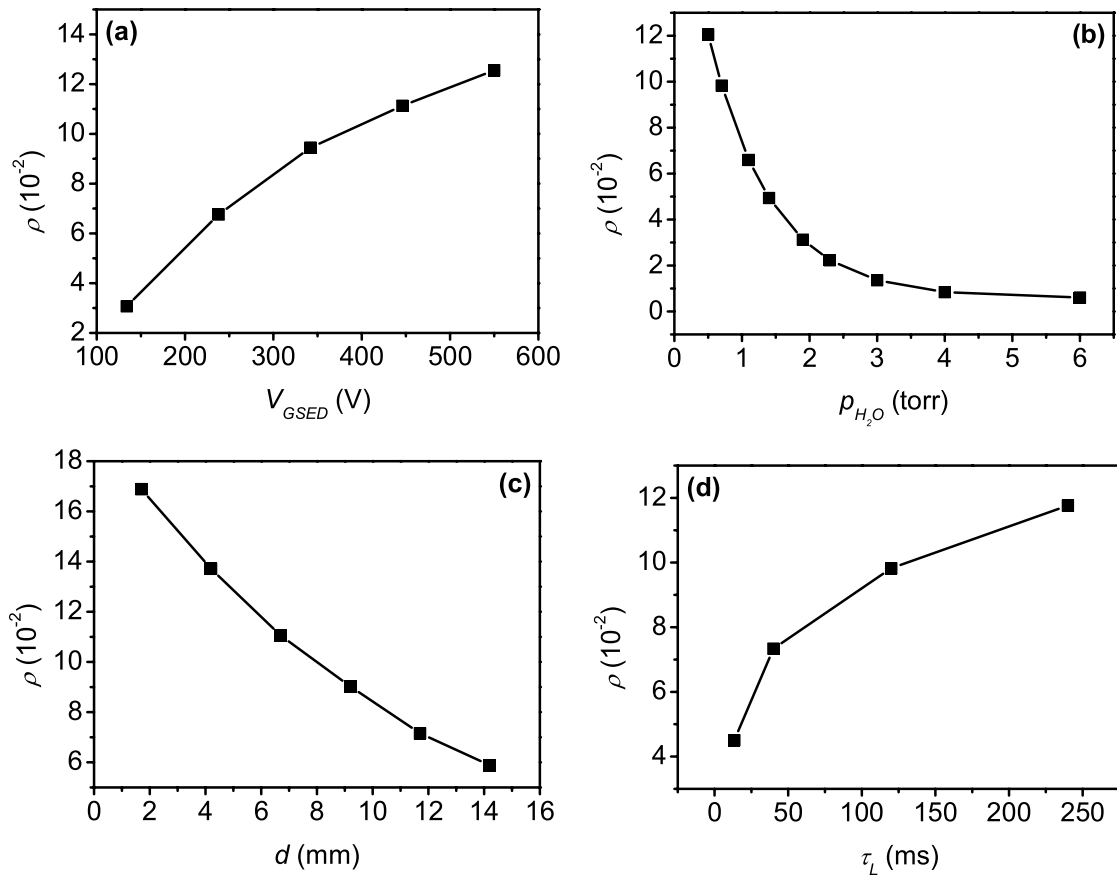


Figure 4.14: Recombination coefficient (ρ) versus (a) gaseous secondary electron detector (GSED) bias (V_{GSED}) [$p_{H_2O} = 0.7$ torr, $d = 9.2$ mm, $\tau_L = 120$ ms]; (b) water vapour pressure (p_{H_2O}) [$V_{GSED} = 342$ V, $d = 9.2$ mm, $\tau_L = 120$ ms]; (c) sample-electrode separation (d) [$V_{GSED} = 342$ V, $p_{H_2O} = 0.7$ torr, $\tau_L = 120$ ms] and (d) line scan time (τ_L) [$V_{GSED} = 342$ V, $p_{H_2O} = 0.7$ torr, $d = 9.2$ mm].

The rate at which low energy electrons and ions are generated in the gas cascade process was shown previously in figure 4.11(b) to generally increase with p_{H_2O} . Hence, as p_{H_2O} increases, there is an increased number of electrons and ions traversing the gap. Also, an increase in p_{H_2O} reduces the average kinetic energy, or drift velocity, of cascading SEs. The drift velocity of cascading electrons, at a constant electric field strength, being proportional to $p^{-1/2}$ (Danilatos 1990c, von Engel 1965, Nasser 1971). Therefore, as p_{H_2O} increases, there is a greater number of ions available in the gap to capture low energy electrons which in turn have increased probabilities of being captured by the ions as a consequence of their low kinetic energies (Hahn 1997). Based on this premise, the probability of recombination occurring in the gas, or ρ , should increase with p_{H_2O} , which is inconsistent with the results presented. However, along with the phenomena described above, increasing p_{H_2O} decreases the mean free path for ion-ion or ion-molecule scattering. The ionic mean free path being proportional to $p^{-1/2}$ (Nasser 1971). A reduction in ionic mean free path decreases the flux at which ions can arrive at the sample surface and recombine with low energy SEs or electrons within the sample surface (Toth *et al.* 2002d). The efficiency at which electrons can be captured by ions maximizes in the vicinity of the sample surface as a result of their low energies through insufficient electric field acceleration. The aforementioned demonstrates that the overall probability of recombination occurring in the gas, with p_{H_2O} , is governed mostly by the flux at which ions arrive at the sample surface, hence the ionic mean free path, which is consistent with previous models on steady state electron-ion recombination by Toth *et al.* (2002a) and Toth *et al.* (2002d).

An increase in d will generally increase the magnitude of the ion density, due to the increase in total gas path length of cascading electrons, to a greater extent than the decrease in electron kinetic energy as a result of a diminished E . As ρ or the average SE capture probability reduces with d , as seen in figure 4.14(c), it can be suggested that the magnitude of signal scavenging through SE-ion recombination is

governed mostly by variations in ion concentration within the recombination volume rather than electron energies.

The number of electrons injected into the gas at each pixel point on the sample should increase directly proportionally to τ_L . However, figure 4.14(d) illustrates that as τ_L , and hence the number of SEs entering the gas at each pixel, increases, ρ increases with decreasing gradient, obviously saturating at very slow scan speeds. This implies that as the scan speed is reduced and hence the current injected into the gas increases, the effective SE emission coefficient reduces through SE-ion recombination, which is consistent with existing models of steady state SE-ion recombination (Toth *et al.* 2002a).

In order to obtain a complete picture of SE-ion recombination in the ESEM over all gaseous parameters such as V_{GSED} , p_{H_2O} and d figure 4.15 shows a plot of ρ versus E/p_{H_2O} . The plot quantitatively shows, for the first time in ESEM, the actual dependence that the effects of SE-ion recombination has on reduced electric field. The plot illustrates that ρ has an inverse power dependency on E/p_{H_2O} and hence SE-ion recombination dominates at high E/p_{H_2O} , which is consistent with existing steady state qualitative models of SE-ion recombination (Toth *et al.* 2002d). It is also interesting to note that ρ follows a similar trend with E/p_{H_2O} as that of v_e (see figure 4.13) and v_i (akin to v_e , has a square root dependency with E/p_{H_2O} (Danilatos 1990c, von Engel 1965, Nasser 1971)). Once again, this demonstrates that it is not the drift velocity of SEs that dominates the magnitude of SE-ion recombination, but is the speed at which ions can traverse the gap from their point of production to the sample surface where they can neutralize.

It is obvious from the trends observed above that in order for the effects of SE-ion recombination, and hence streaking effects, to be reduced or possibly eliminated one must work at low reduced electric fields (low E /high p), where the probability of electron capture, and hence the average recombination rate is minimized. However,

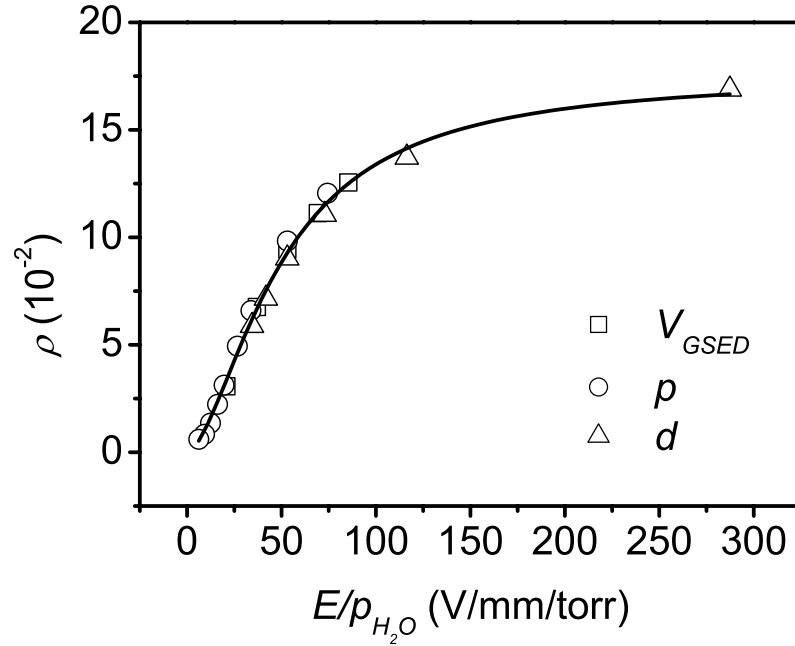


Figure 4.15: Recombination coefficient (ρ) versus reduced pressure (E/p_{H_2O}). [$\tau_L = 120$ ms]

in order for this to be accomplished a sacrifice in SE amplification and hence signal-to-noise ratio in images may be necessary.

4.6.4 Recombination Rates

Shown in figure 4.16 are profiles of normalized $\zeta(t)$ versus (a) V_{GSED} , (b) p_{H_2O} , (c) d and (d) τ_L obtained from equation (4.3.20). All profiles were normalized by dividing the complete data set by ψ to show the full shape and trends of all of the individual profiles. The profiles show the instantaneous rate of recombination relative to ψ from the exact moment the enhanced SE emission region ceases to be scanned until steady state conditions are obtained when the streaking stops at $\zeta(t) = \psi$. Therefore, each of the profiles show the total length of the streaks generated in GSED

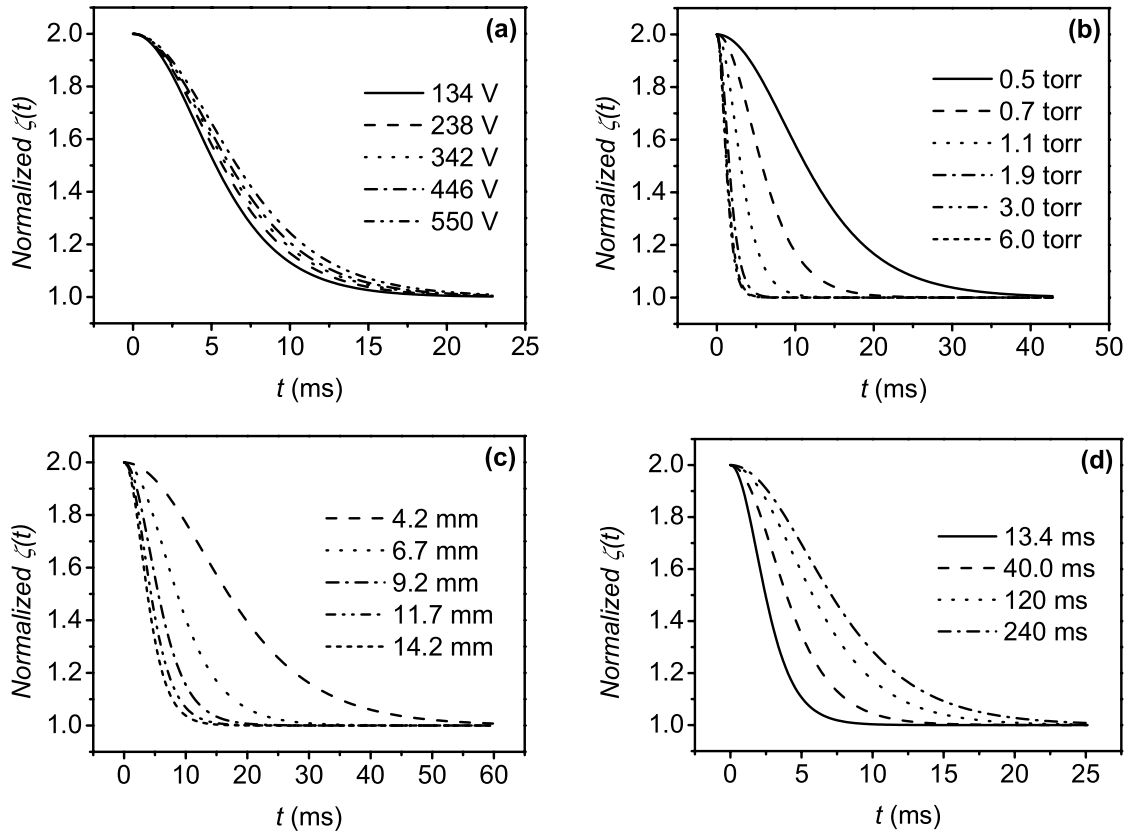


Figure 4.16: Normalized recombination rate (ζ) versus time (t) acquired as a function of (a) gaseous secondary electron detector (GSED) bias (V_{GSED}) [$p_{H_2O} = 0.7$ torr, $d = 9.2$ mm, $\tau_L = 120$ ms]; (b) water vapour pressure (p_{H_2O}) [$V_{GSED} = 342$ V, $d = 9.2$ mm, $\tau_L = 120$ ms]; (c) sample-electrode separation (d) [$V_{GSED} = 342$ V, $p_{H_2O} = 0.7$ torr, $\tau_L = 120$ ms] and (d) line scan time (τ_L) [$V_{GSED} = 342$ V, $p_{H_2O} = 0.7$ torr, $d = 9.2$ mm].

images at various microscope operating parameters. The profiles illustrate that $\zeta(t)$ follows an ‘S’ shaped (sech^2) dependency on t , as indicated previously in equation (4.3.20). The most interesting feature obtained from all of the profiles is that the greater the average value of ζ the longer the total streak length or time, which is consistent with all results presented. The length of the streaks being governed by the time taken for the large concentration of ions (generated whilst the enhanced region was scanned) to dissipate, via (i) ion-ion repulsion, (ii) ion-gas molecule scattering, (iii) recombination at the sample surface, (iv) recombination at the chamber walls and (v) SE-ion recombination. The rate at which process (iii) occurs is obviously dependent on ion drift velocity, which akin to electrons, is proportional to $(E/p)^{1/2}$ (von Engel 1965, Nasser 1971). As the average value of $\zeta(t)$ is proportional to ρ , the dependency of the time taken for ions to dissipate as a function of microscope operating parameters was previously discussed in section 4.6.3.

4.6.5 Time Constants

The total time constant (RC) of the GSED electronics and external circuitry, obtained by fitting equation (4.3.18) to the experimental GSI profiles, was found to (i) remain at a constant value when V_{GSED} , p_{H_2O} and d were varied and (ii) increase with a sub-linear dependency on τ_L , as illustrated in figure 4.17. Incorporated into the GSED preamplifier are low-pass noise filters that extract high frequency shot and thermal noise from imaging signals (Philips Electron Optics 1997). The clipping time or time constant of the noise filters, RC_{nf} , varies as a function of τ_L via a digital switching circuit that selects different combinations of R and C in order to vary the BWD. The variation in RC_{nf} , obtained from Philips Electron Optics (1997), is also shown in figure 4.17. It can be seen that RC_{nf} varies with τ_L identically to that of RC , but with a magnitude of 11 times smaller. As mentioned previously in section 4.3, the

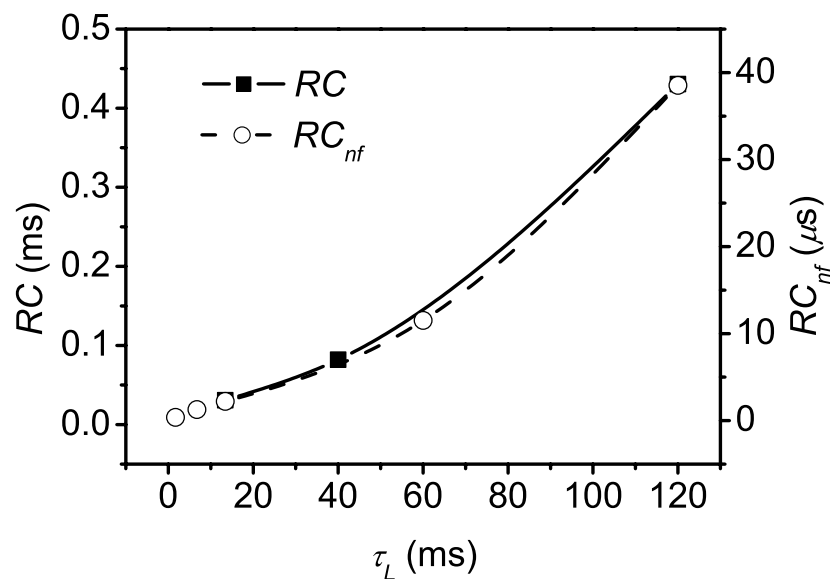


Figure 4.17: Total detection system time constant (RC) and gaseous secondary electron detector (GSED) noise filter time constant (RC_{nf}) versus line scan time (τ_L). [$V_{GSED} = 342$ V, $p_{H_2O} = 0.7$ torr, $d = 9.2$ mm]

total time constant of the GSED electronics and external circuitry, RC , is comprised of (i) RC_{nf} , (ii) the time constant due to the input resistance and capacitance of the GSED electronics and (iii) the time constant associated with coaxial cables used to transmit signals, R_4C_4 , as illustrated previously in figure 2.13.

4.7 Future Work

Streaking effects seen in GSED and ISC images after regions of high SE emission as a result of electron-ion recombination was investigated in the present study using only water vapour as the imaging gas. In order to obtain a full understanding of signal formation and image interpretation in a low vacuum environment one can replicate the recombination model and experimental techniques used in this thesis to obtain a full set of recombination data over a wide range of imaging gases. Doing this will determine the most suitable imaging gases for use in ESEM. Water vapour, with its excellent electronic amplification properties (Fletcher *et al.* 1997), but significant signal loss characteristics through recombination, as indicated by the streaking shown in this chapter, may not be the ultimate choice of gas. By possibly utilizing gases with smaller ionization cross sections, to reduce ion buildup, and low recombination coefficients, the adverse streaking effects seen in images may be reduced or possibly even eliminated.

The present study demonstrated that the time constant of the detection electronics and external circuitry affects the rate at which induced charge can be collected to generate images. Gaseous scintillation detectors (see for example (Danilatos 1986, Danilatos 1992b, Mutterer 1982)), due to their very fast response times, have the possibility of greatly reducing such a phenomenon and it should be an aim of such ongoing work to study such devices. Using such devices should also enable studies of radiative electron-ion recombination processes, excitation mechanisms and scintillation phenomena, as well as the direct determination of recombination rates, recombination efficiencies, ionization rates and drift velocities under the non-steady state and inhomogeneous field conditions encountered in ESEM. However, before such investigations are attempted one must implement scintillation detectors with efficient photon collection geometries and obtain steady state photon amplification profiles over various

microscope operating parameters, such as that presented in the following chapter on gaseous scintillation detection and amplification in ESEM.

4.8 Conclusions

The present study developed a theoretical model based on transient electron-ion recombination to accurately quantify and describe the dark streaking seen in GSED images immediately after a region of high SE emission was encountered by a scanning electron beam. Experimental streaking data obtained over a wide range of microscope operating parameters such as detector bias, water vapour pressure, sample-electrode separation and scan speed, was fitted using the transient recombination model to determine (i) relative magnitudes of ionization and recombination rates, recombination coefficients and electron drift velocities, as well as (ii) absolute values of the total time constant of the detection system electronics.

Ionization rates were seen to follow the same trends with microscope operating parameters as that of gaseous cascade amplification, which complied with theoretical predictions. Recombination coefficients were found to have an inverse power dependency on reduced electric field. Instantaneous recombination rates, shown for the first time in an ESEM, were found have a sech^2 dependency on time over all microscope parameters. The total lengths of the streaks seen in GSED images immediately after an enhanced contrast region were found to increase with higher average recombination rates. The average drift velocity of electrons traversing the gap were found to increase with a square root dependency on reduced electric field strength, which is in accordance with existing models of electron kinetics in partially ionized gases. The total time constant of the GSED electronics and the coaxial cables used to transmit signals was found to (i) remain unchanged with variations in detector bias, pressure and sample-electrode separation and (ii) increase in a sup-linear fashion with line scan time. The latter being attributed to a corresponding sup-linear increase in the time constant of the GSED low-pass noise filters with line scan time which adds to the intrinsic time constant of the detection system. The total

time constant of the detection system was found to be approximately $430 \mu\text{s}$ at a scan speed of 120 ms.

The model implicitly demonstrated, by its excellent agreement with experimental data, that field modification due to space charges, although obviously present, is not the foremost phenomenon causing streaking in images, as previously thought. Furthermore, the model clearly demonstrated that the degree of shadowing in images is influenced by the total time constant of the detection system and external circuitry. The time constant controlling the rate at which charge can be induced in the GSED ring to generate images. Future work therefore needs to develop greater bandwidth detection electronics or novel detection systems that utilize 'fast' electroluminescent photon signals in order to reduce or alleviate such a phenomenon.

Overall, the electron-ion recombination model derived, and the results presented, provide further insight into gaseous electron and positive ion transients, the kinetics of signal formation, and image interpretation in a low vacuum environment.

Chapter 5

A Preliminary Investigation of Gaseous Scintillation Detection and Amplification in Environmental SEM

5.1 Introduction

Only recently has it been recognized that image formation in an ESEM can be achieved not only by detecting electron signals induced in grounded or biased electrodes, but also via the detection of ultraviolet (UV), visible (VIS) and infrared (IR) photons generated in the gas through the excitation of atoms and/or molecules by free electrons, known as gaseous scintillation (Danilatos 1986, Danilatos 1990c, Danilatos 1992b). Gaseous scintillation detection (GSD) has several advantages over conventional electron detection such as: (i) Fast transient response - excited states occurring in the gas have lifetimes of the order of nanoseconds which can be collected immediately compared to that of electronic signals which need to be induced on electrodes before subsequent detection (Danilatos 1990c); (ii) High gain x bandwidth products - photomultiplier tubes (PMTs) used to detect photon signals are capable of operating at high gains and fast electron drift times, which generally improves signal-to-noise ratios in images compared to that of amplifiers used to generate electronic signals, provided that a significant number of photons are collected from the gas. The response time of a PMT is of the order 10 ns (Goldstein *et al.* 1992); (iii) Possibility of reducing space charge effects - efficient gaseous scintillation production generally occurs before the onset of ionization (Danilatos 1990c, von Engel 1965, Nasser 1971) and hence the concentration of positive ions generated after each electron avalanche is minimized. Spurious effects due to space charge formation, such as SE-ion recombination (also known as ‘signal scavenging’) (Toth *et al.* 2002c, Toth *et al.* 2002d), contrast reversal (Toth & Phillips 2000a, Toth & Phillips 2000b) and shadowing in images (Toth & Phillips 2000a) has the possibility of being reduced or even alleviated via scintillation detection.

Therefore, from the aforementioned, scintillation detection in the ESEM has great prospects for being an effective tool for achieving high contrast SE imaging at TV

scan rates, which at this stage in ESEM development is rather difficult to accomplish, particularly using existing electronic detection methods.

Most of the work carried out in the area of scintillation detection in an ESEM so far has been carried out on a qualitative level. This chapter shows, for the first time, light or electroluminescence yields (referred to herein as photon amplification (A_{hv})) obtained as a function of (i) various microscope operating parameters such as GSED detector bias (V_{GSED}), gaseous scintillation detector (GSD) bias (V_{GSD}), pressure (p) and working distance (WD)¹, (ii) gas type and (iii) electric field geometry or photon collection efficiency. The photon amplification profiles were obtained by detecting photons over a wavelength (λ) range of 300 to 650 nm and were compared to the amplification produced by steady state electronic signals (referred to herein as electronic amplification (A_e)) normally detected in an ESEM. The main emphasis of this work is to further develop existing theories on gaseous scintillation detection in an ESEM and provide new data that can be used in future theoretical models governing photon amplification.

¹In the Philips XL 30 ESEM the GSED ring is located 5.8 mm below the pole piece. Therefore, the sample-electrode separation (d) is equal to the working distance (WD) less 5.8 mm.

5.2 Theory

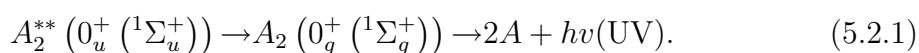
This section briefly describes the mechanisms governing gaseous scintillation in partially ionized gases relevant to ESEM. Extensive theories relating to excitation and photon production in gases can be found in standard texts on ionized gases such as von Engel (1965) and Nasser (1971). Theory governing gaseous scintillation generation and detection in the presence of an electric field as a result of drifting and multiplying electrons can be found in research on gas proportional scintillation counters (GPSC) such as Mutterer (1982), Feio & Policarpo (1983) and Cumpstey & Vass (1980).

5.2.1 Gaseous Proportional Scintillation and Electroluminescence

Inelastic collisions between electrons and gas molecules are capable of exciting molecules from ground state to characteristic electronic, vibrational and rotational levels (von Engel 1965, Nasser 1971). An excited gas molecule will remain in an excited state for a short period of time (typically 10^{-8} s) until it de-excites through the emission of one or several photons (von Engel 1965). The photon emissions, in the UV, VIS, near infrared (NIR) and far infrared (FIR) regions of the electromagnetic spectrum, produced via the passage of an electron swarm under the influence of an applied electric field is referred to as secondary gas proportional scintillation or electroluminescence (Cumpstey & Vass 1980, Dias *et al.* 1999). Indirect scintillation produced by high energy ionizing particles that initiate cascades, such as PEs or BSEs, is referred to as primary scintillation (Danilatos 1990c). The exact nature of the radiation produced is dependent on electron energy. For example, if a continuum electron excites a gas molecule above a particular resonance level the difference between the energy imparted to the molecule by the electron and the resonance level will emit continuous

radiation (von Engel 1965, Nasser 1971). Gaseous luminescence can also be a consequence of electron capture and subsequent de-excitation via photon emissions, as in radiative, dielectronic and radiative dielectronic electron-ion recombination (von Engel 1965, Hahn 1997, Nasser 1971). Although gaseous scintillation and radiative recombination mechanisms produce line spectra and continuous radiation in the UV (Andreson *et al.* 1977, Suzuki & Kubota 1979, Takahashi *et al.* 1983), VIS (Tornow *et al.* 1976, Takahashi *et al.* 1983) and IR (Fraga *et al.* 2000, Lindblom & Solin 1988) regions of the electromagnetic spectrum it is usually most prominent in the vacuum ultraviolet (VUV) region (Cumpstey & Vass 1980, Danilatos 1990c, Fraga *et al.* 2000).

The detection of ionizing radiation using gaseous proportional scintillation detectors is normally performed (i) using noble gases, due to their strong emission characteristics (Al-Dargazelli *et al.* 1981, Feio & Policarpo 1983) and (ii) at reduced electric fields (E/p) less than the threshold of ionization/charge multiplication, in order to reduce statistical fluctuations in photon detection, improving energy resolution and signal-to-noise ratios (Dias *et al.* 1997, Dias *et al.* 1999). In order for E/p to remain low, pressures of several hundred to several thousand torr are commonly employed. Optimum electroluminescence yield and energy resolution has been found to occur at E/p values close to the ionization threshold (Dias *et al.* 1997, Dias *et al.* 1999). The radiation produced in the VUV-FIR range generally consists of two major peaks in the VUV (< 200 nm) region, commonly referred to as the first and second continuums (Suzuki & Kubota 1979). The first continuum is found to occur close to the main resonant line of the gas and occurs through de-excitations from vibrationally unrelaxed ($v \neq 0$) and excited molecular states to the repulsive ground state (Suzuki & Kubota 1979):



Here, A represents a monotonic gas molecule and the excimer, A_2^{**} , is mainly formed

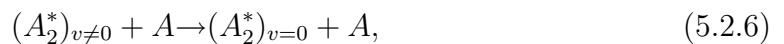
through three-body collisions of the type:



where A^* is an electronically excited atom. Experimental evidence shows that the first continuum only occurs under discharge conditions at pressures of several hundred torr (Suzuki & Kubota 1979). In pure Ar gas the first continuum occurs at ≈ 106 nm with a full-width-half-maximum (FWHM) of ≈ 30 nm (Suzuki & Kubota 1979). The second continuum occurs at longer wavelengths than the first and its emissions are attributed to transitions from vibrationally relaxed ($v = 0$) excited molecular states to the repulsive ground state (Lindblom & Solin 1988, Suzuki & Kubota 1979, Takahashi *et al.* 1983):



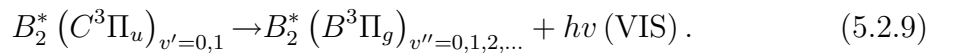
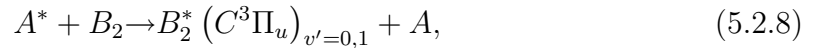
In this case, A_2^* is formed through the collisions (Takahashi *et al.* 1983):



Suzuki & Kubota (1979) and Takahashi *et al.* (1983) have demonstrated that in commercially pure Ar the second continuum occurs at a peak wavelength of 128 nm with a FWHM of 10-100 nm at pressures of 360-1130 torr, anode voltages of 500-2500 V, and reduced electric fields whereby charge multiplication did not occur. In GPSC detection it has been found, for a non-varying collection efficiency, that the total light produced in the gas through scintillation mechanisms is independent of p , however, the ratio of the intensities of the first and second continua varies (Favata *et al.* 1990).

The first continuum being dominant over the second continuum at ‘high’ values of E/p and the second continuum dominating at ‘low’ E/p .

Many PMTs used in GPSC have their peak response in the near UV (300 – 380 nm) to short VIS range (Lindblom & Solin 1988). Therefore, in order to efficiently detect scintillation photons generated in GPSC it is often desirable to convert the strong VUV emissions, such as those described above, to VIS wavelengths using an appropriate wavelength shifting quenching gas such as N_2 (Al-Dargazelli *et al.* 1981, Alves & Policarpo 1967, Garg *et al.* 1995, Mutterer 1982, Takahashi *et al.* 1983). The presence of a small concentration ($\approx 0.1 - 4\%$) of N_2 in an atomic gas, such as Ar, quenches the continuum emissions, described above, and gives rise to corresponding emission lines between 300 and 420 nm that are referred to as the second positive band (Al-Dargazelli *et al.* 1981, Lindblom & Solin 1988). The intensity of the second positive band has been found to (i) increase with increasing admixture partial pressure up to concentrations of $\approx 0.1\%$ and then decrease with increasing admixture concentration and (ii) increase with decreasing p at constant admixture concentration (Takahashi *et al.* 1983). The formation of the second positive band is attributed to the following reactions:



Above A^* is a monatomic gas atom excited to an electronic np state and B_2 is the quenching gas (Lindblom & Solin 1988, Takahashi *et al.* 1983). In the case of N_2 quenching Ar, the VIS emissions occur at 315.9 nm ($v' = 1 \rightarrow v'' = 0$), 333.9 nm ($v' = 1 \rightarrow v'' = 1$), 337.1 nm ($v' = 0 \rightarrow v'' = 0$), 353.7 nm ($v' = 1 \rightarrow v'' = 2$), 357.7 nm ($v' = 0 \rightarrow v'' = 1$), 375.5 nm ($v' = 1 \rightarrow v'' = 3$), 380.5 nm ($v' = 0 \rightarrow v'' = 2$), 399.8 nm ($v' = 1 \rightarrow v'' = 4$), 405.9 nm ($v' = 0 \rightarrow v'' = 3$), 427.0 nm ($v' = 0 \rightarrow v'' = 5$) and 434.4 nm ($v' = 0 \rightarrow v'' = 4$) (Takahashi *et al.* 1983).

From the aforementioned it is evident that primary and secondary scintillations generated in the gas at the low pressures encountered in ESEM should generally produce radiation in the VUV to short VIS region of the electromagnetic spectrum if commercially pure gases are used. In this work photons were detected in the wavelength range of 300-650 nm (see figure 5.2) using Ar, N₂ and H₂O gases, and it is therefore speculated that this photon signal was due to (i) small concentrations of residual gases shifting the VUV continua to UV-VIS wavelengths through the mechanisms described above in equations (5.2.8) and (5.2.9), and/or (ii) UV-VIS scintillations/electroluminescence generated via low energy electronic or vibrational de-excitations, and/or (iii) detection of the low energy tail of second continuum emissions, and/or (iv) UV-VIS recombination luminescence. The possibility of photon generation in the VIS region through cathodoluminescence generated by BSEs impacting insulating surfaces within the chamber, such as the signal track of the GSED or PMT vacuum seal, could also be a contributing factor. However, it will be shown that this effect can be considered insignificant compared to other possible scintillation mechanisms as a result of (i) GSD images showing strong SE contrast and (ii) photon amplification profiles generally exhibiting ‘low’ values at higher pressures.

Studies of proportional scintillation and electroluminescence (i) in gases commonly used in ESEM, such as H₂O and (ii) at pressures and electric field strengths commonly employed in ESEM, are scarce. Hence, spectroscopic studies need to be performed to identify the line spectra and/or continuous emissions, and mechanisms associated with the scintillation and electroluminescence produced in ESEM. However, at this preliminary stage of investigation is a formidable task and is therefore beyond the scope of this work.

Akin to electron amplification, whereby the total number of ion-pairs generated in the gas per unit path length traversed by each cascading electron in the direction of E is defined by α_{ion} , an excitation coefficient (α_{exc}) can be used to describe the

total number of photons, of all wavelengths emitted, for a particular gas per electron per unit length traversed in the direction of E (Feio & Policarpo 1983, Cumpstey & Vass 1980, Dias *et al.* 1997, Dias *et al.* 1999, von Engel 1965, Garg *et al.* 1995, Massey *et al.* 1969, Paviček 1986). It has recently been revealed, through empirical measurements, that α_{exc} can be represented by an expression identical in form to that of equation (3.10.1), described previously in chapter 3.10, with differing constants A and B (Paviček 1986). Electroluminescence yields or gaseous photon amplification can then be predicted by inserting α_{exc} into existing equations governing electronic amplification, with slight modifications.

5.3 Gaseous Scintillation and Electroluminescence Amplification Model

If a current of low energy avalanche electrons, $I_e^g(z)$, traverse an element of gap distance dz at z , ionizing gas molecules, then the current of new electrons generated is (Farley & Shah 1990b, Meredith *et al.* 1996, Moncreiff *et al.* 1978, Thiel *et al.* 1997):

$$dI_e^g = I_e^g(z) \alpha_{ion} dz. \quad (5.3.1)$$

For a current of electrons leaving the sample surface, $I_e^g(0)$, at $z = 0$, integration of equation (5.3.1) gives the total current of electrons reaching a distance z above the sample surface as

$$I_e^g(z) = I_e^g(0) e^{\alpha_{ion} z}. \quad (5.3.2)$$

Whilst traversing the gap distance, the avalanche generated electrons will excite gas molecules, with an efficiency α_{exc} . The number of new photons produced per unit time, of all wavelengths, generated in an element of gap distance dz at z , is (Llewellyn-Jones 1957):

$$dI_e^{hv}(z) = I_e^g(z) \alpha_{exc} dz. \quad (5.3.3)$$

Substitution of equation (5.3.2) into the equation above and integrating over the entire gap distance gives the total number of electron avalanche liberated photons, of any wavelength, created per unit time in the gas between the sample/cathode and the anode ($z = d$) to be

$$I_e^{hv} = \frac{I_e^g(0) \alpha_{exc}}{\alpha_{ion}} (e^{\alpha_{ion} d} - 1). \quad (5.3.4)$$

The rate at which photons are generated in the cascade is dependent on the excitation probability, or in other words, the number of electron collisions leading to optical transitions divided by the total number of collisions that each cascading electron suffers, which is usually of the order of 10^{-2} or lower (von Engel 1965).

Along with low energy electrons such as SEs and ESEs, high energy PEs and BSEs are also capable of generating photons (Danilatos 1990c). The various photon and electronic signals described above are schematically illustrated in figure 5.1. However, photons generated by PEs and BSEs and their cascaded ESEs will reduce the signal-to-noise ratio if electroluminescent SE imaging is to be performed. In analogy to equations (3.11.2)-(3.11.4) in chapter 3.11, expressions for the photon signals produced by PEs, BSEs and SEs can be derived.

If each PE travelling in the negative z direction generates ω_{PE} photons per unit path length per unit p , then the number of new photons created per unit time in an increment of gap distance dz' at z' will be

$$dI_{PE_0}^{hv}(z') = -I_{PE}\omega_{PE}pdz', \quad (5.3.5)$$

where z' is in the opposite direction to z . Integrating equation (5.3.5) over the entire gap distance from the beam entrance point at the GSED ring ($z' = 0$) to the sample surface ($z' = d$) gives the total number of photons, of all wavelengths, generated per unit time by the PE beam alone as

$$I_{PE_0}^{hv} = I_{PE}\omega_{PE}pd. \quad (5.3.6)$$

As ESEs generated by PEs are also capable of producing photons, a z' dependent expression is needed for the current of ESEs produced. If each PE generates S_{PE} ion pairs per unit length per unit p from $z' = 0$ to $z' = d$, and each ESE generated is accelerated by the electric field from $z = z'$ to $z = d$, then, the current of ESEs produced by the PE beam in this increment is (Moncreiff *et al.* 1978):

$$I_{PE}^g(z') = -I_{PE}S_{PE}pe^{\alpha_{ion}(d-z')}. \quad (5.3.7)$$

Substituting the expression above into equation (5.3.3), in place of $I_e^g(z)$, with z replaced by z' , and integrating over the entire gap distance from $z' = d$ to $z' = 0$,

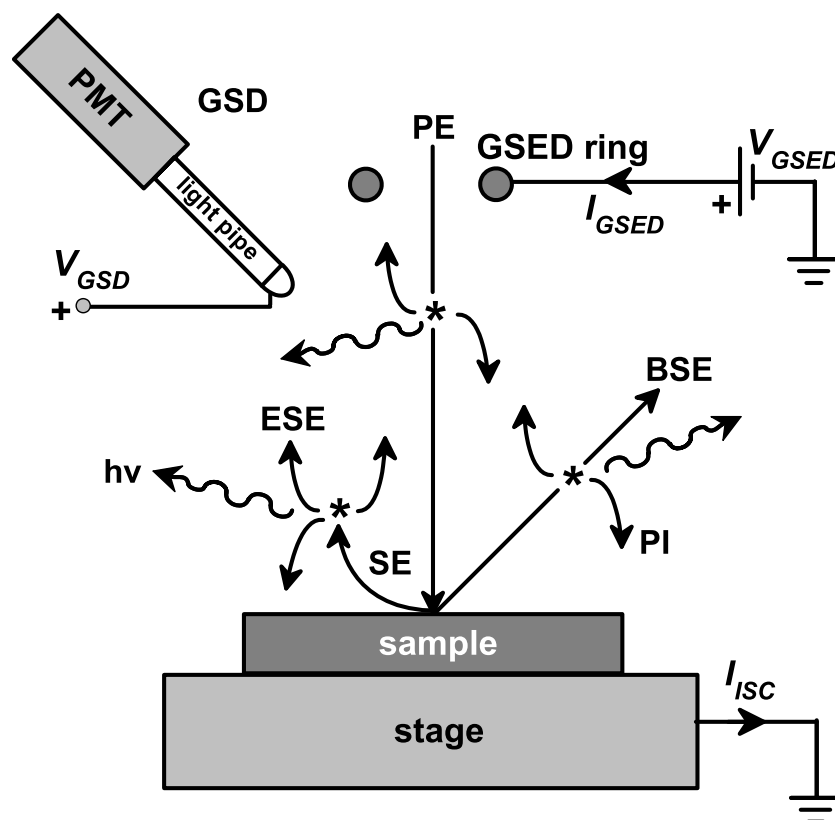


Figure 5.1: Schematic diagram showing the various photon and electronic signals produced in the low vacuum specimen chamber of an ESEM. Excitation and ionizing collisions [*] between gas molecules and (i) primary electrons (PEs), (ii) backscattered electrons (BSEs) and (iii) secondary electrons (SEs) produce photons ($h\nu$) or positive ions (PIs) and environmental SEs (ESEs), respectively. The photons generated in the gas are detected and amplified by a gaseous scintillation detector (GSD).

gives the total number of ESE liberated photons, generated by PEs per unit time, to be

$$I_{PE_1}^{hv} = \frac{I_{PE} S_{PE} p \alpha_{exc}}{\alpha_{ion}} (e^{\alpha_{ion} d} - 1). \quad (5.3.8)$$

The total number of photons produced in the gas by the PE beam is therefore equal to the summation of equations (5.3.6) and (5.3.8):

$$I_{PE}^{hv} = I_{PE} p \left[\omega_{PE} d + \frac{S_{PE} \alpha_{exc}}{\alpha_{ion}} (e^{\alpha_{ion} d} - 1) \right]. \quad (5.3.9)$$

Unlike PEs, BSEs traverse the gap in a positive z direction and each ESE generated initiates further ionizations over a distance z not $(d - z')$ and therefore equation (5.3.7) needs to be modified accordingly. The current of ESEs produced by BSEs is given by

$$I_{BSE}^g(z) = I_{PE} \eta S_{BSE} p e^{\alpha_{ion} z}. \quad (5.3.10)$$

Substituting this expression into equation (5.3.3) and integrating over the gap distance from $z = 0$ to $z = d$ yields the total number of ESE liberated photons per unit time, by BSEs, to be

$$I_{BSE_1}^{hv} = \frac{I_{PE} \eta S_{BSE} p \alpha_{exc}}{\alpha_{ion}} (e^{\alpha_{ion} d} - 1). \quad (5.3.11)$$

Analogous to equation (5.3.6), the number of direct photons produced by BSEs per unit time is

$$I_{BSE_0}^{hv} = I_{PE} \eta \omega_{BSE} p d, \quad (5.3.12)$$

where ω_{BSE} is the number of photons generated by BSEs per unit path length per unit p over the entire gap distance, which is assumed to be constant. The total number of photons produced per unit time by BSEs is equal to the summation of equations (5.3.11) and (5.3.12):

$$I_{BSE}^{hv} = I_{PE} \eta p \left[\omega_{BSE} d + \frac{S_{BSE} \alpha_{exc}}{\alpha_{ion}} (e^{\alpha_{ion} d} - 1) \right]. \quad (5.3.13)$$

For the case of SEs, $I_e^g(0)$ in equation (5.3.4) needs to be replaced by the current of SEs ejected from the specimen surface, $I_{PE} \delta$, yielding the total number of photons

produced per unit time by SEs to be

$$I_{SE}^{hv} = \frac{I_{PE}\delta\alpha_{exc}}{\alpha_{ion}} (e^{\alpha_{ion}d} - 1). \quad (5.3.14)$$

If photon amplification (A_{hv}) is defined as the total number of photons, of all wavelengths, produced in the gas by PEs, BSEs and SEs per electron leaving the sample surface, $I_{PE}(\eta + \delta)$, then

$$A_{hv} = \frac{\alpha_{exc} (e^{\alpha_{ion}d} - 1) [S_{PEP} + \eta S_{BSEP} + \delta]}{(\eta + \delta)} + \frac{pd(\omega_{PE} + \omega_{BSE})}{(\eta + \delta)}. \quad (5.3.15)$$

The first term in equation (5.3.15) represents the secondary scintillation or electroluminescence amplification produced in the cascade, whereas the second term represents primary scintillation amplification generated by PEs and BSEs.

The equations presented above assume that (i) α_{exc} is independent of z and is therefore constant throughout the gap, (ii) the effects of feedback amplification processes on photon generation are negligible and (iii) photoelectron production generated at the stage, sample surface and/or surrounding chamber walls via gaseous photon and metastable interactions is negligible. The latter two phenomena, although most likely present at typical E/p utilized in ESEM, are complex to accurately compute and hence were not included in the above derivations.

5.4 Experimental Techniques

Experiments were performed using a tungsten filament FEI-Philips XL 30 ESEM[®] equipped with a GSED and a purpose built gaseous scintillation detector (GSD). The GSD was constructed using the microscopes existing E-T detector with the scintillator material (p-47) removed and the SE collection grid either grounded or biased at a positive voltage, V_{GSD} , with respect to microscope ground as shown in figure 5.1. An Ortec high voltage power supply was used to generate V_{GSED} and V_{GSD} . A description of E-T detectors can be found in standard electron microscopy text books such as Goldstein *et al.* (1992). The GSD PMT was a Philips XP2012 which consisted of a 10 stage linearly focused Cu-Be dynode system, 32 mm semitransparent Baikaline (SbKCs) type D photocathode and a plano-plano lime glass window (Philips 1984). The pulse transit time of the PMT was 26 ns at maximum gain. The total spectral response of the GSD enabled the detection of photons in the wavelength range of 300 – 650 nm. The radiant spectral response of the PMT photocathode, $sk_e(\lambda)_p$ (obtained from Philips (1984)), and the transmission response of the PMT quartz window, perspex light pipe and perspex vacuum seal, $T(\lambda)$, is shown in figure 5.2. $T(\lambda)$ was calculated by measuring the ratio of the spectral intensity produced at the output of the PMT window, light pipe and vacuum seal of the GSD, to that produced at the input, by a white LED of known total spectral radiant flux. The spectral intensities were measured using an Ocean Optics[®] PC2000 spectroscopy system. A plane mirror was used to direct photons towards the GSD for the case when the GSED was used to generate photons. The output signal from the PMT was either connected to the existing E-T detector preamplifier and associated video card for subsequent imaging or a Keithley 617 programmable electrometer for electronic and photon gain measurements. Throughout experiments the brightness level in images and amplification data was maintained at zero. This was achieved by switching the

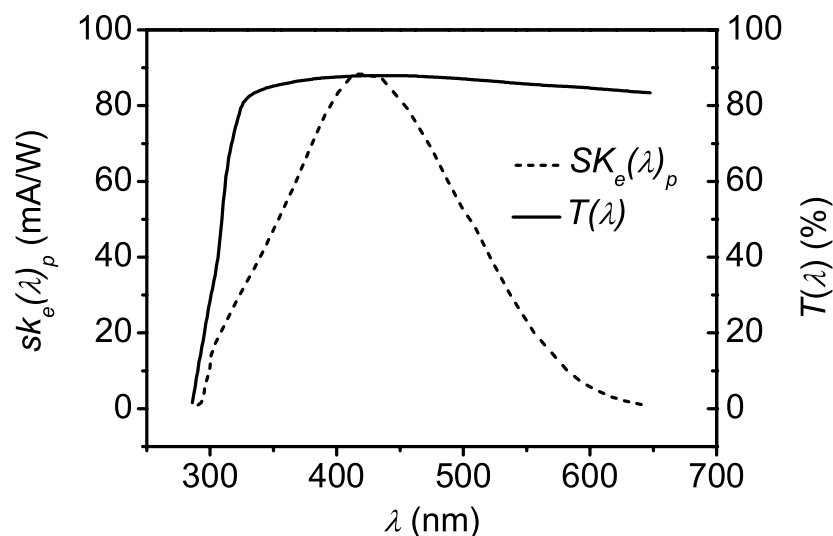


Figure 5.2: PMT photocathode spectral sensitivity ($sk_e(\lambda)_p$) and total (quartz window + perspex light pipe + perspex vacuum seal) transmission response ($T(\lambda)$) versus photon wavelength (λ).

beam off, prior to image or amplification acquisition, and setting the microscopes digital brightness control to a value corresponding to a greyscale intensity level of zero on the scan raster waveform display.

Prior to each set of amplification measurements performed at a specific time, or when the imaging gas was changed, the chamber of the microscope was purged ten times from 0.1 torr to 20 torr, and back, in order to remove as much residual gas left in the chamber as possible ².

The PE beam used to generate GSD and GSED images and amplification profiles was maintained at a constant energy of $\varepsilon_{PE} = 30$ keV and constant current of $I_{PE} =$

²In order to completely remove residual gases from a gaseous chamber it is usually baked-out under high vacuum conditions for approximately 24 to 48 hours. As ESEM is an instrument whereby (i) samples commonly outgas, (ii) imaging gases are frequently changed and (iii) sample preparation is minimal compared to conventional SEM, it would be inappropriate to perform long bake-outs prior to imaging or amplification measurements. Hence, the amplification profiles presented herein represent data that would be obtained in an ESEM operating under typical conditions.

5 nA throughout all measurements. I_{PE} was maintained at a constant value by monitoring the electron beam induced current (EBIC) current read from a cross-sectioned silicon $p - n$ junction diode prior to each set of images or amplification measurements.

The existing stage of the microscope, comprising of aluminium coated with a nickel-phosphorous alloy, was used as the sample for imaging purposes. A silicon-lithium solid state BSE detector and a conventional E-T detector were used to generate high vacuum BSE and SE images, respectively. A flat aluminum stub covering the stage was chosen as the sample when performing photon and electronic gain measurements throughout the entirety of this work in order to eliminate the possibility of any photons generated by the PE beam (Cathodoluminescence (CL)) entering the GSD detection system. The electronic structure of metals forbids the emission of CL (Yacobi & Holt 1990). The secondary and backscattered emission coefficients of aluminium, required to calculate photon and electronic amplification (see equations (5.4.10) and (5.4.12)), at 30 keV, are 0.075 and 0.135, respectively (Wittry 1966).

5.4.1 Determination of Photon Amplification

Steady state photon amplification (A_{hv}) is defined in this work as the total number of gaseous photons detected by the GSD per sample emissive electron. It is obvious that A_{hv} can not be considered an absolute measurement of photon amplification as the number of photons detected by the GSD is limited by its geometrical collection efficiency, $sk_e(\lambda)_p$, and $T(\lambda)$. That is to say that of the total number of photons generated in each electron cascade only a certain fraction of them will actually enter the collection grid and light pipe assembly. This fraction will depend on (i) the geometry of E , generated by V_{GSD} , between the GSD collection grid and the grounded stage/sample chamber and (ii) the solid angle of the GSD. Of those photons that do

enter the GSD collection grid a certain fraction will suffer reflection and absorption from the perspex vacuum seal, the perspex light pipe, glass window and photocathode before being converted into an amplified current signal by the PMT. Ideally one would like to be able to collect all desirable photons generated in the gas from vacuum UV to IR, however, to do this at this stage of development would be formidable task.

The total number of photons detected by the GSD, N_T^{hv} , cannot be determined directly, and therefore an expression must be derived that relates this quantity to the PMT output voltage (V_{PMT}^{out}) that was measured experimentally.

Letting $\Phi_{hv}(\lambda)$ be the radiant flux of photons, of any particular wavelength (λ), entering the GSD vacuum seal and light pipe, then the photoelectron current generated at the input of the PMT by the photocathode will be

$$I_{PMT}^{in} = \int_{\lambda_1}^{\lambda_2} sk_e(\lambda)_p T(\lambda) \Phi_{hv}(\lambda) d\lambda, \quad (5.4.1)$$

where λ_1 and λ_2 , respectively, are the minimum and maximum photon wavelengths that are converted to photoelectrons by the GSD after the absorption of other photon wavelengths in the vacuum seal, light pipe and photocathode (i.e. $\lambda_2 - \lambda_1$ can be considered as the spectral range of the GSD). The gain of the PMT, G_{PMT} , is equal to the ratio of the output current generated at the anode, I_{PMT}^{out} , to the photoelectron current, therefore,

$$I_{PMT}^{out} = G_{PMT} \int_{\lambda_1}^{\lambda_2} sk_e(\lambda)_p T(\lambda) \Phi_{hv}(\lambda) d\lambda. \quad (5.4.2)$$

The output of the PMT voltage-divider circuit contains a load resistance (R_L) which converts the anode output current to the measured voltage signal, V_{PMT}^{out} , hence,

$$V_{PMT}^{out} = G_{PMT} R_L \int_{\lambda_1}^{\lambda_2} sk_e(\lambda)_p T(\lambda) \Phi_{hv}(\lambda) d\lambda. \quad (5.4.3)$$

The radiant flux of photons incident on the GSD is, by definition, equal to the rate at which photon energy is delivered, or more specifically,

$$\Phi_{hv}(\lambda) = \frac{N_T^{hv} hc}{\lambda}, \quad (5.4.4)$$

where h is Planks' constant (6.626×10^{-34} Js) and c is the speed of light in vacuum (2.998×10^8 m/s). Substituting this expression into equation (5.4.3) and rearranging yields

$$N_T^{hv} = \frac{V_{PMT}^{out}}{G_{PMT} R_L h c} \left[\int_{\lambda_1}^{\lambda_2} \frac{sk_e(\lambda)_p T(\lambda)}{\lambda} d\lambda \right]^{-1}. \quad (5.4.5)$$

As the current of electrons leaving the sample surface, at $z = 0$, is equal to $I_{PE}(\eta + \delta)$, where η and δ are the BSE and SE yields (number of BSEs or SEs emitted from the sample per incident PE), respectively, and current is defined as the rate of charge flow, it can be easily seen that the number of electrons liberated from the stage that generate the gas cascade to produce the N_T^{hv} photons is

$$N_e^g(0) = \frac{I_{PE}(\eta + \delta)}{e}, \quad (5.4.6)$$

where e is the charge of an electron (1.602×10^{-19} C). Dividing equation (5.4.5) by equation (5.4.6) gives steady state photon amplification to be

$$A_{hv} = \frac{e V_{PMT}^{out}}{G_{PMT} R_L h c I_{PE}(\eta + \delta)} \left[\int_{\lambda_1}^{\lambda_2} \frac{sk_e(\lambda)_p T(\lambda)}{\lambda} d\lambda \right]^{-1}. \quad (5.4.7)$$

The contrast setting on the microscopes software interface for the E-T detector and hence the GSD, C_{GSD} , controls G_{PMT} by varying the PMT high tension voltage (V_{HT}) via a digital control line. A plot of G_{PMT} versus V_{HT} , obtained from Philips (1984), is shown in figure 5.3. It can be seen from figure 5.3 that the gain of the Philips XP2012 PMT is

$$G_{PMT} = 133.32e^{5.887 \times 10^{-3} V_{HT}}. \quad (5.4.8)$$

Similarly, figure 5.4 shows a plot of V_{HT} versus C_{GSD} which was obtained experimentally. It can be seen from figure 5.4 that the relationship between the PMT high tension and GSD contrast is

$$V_{HT} = 13.75C_{GSD} + 320.1. \quad (5.4.9)$$

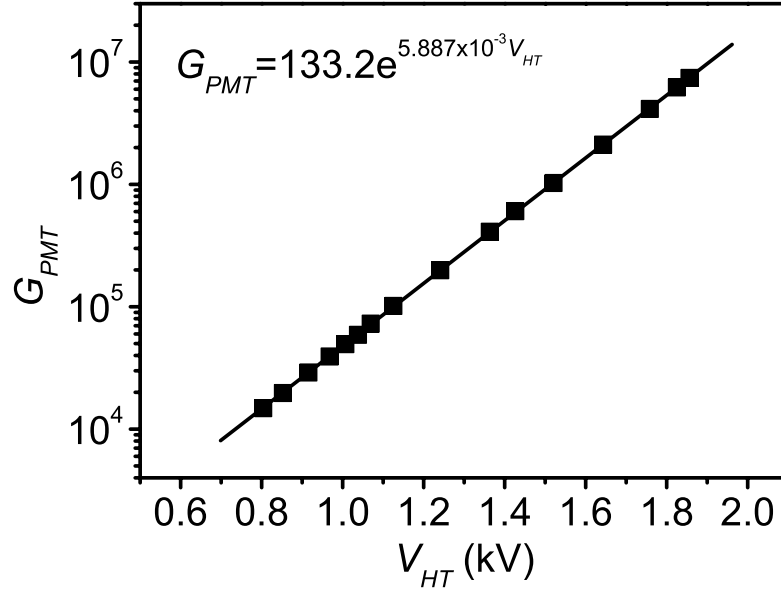


Figure 5.3: PMT gain (G_{PMT}) versus PMT high tension voltage (V_{HT}).

The integral in equation (5.4.7) was numerically integrated over the entire spectral range of the GSD ($\sim 300 - 650$ nm) using Origin[®] (OriginLab Corporation 2002) and was found to be 2.91×10^{-2} W/A.

Substituting equations (5.4.8) and (5.4.9) and the various constants described above into equation (5.4.7) yields an expression for photon amplification, for the GSD used, that is dependant only on microscope parameters and the PMT output voltage recorded:

$$A_{hv} = \frac{9.041 \times 10^{-6} V_{PMT}^{out}}{I_{PE}(\eta + \delta)e^{(8.095 \times 10^{-2} C_{GSD} + 1.884)}}. \quad (5.4.10)$$

It is obvious that the total number of photons reaching the GSD will be a summation of the primary and secondary photon signals generated in the gas by PEs (N_{PE}^{hv}), BSEs (N_{BSE}^{hv}) and SEs (N_{SE}^{hv}) (see section 5.2.1 along with equations (5.3.9), (5.3.13) and (5.3.14)), as well as any CL generated by BSEs impacting insulating surfaces in

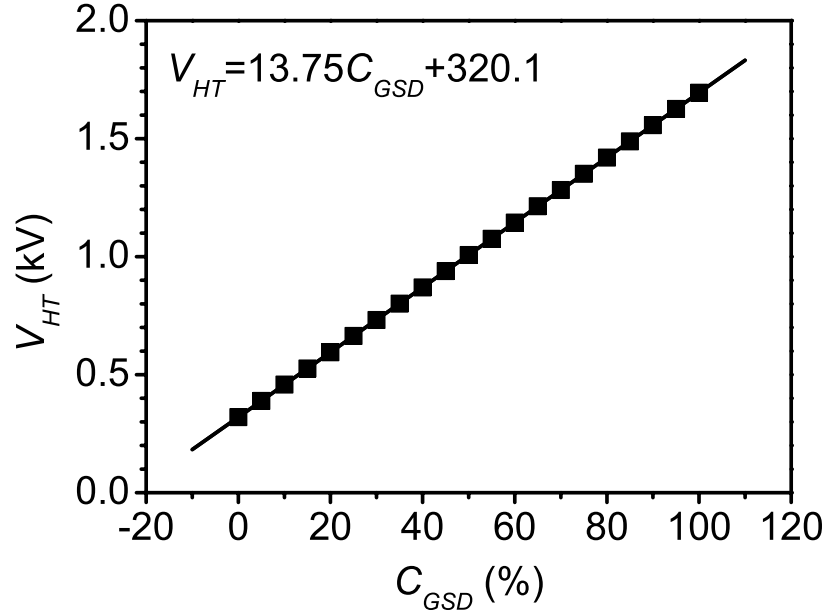


Figure 5.4: PMT high tension voltage (V_{HT}) versus gaseous scintillation detector contrast (C_{GSD}).

the microscope chamber, such as at the plastic vacuum seal of the GSD, N_{CL}^{hv} :

$$N_T^{hv} = N_{PE}^{hv} + N_{BSE}^{hv} + N_{SE}^{hv} + N_{CL}^{hv}. \quad (5.4.11)$$

In order to eliminate most of the contributions from N_{CL}^{hv} the PE beam was initially placed in spot mode at $p \leq 0.1$ torr (minimum pressure obtainable in low vacuum mode) with the GSED ring, or GSD grid, grounded such that the number of gaseous photons generated could be considered negligible and any signal detected would mostly consist of N_{CL}^{hv} . This signal was then measured and subsequently subtracted from the total photon signal obtained at each p , V_{GSED} , V_{GSD} and WD utilized.

5.4.2 Determination of Electronic Amplification

Steady state electronic amplification (A_e) is defined here as the total number of electrons detected by the GSED ring or GSD grid per electron entering the gas cascade at the sample surface. Assuming that charges recombine on the GSED ring or GSD grid continuously and uniformly, then

$$A_e = \frac{I_{GSED/GSD}}{I_{PE}(\eta + \delta)}, \quad (5.4.12)$$

where $I_{GSED/GSD}$ is the current of electrons collected by the GSED ring or GSD grid, depending on which mode of detection was being used (see figure 5.1). In order to generate V_{GSED} , and measure I_{GSED} , the conventional GSED preamplifier was disconnected from the ring and replaced by an Ortec high voltage power supply coupled to a Keithley electrometer, respectively. Similarly, V_{GSD} and I_{GSD} were generated, and measured, using the same circuit.

Akin to A_{hv} , A_e herein cannot be considered a universal measurement of gas amplification that is synonymous to all gaseous SE detection systems, but is only valid in FEI-Philips XL 30 ESEM[®] type microscopes. Electronic gas amplification being dependent on several parameters such as (i) E within the gap and in the vicinity of the detection electrode; (ii) the purity of the imaging gas and (iii) the geometry of the stage, pole piece and surrounding areas of the microscope chamber. Furthermore, the attainment of ‘true’ gas amplification relies on the principles that every electron (i) leaving the sample surface and (ii) generated in the gas cascade via ionization scattering, recombines on the GSED ring or GSD collection grid; and (iii) every positive ion generated in the gas cascade recombines on the stage or sample surface. In reality, a certain fraction of BSEs will not recombine on the GSED ring or GSD grid as a consequence of their cosine emission distribution from the sample (Goldstein *et al.* 1992, Reimer 1985). Also, due to their ‘low’ mobility, diffusion, mutual repulsion and/or electric field effects will cause a certain fraction of gaseous

generated ions to recombine on regions other than the stage or sample surface, such as the chamber walls or pole piece. The extent to which this occurs will depend on the localized ion concentration and E .

5.5 Results and Discussion

In order to study gaseous scintillation detection and amplification in an ESEM one must examine the photon signal collected by the GSD at both quantitative and qualitative levels. In the following, images are shown that were generated using the GSD developed in the present work and the existing GSED in an ESEM. Both imaging modes were used in order for GSD images to be quantitatively investigated as a function of microscope parameters and gas type, and so qualitative comparisons could be made with respect to electronic GSED signals. Following this, photon amplification is quantitatively investigated as a function of microscope operating parameters and gas type using two differing electric field geometries or photon collection methods. The first photon collection method uses the GSED to generate the electron cascade and scintillation, and the GSD to detect the gaseous photons. The second collection method uses the GSD alone to generate, collect and interpret the photon signal generated in the electron cascade. Here, E generated between the GSD collection grid and the grounded stage focuses the electron cascade towards the light pipe assemblage. Using the differing detection techniques enabled the geometrical collection efficiency of photons to be varied in a controlled manner.

5.5.1 Images Obtained Using GSD and GSED

GSD and GSED images of the grounded microscope stage, acquired at various magnitudes of p and E , are shown in figures 5.5, 5.6 and 5.7 when Ar, N₂ and H₂O were employed as the imaging gas, respectively. The GSD images were acquired for the case when the GSED ring was grounded and the GSD was used to generate the electron cascade and detect photons generated in the gas via its positively biased collection grid. It can be seen that the GSD images produced closely replicate the GSED images generated.

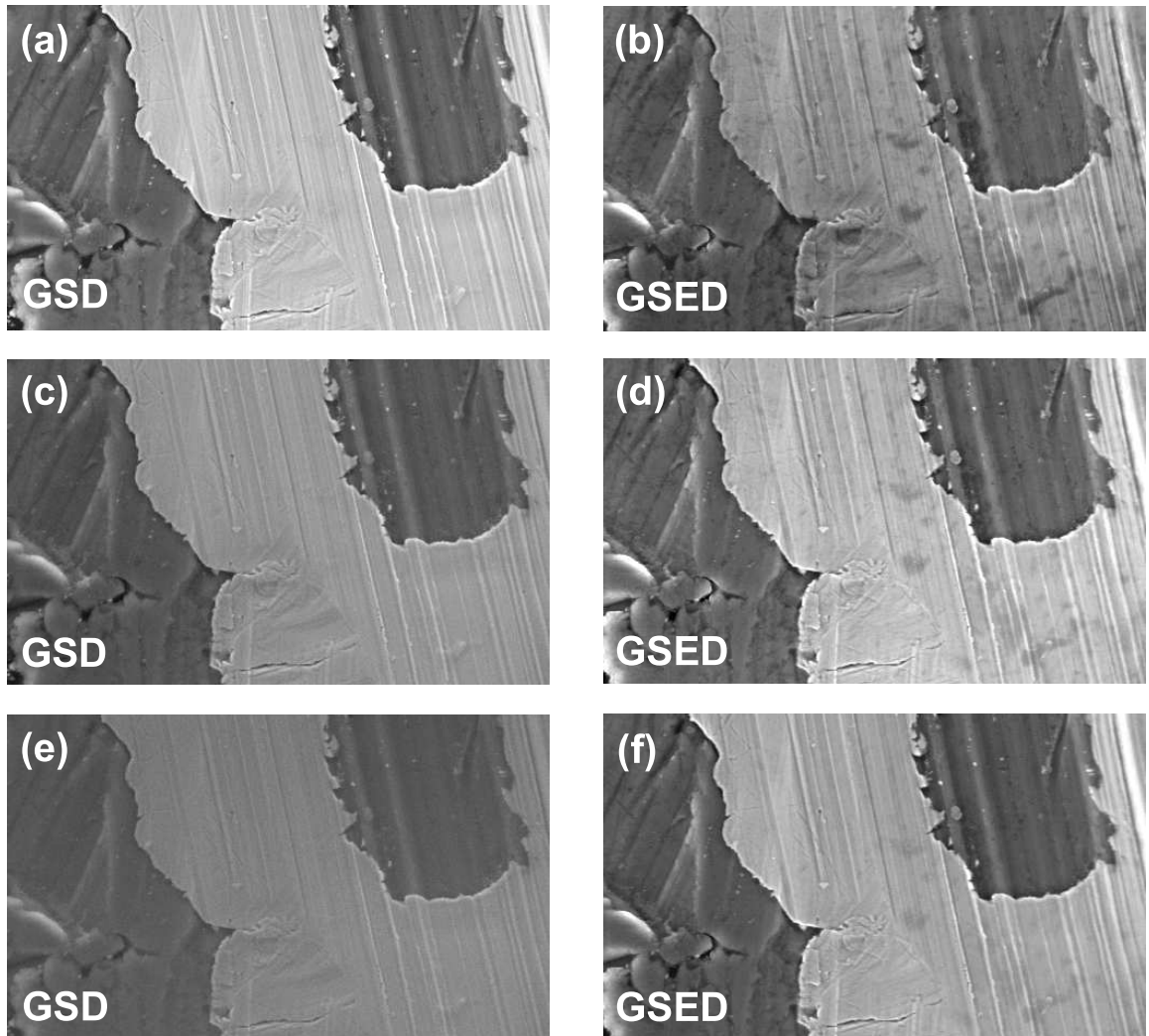


Figure 5.5: Gaseous scintillation detector (GSD) and gaseous secondary electron detector (GSED) images of the microscope stage acquired at various Ar pressures (p_{Ar}) and electric field strengths (E): (a) $V_{GSD} = 390$ V, $p_{Ar} = 0.5$ torr; (b) $V_{GSED} = 334$ V, $p_{Ar} = 0.5$; (c) $V_{GSD} = 330$ V, $p_{Ar} = 0.7$ torr; (d) $V_{GSED} = 248$ V, $p_{Ar} = 0.7$ torr; (e) $V_{GSD} = 290$ V, $p_{Ar} = 0.9$ torr; (f) $V_{GSED} = 221$ V, $p_{Ar} = 0.9$ torr. [$\varepsilon_{PE} = 30$ keV, $WD = 15$ mm, $\tau_L = 60$ ms, $HFW = 190$ μm]

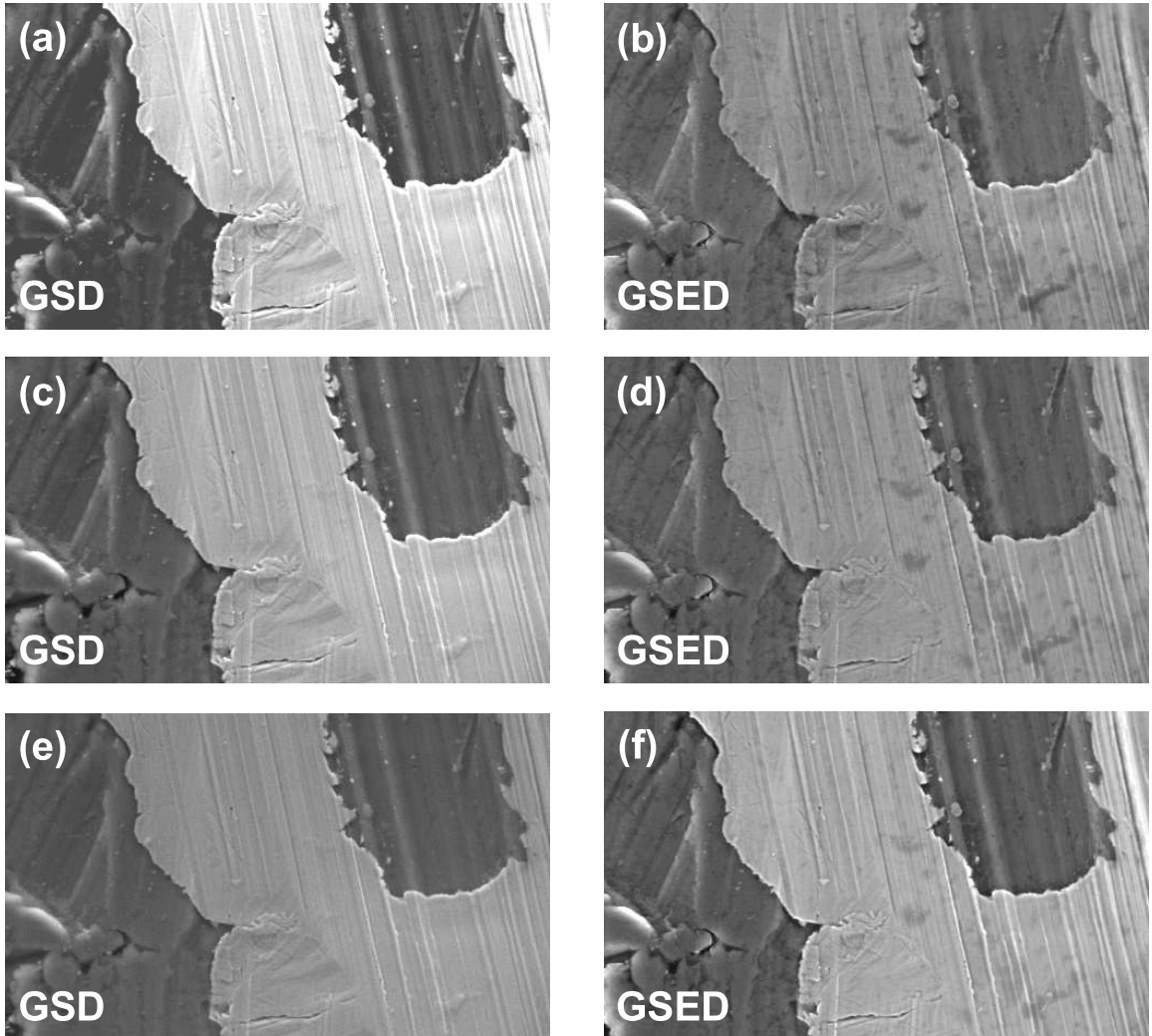


Figure 5.6: Gaseous scintillation detector (GSD) and gaseous secondary electron detector (GSED) images of the microscope stage acquired at various N_2 pressures (p_{N_2}) and electric field strengths (E): (a) $V_{GSD} = 460$ V, $p_{N_2} = 0.5$ torr; (b) $V_{GSED} = 460$ V, $p_{N_2} = 0.5$; (c) $V_{GSD} = 420$ V, $p_{N_2} = 0.7$ torr; (d) $V_{GSED} = 350$ V, $p_{N_2} = 0.7$ torr; (e) $V_{GSD} = 390$ V, $p_{N_2} = 0.9$ torr; (f) $V_{GSED} = 317$ V, $p_{N_2} = 0.9$ torr. [$\epsilon_{PE} = 30$ keV, $WD = 15$ mm, $\tau_L = 60$ ms, $HFW = 190$ μm]

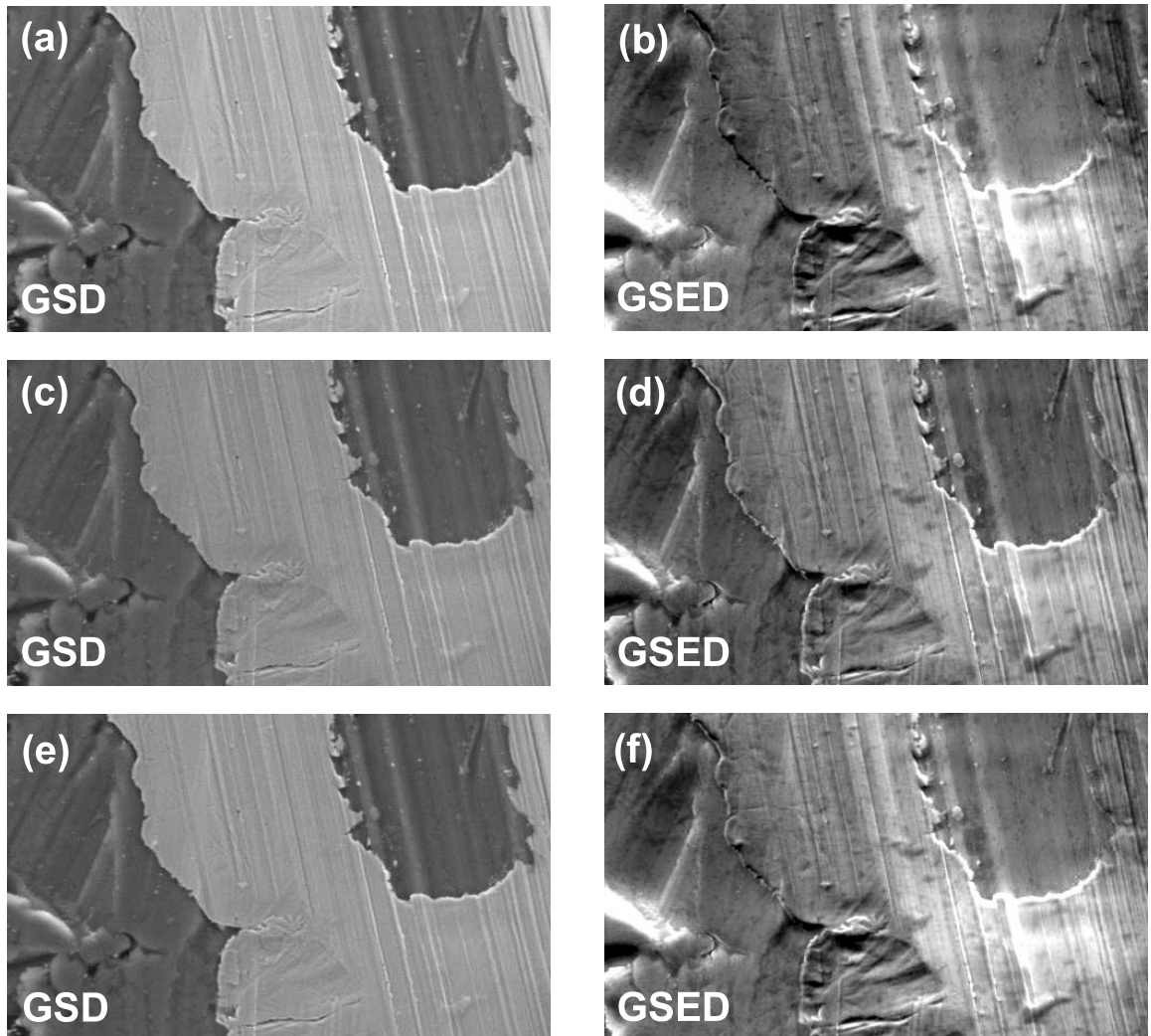


Figure 5.7: Gaseous scintillation detector (GSD) and gaseous secondary electron detector (GSED) images of the microscope stage acquired at various H_2O pressures (p_{H_2O}) and electric field strengths (E): (a) $V_{GSD} = 550$ V, $p_{H_2O} = 0.5$ torr; (b) $V_{GSED} = 550$ V, $p_{H_2O} = 0.5$; (c) $V_{GSD} = 550$ V, $p_{H_2O} = 0.7$ torr; (d) $V_{GSED} = 434$ V, $p_{H_2O} = 0.7$ torr; (e) $V_{GSD} = 560$ V, $p_{H_2O} = 0.9$ torr; (f) $V_{GSED} = 353$ V, $p_{H_2O} = 0.9$ torr. [$\varepsilon_{PE} = 30$ keV, $WD = 15$ mm, $\tau_L = 60$ ms, $HFW = 190$ μm]

In order to identify the contrast associated with figures 5.5-5.7, a BSE and an SE image of the same region of the stage was generated. The BSE and SE images were acquired under high vacuum conditions, with identical microscope operating parameters to that of figures 5.5-5.7, and are shown in figures 5.8(a) and (b), respectively. A low voltage ($\varepsilon_{PE} = 10$ keV) energy dispersive x-ray analysis of the stage revealed that the bright regions are a nickel-phosphorous alloy and the dark regions are aluminium. The edge contrast seen in the SE image of figure 5.8(b) illustrates that the nickel-phosphorous alloy is a thin coating over the aluminium. It can be clearly seen that the strong atomic number contrast (indicated by the bright nickel-phosphorous (higher atomic number) and dark aluminium (lower atomic number) regions) associated with the BSE image is also present in the SE image. The fact that the nickel-phosphorous alloy appears brighter in both the SE and BSE images is a consequence of it possessing much greater SE and BSE yields than that of aluminium (at $\varepsilon_{PE} = 30$ keV: $\delta_{Ni} = 0.106$, $\eta_{Ni} = 0.28$, $\delta_{Al} = 0.075$ and $\eta_{Al} = 0.135$ (Wittry 1966)). The higher resolution topographical contrast (cracks and ridges) seen in the BSE image, which is also present in the SE image to a greater extent, as expected, is due to variations in the number of BSEs emitted from the sample by PEs at the beam impact point (BSE I contrast (Goldstein *et al.* 1992)). By comparing figures 5.5-5.7 with figures 5.8(a) and (b) it can be implied that the contrast associated with the GSD images is due to the generation and detection of gaseous electroluminescence and scintillation arising from both sample emissive SE and BSE signals. The generation of non electroluminescent image contrast, via the detection of photons produced by BSEs striking the Perspex vacuum seal of the GSD, can be eliminated since no image of the stage could be obtained at any pressure when V_{GSD} was set to zero volts. Furthermore, it can be argued that GSD images overall appear to be closer in contrast to GSED and high vacuum SE images than that of BSE images. This demonstrates that the GSD used in this work to investigate photon amplification at a quantitative level is capable of

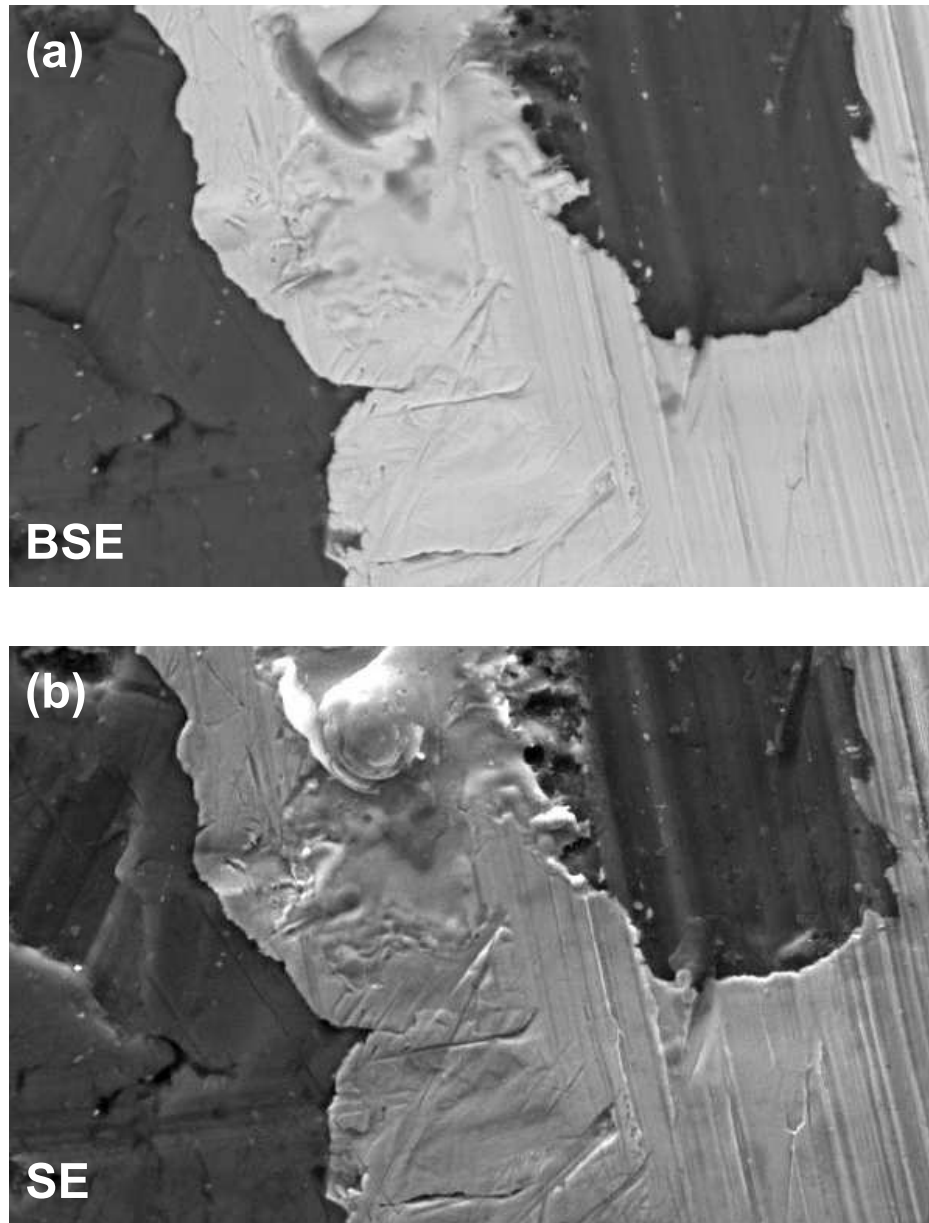


Figure 5.8: Backscattered electron (BSE) (a) and secondary electron (SE) (b) images of the microscope stage acquired under high vacuum conditions, respectively. [$\varepsilon_{PE} = 30$ keV, $WD = 15$ mm, $\tau_L = 60$ ms, $FWHM = 190$ μm]

producing images rich in SE contrast over a wide range of microscope parameters and imaging gases of varying molecular structure. Low pressure peaking of photon amplification versus pressure data, shown and discussed later in sections 5.5.2 and 5.5.3, also supports the above statement.

One of the most important aspects of the images produced is that, for possibly the first time, images were obtained in H₂O, which previously was reported to have a poor scintillation efficiency in ESEM (Danilatos 1986). Interestingly for H₂O (figure 5.7), the GSED image is seen to saturate in contrast whilst the GSD image shows smooth contrast throughout its entirety although the GSD image was obtained at similar E/p . It will be demonstrated in the following photon and electronic amplification results that, of the gases and microscope operating parameters utilized, conditions exist whereby A_e shows onsets of gaseous breakdown, which in turn would produce image saturation, whilst A_{hv} results suggest that such a phenomenon does not occur. This implies that, once refined, gaseous scintillation detection could be superfluous over existing detection methods in producing high contrast SE images in low vacuum SEM.

5.5.2 Photon and Electronic Amplification Using the GSED to Generate Gaseous Scintillation

Here, results are presented for the case when the GSED was used to generate the electron cascade and subsequent electroluminescence (see figure 5.1). The photons produced in the region between the GSED and the stage were detected by the GSD with a grounded collection grid. It is therefore obvious that due to the off axis symmetry of the GSD, relative to the GSED, any photons collected were either (i) direct 'line of site' photons that radiated spherically from electron avalanches within the gap or (ii) photons that suffered reflection(s) from the plane mirror used to direct

light towards the GSD collector grid/light pipe or the specimen chamber walls, pole piece and stage etc.

Gaseous Secondary Electron Detector Bias Dependence on Amplification

Steady state gaseous photon and electronic amplification versus V_{GSED} are shown in figure 5.9 for (a) Ar, (b) N₂ and (c) H₂O at $p_{Ar} = p_{N_2} = p_{H_2O} = 1$ torr and $WD = 15$ mm. The amplification profiles were obtained up to the largest V_{GSED} achievable before the onset of gaseous breakdown. It can be seen from the figure that (i) both A_{hv} and A_e increase exponentially with V_{GSED} and (ii) $A_e > A_{hv}$. The relative trend in A_{hv} closely resembles A_e for all the gases over the entire range of V_{GSED} used. The slight differences between trends in A_{hv} and A_e can be attributed to random experimental errors as a result of small fluctuations in microscope parameters and gas properties, such as p and PE beam power. Ar exhibits the greatest A_{hv} , followed by N₂, and then H₂O. However, on the contrary A_e is greatest for H₂O, followed by Ar and then N₂. Generally speaking, the excitation energy transferred to a monatomic gas species such as Ar from cascading electrons is mostly electronic as the atom has no vibrational modes to absorb energy. This means that there is a higher probability that a monatomic molecule will reach a particular resonant electronic level(s) and hence a greater probability of photon emission after the atom relaxes. For the case of diatomic and polyatomic gas molecules, such as N₂ and H₂O, respectively, the excitation energy absorbed during an electron-molecule inelastic collision is also converted into differing modes of rotation and vibration (or dissociation) and hence the probability of resonant photon production in the wavelength range of the detection system utilized is lower than that of a monatomic gas (von Engel 1965).

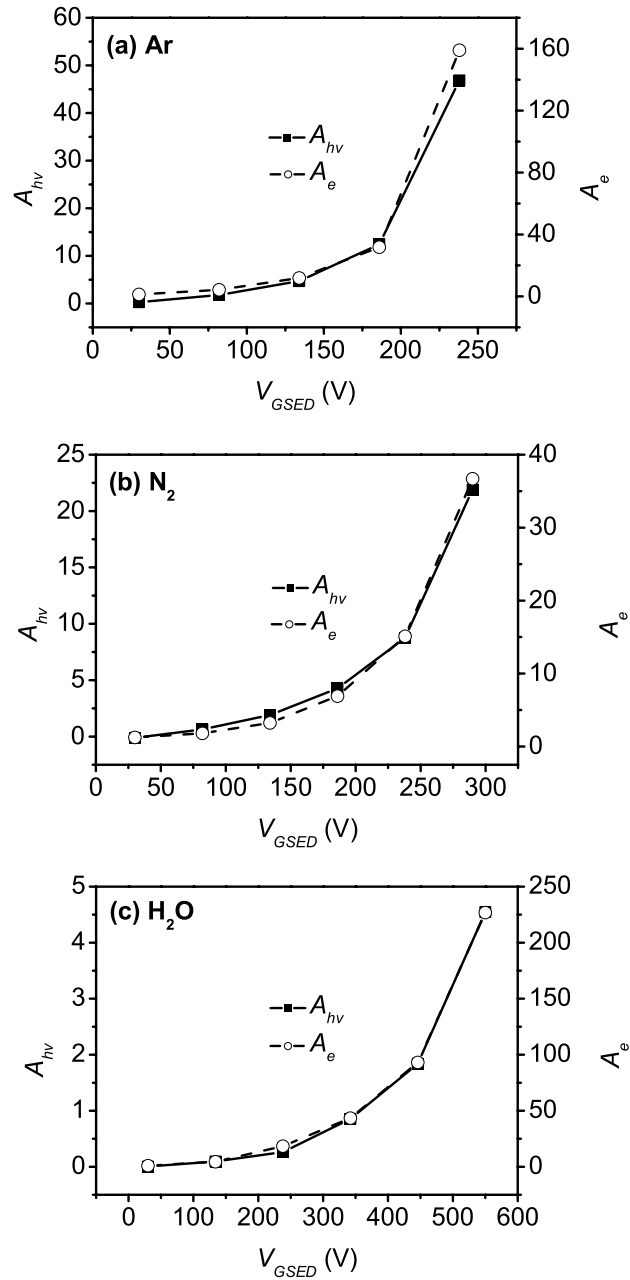


Figure 5.9: Steady state photon amplification (A_{hv}) and electronic amplification (A_e) versus gaseous secondary electron detector (GSED) bias (V_{GSED}) in (a) Ar, (b) N₂ and (c) H₂O. [$\varepsilon_{PE} = 30$ keV, $p_{Ar} = p_{N_2} = p_{H_2O} = 1$ torr, $WD = 15$ mm]

Specimen Chamber Pressure Dependence on Amplification

Steady state photon and electronic amplification versus p are plotted in figure 5.10 for (a) Ar [$V_{GSED} = 186$ V], (b) N₂ [$V_{GSED} = 186$ V] and (c) N₂ [$V_{GSED} = 290$ V], at $WD = 15$ mm. Corresponding amplification profiles for H₂O are shown separately in figure 5.11 for (a) $V_{GSED} = 186$ V, (b) $V_{GSED} = 238$ V, (c) $V_{GSED} = 446$ V and (d) $V_{GSED} = 498$ V. It can be seen from all of the plots that Ar exhibits the greatest magnitude of A_{hv} , over the entire pressure range, of the gases used, followed by N₂ then H₂O. Once again it can be seen that $A_e > A_{hv}$. In Ar, maximum A_{hv} occurs at $p_{Ar} = 2$ torr whilst A_e peaks at 3 torr. The range over which V_{GSED} could be varied in Ar was limited as a consequence of its low breakdown potential. Ar was found to suffer gaseous breakdown and flashover, under the conditions utilized, at $V_{GSED} \approx 200$ V. For the case of N₂, A_{hv} peaks at $p_{N_2} = 2$ torr for $V_{GSED} = 186$ V and peaks at a slightly higher p_{N_2} at $V_{GSED} = 290$ V, whereas A_e peaks at $p_{N_2} = 3$ torr for both $V_{GSED} = 186$ V and $V_{GSED} = 290$ V. Interestingly, in H₂O and N₂ it can be seen that the peak in A_e remains independent of V_{GSED} , whilst p_{H_2O} at which maximum A_{hv} occurs, increases with increasing V_{GSED} . In H₂O, the peak in A_{hv} occurs at similar p_{H_2O} to that of A_e under conditions of high E .

The efficiency at which BSEs and PEs ionize the gas and produce subsequent amplified ESE signals as well as the extent to which PEs are scattered out of the focused probe, forming a skirt of electrons that degrades signal in images, increases with increasing p (Danilatos 1988, Farley & Shah 1990a, Meredith *et al.* 1996, Moncreiff *et al.* 1979). Therefore, the ratio of the peak amplification to the ‘high’ pressure plateau region of gas amplification data versus pressure can be used to represent signal-to-background, or more specifically, as SE amplification dominates at ‘low’ p (Fletcher *et al.* 1997, Fletcher *et al.* 1999), SE signal-to-background ratios ($(S/B)_{SE}$). It must be noted that $(S/B)_{SE}$, quoted herein, specifically refers to the ratio of (i) SE scintillation or electronic SE amplified signals to that of (ii) PE and BSE scintillation

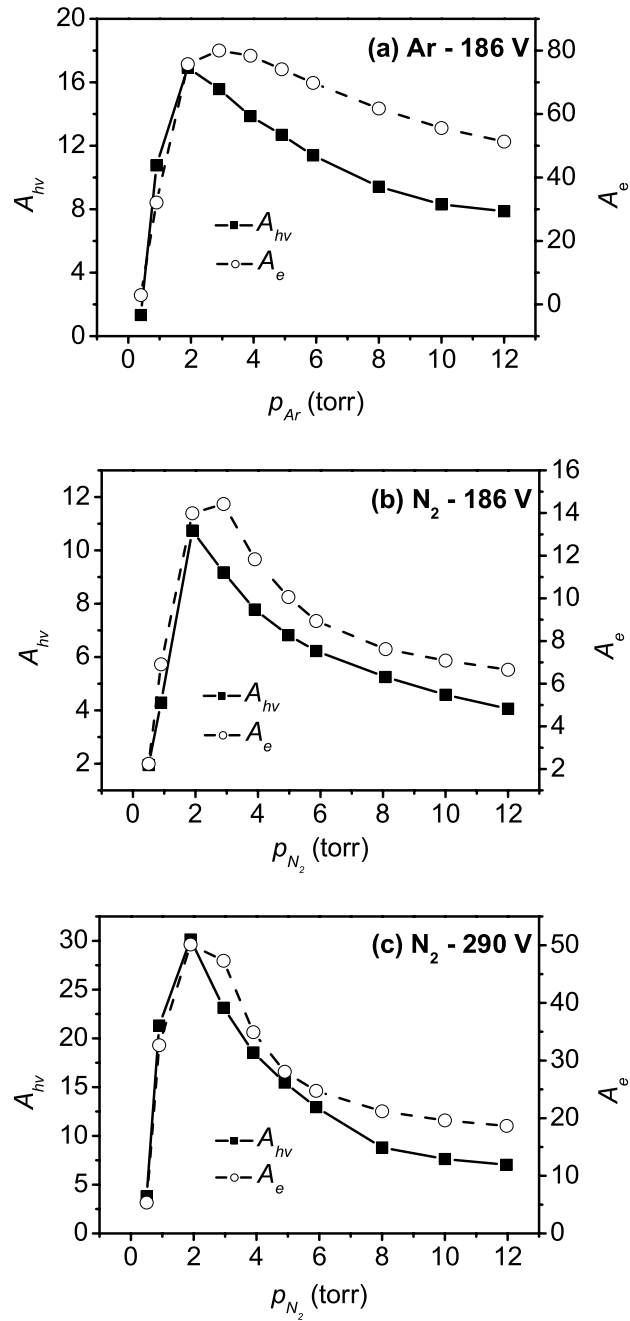


Figure 5.10: Steady state photon amplification (A_{hv}) and electronic amplification (A_e) versus specimen chamber pressure (p) in (a) Ar [$V_{GSED} = 186$ V], (b) N₂ [$V_{GSED} = 186$ V] and (c) N₂ [$V_{GSED} = 290$ V]. [$\varepsilon_{PE} = 30$ keV, $WD = 15$ mm]

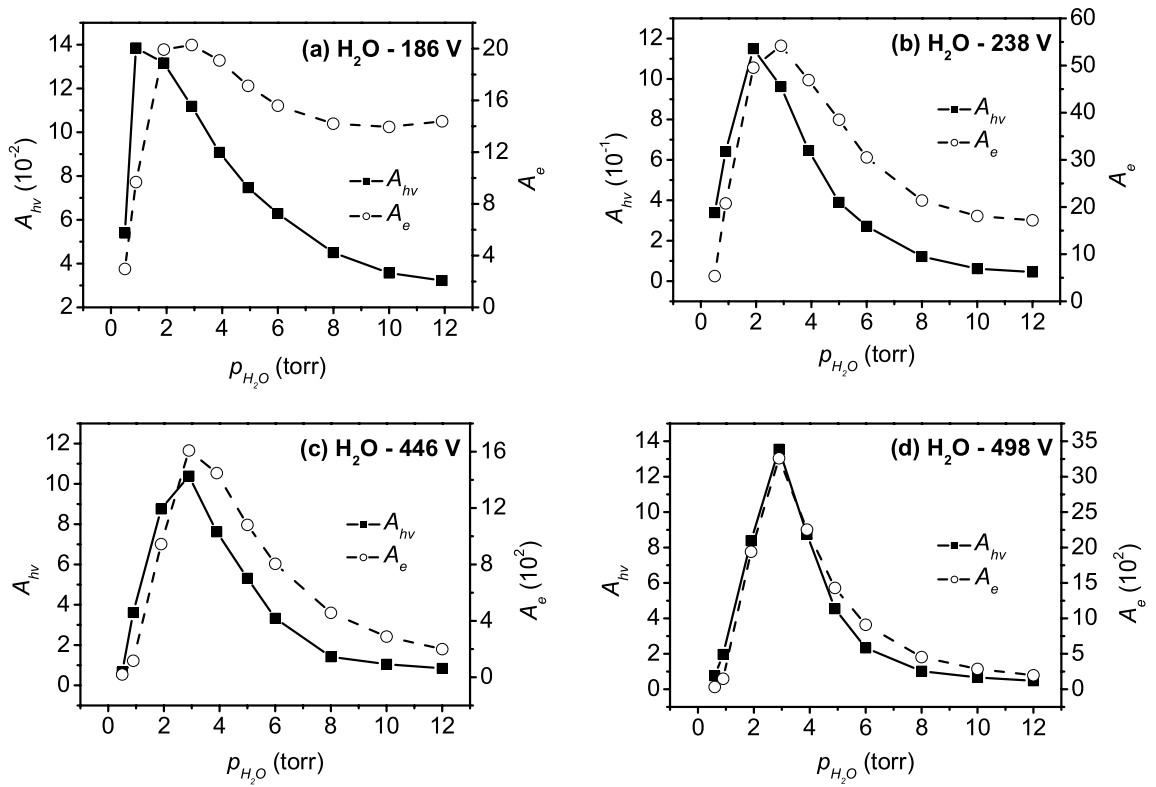


Figure 5.11: Steady state photon amplification (A_{hv}) and electronic amplification (A_e) versus specimen chamber pressure (p) in (a) H_2O [$V_{GSED} = 186$ V], (b) H_2O [$V_{GSED} = 238$ V], (c) H_2O [$V_{GSED} = 446$ V] and (d) H_2O [$V_{GSED} = 498$ V]. [$\varepsilon_{PE} = 30$ keV, $WD = 15$ mm]

or electronic PE and BSE amplified signals, respectively. Shot and thermal noise, which are obviously present, were not considered in the present analysis.

It can therefore be proposed, by comparing the amplification data obtained from each of the gases, that: (i) Electroluminescent SE signal-to-background ratios $((S/B)_{SE}^{hv})$ are greater in magnitude than that of electronic SE signal-to-background ratios $((S/B)_{SE}^e)$; (ii) Both $(S/B)_{SE}^{hv}$ and $(S/B)_{SE}^e$ increase with increasing V_{GSED} accompanied by a shift in maximum A_{hv} to higher p with increasing V_{GSED} (the trends in electronically amplified signals associated with variations in microscope operating parameters has recently been reported by Fletcher *et al.* (1997) and Fletcher *et al.* (1999) and therefore will not be discussed further); (iii) H₂O exhibits the greatest $(S/B)_{SE}^{hv}$ followed by N₂ and Ar.

The former (i above) is based on the premise that low energy electrons, such as SEs and ESEs, are capable of efficiently exciting gas molecules to electroluminescent resonance levels below the onset of ionization (ionization threshold). Conversely, high energy BSEs and PEs involved in inelastic collisions with gas molecules have greater probabilities of exciting molecules to energies that exceed the ionization potential of the gas, hence promoting ionization rather than scintillation. Therefore, at low p , where low energy electrons are rapidly accelerated to kinetic energies whereby efficient electroluminescence and ionization occurs, SE signals dominate over PE and BSE signals. At such pressures the kinetic energies of most high energy electrons are too great to cause them to deviate from their initial paths, via Coulombic attractions with gas molecules, and undergo subsequent excitation or ionization reactions. Hence, head-on type collisions will generally only produce excitation or ionization reactions. However, at higher p , contrary to BSEs and PEs, SEs are not capable of gaining sufficient energy between collisions with gas molecules to promote ionization but are still capable of exciting molecules to optical levels that produce electroluminescence. Therefore, the magnitude of the high pressure background level relative to

the low pressure SE peak, at fixed V_{GSED} , is greater for electronic signals than that of photon signals or $(S/B)_{SE}^{hv} > (S/B)_{SE}^e$. Although electroluminescent SE signal-to-background ratios are seen to be superior to that of electronic amplification signals, the net gain possessed by that of electronic signals are greater in magnitude. This obviously being a consequence of the rather low photon collection efficiency obtained, which at this stage of investigations has not been optimized. Enhancement of photon signals possibly being achieved via the use of specialized mirrors to direct photons towards the light pipe assemblage, or as will be seen in the proceeding section, electrostatic focusing of the cascade and resulting electroluminescent emissions.

In response to (ii) ascribed above, the efficiency with which low energy electrons produce both ionization and excitation can be described by equation (3.10.1) of chapter 3.10. It can easily be seen through taking the derivative of equation (3.10.1) with respect to p , that the magnitude of p at which maximum ionization or excitation efficiency occurs is given by

$$p_{max} = \frac{E}{B}. \quad (5.5.1)$$

The gas specific constant B in Eq. (5.5.1) is defined as the ratio of (i) the average electron energy required to produce ionization or excitation, which can be estimated as the first ionization potential (V_i^1), in the case of electronic amplification, or the first excitation potential (V_e^1), for photon amplification, respectively; and (ii) the mean free path of SEs (λ_{SE}) (von Engel 1965, Nasser 1971). For the case of electronic amplification Eq. (5.5.1) can be expressed as

$$p_{max}^e = \frac{E\lambda_{SE}^e}{V_i^1}, \quad (5.5.2)$$

and similarly for photon amplification

$$p_{max}^{hv} = \frac{E\lambda_{SE}^{hv}}{V_e^1}, \quad (5.5.3)$$

where λ_{SE}^e and λ_{SE}^{hv} are the SE mean free paths, at unit pressure, associated with ionization and excitation, respectively (von Engel 1965, Nasser 1971). It can be seen

from Eqs. (5.5.2) and (5.5.3) that the magnitude of p at which maximal SE efficiency occurs increases with increasing E . For all gases, the condition $V_e^1 < V_i^1$, occurs as a result of the numerous electronic and vibrational levels that exist below V_i^1 . In the case of Ar, $V_e^1 = 11.6$ eV and $V_i^1 = 15.7$ eV, and for N₂, $V_e^1 = 6.1$ eV and $V_i^1 = 15.5$ eV (von Engel 1965). Therefore, from the condition stated above, and the observations from Fig. 5.10, that p_{max}^{hv} shifts to higher values with increasing V_{GSED} and $p_{max}^e > p_{max}^{hv}$ at fixed E , it is evident that the trends seen are a consequence of the condition: $\lambda_{SE}^e \gg \lambda_{SE}^{hv}$. Although it can be speculated that the shifts in p_{max}^{hv} are due to an increase in the number of photons, generated by cascaded SEs that were produced via BSEs impacting the GSD grid and light pipe assemblage, the fact that $(S/B)_{SE}^{hv}$ increases, and peak widths decrease, with increasing V_{GSED} , eliminates this possibility. If electroluminescent PE and BSE amplified signals increased with increasing V_{GSED} one would expect the resulting A_{hv} profiles to not look as sharp and well defined at higher p , but rounded with their FWHMs extending over a greater p range.

The latter (response (iii) ascribed above) is attributed to Ar exhibiting the largest ‘effective’ atomic radius, and hence the greatest PE and BSE ionization efficiencies as well as primary scintillation efficiencies, followed by those for N₂ and subsequently H₂O (see chapter 2.3.1 and figure 2.3). Along with the enhanced primary scintillation produced, subsequent ESE cascades produced by the PEs and BSEs efficiently exciting electroluminescent (secondary scintillation) levels in Ar, via the mechanisms described previously in sections 5.2.1 and 5.5.2. As a consequence of their molecular nature, both N₂ and H₂O should indeed exhibit lower primary scintillation efficiencies relative to secondary SE scintillation efficiencies, and hence greater $(S/B)_{SE}^{hv}$ values, than that of Ar, in the photon wavelength range utilized. Secondary SE scintillation efficiencies being greater than that of primary scintillation efficiencies in N₂ and H₂O as a result of their efficient SE production ability,

through ionization, increasing the number of cascading electrons capable of generating photons.

Working Distance Dependence on Amplification

Plots of A_{hv} and A_e versus WD are shown in figure 5.12 for (a) Ar, (b) N_2 and (c) H_2O , at $V_{GSED} = 186$ V and $p_{Ar} = p_{N_2} = p_{H_2O} = 1$ torr. It can be seen that (i) $A_e > A_{hv}$ and (ii) both A_{hv} and A_e increases with WD and, in both Ar and N_2 , follow a similar trend with WD . In H_2O , however, there is a significant difference between A_{hv} and A_e . Here, A_{hv} is seen to rise initially at a greater rate than A_e , reach a maximum at approximately $WD = 12$ mm, then decrease with increasing WD before levelling off. An increase in WD is accompanied by an increase in the total gas path length through which ionization and excitation reactions can occur with gas molecules. However, this increase in path is also accompanied by a reduction in E through which electrons are accelerated. The peak in A_{hv} versus WD , in H_2O , can therefore be attributed to the point at which retardation in electroluminescent gain through decreasing E overcomes the increase in amplification via increasing path length. The peak in A_{hv} for H_2O occurring at a lower WD than that of Ar and N_2 as a result of its requirements for a greater magnitude of E for equivalent photon production.

When the GSED is used to generate the electron cascade and subsequent gaseous scintillation, it is suggested that changes in WD may cause variations in photon collection efficiency. Changing the total gas path length through which electrons can cause ionization and excitation reactions with gas molecules also affects the localized magnitude of E within the gap and subsequently the localized photon generation rate. As gas luminescence through direct excitation and recombination processes is expected to maximize in localized regions of enhanced E , it is proposed that differences in A_{hv} , with respect to A_e , may also be a consequence of localized enhanced

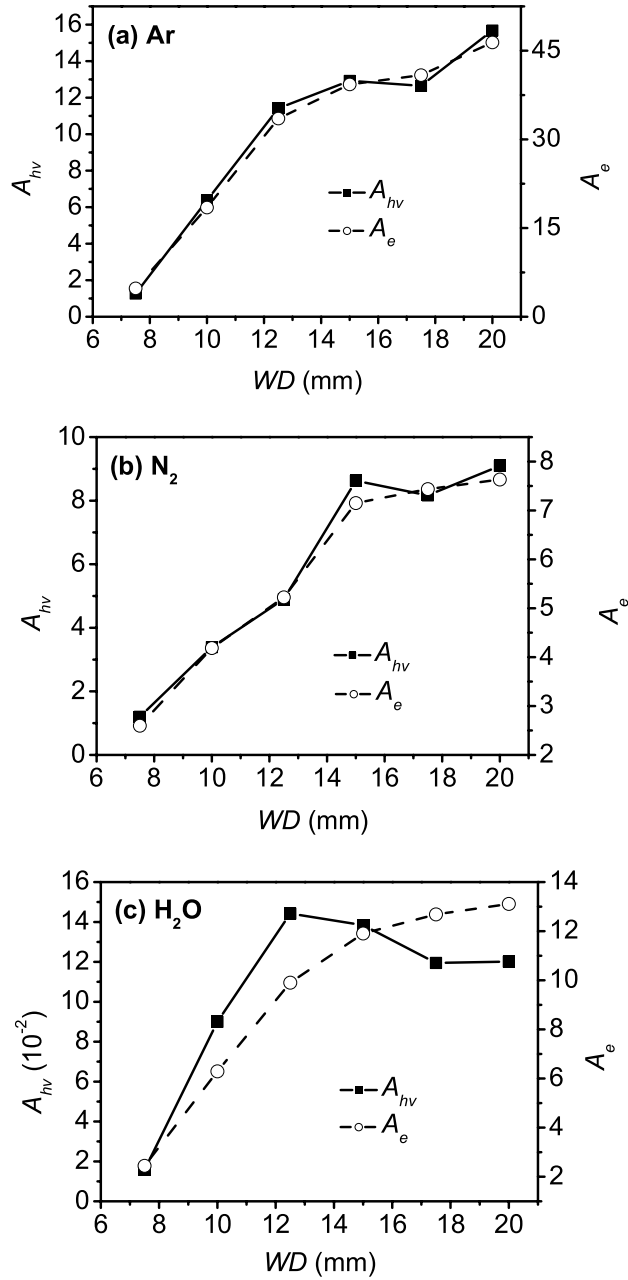


Figure 5.12: Steady state photon amplification (A_{hv}) and electronic amplification (A_e) versus working distance (WD) in (a) Ar, (b) N₂ and (c) H₂O. [$\varepsilon_{PE} = 30$ keV, $V_{GSED} = 186$ V, $p_{Ar} = p_{N_2} = p_{H_2O} = 1$ torr]

luminescence regions shifting within the gap with WD , hence altering the ‘effective’ solid angle for photon collection.

In summary, it can be seen from all of the results presented here, whereby secondary scintillation/electroluminescence is generated by the GSED ring and detected by GSD, that relative trends in the magnitude of A_{hv} with V_{GSED} and WD exhibit only subtle deviations from A_e . However, as p varies, there is a significant difference between A_{hv} and A_e profiles. It is also seen that A_e is greater in magnitude than that of A_{hv} . Obviously the latter is a major consequence of the ‘effective’ solid angle for photon collection being significantly small when the light pipe used to collect photon signals is positioned at relatively large distances from the region where most of the scintillation and electroluminescence is generated in the gap. Furthermore, differences in the magnitudes of A_{hv} and A_e are likely to be a consequence of photon emissions being quenched by the imaging gas, which would be strongly dependent on p .

5.5.3 Photon and Electronic Amplification Using the GSD to Generate Gaseous Scintillation - Enhancement of Photon Collection Utilizing Electrostatic Focusing

The efficiency at which photons are generated in a gas has been shown previously (see equation (3.10.1)) to increase with increasing E . Therefore, regions within the gap experiencing elevated E should exhibit enhanced electroluminescence production compared to that of other regions of lower E . To illustrate this, figure 5.13 shows an image of the visible gas luminescence produced in Ar under discharge conditions. The toroidal symmetry of the GSED ring produces an intense electric field gradient that extends with decreasing strength towards the stage. It can be seen from figure 5.13 that just below the ring exists a localized region of enhanced luminescence corresponding to the intense magnitude of E in this region. It is therefore evident

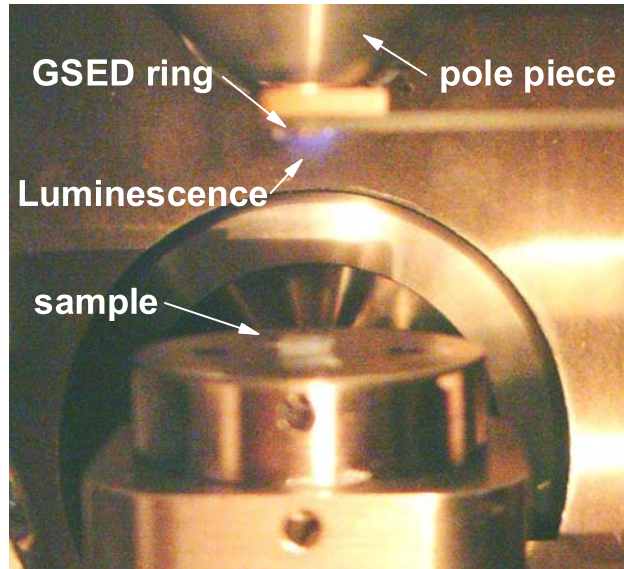


Figure 5.13: Visible gas luminescence produced in argon (Ar) under discharge conditions. [$\varepsilon_{PE} = 30$ keV, $V_{GSED} = 290$ V, $p_{Ar} = 1$ torr, $WD = 15$ mm]

that if electroluminescent signals are collected from a region of enhanced E , where the photon generation rate is enhanced and electroluminescence is confined, that the ‘effective’ solid angle for collection will be larger compared to that of attempting to collect the diffuse plume of symmetrically radiating photons from larger distances. One way that this can be achieved, without the use of mirrors that may contribute further to unwanted background signals, is to electrostatically focus the electron cascade towards the entrance of a light pipe exhibiting strong E , such as the GSD used in the present work.

Here, results are presented for the case when the GSD was used to both generate, and detect, the electron cascades and subsequent electroluminescence, respectively. During operation of the GSD the GSED was maintained at ground potential to ensure that the magnitude of E in the vicinity of the GSD collection grid was maximized.

Utilizing the GSD enabled the electron cascade to be directed towards its collection grid which subsequently focused electroluminescent signals towards the light pipe, enhancing the photon collection efficiency.

Gaseous Scintillation Detector Bias and Working Distance Dependence on Amplification

The data shown in figures 5.14 and 5.15 represent steady state A_{hv} and A_e obtained as a function of V_{GSD} and WD in (a) Ar, (b) N₂ and (c) H₂O, respectively. It can be seen that (i) in Ar and N₂, $A_{hv} > A_e$ and (ii) both A_{hv} and A_e follow very similar trends with V_{GSD} and WD as that of when the GSED was used to generate electronic and electroluminescent signals, shown previously in figures 5.9 and 5.12. Therefore, the discussions presented in sections 5.5.2 and 5.5.2 are also applicable to describe the trends associated with A_{hv} and A_e for the case of when the GSD was utilized to generate and detect amplified signals.

Specimen Chamber Pressure Dependence on Amplification

Figure 5.16 shows profiles of A_{hv} and A_e versus p for (a) Ar [$V_{GSD} = 186$ V], (b) N₂ [$V_{GSED} = 186$ V], (c) N₂ [$V_{GSED} = 290$ V], (d) H₂O [$V_{GSED} = 186$ V] and (e) H₂O [$V_{GSED} = 446$ V], at $WD = 15$ mm. The profiles once again show that (i) in Ar and N₂, $A_{hv} > A_e$, (ii) $(S/B)_{SE}^{hv}$ values increase with V_{GSD} and (iii) $(S/B)_{SE}^{hv}$ is greatest in H₂O followed by N₂ and Ar; as was the case when the GSED was used to generate signals. However, the main feature of the profiles is that whilst electronic signals show a continual increase in total amplification with p , indicating rather poor $(S/B)_{SE}^e$ levels, as a result of enhanced amplification of sample emissive PE and BSE signals, A_{hv} exhibits exceptional $(S/B)_{SE}^{hv}$ values. The high background levels associated with electronic amplified signals is attributed to BSEs striking the biased grid of the GSD,

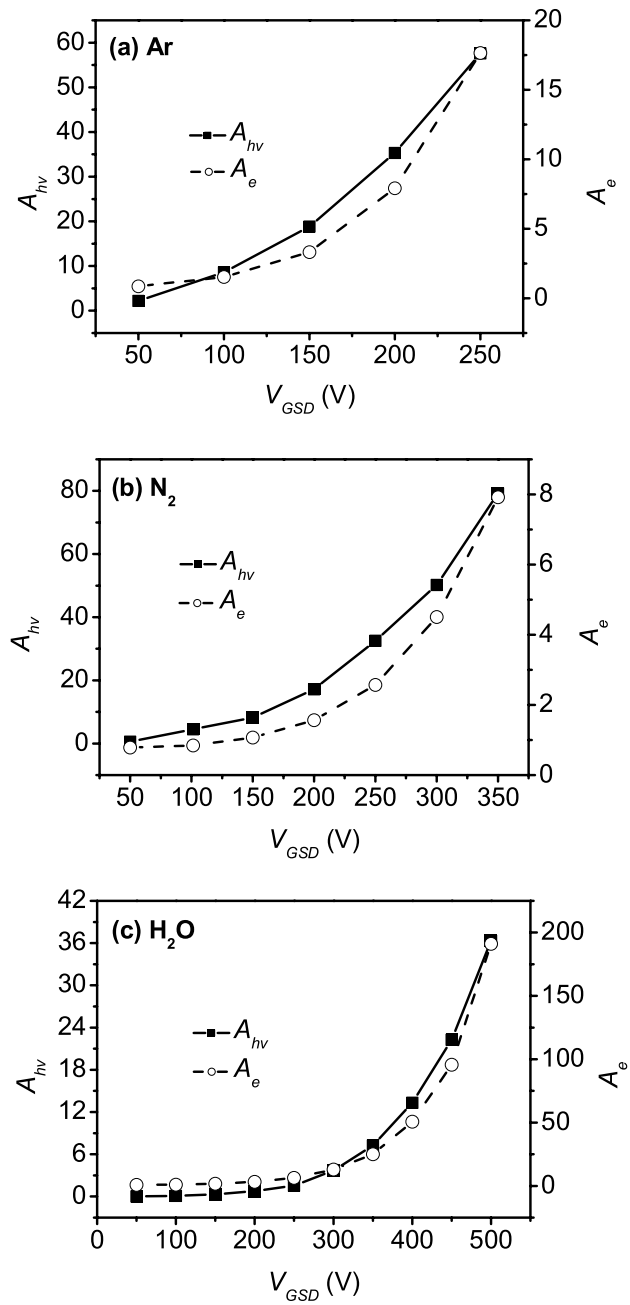


Figure 5.14: Steady state photon amplification (A_{hv}) and electronic amplification (A_e) versus gaseous scintillation detector (GSD) grid bias (V_{GSD}) in (a) Ar, (b) N_2 and (c) H_2O . [$\varepsilon_{PE} = 30$ keV, $p_{Ar} = p_{N_2} = p_{H_2O} = 1$ torr, $WD = 15$ mm]

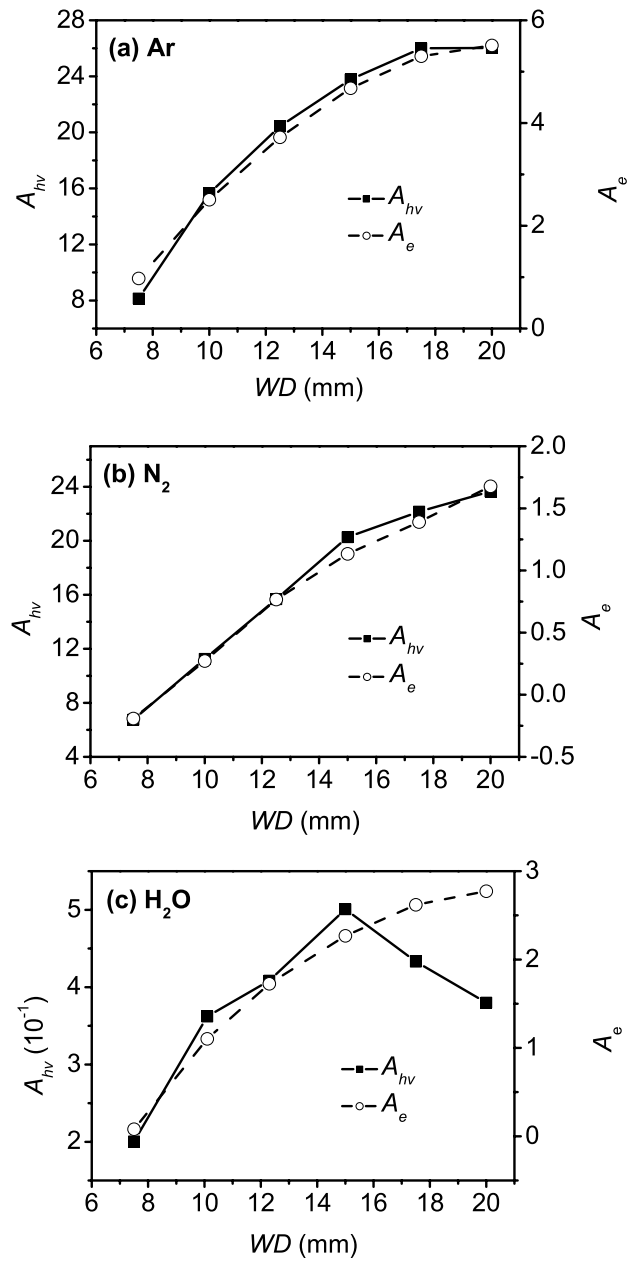


Figure 5.15: Steady state photon amplification (A_{hv}) and electronic amplification (A_e) versus working distance (WD) in (a) Ar, (b) N₂ and (c) H₂O. [$\varepsilon_{PE} = 30$ keV, $V_{GSD} = 186$ V, $p_{Ar} = p_{N_2} = p_{H_2O} = 1$ torr]

generating type III SEs (spurious electrons generated at chamber walls or other non detecting media (Goldstein *et al.* 1992, Reimer 1985)) that are further amplified and detected. The profiles shown in figures 5.10 and 5.11, for the case when the GSED was used to generate and detect electronic signals, exhibited greater $(S/B)_{SE}^e$ values than those shown here as a consequence of the GSED suppressor electrode (see section 2.4 and figure 2.11) being capable of discriminating against type III SEs (Philips Electron Optics 1997).

Comparing all of the photon amplification data versus microscope operating parameters here to those in section 5.5.2 illustrates that detected electroluminescent/scintillation signals are (i) greater in magnitude than that of electronic signals, in the case of Ar and N₂ and (ii) up to ≈ 7 times greater in magnitude, utilizing the GSD to both generate and detect photons compared to that of when the GSED is used to generate signals. This demonstrates that dragging the electron cascade towards the light pipe or electrostatic focusing significantly improves the collection efficiency of cascade generated electroluminescent photon signals. This overall enhancement of photon signal being attributed to a greater ‘effective’ solid angle of collection and a reduction in gaseous quenching effects.

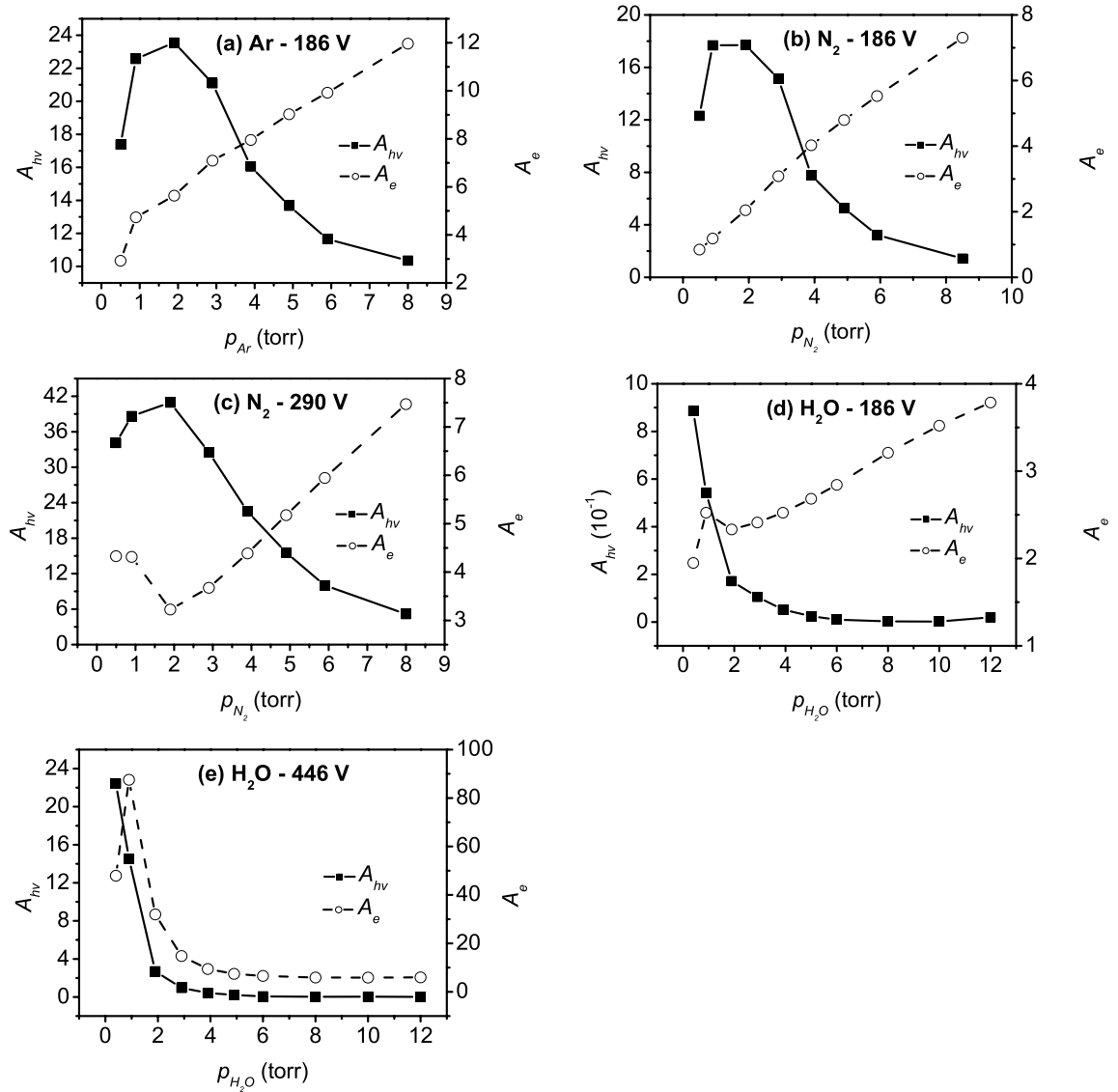


Figure 5.16: Steady state photon amplification (A_{hv}) and electronic amplification (A_e) versus specimen chamber pressure (p) in (a) Ar [$V_{GSD} = 186$ V], (b) N₂ [$V_{GSD} = 186$ V], (c) N₂ [$V_{GSD} = 290$ V], (d) H₂O [$V_{GSD} = 186$ V] and (e) H₂O [$V_{GSD} = 446$ V]. [$\varepsilon_{PE} = 30$ keV, $p_{Ar} = p_{N_2} = p_{H_2O} = 1$ torr, $WD = 15$ mm]

5.6 Future Work

The detection of gaseous proportional scintillation has several major benefits over conventional methods of image formation in an ESEM that rely on ionization and subsequent collection of electronic signals. For example, electroluminescence can be generated in the gas at electron energies below the ionization potential of the gas due to the existence of various resonance lines in this energy region. Therefore, scintillation detection can be performed at 'low' reduced electric fields prior to the onset of ionization. Consequently, the concentration of ions in the gap can be minimized, reducing or possibly eliminating the detrimental effects of (i) space charge formation (e.g. contrast reversal effects in images), (ii) signal loss through SE-ion recombination (e.g. reduced SE amplification and streaking in images) and (iii) cathodic SE emission and gas breakdown via ion impact (e.g. saturation of electronics). Furthermore, wavelength filtering of the primary and secondary scintillation produced in the gas, using optical bandpass filters, quenching or wavelength shifting gases (Al-Dargazelli *et al.* 1981, Alves & Policarpo 1967, Mutterer 1982, Policarpo *et al.* 1971), or convolution techniques, can also be employed in order to eliminate unwanted PE, skirt, BSE and SE type II, III, IV signals (see Goldstein *et al.* (1992) and Philips Electron Optics (1996) for definitions of SE signal types). This approach should enable, true, high resolution SE I imaging with dramatic improvements in image quality and signal-to-background ratios. However, before such filtering can be accomplished spectroscopic studies need to be performed to identify the characteristic wavelengths associated with each of the signal types ascribed above as well as other reaction processes occurring, such as recombination luminescence. Once the desired wavelengths are known then efficient GSD systems can be implemented utilizing PMTs of optimum spectral range in conjunction with efficient photon collection electric fields and optical geometries.

5.7 Conclusions

This work showed that gaseous scintillation detection in an ESEM can produce images abundant in SE contrast when primary and avalanche generated photons are detected over a wavelength range of 300-650 nm in Ar, N₂ and H₂O. The present study also developed a theoretical model, based on existing Townsend relations, to describe the generation of primary scintillation and electroluminescent signals in a gaseous environment.

Photon and electronic amplification profiles, obtained as a function of various microscope operating parameters such as detector bias, pressure and working distance, showed that: (i) Photon amplification is greater than electronic amplification, in both Ar and N₂, when the GSD was utilized; (ii) Photon amplification increases with increasing detector bias and working distance; (iii) The relative trends in photon amplification associated with variations in detector bias and working distance closely followed that of electronic amplification for the case of when the GSD was used to generate and detect photon signals and when the GSED was used as a photon generation source; (iv) Peaks in photon amplification versus pressure profiles occurred at lower pressures, with smaller full-width-half-maximums, than electronic amplification profiles. The peaks in photon and electronic amplification versus pressure profiles moving to greater pressures with increasing detector bias, whilst peaks in electronic amplification versus pressure profiles remained fixed at a certain pressure. Over all operating parameters and photon detection configurations, of the gases trialled, Ar exhibited the greatest magnitude in photon amplification followed by N₂ then H₂O, even though an opposite trend was observed in electronic amplification data. It was also demonstrated that dragging the electron cascade and subsequent electroluminescence towards the entrance of the light pipe, through electrostatic focusing using a novel GSD design, severely enhanced the collection efficiency of photon signals.

Furthermore, electroluminescent SE signal-to-background ratios were found to (i) increase with increasing detector bias and (ii) be greatest in H₂O followed by N₂ and Ar. Although electronic amplification was seen to be greater in magnitude than that of photon amplification when the GSED was used to generate signals, electroluminescent SE signal-to-background ratios were found to be superior over electronic SE signal-to-background ratios.

Overall, the work clearly demonstrated that the detection of primary scintillation and electroluminescent signals has great possibilities of being superior to that of conventional electronic detection once characteristic photon emission wavelengths are assigned to their respective sample emissive electronic signals, and photon collection efficiencies are further developed. The following chapter investigates the emission spectra of electroluminescent gases in ESEM, in an attempt to characterize the photon wavelengths arising from direct and secondary scintillation reactions.

Chapter 6

Photon Emission Spectra of Electroluminescent Imaging Gases Commonly Utilized in the Environmental SEM

6.1 Introduction

In order for gaseous scintillation and electroluminescent detection in an environmental scanning electron microscope (ESEM) to be fully optimized, the emission spectra of photons emitted in the electron cascades of imaging gases that scintillate in an ESEM need to be studied. Once the emission spectra of scintillating gases have been collected and correctly interpreted, future studies may possibly enable the scintillation and electroluminescence produced by signals carrying strong topographical information, such as secondary electrons (SEs), to be separated from normally unwanted primary scintillation photon signals arising from backscattered (BSE) and primary beam electrons (PEs). Alternatively, in some instances, such as phase contrast imaging, BSE imaging may be the preferred signal of choice. The separation of individual signals, or wavelength filtering, can be accomplished using optical bandpass filters, monochromators, quenching techniques and wavelength shifting gases (Al-Dargazelli *et al.* 1981, Alves & Policarpo 1967, Mutterer 1982, Policarpo *et al.* 1971). Wavelength filtering of gaseous photon signals in an ESEM will also enable areas of microscopic and plasma physics to be investigated such as (i) dynamic studies of electron ion recombination mechanisms, (ii) cathodoluminescence (CL) detection (Danilatos 1986), (iii) investigations into many of the reaction processes that occur in ionized gases and discharges such as those shown in appendix A and (iv) atomic and molecular ionization states. Furthermore, the photomultiplier tubes and light pipe assemblages utilized for gaseous scintillation detection (GSD) imaging need to be optimized to collect wanted spectral emissions with high efficiencies.

This chapter investigates, for the first time, the emission spectra of gases such as argon (Ar) and nitrogen (N₂), in ESEM, that have previously been shown in chapter 5 to produce efficient electroluminescence capable of generating images rich in

SE contrast (see figures 5.5-5.7 of chapter 5.5.1). Water vapour (H_2O) was not investigated in the present study as a consequence of its relatively low efficiency for producing photons. H_2O , however, should not be neglected in future studies adapting detection systems with greater photon collection efficiencies due to its excellent signal-to-background qualities demonstrated in chapter 5. Emission spectra of Ar and N_2 were collected under glow discharge conditions (conditions whereby a luminous glow is observed in the microscope chamber and current densities are sufficiently high that imaging without saturation effects cannot be accomplished) as it was discovered that an insufficient number of photons were collected to obtain spectra well above noise levels. Attempts were made to collect spectra from the GSD using a PMT coupled to photon counting unit and a high resolution monochromator under pre-breakdown voltages normally used for imaging, however, it was once again discovered that signals were well below that needed for accurate quantification. It is therefore proposed that the electroluminescent images shown in chapter 5.5.1 were capable of being generated as a consequence of the scintillation and electroluminescent emission signals being both detected and amplified by the PMT of the GSD panchromatically over all detectable wavelengths. Although there was insufficient signal produced at each wavelength to be detected alone, above noise levels, the summation of all photon wavelengths produced ample signal to produce images rich in SE contrast. It is speculated that photon emissions under glow discharge conditions are somewhat representative of the primary scintillation and electroluminescent emissions from electrons under pre-breakdown conditions. A detailed discussion of the theory of gaseous scintillation and electroluminescence generation, detection and amplification, was presented previously in chapter 5.2.1. The spectra illustrated herein, of Ar and N_2 , was collected as a function of gas pressure (p) at various gaseous scintillation detector biases (V_{GSD}).

6.2 Experimental Techniques

Experiments were performed using a tungsten filament FEI-Philips XL 30 ESEM[®] equipped with a GSED and the purpose built gaseous scintillation detector (GSD) previously shown in figure 5.1. The photomultiplier of the GSD, previously used to generate images and compute photon amplification, was removed and the output of the light pipe was connected to a light focusing lens and an optical fibre. The output of the optical fibre was coupled to the input of an Ocean Optics[®] PC2000 spectroscopy system and related analysis software. The GSD system and spectroscopy system is shown below in figure 6.1. The 2048 element linear CCD, 500 nm blaze wavelength grating and 25 μm entrance slit of the spectrometer enabled photons to be efficiently detected over a wavelength range of 300-1100 nm with a 3.49 nm full-width-half-maximum (FWHM) optical resolution. To maximize the photon collection efficiency the collection grid of the GSD was positively biased at V_{GSD} , with the GSED grounded, throughout all measurements. As previously shown in chapter 5, biasing the GSD collection grid electrostatically drags the electron cascade, and resulting gas luminescence, towards the entrance of the light pipe, dramatically enhancing the ‘effective’ solid angle for photon collection. All spectra collected at a certain p and V_{GSD} were corrected for electrical dark noise by subtracting the wavelength intensities produced with the beam off and V_{GSD} set to zero volts. All spectra were collected using an integration time of 100 ms and working distance (WD) of 15 mm. V_{GSD} was set to a voltage whereby the onset of glow discharge conditions occurred.

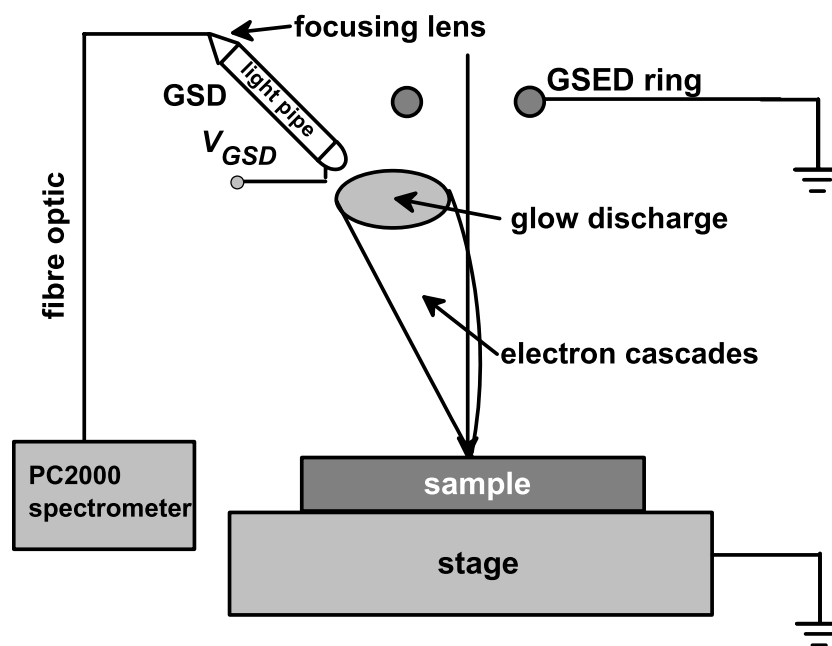


Figure 6.1: Schematic diagram showing the Gaseous Scintillation Detector (GSD) and spectroscopy system used to detect photon wavelengths.

6.3 Results and Analysis

6.3.1 Emission Spectra of Argon

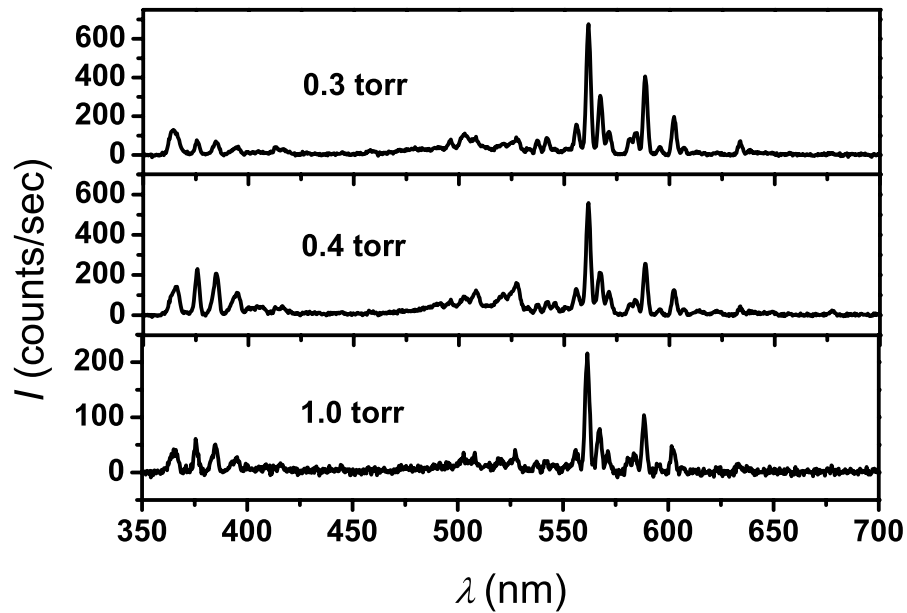


Figure 6.2: Emission spectra of Ar at $p_{Ar} = 0.3, 0.4$ and 1.0 torr. [$V_{GSD} = 238$ V]

Figure 6.2 shows the emission spectrum of Ar obtained under glow discharge conditions at pressures of 0.3, 0.4 and 1.0 torr. It can be seen from the spectra that, of the multitude of emission lines produced, there are several of reasonable intensity. Close inspection of figure 6.2 reveals that two distinct emission bands occur at 350-400 nm (ultra violet to violet region of the electromagnetic spectrum) and 550-600 nm (yellow to orange region of the electromagnetic spectrum). It is obvious that the addition of these two distinct bands produce the characteristic purple/orange glow of Ar discharges at commonly utilized pressures and electric fields. It is also seen that

Table 6.1: Atomic transitions and accompanying wavelengths in neutral Ar (Ar I) (Shirai *et al.* 1999).

Wavelength in Air (nm)	Intensity (a.u)	Transition
377.0369	20	$3s^23p^5(^2P_{1/2}^0)4s - 3s^23p^5(^2P_{3/2}^0)6p$
383.4678	7	$3s^23p^5(^2P_{1/2}^0)4s - 3s^23p^5(^2P_{3/2}^0)6p$
560.6733	35	$3s^23p^5(^2P_{3/2}^0)4p - 3s^23p^5(^2P_{1/2}^0)7s$
565.0704	20	$3s^23p^5(^2P_{3/2}^0)4p - 3s^23p^5(^2P_{3/2}^0)5d$
588.8584	25	$3s^23p^5(^2P_{3/2}^0)4p - 3s^23p^5(^2P_{3/2}^0)7s$

the intensity of photon emissions vary as a function of p_{Ar} . The lower wavelength band generally increasing as p_{Ar} is increased and the higher wavelength band decreasing with increasing p_{Ar} . There are several major emission lines that occur at 375.79 nm, 384.45 nm, 561.59 nm, 567.11 nm, and 588.42 nm. It is believed that these main emissions arise from neutral atomic Ar (Ar I) and occur at the wavelengths, and corresponding electron transitions, shown in table 6.1.

In order to quantify the exact nature in which the intensity of the wavelengths vary with p_{Ar} , figure 6.3 shows a plot of the intensity of the major emission wavelengths versus p_{Ar} . It can be seen from the plot that the three highest intensity lines, corresponding to 561.59 nm, 588.42 nm and 567.11 nm, decrease in intensity with increasing p_{Ar} . Alternatively, the 375.79 nm and 384.45 nm increase in intensity with increasing pressure below $p_{Ar} = 0.4$, after which decreasing with p_{Ar} . Comparing the intensities shown in table 6.1 to those of figure 6.3 seems to indicated that there is a

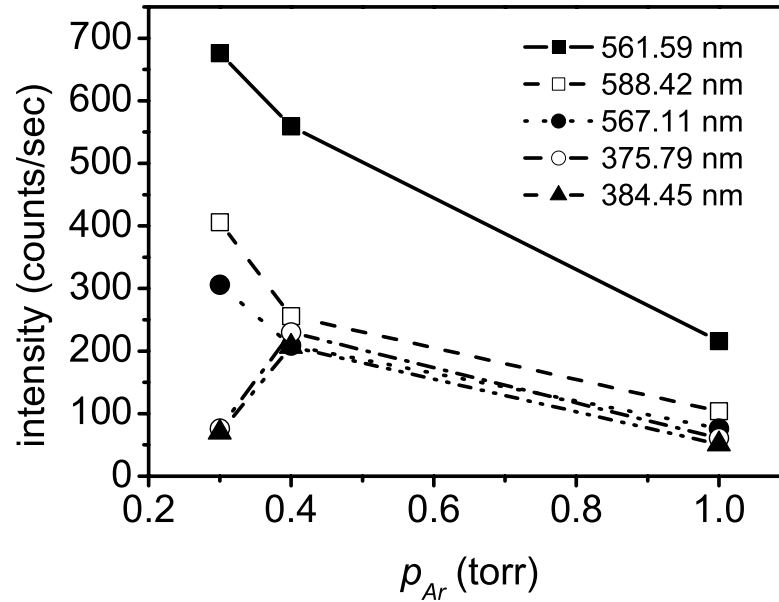


Figure 6.3: Emission intensities versus p_{Ar} for the major 375.79 nm, 384.45 nm, 561.59 nm, 567.11 nm, and 588.42 nm wavelengths found in Ar.

distinct ratio of intensities, suggesting that the proposed wavelengths of atomic Ar I are those found experimentally herein.

The fact that, at higher pressures, intensities decrease rather linearly with pressure suggests that photon emissions are being quenched or absorbed by gas molecules. Higher energy photons suffering more quenching at higher pressures than that of lower energy photons, as indicated by the peaks in intensities versus pressure for high energy photons.

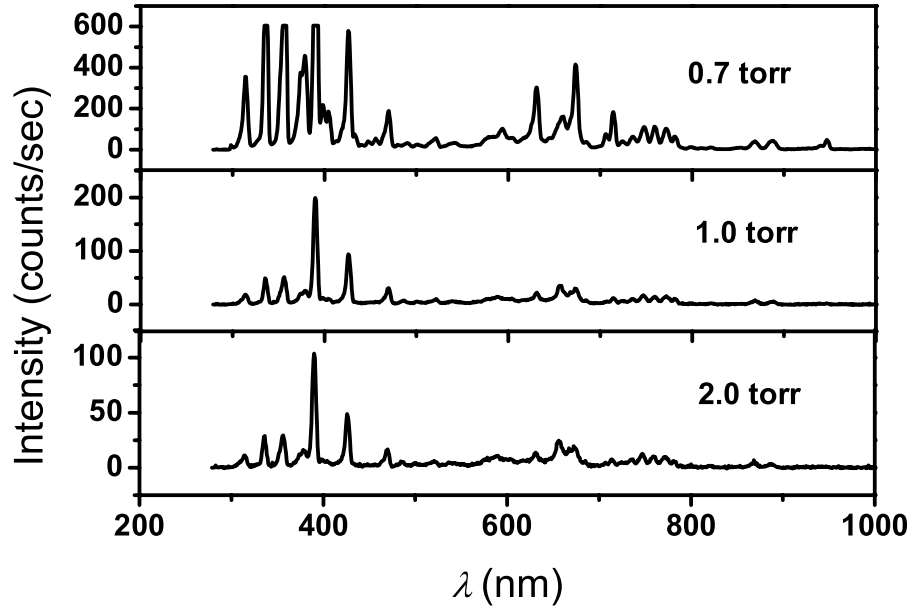


Figure 6.4: Emission spectra of N_2 at $p_{N_2} = 0.7, 1.0$ and 2.0 torr. [$V_{GSD} = 342$ V]

6.3.2 Emission Spectra of Nitrogen

The emission spectrum of N_2 , under glow discharge conditions, is shown in figure 6.4 for $p_{N_2} = 0.7, 1.0$ and 2.0 torr. It can be seen that there are, akin to Ar, several photon wavelengths that vary with pressure. The major detected emission lines occurring in N_2 , under discharge conditions, were found to occur at wavelengths of 313.83 nm, 336.23 nm, 356.26 nm, 390.04 nm, 425.96 nm, 470.04 nm, 630.38 nm and 673.22 nm. The wavelengths found between 300 and 500 nm are speculated to arise from second positive band emissions of molecular nitrogen as a consequence of their excellent agreement with the theory discussed in chapter 5.2.1 (Al-Dargazelli *et al.* 1981, Lindblom & Solin 1988, Takahashi *et al.* 1983). The higher wavelength emissions being attributed to electronic de-excitations of atomic nitrogen. Under the typical

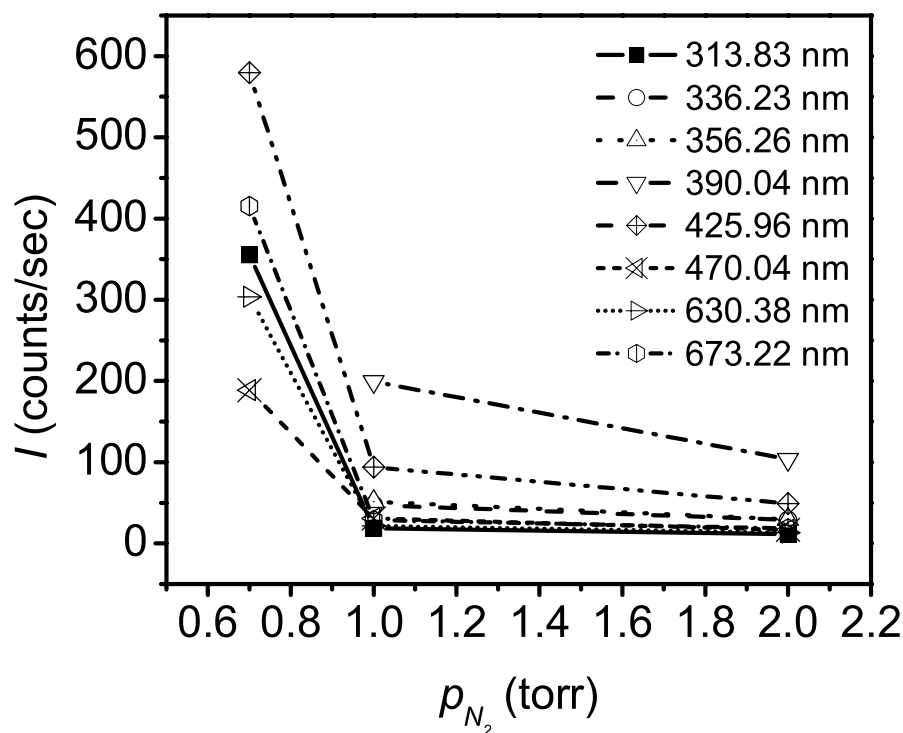


Figure 6.5: Emission intensities versus p_{N_2} for the major 313.83 nm, 336.23 nm, 356.26 nm, 390.04 nm, 425.96 nm, 470.04 nm, 630.38 nm and 673.22 nm wavelengths found in N_2 .

pressures encountered dissociation reactions from the molecular state to atomic state are quite common. The second positive band emissions arising from $C^3\Pi_u \rightarrow B^3\Pi_g$ vibrational de-excitations of molecular N_2 (see chapter 5.2.1 and equations (5.2.8) and (5.2.9) therein for a full description of the vibrational transitions and resulting wavelength emissions of the second positive band in N_2).

Figure 6.5 shows a plot of the intensity of the major emission wavelengths versus p_{N_2} . It can be seen from the plot that all of the emission lines detected in N_2 decrease in intensity with increasing pressure. This phenomenon is in strong agreement with the observations of Takahashi *et al.* (1983) that the intensity of the second positive

band increases with decreasing pressure at constant admixture concentration. The decrease in intensity with increasing pressure, along with quenching effects, may also be attributed to reductions in excitation mean free paths with increasing pressure.

6.4 Conclusions

This work showed, for the first time in ESEM, the emission spectra of excitation reactions produced in Ar and N₂ under glow discharge conditions over a wavelength range of 300-1100 nm. Comparisons of the experimentally obtained emission spectra herein with that of previously obtained spectra by Shirai *et al.* (1999) strongly suggests that the major photon emissions in Ar are consequential of $6p \rightarrow 4s$, $7s \rightarrow 4p$ and $5d \rightarrow 4p$ atomic de-excitation transitions. Initial excitation of Ar I being attributed to arise from electron-atom collisions. For the case of N₂, major emissions are attributed to arise from second positive band ($C^3\Pi_u \rightarrow B^3\Pi_g$) vibrational de-excitation reactions of molecular N₂ (Al-Dargazelli *et al.* 1981, Lindblom & Solin 1988). The spectra obtained illustrated that the major photon emissions, in both Ar and N₂, decrease with increasing imaging gas pressure. This phenomenon suggesting that quenching effects, and plausibly, reductions in excitation mean free paths with pressure, play an important role in luminescent signal detection.

The attainment of images rich in SE emission utilizing gaseous scintillation detection (GSD), shown previously in chapter 5.5.1, without correspondingly strong emission spectra below the onset of glow discharge conditions, ascribed herein, demonstrated that the generation of GSD images are a consequence of panchromatic detection over the complete spectral range of the system. This implies that once greater efficiency GSD systems are implemented, and exact electroluminescent wavelengths are known whereby filtering techniques can be employed to further extract SE signals, GSD imaging has great prospects of being far superior to that of conventional electronic detection.

Therefore, future work performed in this area needs to further develop, and utilize, spectroscopy systems of greater photon collection efficiencies in order for gaseous scintillation and electroluminescence to be studied effectively. Furthermore, high

wavelength resolution studies need to be performed in the vacuum ultraviolet region of the electromagnetic spectrum, based on previous studies into gaseous proportional scintillation detection of nuclear radiation by Andreson *et al.* (1977), Cumpstey & Vass (1980), Fraga *et al.* (2000), Suzuki & Kubota (1979) and Takahashi *et al.* (1983), that demonstrate that significant scintillation and electroluminescence radiation is produced in this region.

Appendix A

Atomic and Molecular Collisions in Partially Ionized Gases

Table A.1: Atomic and molecular collisions in partially ionized gases (adopted from von Engel 1965, Hahn 1997, Hasted 1964, Nasser 1971). [A, B, C, D = ground state atom or molecule, $[AB]$ = ground state molecule, $h\nu$ = photon of frequency ν , e^- = incident electron, e_{ESE}^- = ejected or environmental secondary electron, $+$ = positive ion, $-$ = negative ion, $*$ = singly excited, $**$ = doubly excited, e = electronic state, m = metastable state, ν = vibrational state, s = slow, f = fast]

Collision	Description	No.
photon-atom/molecule		
$A + h\nu \rightarrow A_e^*$	photoexcitation/bound-bound absorption	1
$A + h\nu \rightarrow A_\nu^*$	vibrational photoexcitation	2
$A + h\nu \rightarrow A_m^*$	metastable photoexcitation	3
$A + h\nu \rightarrow A^+ + e_{ESE}^-$	photoionization/bound-free absorption	4
$[AB] + h\nu_1 \rightarrow A_e^* + B \rightarrow A + B + h\nu_2$	photodissociation into excited atoms	5
$A + h\nu_1 \rightarrow A + h\nu_2$	chemiluminescence	6
$A + h\nu_1 \rightarrow A_{ee}^{**} \rightarrow A_e^* + h\nu_2$	line fluorescence	7
$A + h\nu \rightarrow A_e^* \rightarrow A + h\nu$	spontaneous emission	8
photon-excited atom/molecule		
$A_e^* + h\nu \rightarrow A_{ee}^{**}$	photoexcitation	9
$A_e^* + h\nu \rightarrow A_{ev}^{**}$	vibrational photoexcitation	10
$A_e^* + h\nu \rightarrow A^+ + e_{ESE}^-$	photoionization	11

Table A1: Continued...

Collision	Description	No.
$A_v^* + hv \rightarrow A^+ + e_{ESE}^-$	photoionization	12
$[AB]_e^* + hv \rightarrow A_e^* + B_e^*$	photodissociation	13
$[AB]_v^* + hv \rightarrow A + B$	photodissociation	14
$[AB]_e^* + hv \rightarrow A_e^* + B^+ + e_{ESE}^-$	dissociative photoionization	15
$A_e^* + hv \rightarrow A_{ee}^{**} \rightarrow A^+ + e_{ESE}^-$	autoionization/Auger ionization	16
$A_e^* + hv \rightarrow A_{ee}^{**} \rightarrow A^{2+} + 2e_{ESE}^-$	autoionization/Auger ionization	17
$A_e^* + hv_1 \rightarrow A_{ee}^{**} \rightarrow A_e^* + hv_2$	stepwise/anomalous radiation	18
$A_{1e}^* + hv_1 \rightarrow A_{2e}^* + hv_1 + hv_2$	induced bound-bound emission	19
photon-positive ion		
$A^+ + hv \rightarrow A_e^{+*}$	photoexcitation	20
$A^+ + hv \rightarrow A_v^{+*}$	vibrational photoexcitation	21
$A^+ + hv \rightarrow A_e^{2+} + e_{ESE}^-$	photoionization	22
$[AB^+] + hv \rightarrow A + B^+$	photodissociation	23

Table A1: Continued...

Collision	Description	No.
photon-negative ion		
$A^- + hv \rightarrow A + e_{ESE}^-$	photodetachment	24
$[AB^-] + hv \rightarrow A + B + e_{ESE}^-$	dissociative photodetachment	25
$[AB^-] + hv \rightarrow A + B^-$	photodissociation	26
electron-photon-atom/molecule		
$A + e^- + hv \rightarrow A + e^-$	free-free absorption	27
electron-atom/molecule		
$A + e^- \rightarrow A_e^* + e^-$	electron impact electronic excitation	28
$A + e^- \rightarrow A_v^* + e^-$	electron impact vibrational excitation	29
$A + e^- \rightarrow A_m^* + e^-$	electron impact metastable excitation	30
$A + e^- \rightarrow A^+ + e^- + e_{ESE}^-$	electron impact ionization	31
$A + e^- \rightarrow A^{n+} + e^- + ne_{ESE}^-$	multiple electron impact ionization	32
$A + e^- \rightarrow A^{K+} + e^- + e_{ESE}^-$	K-shell ionization	33

Table A1: Continued...

Collision	Description	No.
$[AB] + e^- \rightarrow A + B + e^-$	neutral electron impact dissociation	34
$[AB] + e^- \rightarrow A_e^* + B + e^-$	electron impact dissociative excitation	35
$[AB] + e^- \rightarrow A^+ + B + e^- + e_{ESE}^-$	electron impact dissociative ionization	36
$[AB] + e^- \rightarrow [AB]_e^{+*} + e^- + e_{ESE}^- \rightarrow A^+ + B + e^- + e_{ESE}^-$	fragmentation	37
$[AB] + e^- \rightarrow A^+ + B^- + e^-$	simultaneous positive and negative ion production	38
$A + e^- \rightarrow A_e^{+*} + e^- + e_{ESE}^- \rightarrow A + e^- + 2e_{ESE}^- + hv$	radiative ionization	39
$A + e^- \rightarrow A^- + hv$	radiative attachment	40
$A + e^- \rightarrow A^{-*} \rightarrow A^- + hv$	dielectronic attachment	41
$A + e^- \rightarrow A + B^-$	dissociative attachment	42
$A + e^- \rightarrow A_v^{-*} + B \rightarrow A^- + B$	attachment with collisional stabilization	43
$A + B + e^- \rightarrow A^- + B$	three-body attachment	44
$A + e^- \rightarrow A + e^- + hv$	Bremsstrahlung/free-free emission	45
$A + e^- \rightarrow A + e_{ESE}^-$	electron exchange	46

Table A1: Continued...

Collision	Description	No.
electron-excited atom/molecule		
$A_e^* + e^- \rightarrow A_{ee}^{**} + e^-$	electron excitation	47
$A_e^* + e^- \rightarrow A_{ev}^{**} + e^-$	vibrational excitation by electrons	48
$A_e^* + e^- \rightarrow A_{ee}^{**} + e^- \rightarrow A^+ + e^- + e_{ESE}^-$	autoionization/Auger ionization	49
$A_e^* + e^- \rightarrow A_{ee}^{**} + e^- \rightarrow A^{2+} + e^- + 2e_{ESE}^-$	autoionization/Auger ionization	50
$A_e^* + e^- \rightarrow A_{ee}^{**} + e^- \rightarrow A_e^* + e^- + h\nu$	anomalous radiation	51
$A_e^* + e^- \rightarrow A^+ + e^- + e_{ESE}^-$	electron impact ionization	52
$[AB]_e^* + e^- \rightarrow A_e^* + B_e^* + e^-$	electron impact dissociation	53
$[AB]_v^* + e^- \rightarrow A + B + e^-$	electron impact dissociation	54
$[AB]_e^* + e^- \rightarrow A_e^* + B^+ + e^- + e_{ESE}^-$	dissociative electron impact ionization	55
$[AB]_v^* + e^- \rightarrow A + B^+ + e^- + e_{ESE}^-$	dissociative electron impact ionization	56
$A_e^* + e^- \rightarrow A + e^-$	superelastic collision	57
$A_v^* + e^- \rightarrow A + e^-$	superelastic collision	58

Table A1: Continued...

Collision	Description	No.
electron-positive ion		
$A^+ + e^- \rightarrow A_e^{+*} + e^-$	electron impact excitation	59
$A^+ + e^- \rightarrow A_v^{+*} + e^-$	electron impact vibrational excitation	60
$A^+ + e^- \rightarrow A^{2+} + e^- + e_{ESE}^-$	electron impact ionization	61
$[AB^+] + e^- \rightarrow A + B^+ + e^-$	electron impact dissociation	62
$[AB^+] + e^- \rightarrow A^+ + B^+ + e^- + e_{ESE}^-$	electron impact dissociative ionization	63
$A^+ + e^- \rightarrow A_e^* + h\nu$	radiative recombination	64
$A^+ + e^- \rightarrow A_{ee}^{**} \rightarrow A_e^* + h\nu$	dielectronic recombination	65
$A^+ + e^- \rightarrow A_{ee}^{**} \rightarrow A_e^{+*} + e_{ESE}^-$	autoionization/Auger effect	66
$[AB^+] + e^- \rightarrow A_e^* + B_e^*$	dissociative recombination	67
$A^+ + B + e^- \rightarrow A_e^* + B$	three-body recombination	68
$A^+ + e^- + e^- \rightarrow A_e^* + e^-$	three-body recombination	69
$A^+ + e^- + h\nu \rightarrow A^+ + e^-$	free-free absorption	70
$A^+ + e^- \rightarrow A^+ + e^- + h\nu$	Bremsstrahlung/free-free emission	71

Table A1: Continued...

Collision	Description	No.
electron-negative ion		
$A^- + e^- \rightarrow A + e^- + e_{ESE}^-$	electron detachment	72
$[AB^-] + e^- \rightarrow A + B^- + e^-$	electron impact dissociation	73
excited atom/molecule- atom/molecule		
$A_e^* + B \rightarrow A_e^* + B_e^*$	excitation	74
$A_e^* + B \rightarrow A + B_e^*$	excitation exchange	75
$A_e^* + B_s \rightarrow A + B_f$	momentum transfer	76
$A_{1e}^* + B_2 \rightarrow A_1 + B_{2e}^*$	sensitized fluorescence	77
$A_v^* + B \rightarrow A + B_v^*$	vibrational excitation exchange	78
$A_{ee}^{**} + B \rightarrow A_e^* + B_v^*$	mixed gas fluorescence	79
$A_v^* + B \rightarrow A + B$	vibrational deactivation	80
$A_e^* + [BC] \rightarrow A + B + C$	sensitized chemical reaction/dissociation	81
$A_e^* + B \rightarrow A + B + h\nu$	band resonance radiation	82
$A_m^* + B \rightarrow A + B^+ + e_{ESE}^-$	Penning ionization	83
$A_e^* + B \rightarrow A_m^* + B_v^*$	quenching of resonance radiation	84

Table A1: Continued...

Collision	Description	No.
$A_e^* + B \rightarrow [AB]_e^* + A^+ + e_{ESE}^-$	associative ionization and band fluorescence	85
excited atom/molecule- excited atom/molecule		
$A_e^* + B_e^* \rightarrow A + B^+ + e_{ESE}^-$	ionization	86
$A_e^* + B_v^* \rightarrow A_e^* + B$	deactivation	87
$A_{e1}^* + B_{e2}^* \rightarrow A_{e2}^* + B_{e1}^*$	excitation exchange	88
$A_e^* + [BC]_e^* \rightarrow A + B_e^* + C_e^*$	dissociation	89
excited atom/molecule- positive ion		
$A_e^* + B^+ \rightarrow A^+ + B$	charge transfer	90
$A_e^* + B^+ \rightarrow A + B^{2+} + e_{ESE}^-$	ionization	91
$A_v^* + B^+ \rightarrow A + B^+$	deactivation	92
$[AB]_e^* + C^+ \rightarrow A + B + C^+$	dissociation	93
excited atom/molecule- negative ion		
$A_e^* + B^- \rightarrow A + B + e_{ESE}^-$	detachment/ionization	94

Table A1: Continued...

Collision	Description	No.
$A_v^* + B^- \rightarrow A + B^-$	deactivation	95
$[AB]_e^* + C^- \rightarrow A + B + C^-$	dissociation	96
positive ion-atom/molecule		
$A^+ + B \rightarrow A^+ + B^+ + e_{ESE}^-$	ionization	97
$A^+ + B \rightarrow A^{2+} + B + e_{ESE}^-$	ionization	98
$A^+ + B \rightarrow A^{n+} + B^{n+} + (n-1)e_{ESE}^-$	multiple ionization	99
$A^+ + B \rightarrow A + B^+$	charge transfer	100
$A^{2+} + B \rightarrow A^+ + B^+$	partial charge transfer	101
$A^+ + [BC] \rightarrow A + B^+ + C$	dissociative charge transfer/dissociative ionization	102
$A^+ + B \rightarrow A^- + B^{2+}$	attachment	103
$A^+ + B \rightarrow A^+ + B_e^*$	excitation	104
$A^+ + B \rightarrow A_e^{+*} + B$	excitation	105
$A^+ + [BC] \rightarrow A^+ + B + C$	dissociation	106
$A^+ + [BC] \rightarrow [A^+B] + C$	ion-atom interchange	107
$A^+ + B \rightarrow A + B_e^* \rightarrow A + B^+ + h\nu$	spark line enhancement	108

Table A1: Continued...

Collision	Description	No.
positive ion-positive ion		
$A^+ + B^+ \rightarrow A^+ + B^{2+} + e_{ESE}^-$	ionization	109
$A^+ + B^+ \rightarrow A^{2+} + B$	charge transfer	110
$A^+ + B^+ \rightarrow A_e^{+*} + B^+$	excitation	111
$A^+ + [BC^+] \rightarrow A^+ + B^+ + C$	dissociation	112
positive ion-negative ion		
$A^+ + B^- \rightarrow A_e^* + B_e^*$	mutual neutralization	113
$A^+ + B^- \rightarrow A_e^{+*} + B^-$	excitation	114
$A^+ + B^- \rightarrow A^+ + B + e_{ESE}^-$	detachment	115
$[AB^+] + C^- \rightarrow A + B^+ + C^-$	dissociation	116
negative ion-atom/molecule		
$A^- + B \rightarrow A + B + e_{ESE}^-$	collisional detachment	117
$A^- + B \rightarrow A + B^-$	charge transfer	118
$A^- + B \rightarrow [AB] + e_{ESE}^-$	associative detachment	119
$A^- + [BC] \rightarrow A^- + B + C$	dissociation	120
$A^- + B \rightarrow A^- + B^+ + e_{ESE}^-$	ionization	121

Table A1: Continued...

Collision	Description	No.
$A^- + B \rightarrow A^- + B_e^*$	excitation	122
$A^+ + [BC] \rightarrow [A^- B] + e_{ESE}^-$	ion-atom interchange	123
negative ion-negative ion		
$A^- + B^- \rightarrow A^- + B + e_{ESE}^-$	detachment	124
atom/molecule-atom/molecule		
$A + B \rightarrow A^+ + B + e_{ESE}^-$	electron loss/ionization by rearrangement	125
$A + B \rightarrow A^+ + B^-$	electron capture	126
$A + [BC] \rightarrow [AB] + C$	chemical reaction	127
$A + B \rightarrow A + B_v^*$	vibrational excitation	128

Bibliography

- Adamiak B. & Mathieu C., The reduction of the beam gas interactions in the variable pressure scanning electron microscope with the use of helium gas, *Scanning* 22, 178–181 (2000)
- Al-Dargazelli S.S., Ariyaratne T.R., Breare J.M. & Nandi B.C., Charge and light gain measurements in argon-nitrogen mixtures using a gas scintillation proportional counter, *Nuclear Instruments and Methods* 180, 497–501 (1981)
- Almeida D.P., Becker K.H. & Deutsch H., Electron-impact ionization cross-section of argon (σ_{n+} , $n = 7, 8$), *International Journal of Mass Spectrometry and Ion Processes* 163, 39–45 (1997)
- Almeida D.P., Fontes A.C., Mattos I.S. & Godinho C.L., Electron impact multiple ionization cross section of argon (σ_{n+} , $n = 3 - 6$), *Journal of Electron Spectroscopy and Related Phenomena* 67, 503–510 (1994)
- Alves M.A.F. & Policarpo A.J.P.L., The effect of wavelength shifter on the light output of the Ar-N₂ proportional scintillation counter, *Nuclear Instruments and Methods* 57, 321–324 (1967)
- Andreson R.D., Leimann E.A. & Peacock A., The nature of light produced inside a gas scintillation proportional counter, *Nuclear Instruments and Methods* 140, 371–374 (1977)

- Asundi R.K. & Kurepa M.V., Ionization cross section in He, Ne, Ar, Kr and Xe by electron impact, *Journal of Electronics and Control* 15, 41–50 (1963)
- Bolorizadeh M.A. & Rudd M.E., Angular and energy dependence of cross sections for ejection of electrons from water vapor. I. 50–2000 eV electron impact, *Physical Review A* 33, 882–887 (1986)
- Bower N.W., Stulik D.C. & Doehne E., A critical evaluation of the environmental scanning electron microscope for the analysis of paint fragments in art conservation, *Journal of Analytical Chemistry* 348, 402–410 (1994)
- Burge R.E. & Smith G.H., A new calculation of electron scattering cross-sections and a theoretical discussion of image contrast in the electron microscope, *Proceedings of the Physical Society* 79, 673–690 (1962)
- Burke P.G. & Moiseiwitsch B.L., editors, *Atomic Processes and Applications*, chapter 6, 133–198, North-Holland Publishing Company, Amsterdam (1976)
- Carlton R.A., The effects of some instrument operating parameters on the x-ray microanalysis of particles in the environmental scanning electron microscope, *scanning* 19, 85–91 (1997)
- Cazaux J., Mechanisms of charging in electron spectroscopy, *Journal of Electron Spectroscopy and Related Phenomena* 105, 155–185 (1999a)
- Cazaux J., Some considerations on the secondary electron emission, δ , from e^- irradiated insulators, *Journal of Applied Physics* 85, 1–11 (1999b)
- Chen W.K., *Passive and Active Filters: Theory and Implementations*, John Wiley & Sons, New York (1986)
- Craven J.P., Baker F.S., Thiel B.L. & Donald A.M., Consequences of positive ions upon imaging in low vacuum scanning electron microscopy, *Journal of Microscopy* 205, 96–105 (2002)

- Cumpstey D.E. & Vass D.G., The scintillation process in gas proportional scintillation detectors with uniform electric fields, *Nuclear Instruments and Methods* 171, 473–478 (1980)
- Danilatos G.D., An atmospheric scanning electron microscope (ASEM), *Scanning* 3, 215–217 (1980a)
- Danilatos G.D., The examination of fresh or living plant material in an environmental scanning electron microscope, *Journal of Microscopy* 121, 235–238 (1980b)
- Danilatos G.D., Design and construction of an atmospheric or environmental SEM (part 1), *Scanning* 4, 9–20 (1981)
- Danilatos G.D., Design and construction of an atmospheric or environmental SEM (part 3), *Scanning* 7, 26–42 (1985)
- Danilatos G.D., Cathodoluminescence and gaseous scintillation in the environmental SEM, *Scanning* 8, 279–284 (1986)
- Danilatos G.D., Foundations of environmental scanning electron microscopy, *Advances in Electronics and Electron Physics* 71, 109–250 (1988)
- Danilatos G.D., Equations of charge distribution in the environmental scanning electron microscope, *Scanning Microscopy* 4, 799–823 (1990a)
- Danilatos G.D., Mechanisms of detection and imaging in the ESEM, *Journal of Microscopy* 160, 9–19 (1990b)
- Danilatos G.D., Theory of the gaseous detector device in the environmental scanning electron microscope, *Advances in Electronics and Electron Physics* 78, 1–102 (1990c)
- Danilatos G.D., Gas flow properties in the environmental SEM, *Microbeam Analysis* 201–203 (1991)

- Danilatos G.D., Gas-flow field in the environmental SEM, *Proceedings of the 50th Annual Meeting of the Electron Microscopy Society of America* 1298–1299 (1992a)
- Danilatos G.D., Secondary electron imaging by scintillating gaseous detection device, in *Proceedings of the 50th Annual Meeting of the Electron Microscopy Society of America*, 1302–1303 (1992b)
- Danilatos G.D., Environmental scanning electron microscopy and microanalysis, *Mikrochimica Acta* 114/115, 143–155 (1994)
- Danilatos G.D. & Postle R., The environmental scanning electron microscope and its applications, *Scanning Electron Microscopy* 1, 1–16 (1982)
- Deutsch H., Becker K., Matt S. & Märk T.D., Theoretical determination of absolute electron-impact ionization cross sections of molecules, *International Journal of Mass Spectrometry* 197, 37–69 (2000)
- Dias T.H.V.T., Santos F.P., Rachinhas P.J.B.M., Borges F.I.G.M., dos Santos J.M.F. & Conde C.A.N., Xenon-neon gas proportional scintillation counters: Experimental and simulation results, *Journal of Applied Physics* 85, 6303–6312 (1999)
- Dias T.H.V.T., Santos F.P., Rachinhas P.J.B.M., Borges F.I.G.M., dos Santos J.M.F., Stauffer A.D. & Conde C.A.N., The effect of electron multiplication on the electroluminescence yield of pure xenon and xenon-neon gas proportional scintillation counters: Experimental and simulation results, *IEEE Nuclear Science Symposium Conference Record* 1, 447–451 (1997)
- Djurić N., Čadež I.M. & Kurepa M.V., H₂O and D₂O total ionization cross-sections by electron impact, *International Journal of Mass Spectrometry and Ion Processes* 83, R7–10 (1988)

- Doehne E., A new correction method for high-resolution energy dispersive x-ray analysis in the environmental scanning electron microscope, *Scanning* 19, 75–78 (1997)
- Doehne E. & Bower N.W., Empirical evaluation of the electron skirt in the environmental SEM: Implications for energy dispersive x-ray analysis, *Microbeam Analysis* 2, S35–36 (1993)
- Dolan T.J., Electron and ion collisions with water vapour, *Journal of Physics D: Applied Physics* 26, 4–8 (1993)
- Druyvesteyn M.J. & Penning F.M., The mechanism of electrical discharges in gases of low pressure, *Reviews of Modern Physics* 12, 87–174 (1940)
- Durkin R. & Shah J.S., Amplification and noise in high-pressure scanning electron microscopy, *Journal of Microscopy* 169, 33–51 (1993)
- Farley A.N. & Shah J.S., Primary considerations for image enhancement in high-pressure scanning electron microscopy 1: Electron beam scattering and contrast, *Journal of Microscopy* 158, 379–388 (1990a)
- Farley A.N. & Shah J.S., Primary considerations for image enhancement in high-pressure scanning electron microscopy 2: Image contrast, *Journal of Microscopy* 158, 389–401 (1990b)
- Farley A.N. & Shah J.S., High-pressure scanning electron microscopy of insulating materials: a new approach, *Journal of Microscopy* 164, 107–126 (1991)
- Favata F., Smith A., Bavdaz M. & Kowalski T., Light yield as a function of gas pressure and electric field in gas scintillation proportional counters, *Nuclear Instruments and Methods in Physics Research A* 294, 595–601 (1990)

- Feio M.A. & Policarpo A.J.P.L., Secondary light emission by noble gases, *Nuclear Instruments and Methods* 217, 473–478 (1983)
- Fletcher A.L., Thiel B.L. & Donald A.M., Amplification measurements of alternative imaging gases in environmental SEM, *Journal of Physics D: Applied Physics* 30, 2249–2257 (1997)
- Fletcher A.L., Thiel B.L. & Donald A.M., Signal components in the environmental scanning electron microscope, *Journal of Microscopy* 196, 26–34 (1999)
- Fletcher J. & Cowling I.R., Electron impact ionization of neon and argon, *Journal of Physics B: Atomic and Molecular Physics* 6, L258–L261 (1973)
- Fraga M.M.F.R., Fraga F.A.F. & Policarpo A.J.P.L., Modelling of an IR scintillation counter, *Nuclear Instruments and Methods in Physics Research A* 442, 423–427 (2000)
- Garg S.P., Murthy K.B.S. & Sharma R.C., Development of a semi-empirical expression for light gain factors in gas scintillation proportional counters, *Nuclear Instruments and Methods in Physics Research A* 357, 406–417 (1995)
- Gauvin R., Some theoretical considerations on x-ray microanalysis in the environmental or variable pressure scanning electron microscope, *Scanning* 21, 388–393 (1999)
- Gauvin R. & Drouin D., A formula to compute total elastic scattering Mott cross-sections, *Scanning* 15, 140–150 (1993)
- Gill E.W.B. & von Engel A., Starting potentials of electrodeless discharges, *Proceedings of the Royal Society of London. Series A, Mathematical and Physical Sciences* 197, 107–124 (1949)

- Gillen G., Wight S., Bright D. & Herne T., Quantitative secondary ion mass spectrometry imaging of self-assembled monolayer films for electron dose mapping in the environmental scanning electron microscope, *Scanning* 20, 404–409 (1998)
- Goldstein J.I., Newbury D.E., Echlin P., Joy D.C., Jr. A.D.R., Lyman C.E., Fiori C. & Lifshin E., *Scanning Electron Microscopy and Microanalysis*, Plenum Press, New York & London, 2nd edition (1992)
- Griffin B.J., Charge contrast imaging of material growth and defects in environmental scanning electron microscopy-linking electron emission and cathodoluminescence, *Scanning* 22, 234–242 (2000)
- GW Electronics Inc., *Specimen Current Amplifier Type 31 & 103 Instruction and Installation Manual*, Norcross (1988)
- Hagstrum H.D., Studies of adsorbate electronic structure using ion neutralization and photoemission spectroscopies, in Fiermans L., Vennik J. & Dekeyser W., editors, *Electron and Ion Spectroscopy of Solids*, 273–323, Plenum Press, New York (1978)
- Hahn Y., Electron-ion recombination processes-an overview, *Reports on Progress in Physics* 60, 691–759 (1997)
- Hwang W., Kim Y.K. & Rudd M.E., New model for electron-impact ionization cross sections of molecules, *Journal of Chemical Physics* 104, 2956–2966 (1996)
- Jain D.K. & Khare S.P., Ionizing collisions of electrons with CO₂, CO, H₂O, CH₄ and NH₃, *Journal of Physics B: Atomic, Molecular and Optical Physics* 9, 1429–1438 (1976)
- Jost K. & Kessler J., Die Ortsverteilung mittleschneller Elektronen bei Mehrfachstreuung (The spatial distribution of medium energy electrons during plural scattering), *Zeitschrift Physik* 176, 126–142 (1963)

- Joy D.C. & Joy C.S., Low voltage scanning electron microscopy, *Micron* 27, 247–263 (1996)
- Kadoun A., Belkorissat R., Khelifa B. & Mathieu C., Comparative study of electron beam-gas interaction in an SEM operating at pressures up to 300 Pa, *Vacuum* 69, 537–543 (2003)
- Khare S.P. & Meath W.J., Cross sections for the direct and dissociative ionisation of NH_3 , H_2O and H_2S by electron impact, *Journal of Physics B: Atomic, Molecular and Optical Physics* 20, 2101–2116 (1987)
- Kim Y.K. & Rudd M.E., Binary-encounter-dipole model for electron-impact ionization, *Physical Review A* 50, 3954–3967 (1994)
- Knowles R.W., Schultz W.G. & Armstrong A.E., Environmental Scanning Electron Microscope, *United States Patent No. 5362964* (1994)
- Krishnakumar E. & Srivastava S.K., Cross-sections for electron impact ionization of O_2 , *International Journal of Mass Spectrometry and Ion Processes* 113, 1–12 (1992)
- Lenz F., Zur streuung mittelschneller elektronen in kleinste winkel (Scattering of medium energy electrons in very small angles), *Zeitschrift Naturforschung* 9a, 185–204 (1954)
- Lindblom P. & Solin O., Atomic near-infrared noble gas scintillations I: Optical spectra, *Nuclear Instruments and Methods in Physics Research A* 268, 204–208 (1988)
- Llewellyn-Jones F., *Ionization and Breakdown in Gases*, Methuen & Co. Ltd, London and John Wiley & Sons Inc., New York (1957)

- Loeb L.B., Secondary processes active in the electrical breakdown of gases, *British Journal of Applied Physics* 3, 341–349 (1952)
- Loeb L.B., *Basic Processes of Gaseous Electronics*, University of California Press, Berkeley (1961)
- Massey H.S.W., Burhop E.H.S. & Gilbody L.B., *Electronic and Ionic Impact Phenomena*, Clarendon Press, Oxford, 2nd edition (1969)
- McDaniel E.W., *Collision Phenomena in Ionized Gases*, Wiley, New York (1964)
- Märk T.D., Fundamental aspects of electron impact ionization, *International journal of Mass Spectrometry and Ion Physics* 45, 125–145 (1982)
- Meredith P. & Donald A.M., Study of ‘wet’ polymer latex systems in environmental scanning electron microscopy: some imaging considerations, *Journal of Microscopy* 181, 23–35 (1996)
- Meredith P., Donald A.M. & Thiel B.L., Electron-gas interactions in the environmental scanning electron microscopes gaseous detector, *Scanning* 18, 467–473 (1996)
- Mohan A., Khanna N., Hwu J. & Joy D.C., Secondary electron imaging in the variable pressure scanning electron microscope, *Scanning* 20, 436–441 (1998)
- Molnar J.P., Studies of γ -processes of electron emission employing pulsed Townsend discharges on a millisecond time scale, *Physical Review* 83, 940–952 (1951)
- Moncreiff D.A., Barker P.R. & Robinson V.N.E., Electron scattering by gas in the scanning electron microscope, *Journal of Physics D: Applied Physics* 12, 481–488 (1979)

- Moncreiff D.A., Robinson V.N.E. & Harris L.B., Charge neutralisation of insulating surfaces in the SEM by gas ionisation, *Journal of Physics D: Applied Physics* 11, 2315–2325 (1978)
- Mott N.F. & Massey H.S.W., *The Theory of Atomic Collisions*, Clarendon Press, Oxford (1965)
- Mutterer M., Gas scintillation nuclear particle detectors, *Nuclear Instruments and Methods* 196, 73–81 (1982)
- Nasser E., *Fundamentals of Gaseous Ionisation and Plasma Electronics*, Wiley-Interscience, New York (1971)
- Newbury D.E., Imaging deep holes in structures with gaseous secondary electron detection in the environmental scanning electron microscope, *Scanning* 18, 474–482 (1996)
- Newton R.R., Transients in Townsend discharges, *Physical Review* 73, 570–583 (1948)
- OriginLab Corporation, *Origin[®] 7 SR1 v7.03(B300) Software*, Northhampton MA (2002)
- Paviček Z., An empirical formula for the impact excitation coefficient of xenon-filled scintillation counters, *Nuclear Instruments and Methods in Physics Research A* 244, 537–541 (1986)
- Pejović M.M., Ristić G.S. & Karamarković J.P., Electrical breakdown in low pressure gases, *Journal of Physics D: Applied Physics* 35, R91–103 (2002)
- Philips, *XP2012 and XP2012B 10-stage photomultiplier tubes data sheet*, USA (1984)
- Philips Electron Optics, *Environmental Scanning Electron Microscopy, An Introduction to ESEM[®]*, Robert Johnson Associates, El Dorado Hills (1996)

- Philips Electron Optics, *XL30 ESEM[®] Electronics Manual: Issue 2*, Eindhoven (1997)
- Phillips M.R., Toth M. & Drouin D., A novel technique for probe intensity characterisation in the environmental scanning electron microscope, *Microscopy and Microanalysis* 5 (Supplement 2: Proceedings), 294–295 (1999)
- Policarpo A.J.P.L., Alves M.A.F. & Carvalho M.J.T., Charge and light peak shifts in an x-ray detector, *Nuclear Instruments and Methods* 97, 491–496 (1971)
- Raether H., *Electron Avalanches and Breakdown in Gases*, Butterworths, London (1964)
- Rao M.V.V.S., Iga I. & Srivastava S.K., Ionization cross-sections for the production of positive ions from H₂O by electron impact, *Journal of Geophysical Research* 100, 421–425 (1995)
- Rapp D. & Englander-Golden P., Total cross-sections for ionization and attachment in gases by electron impact. I. Positive ionization, *Journal of Chemical Physics* 43, 1465–1479 (1965)
- Ray R., Little B., Wagner P. & Hart K., Environmental scanning electron microscopy investigations of biodeterioration, *Scanning* 19, 98–103 (1997)
- Reimer L., *Scanning Electron Microscopy*, Springer, Berlin (1985)
- Robinson V.N.E., The elimination of charging artefacts in the scanning electron microscope, *Journal of Physics E: Scientific Instruments* 8, 638–640 (1975a)
- Robinson V.N.E., A wet stage modification to a scanning electron microscope, *Journal of Microscopy* 103, 71–77 (1975b)
- Robinson V.N.E., The SEM examination of wet specimens, *Scanning* 1, 149–156 (1978)

- Royall C.P., Thiel B.L. & Donald A.M., Radiation damage of water in environmental scanning electron microscopy, *Journal of Microscopy* 204, 185–195 (2001)
- Saksena V., Kushwaha M.S. & Khare S.P., Electron impact ionisation of molecules at high energies, *International Journal of Mass Spectrometry and Ion Processes* 171, L1–L5 (1997a)
- Saksena V., Kushwaha M.S. & Khare S.P., Ionization cross-sections of molecules due to electron impact, *Physica B* 233, 201–212 (1997b)
- Schnarr H. & Fütting M.W., Some aspects of optimizing contrasts for the investigation of joint materials in the environmental scanning electron microscope, *Scanning* 19, 79–84 (1997)
- Schram B.L., de Heer F.J., van der Wiel M.J. & Kistemaker J., Ionization cross sections for electrons (0.6-20 keV) in noble and diatomic gases, *Physica* 31, 94–112 (1965)
- Schram B.L., Moustafa H.R., Schutten J. & de Heer F.J., Ionization cross sections for electrons (100-600 eV) in noble and diatomic gases, *Physica* 32, 734–740 (1966)
- Schutten J., de Heer F.J., Moustafa H.R., Boerbom A.J.H. & Kistemaker J., Gross- and partial-ionization cross sections for electrons on water vapor in the energy range 0.1-20 keV, *Journal of Chemical Physics* 44, 3924–3928 (1966)
- Scion Corporation, *Scion Image for Windows Beta 4.0.2*, USA (2000)
- Shah J.S. & Beckett A., A preliminary evaluation of moist environment ambient temperature scanning electron microscopy, *Micron* 10, 13–23 (1979)
- Shirai T., Sugar J. & Musgrove A., NIST atomic spectra database, http://physics.nist.gov/cgi-bin/AtData/lines_form (1999)

- Smith P.T., The ionization of helium, neon and argon by electron impact, *Physical Review* 36, 1293–1302 (1930)
- Spekowitz G. & Brehm B., Cross sections and thresholds for electron impact triple and quadruple ionization processes of CO, N₂ and O₂, *Chemical Physics Letters* 187, 442–446 (1991)
- Srinivasan V. & Rees J.A., A note on the total ionization cross section for electrons in the inert gases and carbon monoxide, *British Journal of Applied Physics* 18, 59–64 (1967)
- Stelmashenko N.A., Craven J.P., Donald A.M., Terentjev E.M. & Thiel B.L., Topographic contrast of partially wetting water droplets in environmental scanning electron microscopy, *Journal of Microscopy* 204, 172–183 (2001)
- Stevens-Kalceff M.A., Micromodification of silicon dioxide in a variable pressure/environmental scanning electron microscope, *Applied Physics Letters* 79, 3050–3052 (2001)
- Stokes D.J., Thiel B.L. & Donald A.M., Direct observation of water-oil emulsion systems in the liquid state by environmental scanning electron microscopy, *Langmuir* 14, 4402–4408 (1998)
- Stokes D.J., Thiel B.L. & Donald A.M., Dynamic secondary electron contrast effects in liquid systems studied by environmental scanning electron microscopy, *Scanning* 22, 357–365 (2000)
- Stowe S.J. & Robinson V.N.E., The use of helium gas to reduce beam scattering in high vapour pressure scanning electron microscopy applications, *Scanning* 20, 57–60 (1998)

- Straub H.C., Lindsay B.G., Smith K.A. & Stebbings R.F., Absolute partial cross sections for electron-impact ionization of H₂O and D₂O from threshold to 1000 eV, *Journal of Chemical Physics* 108, 109–116 (1998)
- Straub H.C., Renault P., Lindsay B.G., Smith K.A. & Stebbings R.F., Absolute partial and total cross sections for electron-impact ionization of argon from threshold to 1000 eV, *Physical Review A* 52, 1115–1124 (1995)
- Straub H.C., Renault P., Lindsay B.G., Smith K.A. & Stebbings R.F., Absolute partial cross sections for electron-impact ionization of H₂, N₂, and O₂ from threshold to 1000 eV, *Physical Review A* 54, 2146–2153 (1996)
- Suzuki M. & Kubota S., Mechanism of proportional scintillation in argon, krypton and xenon, *Nuclear Instruments and Methods* 164, 197–199 (1979)
- Takahashi T., Himi S., Suzuki M., Ruan J. & Kubota S., Emission spectra from Ar-Xe, Ar-Kr, Ar-N₂, Ar-CH₄, Ar-CO₂ and Xe-N₂ gas scintillation proportional counters, *Nuclear Instruments and Methods* 205, 591–596 (1983)
- Terrissol M., Bordage M.C., Caudrekier V. & Segur P., Cross Sections for 0.025-1 keV electrons and 10 eV-1 keV photons, *Atomic and Molecular Data for Radiotherapy* IAEA-TECDOC-506, International Atomic Energy Agency, Vienna (1989)
- Thiel B.L., Master curves for gas amplification in low vacuum and environmental scanning electron microscopy, *Ultramicroscopy* 99, 35–47 (2003)
- Thiel B.L., Bache I.C., Fletcher A.L., Meredith P. & Donald A.M., An improved model for gaseous amplification in the environmental SEM, *Journal of Microscopy* 187, 143–157 (1997)

- Thiel B.L., Bache I.C. & Smith P., Imaging the probe skirt in the environmental SEM, *Microscopy and Microanalysis* 6 (Supplement 2: Proceedings), 794–795 (2000)
- Thiel B.L. & Donald A.M., The study of water in heterogeneous media using environmental scanning electron microscopy, *Journal of Molecular Liquids* 80, 207–230 (1999)
- Tornow W., Huck H., Kober H.J. & Mertens G., Properties of high pressure nitrogen-argon and nitrogen-xenon gas scintillators, *Nuclear Instruments and Methods* 133, 435–443 (1976)
- Toth M., Daniels D.R., Thiel B.L. & Donald A.M., Quantification of electron-ion recombination in an electron-beam-irradiated gas capacitor, *Journal of Physics D: Applied Physics* 35, 1–9 (2002a)
- Toth M., Kucheyev S.O., Williams J.S., Jagadish C., Phillips M.R. & Li G., Imaging charge trap distributions in GaN using environmental scanning electron microscopy, *Applied Physics Letters* 77, 1342–1344 (2000)
- Toth M. & Phillips M.R., The effects of space charge on contrast obtained using the environmental scanning electron microscope, *Scanning* 22, 319–325 (2000a)
- Toth M. & Phillips M.R., The role of induced contrast in images obtained using the environmental scanning electron microscope, *Scanning* 22, 370–379 (2000b)
- Toth M., Phillips M.R., Craven J.P., Thiel B.L. & Donald A.M., Electric fields produced by electron irradiation of insulators in a low vacuum environment, *Journal of Applied Physics* 91, 4492–4499 (2002b)
- Toth M., Phillips M.R., Thiel B.L. & Donald A.M., Electron imaging of dielectrics under simultaneous electron-ion irradiation, *Journal of Applied Physics* 91, 4479–4491 (2002c)

- Toth M., Thiel B.L. & Donald A.M., On the role of electron-ion recombination in low vacuum scanning electron microscopy, *Journal of Microscopy* 205, 86–95 (2002d)
- Varney R.N., Drift velocity of ions in oxygen, nitrogen, and carbon monoxide, *Physical Review* 89, 708–711 (1953)
- von Engel A., *Ionized Gases*, Clarendon Press, Oxford, 2nd edition (1965)
- Wallace S.J., Berg R.A. & Green A.E.S., Electron-Impact Ionization of Ne and Ar in the Eikonal and Born Approximations, *Physical Review A* 7, 1616–1629 (1973)
- Wentzel G., Dispersion of corpuscular rays as diffraction appearances, *Zeitschrift fur Physik* 40, 590–593 (1926)
- Wetzel R.C., Baiocchi F.A., Hayes T.R. & Freund R.S., Absolute cross sections for electron-impact ionization of the rare-gas atoms by the fast-neutral-beam method, *Physical Review A* 35, 559–577 (1987)
- Wight S., Gillen G. & Herne T., Development of environmental scanning electron microscopy electron beam profile imaging with self-assembled monolayers and secondary ion mass spectroscopy, *Scanning* 19, 71–74 (1997)
- Wight S.A., Experimental data and model simulations of beam spread in the environmental scanning electron microscope, *Scanning* 23, 320–327 (2001)
- Wight S.A. & Zeissler C.J., Direct measurement of electron beam scattering in the environmental scanning electron microscope using phosphor imaging plates, *Scanning* 22, 167–172 (1999)
- Wilkinson D.H., *Ionization Chambers and Counters*, Cambridge University Press, Cambridge (1958)

- Wittry D.B., *Proceedings of the 4th Conference on X-ray Optics and Microanalysis* 168 (1966)
- Yacobi B.G. & Holt D.B., *Cathodoluminescence Microscopy of Inorganic Solids*, Plenum Press, New York (1990)
- Young H.D., *University Physics*, Addison-Wesley Publishing Company, Inc., 8th edition (1992)
- Yousfi M. & Benabdessadok M.D., Boltzmann equation analysis of electron-molecule collision cross sections in water vapor and ammonia, *Journal of Applied Physics* 80, 6619–6630 (1996)